

**TRAILING-EDGE NOISE ATTENUATION OF AIRFOIL  
BY MEANS OF COMB-SERRATION AT LOW  
REYNOLDS NUMBERS**

**BY**

**MOHAMED IBREN HASSAN**

**A thesis submitted in fulfilment of the requirement for the  
degree of Doctor of Philosophy in Engineering**

**Kulliyyah of Engineering  
International Islamic University Malaysia**

**NOVEMBER 2023**

## ABSTRACT

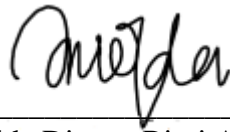
Low Reynolds number flow is three-dimensional and intricate due to multiple vortical phenomena. This research contributes by investigating the impact of laminar Separation Bubble (LSB) on noise generated by passive control techniques. It also enhances the understanding of the efficiency of various trailing edge designs such as serrations, comb, comb-serrated, and porous configurations, across different flow conditions and Reynolds numbers, while also addressing the limitations of existing geometrical models for trailing edges. The study intends to examine the performance of different configurations, emphasizing their effect on flow structure and acoustic responses. The methodology of this study encompasses a combination of techniques that includes conducting 2D simulations using the SST model, performing 3D simulations using large eddy simulation, employing FW-H acoustic modeling, and utilizing an experimental PIV setup. These methods collectively provide a comprehensive and robust platform for in-depth exploration of the research objectives. The analysis of the NACA0015 airfoil's flow characteristics revealed the presence of laminar separation bubbles (LSBs) at low Reynolds numbers and angles of attack. Two types of flow patterns, with and without reattachment, were identified. On the suction side, increasing the Angle of attack leads to a noticeable upstream shift of these points, while they move downstream along the pressure side. In 3D simulations, pressure distribution was symmetrical, with the maximum at the leading edge. No separation was observed except at the trailing edge tip. At higher angles of attack, the baseline airfoil experienced flow disturbances, laminar separation bubbles, and vortex shedding. The serrated, combed, and comb-serrated designs exhibited more stable flow patterns and fewer separation bubbles than the baseline, potentially reducing tonal noise. Conversely, the poro-serrated design led to distorted flow and an upstream-moving separation bubble, suggesting a possible increase in tonal noise. Moreover, results showed irregular broadband noise (300 - 600 Hz) with increased noise and shifting peak frequency as the Angle of attack rose. The serrated trailing edge design notably reduced noise levels by roughly 21 dB, especially for low frequencies. Comb-serration increased high-frequency noise by about 9 dB for angles of attack at 0, -1, and -2 degrees reduced approximately 9 dB for angles of attack at 1 degree and 2 degrees. On the other hand, the directivity pattern showed that the maximum noise level is observed to predominantly radiate at an azimuth angle of around 90 degrees for all the cases, ranging from 90 to 270 degrees, indicating that the majority of the source's acoustic energy is being emitted on the suction and pressure sides of the wing. In conclusion, the findings demonstrate that serrated and comb-serrated designs are beneficial in reducing noise levels, and that the Angle of attack can significantly impact both the noise level and directivity pattern.

## خلاصة البحث

تدفق أرقام رينولدز المنخفض ثلاثي الأبعاد معقد للغاية بطبيعته لتعدد أنواع الظواهر الدوامية. يساهم هذا البحث من خلال دراسة تأثير فقاعة الفصل الصفائحي (LSB) على الضوضاء الناتجة عن تقنيات التحكم السليبي. كما يحسن فهم كفاءة تصميمات الحواف الخلفية المختلفة مثل المسننات، والمشط، والمشط المسنن، والتكوينات المسامية، عبر مختلف حالات التدفق وأرقام رينولدز، مع معالجة القصور في النماذج الهندسية الموجودة للحواف الخلفية. الدراسة تهدف إلى فحص أداء تكوينات مختلفة، مع التركيز على تأثيرها على بنية التدفق والاستجابات الصوتية. منهجية الدراسة تشمل مزيجاً من التقنيات، تتضمن إجراء عمليات محاكاة ثنائية الأبعاد باستخدام نموذج SST و عمليات محاكاة ثلاثية الأبعاد باستخدام LES، واستخدام نموذج صوتي FW-H وإعدادات PIV التجريبي. هذه الأساليب مجتمعة توفر منصة شاملة وقوية للاستكشاف المتعمق لأهداف البحث. كشف تحليل خصائص تدفق الجنيح NACA0015 عن وجود فقاعات الفصل الصفائحي (LSBs) عند أعداد رينولدز المنخفضة وزوايا الهجوم. تم تحديد نوعين من أنماط التدفق، مع وبدون إعادة الارتباط. من جهة الشفط، تؤدي زيادة زاوية الهجوم إلى تحول ملحوظ في الاتجاه الصعودي لهذه النقاط نحو المنبع، بينما تتحرك باتجاه نزولي على طول جانب الضغط. في عمليات المحاكاة ثلاثية الأبعاد، كان توزيع الضغط متماثلاً، مع حد أقصى عند الحافة الأمامية. لم يلاحظ أي انفصال إلا عند طرف الحافة الخلفية. عند زوايا الهجوم الأعلى، تعرض الجنيح الأساسي لاضطرابات التدفق، وفقاعات الفصل الصفائحي، وتساقط الدوامية. أظهرت التصميمات المسننة والمشطية والمسننة أنماط تدفق أكثر استقراراً وفقاعات فصل أقل مقارنة بالأساس، مما يؤدي إلى تقليل الضوضاء النغمية. على العكس من ذلك، أدى التصميم المسنن المسامي إلى تدفق مشوه وفقاعة فصل تتحرك في اتجاه صعودي، مما يشير إلى زيادة محتملة في الضوضاء النغمية. علاوة على ذلك، أظهرت النتائج عدم انتظام ضوضاء النطاق العريض (300 - 600 هرتز) مع زيادة الضوضاء وتغير تردد الذروة كلما ارتفعت زاوية الهجوم. أدى تصميم الحافة الخلفية المسننة إلى تقليل مستويات الضوضاء بشكل ملحوظ بحوالي 21 ديسيبل، خاصة بالنسبة للترددات المنخفضة. أدى المشط المسنن إلى زيادة الضوضاء عالية التردد بنحو 9 ديسيبل لزوايا الهجوم عند درجات 0 و-1 و-2، كما حقق انخفاضاً بنحو 9 ديسيبل لزوايا الهجوم عند درجة ودرجتين. من ناحية أخرى، أظهر نمط الاتجاه أن مستوى الضوضاء الأقصى يشع في الغالب بزواوية سمت تبلغ حوالي 90 درجة لجميع الحالات، وتتراوح من 90 إلى 270 درجة، مما يشير إلى أن غالبية مصدر الطاقة الصوتية للمصدر تنبعث على جانبي الشفط والضغط للجناح. في الحتام، أظهرت النتائج أن التصميمات المسننة والمشطية مفيدة في تقليل مستويات الضوضاء، خاصة عند زوايا الهجوم العالية، وأن زاوية الهجوم يمكن أن يكون لها تأثير كبير على كل من مستوى الضوضاء ونمط الاتجاه.


## APPROVAL PAGE

The thesis of Mohamed Ibren Hassan has been approved by the following:



---

Amelda Dianne Binti Andan  
Supervisor



---

Waqar Asrar  
Chairman/ Co-Supervisor

---

Moumen Mohammed Mahmoud Idres  
Internal Examiner

---

Azmin Shakrine Mohd Rafie  
External Examiner

---

Akram M Z M Khedher  
Chairman

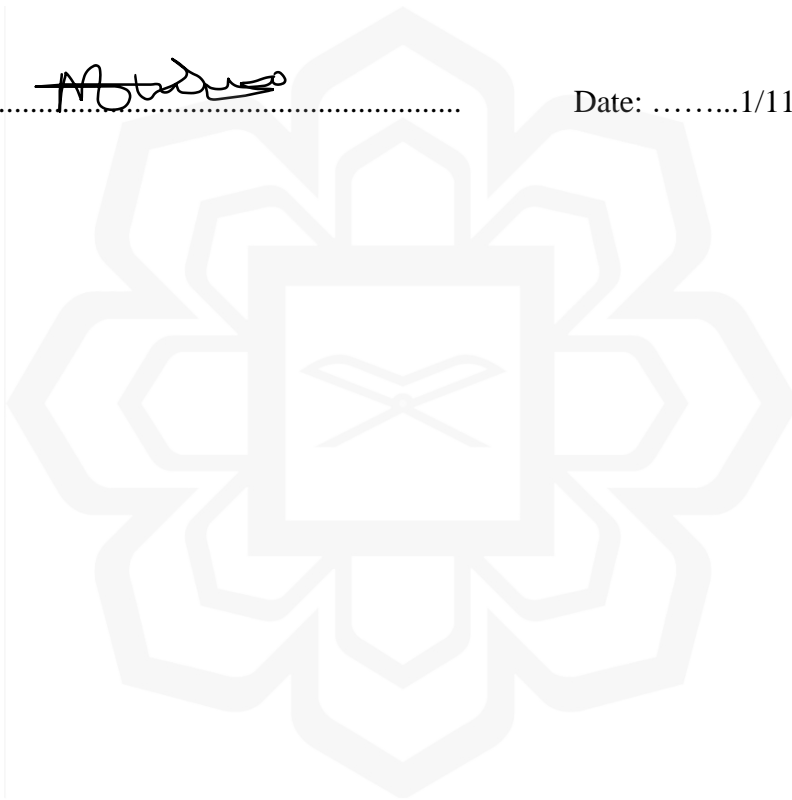


## DECLARATION

I hereby declare that this thesis is the result of my own investigations, except where otherwise stated. I also declare that it has not been previously or concurrently submitted as a whole for any other degrees at IIUM or other institutions.

Mohamed Ibren Hassan

Signature .....  ..... Date: .....1/11/2023.....



**DECLARATION OF COPYRIGHT AND AFFIRMATION OF  
FAIR USE OF UNPUBLISHED RESEARCH**

**TRAILING-EDGE NOISE ATTENUATION OF AIRFOIL BY  
MEANS OF COMB-SERRATION AT LOW REYNOLDS  
NUMBERS**

I declare that the copyright holders of this Thesis are jointly owned by the student and IIUM.

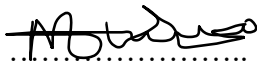
Copyright © 2023 Mohamed Ibren and International Islamic University Malaysia. All rights reserved.

No part of this unpublished research may be reproduced, stored in a retrieval system, or transmitted, in any form or by any means, electronic, mechanical, photocopying, recording or otherwise without prior written permission of the copyright holder except as provided below.

1. Any material contained in or derived from this unpublished research may be used by others in their writing with due acknowledgement.
2. IIUM or its library will have the right to make and transmit copies (print or electronic) for institutional and academic purposes.
3. The IIUM library will have the right to make, store in a retrieved system and supply copies of this unpublished research if requested by other universities and research libraries.

By signing this form, I acknowledged that I have read and understand the IIUM Intellectual Property Right and Commercialization policy.

Affirmed by Mohamed Ibren Hassan

  
.....

Signature

.....1/11/2023.....

Date

## ACKNOWLEDGEMENTS

*In the Name of Allah, the Most Compassionate, the Most Merciful*

With the blessings of Allah, the Most Merciful, the Most Compassionate, I begin this acknowledgement. All glory and praise belongs to Allah, the Sovereign Lord of all creation, and, peace be upon our beloved Prophet Mohammed (peace be upon Him).

I would like to express my sincere gratitude and offer my heartfelt thanks to all those who have supported me in this endeavor. Their encouragement and unwavering support have been a source of inspiration for me and has enabled me to reach this point. I am truly grateful for their presence in my life and the role they have played in helping me achieve this milestone.

I would like to express my sincerest gratitude to the aerodynamics laboratory of Universiti Pertahanan Nasional Malaysia (UPNM) for their generous support and provision of essential equipment that has enabled me to carry out my experimental work. I am deeply thankful to my colleagues in our mechanical lab for their tremendous collaboration and encouragement throughout this journey. I would like to extend a special recognition to my supervisory committee consisting of Dr. Amelda Dianne Binti Andan, Professor Waqar Asrar, and Dr. Erwin Suleiman, for their unwavering encouragement, guidance, and support. Their invaluable advice, constructive feedback, and relentless dedication to my success have been an integral part of my journey. I would also like to extend my acknowledgement to Dr. Mohammed Abdulmalek Aldheeb for his invaluable input and assistance in my experimental work. I am truly grateful for the support and guidance I have received from everyone involved in this project. Their contributions have made this experience truly enriching and rewarding.

My sincerest thanks go to my parents and my wife for their unwavering belief in me and their immense patience throughout this study. Their support has been invaluable, and I am deeply grateful. I would also like to extend my gratitude to my siblings for their constant encouragement and prayers throughout my life. Their love and support have been a constant source of strength and motivation, and I am blessed to have them in my life.

# TABLE OF CONTENTS

|   |           |
|---|-----------|
| Abstract .....                                      | ii        |
| Abstract in Arabic .....                            | iii       |
| Approval Page.....                                  | iv        |
| Declaration .....                                   | v         |
| Copyright Page.....                                 | vi        |
| Acknowledgements .....                              | vii       |
| Table of Contents .....                             | viii      |
| List of Tables .....                                | xi        |
| List of Figures .....                               | xii       |
| List of Symbols .....                               | xvi       |
| List of Abbreviations .....                         | xvii      |
| <br>  |           |
| <b>CHAPTER ONE: INTRODUCTION .....</b>              | <b>1</b>  |
| 1.1. Overview.....                                  | 1         |
| 1.2. Background of the Study .....                  | 1         |
| 1.3. Statement of the Problem.....                  | 4         |
| 1.4. Research Philosophy.....                       | 6         |
| 1.5. Research Objectives.....                       | 6         |
| 1.6. Research Scope .....                           | 6         |
| 1.7. Limitations of the Study .....                 | 8         |
| 1.8. Significance of the Study.....                 | 8         |
| 1.9. Thesis Structure .....                         | 9         |
| <br>  |           |
| <b>CHAPTER TWO: LITERATURE REVIEW.....</b>          | <b>10</b> |
| 2.1. Overview.....                                  | 10        |
| 2.2. Flow Structure at Low Reynold’s Number.....    | 10        |
| 2.3. Noise Mechanisms.....                          | 14        |
| 2.3.1. Types of Noise .....                         | 14        |
| 2.3.2. Noise Generation Mechanism.....              | 16        |
| 2.3.3. Factors Affecting Airfoil Noise .....        | 18        |
| 2.4. Flow and Noise Control.....                    | 20        |
| 2.4.1. Flow Control .....                           | 20        |
| 2.4.2. Influence on Aerodynamic Performance .....   | 21        |
| 2.4.3. Noise Control .....                          | 22        |
| 2.5. Parametric Designs of the Present Models ..... | 28        |
| 2.5.1. Design Based on Skin Friction.....           | 29        |
| 2.5.2. Design Based on Aperture Parameters.....     | 31        |
| 2.5.3. Design Based on Flow Characteristics.....    | 32        |
| 2.5.4. Design Based on Sawtooth Parameters.....     | 32        |
| 2.5.5. Future Studies .....                         | 33        |
| 2.6. Numerical Analysis .....                       | 34        |
| 2.7. Summary.....                                   | 39        |
| <br>  |           |
| <b>CHAPTER THREE: METHODOLOGY.....</b>              | <b>40</b> |
| 3.1. Introduction.....                              | 40        |
| 3.2. Model Descriptions.....                        | 41        |

|   |            |
|---|------------|
| 3.2.1. Baseline Model .....   | 42         |
| 3.2.2. Serrated Trailing-Edge Configuration .....                   | 43         |
| 3.2.3. Combed Trailing-Edge Type .....                              | 45         |
| 3.2.4. Comb-Serrated Trailing-Edge Model .....                      | 46         |
| 3.2.5. Poro-Serrated Trailing-Edge Configuration.....               | 47         |
| 3.3. Numerical Method .....   | 48         |
| 3.3.1. Computational Domain and Boundary Conditions.....            | 49         |
| 3.3.2. Spatial Grid .....   | 51         |
| 3.3.3. Numerical Scheme .....                                       | 53         |
| 3.3.4. Data Validation .....  | 60         |
| 3.4. Experimental Set-Up .....                                      | 61         |
| 3.4.1. Flow Facility .....  | 61         |
| 3.4.2. Particle Image Velocimetry (PIV) .....                       | 63         |
| 3.4.3. Surface Reflection.....                                      | 65         |
| 3.5. Summary.....   | 67         |
| <br>  |            |
| <b>CHAPTER FOUR: AERODYNAMIC AND FLOW FIELD INVESTIGATIONS.....</b> | <b>68</b>  |
| 4.1. Introduction.....  | 68         |
| 4.2. Computational Simulation .....                                 | 69         |
| 4.2.1. Two-Dimensional Numerical Simulation .....                   | 69         |
| 4.2.1.1 Comparison with other Study .....                           | 69         |
| 4.2.1.2 Mean Aerodynamic Characteristics.....                       | 71         |
| 4.2.2. Three-Dimensional Numerical Simulation .....                 | 78         |
| 4.2.2.1 Validation of the Computational Method.....                 | 79         |
| 4.2.2.2 Baseline Flow Field .....                                   | 82         |
| 4.2.2.3 Modified Trailing-Edge Flow Field .....                     | 85         |
| 4.2.3. Summary of the Numerical Simulation .....                    | 92         |
| 4.3. Experimental Results .....                                     | 93         |
| 4.3.1. Streamwise Velocity Field .....                              | 93         |
| 4.3.2. Flow Velocity Distribution .....                             | 98         |
| 4.3.3. Spanwise Vorticity .....                                     | 105        |
| 4.3.4. Summary of the Experimental Work .....                       | 112        |
| 4.4. Summary.....   | 113        |
| <br>  |            |
| <b>CHAPTER FIVE: AEROACOUSTIC SIMULATIONS.....</b>                  | <b>114</b> |
| 5.1. Introduction.....  | 114        |
| 5.2. Comparison with other Study .....                              | 114        |
| 5.3. Far-Field Noise Prediction.....                                | 116        |
| 5.3.1. Surface Pressure Fluctuations .....                          | 116        |
| 5.3.2. Sound Pressure Level.....                                    | 121        |
| 5.3.3. Peak Noise Level .....                                       | 126        |
| 5.3.4. Peak Frequency .....   | 130        |
| 5.3.5. Directivity Pattern .....                                    | 134        |
| 5.4. Summary.....   | 136        |
| <br>  |            |
| <b>CHAPTER SIX: CONCLUSION AND RECOMMENDATIONS .....</b>            | <b>138</b> |
| 6.1. Objective 1 – Conclusion 1 .....                               | 138        |
| 6.2. Objective 2 – Conclusion 2 .....                               | 139        |

|  |            |
|--|------------|
| 6.3. Objective 3 – Conclusion 3 .....          | 140        |
| 6.4. Objective 4 – Conclusion 4 .....          | 141        |
| 6.5. Recommendations for Further Studies ..... | 141        |
| <b>REFERENCES.....</b>                         | <b>143</b> |
| <b>PUBLICATIONS .....</b>                      | <b>155</b> |
| <b>APPENDIX A: ISO-POINTS JOURNAL .....</b>    | <b>156</b> |
| <b>APPENDIX B: ISO-SURFACE JOURNAL .....</b>   | <b>159</b> |
| <b>APPENDIX C: AUTOMATIC JOURNAL .....</b>     | <b>163</b> |



## LIST OF TABLES

|           |  |    |
|-----------|--|----|
| Table 2.1 | Comparison of previous trailing edge designs, limitations, and proposed present study design | 36 |
| Table 2.2 | Comparison of previous trailing edge designs, limitations, and proposed present study design | 40 |
| Table 3.1 | Parameters Used in 2D Particle Image Velocimetry (PIV) Measurements                          | 67 |



## LIST OF FIGURES

|             |  |    |
|-------------|--|----|
| Figure 1.1  | An Example of Noise Spectra of An Airfoil Discrete Tonal Noise (Arcondoulis, Arcondoulis, Doolan, & Zander, 2005)        | 2  |
| Figure 1.2  | The Unique Feather Features of the Owl, Key to its Silent Flight   | 4  |
| Figure 2.1  | Effect of Angle of attack on Separation Bubble   | 14 |
| Figure 2.2  | Types of Airfoil Self-Noise (Thomas F Brooks Et Al., 1989)   | 16 |
| Figure 2.3  | Necessary Criterion for Whistle Noise Emission (Desquesnes Et Al., 2007)   | 19 |
| Figure 2.4  | Sketch of a serrated trailing-edge incorporating the investigated dimensions of $h$ and $\lambda$ (Gruber et al., 2011a) | 24 |
| Figure 2.5  | Relationship between Skin Friction Ratio and Reynolds Number Based on Aperture Diameter                                  | 31 |
| Figure 2.6  | Relationship between Skin Friction Ratio and Depth-to-Diameter Ratio (Hwang, 2004)                                       | 32 |
| Figure 2.7  | Relationship between Skin Friction Ratio against void fraction (Hwang, 2004)   | 33 |
| Figure 3.1  | Flowchart of the methodology   | 43 |
| Figure 3.2  | Side view of the airfoil inside test section   | 44 |
| Figure 3.3  | Geometry of NACA0015 Airfoil Used in this Research   | 45 |
| Figure 3.4  | Top View of the Baseline Airfoil Model   | 45 |
| Figure 3.5  | Top View of the Serrated Model   | 46 |
| Figure 3.6  | Top View of the Serrated Model   | 46 |
| Figure 3.7  | Top View of the Comb Configuration   | 47 |
| Figure 3.8  | Top View of the Comb Configuration   | 47 |
| Figure 3.9  | Top View of the Comb-Serrated Model  | 48 |
| Figure 3.10 | Top View of the Comb Serrated Configuration  | 49 |
| Figure 3.11 | Top View of the Poro-Serrated Model  | 50 |
| Figure 3.12 | Top View of the Poro-Serrated Configuration  | 50 |
| Figure 3.13 | Boundaries and Dimensions of 2D Analysis Domain  | 52 |



|             |   |    |
|-------------|---|----|
| Figure 3.14 | Boundaries and Dimensions of 3D Analysis Domain   | 52 |
| Figure 3.15 | (a) C-Type Grid Topology (b) Detailed View of the LE (c) Detailed View of the TE                                | 53 |
| Figure 3.16 | (a) Mesh Convergence Analysis at $Re = 8.4 \times 10^4$ (b) Mesh Convergence Analysis at $Re = 1.7 \times 10^5$ | 54 |
| Figure 3.17 | Detailed View of the Mesh Around the Airfoil and at the TE  | 55 |
| Figure 3.18 | Schematic diagram illustrating the receiver locations   | 62 |
| Figure 3.19 | Turbulence Intensity as a Function of the Vertical Distance (UPNM, 2022)  | 64 |
| Figure 3.20 | Schematic of UPNM Open Loop Wind Tunnel (UPNM, 2014)  | 64 |
| Figure 3.21 | Schematic of PIV Setup in the Wind Tunnel   | 65 |
| Figure 3.22 | Surface Reflection from Musou and Flat Black Painted Surface at $\alpha = 0^0$                                  | 69 |
| Figure 4.1  | Comparison of Cl at Different Reynolds Numbers  | 72 |
| Figure 4.2  | Comparison of Cd at Different Reynolds Numbers  | 72 |
| Figure 4.3  | Pressure Coefficient at Different Reynolds Numbers  | 75 |
| Figure 4.4  | Skin Friction Coefficient at Different Reynolds Numbers   | 75 |
| Figure 4.5  | Mean Streamlines at Different Reynolds Numbers  | 77 |
| Figure 4.6  | Movement of Laminar Separation Bubble on the Suction of NACA 0015   | 78 |
| Figure 4.7  | Movement of Laminar Separation Bubble Pressure Side   | 78 |
| Figure 4.8  | Average Velocity Profile on the Pressure Side   | 79 |
| Figure 4.9  | Average Velocity Profile on the Suction Side  | 79 |
| Figure 4.10 | Comparison of the Present Work with a Numerical Study.  | 81 |
| Figure 4.11 | Validation of the Predicted Values with the Experimental Data   | 82 |
| Figure 4.12 | Validation of Numerical Result (a) with the Experimental Work (b) at $\alpha = 0^0$                             | 83 |
| Figure 4.13 | Validation of Numerical Result (a) with the Experimental Work (b) at $\alpha = 0^0$                             | 84 |
| Figure 4.14 | Pressure and Skin Friction Coefficient of the Baseline Airfoil at $\alpha = 0^0$                                | 85 |
| Figure 4.15 | X-Velocity Magnitude of the Baseline Airfoil at $\alpha = 0^0$  | 86 |
| Figure 4.16 | Velocity Profile of the Baseline Airfoil at $\alpha = 0^0$  | 87 |

|             |   |     |
|-------------|---|-----|
| Figure 4.17 | Pressure Coefficient of the Modified Models at $\alpha = 0^0$                       | 89  |
| Figure 4.18 | Skin Friction Coefficient of the Modified Models at $\alpha = 0^0$                  | 89  |
| Figure 4.19 | X-Velocity Contour at the Tip of the Modified Models ( $\alpha = 0^0$ ).            | 91  |
| Figure 4.20 | X-Velocity Contour at the Root of the Modified Models ( $\alpha = 0^0$ )            | 92  |
| Figure 4.21 | Top View Contour of X-Velocity Component for the Modified Models ( $\alpha = 0^0$ ) | 93  |
| Figure 4.22 | Velocity Profile of the Modified Airfoil Models at $\alpha = 0^0$                   | 94  |
| Figure 4.23 | Streamwise Velocity Component at $\alpha = 0^0$                                     | 96  |
| Figure 4.24 | Streamwise Velocity Component at $\alpha = 2^0$                                     | 97  |
| Figure 4.25 | Streamwise Velocity Component at $\alpha = 3^0$                                     | 98  |
| Figure 4.26 | Streamwise Velocity Component at $\alpha = 6^0$                                     | 98  |
| Figure 4.27 | Streamwise Velocity Component at $\alpha = 8^0$                                     | 100 |
| Figure 4.28 | Streamwise Velocity Component at $\alpha = 10^0$                                    | 101 |
| Figure 4.29 | Velocity Profile at $\alpha = 0^0$  | 102 |
| Figure 4.30 | Velocity Profile at $\alpha = 2^0$  | 103 |
| Figure 4.31 | Velocity Profile at $\alpha = 3^0$  | 104 |
| Figure 4.32 | Velocity Profile at $\alpha = 6^0$  | 105 |
| Figure 4.33 | Velocity Profile at $\alpha = 8^0$  | 106 |
| Figure 4.34 | Velocity Profile at $\alpha = 10^0$   | 107 |
| Figure 4.35 | Spanwise Vorticity at $\alpha = 0^0$  | 109 |
| Figure 4.36 | Spanwise Vorticity at $\alpha = 2^0$  | 109 |
| Figure 4.37 | Spanwise Vorticity at $\alpha = 3^0$  | 111 |
| Figure 4.38 | Spanwise Vorticity at $\alpha = 6^0$  | 112 |
| Figure 4.39 | Spanwise Vorticity at $\alpha = 8^0$  | 114 |
| Figure 4.40 | Spanwise Vorticity at $\alpha = 10^0$   | 114 |
| Figure 5.1  | Normalized Surface Pressure Fluctuations at $\alpha = 4^0$                          | 119 |
| Figure 5.2  | Time Histories Of The Normalized Wall Pressure at $\alpha = 0^0$                    | 120 |
| Figure 5.3  | Time Histories Of The Normalized Wall Pressure at $\alpha = 1^0$                    | 122 |
| Figure 5.4  | Time Histories Of The Normalized Wall Pressure at $\alpha = -1^0$                   | 122 |
| Figure 5.5  | Time Histories Of The Normalized Wall Pressure at $\alpha = 2^0$                    | 123 |
| Figure 5.6  | Time Histories Of The Normalized Wall Pressure at $\alpha = -2^0$                   | 125 |

|             |   |     |
|-------------|---|-----|
| Figure 5.7  | Sound Pressure Level as a Function of Frequency at the Suction Side (a) $\alpha = 0^{\circ}$ (b) $\alpha = 1^{\circ}$ (c) $\alpha = -1^{\circ}$ (d) $\alpha = 2^{\circ}$ And (e) $\alpha = -2^{\circ}$  | 126 |
| Figure 5.8  | Sound Pressure Level as a Function of Frequency at the Wake Region (a) $\alpha = 0^{\circ}$ (b) $\alpha = 1^{\circ}$ (c) $\alpha = -1^{\circ}$ (d) $\alpha = 2^{\circ}$ And (e) $\alpha = -2^{\circ}$   | 128 |
| Figure 5.9  | Sound Pressure Level as a Function of Frequency at the Pressure Side (a) $\alpha = 0^{\circ}$ (b) $\alpha = 1^{\circ}$ (c) $\alpha = -1^{\circ}$ (d) $\alpha = 2^{\circ}$ And (e) $\alpha = -2^{\circ}$ | 129 |
| Figure 5.10 | The Influence of Angle of attack on the Maximum Noise Level on the Suction Side of the Airfoil  | 131 |
| Figure 5.11 | The Influence of Angle of attack on the Maximum Noise Level at the Wake Region of the Airfoil   | 132 |
| Figure 5.12 | The Influence of Angle of attack on Maximum Noise Level on the Pressure Side of the Airfoil   | 133 |
| Figure 5.13 | The Frequency of the Highest Noise Level on the Suction Side for Various Angles of Attack   | 135 |
| Figure 5.14 | The Frequency of the Highest Noise Level at the Wake Region for Various Angles of Attack  | 136 |
| Figure 5.15 | The Frequency of the Highest Noise Level on the Pressure Side for Various Angles of Attack  | 138 |
| Figure 5.16 | The Directivity of the Acoustic Signals Measured at a Radial Distance of 12 Chords from the Airfoil Center  | 140 |

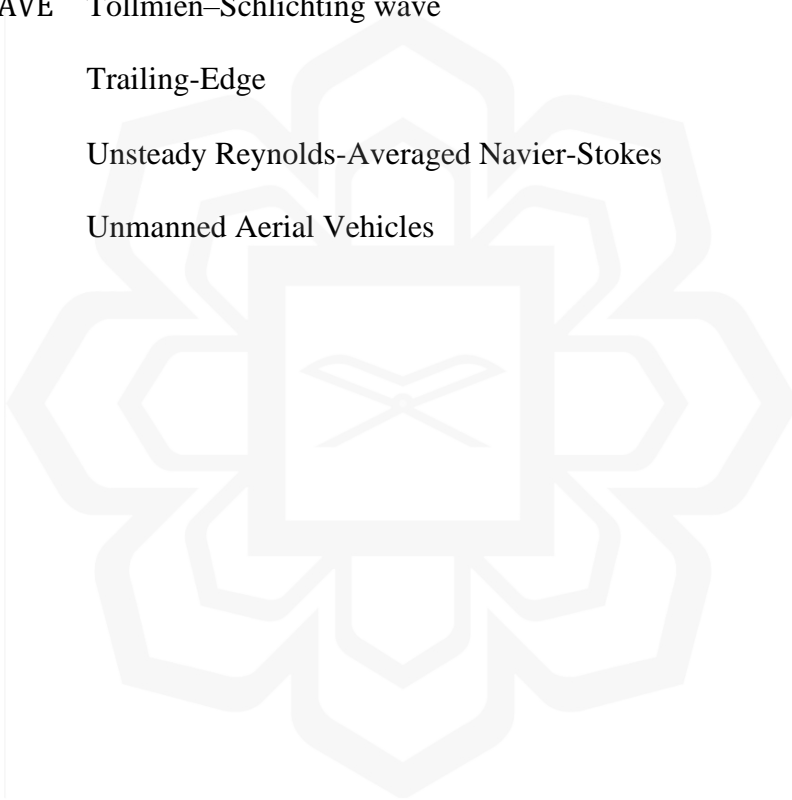
## LIST OF SYMBOLS

|            |  |
|------------|--|
| $c$        | Chord Length                                       |
| $C_d$      | Drag Coefficient                                   |
| $C_f$      | Skin Friction Coefficient                          |
| $C_l$      | Lift Coefficient                                   |
| $C_p$      | Pressure Coefficient                               |
| $E$        | Porosity   |
| $f_n$      | Centre frequency of the broadband noise            |
| $f_s$      | Series of Secondary Tone                           |
| $2h$       | Height of the sawtooth part                        |
| $l$        | Extent of the porous region                        |
| $P'$       | Normalized Pressure Fluctuation                    |
| $\Delta t$ | Interval Time                                      |
| $U$        | Free-Stream Velocity                               |
| $V$        | Normal Velocity                                    |
| $\omega_z$ | Spanwise Vorticity                                 |
| $\Delta x$ | Displacement                                       |
| $\alpha$   | Angle of attack                                    |
| $\alpha_s$ | Angle of ridges with respect to the flow direction |
| $\lambda$  | Wavelength of the ridges                           |

## LIST OF ABBREVIATIONS

|        |                             |
|--------|-----------------------------|
| 2D     | Two-Dimensional             |
| 3D     | Three-Dimensional           |
| AOA    | Angle of attack             |
| BL     | Boundary Layer              |
| CAA    | Computational Aeroacoustics |
| Cd     | Drag Coefficient            |
| CFD    | Computational Fluid Dynamic |
| Cl     | Lift Coefficient            |
| DNS    | Direct Numerical Simulation |
| dB     | Decibels                    |
| FW – H | Ffowcs Williams–Hawkings    |
| HLFC   | Hybrid Laminar Flow Control |
| LBL    | Laminar Boundary Layer      |
| LE     | Leading-Edge                |
| LES    | Large Eddy Simulation       |
| LFC    | Laminar Flow Control        |
| LSB    | Laminar Separation Bubble   |
| MAVs   | Micro Air Vehicles          |
| MBT    | Micro-Blowing Technology    |
| NLF    | Natural Laminar Flow        |
| PTU    | Programmable Timing Unit    |
| PIV    | Particle Image Velocimetry  |

|                    |  |
|--------------------|--|
| RANS               | Reynolds-Averaged Navier-Stokes          |
| Re                 | Reynolds Number                          |
| SA                 | Spalart-Allmaras Turbulence Model        |
| SGS                | Subgrid-Scale                            |
| SPL                | Sound Pressure Level                     |
| SPL <sub>1/3</sub> | Third Octave Sound Pressure Level        |
| SST                | Shear-Stress Transport                   |
| TS – WAVE          | Tollmien–Schlichting wave                |
| TE                 | Trailing-Edge                            |
| URANS              | Unsteady Reynolds-Averaged Navier-Stokes |
| UAVs               | Unmanned Aerial Vehicles                 |



# CHAPTER ONE

## INTRODUCTION

### 1.1. OVERVIEW

The introduction chapter of this thesis includes a complete review of the study background, problem statement, research philosophy, scope, limitations, and objectives. This chapter commences with an overview of the introduction to the topic under consideration, followed by a concise description of the research problem and the reasoning for the suggested solution based on the philosophical approach of the study. The scope of the research is clearly defined, with a special focus on addressing the problem statement. The research objectives are then provided in a systematic and ordered way, offering a roadmap for the completion of the study. Finally, the chapter concludes with the outline of the thesis, offering a comprehensive summary of the organization and content of the research.

### 1.2. BACKGROUND OF THE STUDY

Noise pollution is a continuous issue that substantially influences the environment and the well-being of humans. Loud and undesired noises can induce disruption and stress and might be regarded as a severe environmental stressor. Research has found that airfoils operating within low to moderate Reynolds numbers ( $Re = 10^4 - 10^5$ ) are known to emit a unique sort of noise known as whistle-like tonal noise. This form of noise adds to the total environmental noise and is viewed as discomforting by people exposed to it (Wagner et al., 2007). Tonal noise may be experienced in several of circumstances, such as on blunt models and airfoil-like designs, buildings, fans, wind turbines, unmanned aerial vehicles (UAVs), and more. Given the widespread prevalence and effect of tone noise, it is vital to know the underlying mechanisms and situations that create it. This information may be utilized to design effective methods for limiting its impact and decreasing the related environmental and health hazards. Furthermore, understanding the behaviour of tonal noise can lead to the development of

new technology and ways to decrease noise pollution, increase human quality of life, and safeguard the environment.

Schumacher et al. (2014) first described the generation of discrete tonal noise from airfoil surfaces operating at relatively moderate Reynolds numbers (Schumacher et al. 2014). The tonal noise is a composition of broadband noise focused on a single frequency, and discrete tonal noise. The occurrence of tonal noise is influenced by the thickness of the Trailing-edge (TE) and the Boundary Layer (BL) displacement thickness, as evidenced by Ramirez and Wolf (Ramírez & Wolf, 2016). The noise generation can also be affected by various geometric factors, such as thickness, chord, profile, and Angle of attack. Other factors such as spanwise curvature and surface roughness also play a role but are subject to strict engineering constraints. Paterson et al. (1973) reported the presence of discrete and numerous tones in a ladder-like structural pattern, which is dependent on the frequency and free-stream velocity. Tonal noise with high intensity is often regarded as more disturbing than broadband noise. Arbey & Bataille (1983) ascribed the broadband contribution to the diffraction of pressure waves near the TE. The discrete frequencies are made of a primary frequency tone with the maximum intensity, and its respective secondary frequency tones are uniformly spaced, as indicated in Figure 1.1.

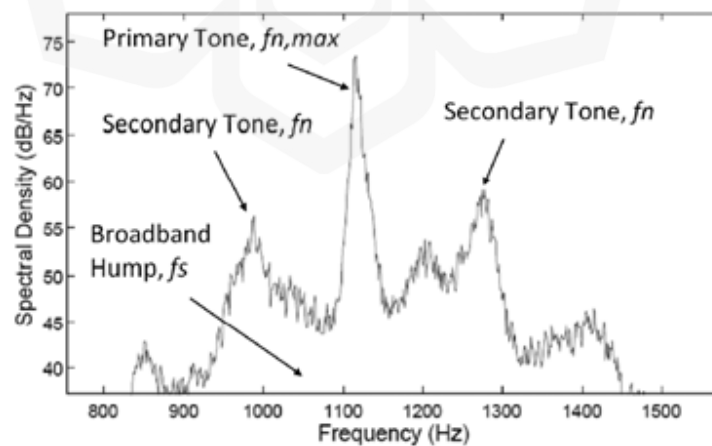


Figure 1.1 An example of noise spectra of an airfoil discrete tonal noise (Arcondoulis et al., 2005)



The aviation industry has made tremendous progress in lowering the noise created by aircraft airfoils and helicopter blades via acoustically adapted materials and design improvements. Efforts to regulate fluid flow have led to the suggestion of strategies such as Laminar Flow Control (LFC), Natural Laminar Flow (NLF), and Hybrid Laminar Flow Control (HLFC) (Joslin, 1998). However, the practical implementation of NLF is hindered by its association with substantial pressure drag. Milestones have been made in the knowledge of flow physics, acoustic wave scattering, and noise propagation, leading to the introduction of various trailing-edge noise-reducing technologies (Joslin, 1998). These techniques are categorized into passive and active control approaches, with the former aiming to improve scattering conditions by altering physical and geometrical features of the TE and the latter acting on changing the flow structure through unsteady pressure fluctuations upstream of the trailing edge. Recently, numerous passive control approaches have been proposed and investigated, including using serrations, porous materials, finlets, surface treatments, shape optimization, morphing, and flexible materials. These strategies seek to increase aerodynamic performance while minimizing noise produced at the TE (Tze et al., 2016).

The study of silent flight in birds, notably the owl, has been a topic of continuous research in of aerodynamics. Figure 1.2 highlights the distinctive feather characteristics of the owl, which play a significant role in decreasing noise and contributing to the owl's reputation as the quietest flying bird. This has prompted contemporary research attempts to study the processes behind the owl's ability to fly so softly and to apply these results to numerous sectors, such as aviation. The attention to the owl's feather characteristics underlines the value of learning from nature and transferring these lessons into human technology. By acquiring a greater knowledge of the owl's quiet flight, researchers want to create more effective and efficient noise reduction solutions for many applications. This study primarily focuses on applying poro-serrated, serrated, combed, and comb-serrated trailing-edge designs to optimize the flow structure and minimize noise generation at the TE, as shown in Figure 3.4 – 3.12.

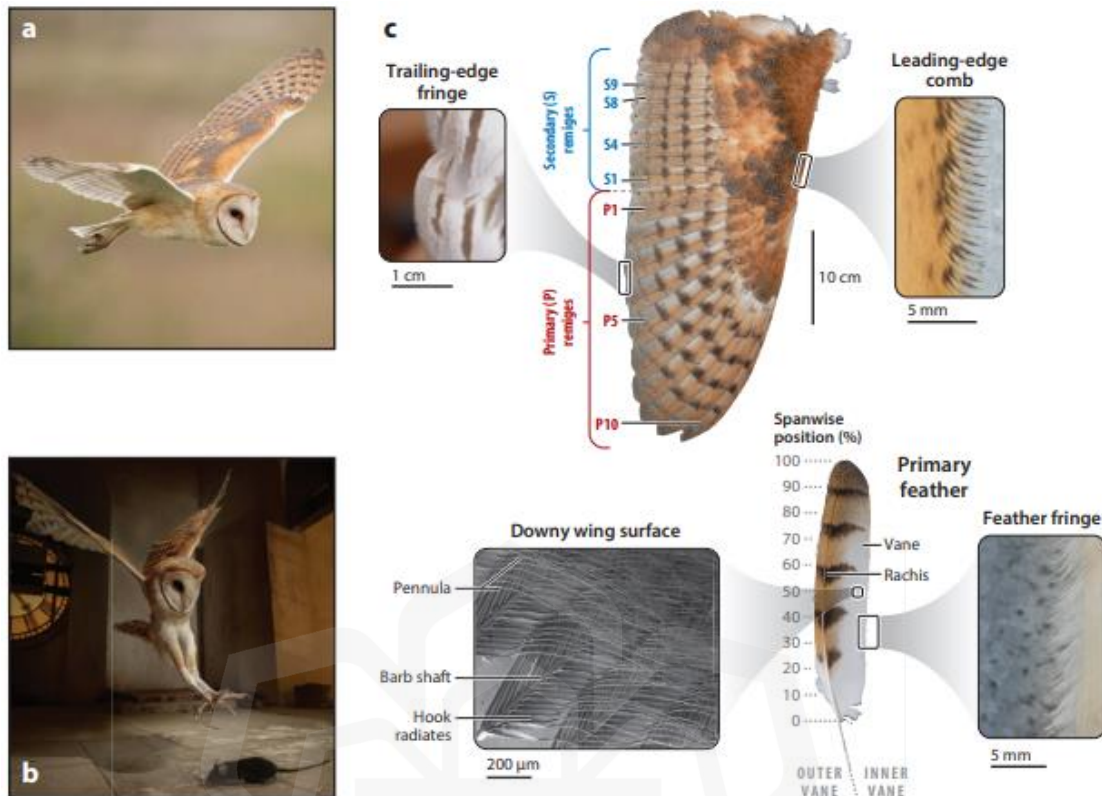


Figure 1.2 The Unique Feather Features of the Owl, Key to Its Silent Flight (Jaworski & Peake, 2020).

### 1.3. STATEMENT OF THE PROBLEM

Aircraft noise has become a critical concern since the 1970s as the number of airports and commercial aircraft has increased. The adverse effects of aeroplane noise on human health have necessitated stricter regulations in the aviation sector. Although great progress has been achieved in decreasing jet engine noise, experts have advocated for more investigations into reducing noise from other aircraft elements. Various experimental, computational, and theoretical studies have focused on minimizing trailing-edge noise, with serrations being regarded as one of the most successful methods based on bio-inspired research. However, the efficiency of serrations, comb, and porous trailing edge is still not well understood. It is reliant on flow topology, and most experiments have been undertaken at low Reynolds numbers ( $R_e \approx 10^4$ ). Furthermore, the collective impact of the serrated and comb design models has not been

thoroughly examined. Upon closer examination of owl feathers, it is evident that their shapes exhibit inconsistency. Consequently, it is imperative to delve comprehensively into this aspect to grasp its contribution to effective noise reduction. This is precisely why the comb-serrated model is being employed as one of the models in this study.

Additionally, there is a need to broaden the current understanding of the discrete tonal behaviour of NACA0015 airfoil, as relatively little experimental and numerical analysis has been undertaken at moderate Reynolds numbers and various angles of attack, which have more practical applications. Additionally, the NACA 0015 airfoil is preferred due to its utilization as a symmetric airfoil with increased thickness in compared to the more frequently employed NACA 0012 airfoil. Investigating the effect of this difference in thickness becomes essential in comprehending the distinctive tonal behavior exhibited by the NACA 0015 airfoil. The airfoil tonal emission is tied to the amplification of naturally existing instabilities inside the laminar boundary layer (LBL); however, these instabilities alone do not always contribute to tonal noise. Instead, the extent and location of the LSB also have an impact on the emitted tonal noise. Despite the viability of this finding, the fundamental physical reasons causing airfoil tonal noise still need to be fully understood.

The present research strives to thoroughly understand the tonal noise process and related physical phenomena by conducting wind tunnel tests and CFD simulations, evaluating the flow structure and tonal noise over an airfoil impacted by whistle tonal noise. Additionally, the study will evaluate the influence of passive flow control systems on airfoil noise emission and flow structure. Given the limited research on controlling airfoil tonal noise without negatively affecting flow structure, the study seeks to find effective methods to improve the noise performance and enhance the flow characteristics at relatively moderate Reynolds number ( $1.7 \times 10^5$ ) and varying angles of attack ( $-2 \leq \alpha \leq 2$  deg). The selection of Reynolds numbers and angles of attack for investigation is based on the observation that discrete tonal noise becomes more noticeable at lower Reynolds numbers and angles of attack, following previous research findings.

#### **1.4. RESEARCH PHILOSOPHY**

The scientific concept driving the analysis of airfoil tonal noise and its reduction is based on the knowledge of the link between the physics of flow and the generation of tonal noise. This research will tackle this problem by conducting flow visualization using wind tunnel experiments and CFD simulations to examine the flow structure and tonal noise mechanism over an airfoil under the effect of whistle tonal noise. It has been noted that the induced tonal radiation is dependent primarily on the Reynolds number and Angle of attack. Therefore, this research will examine the airfoil tonal emission at moderate Reynolds numbers and varied angles of attack that have more practical uses. In addition, the influence of flow control techniques on airfoil noise emission and flow structure needs to be explored. Therefore, this research will also attempt to conduct passive flow control over the NACA0015 airfoil to enhance its noise performance and flow characteristics. Overall, this study is motivated by the notion that a better understanding of the underlying physics of flow and tonal noise will lead to developing effective and efficient noise-reducing strategies for many practical applications.

#### **1.5. RESEARCH OBJECTIVES**

The main objectives of this research are:

- 1- To determine the influence of Reynolds number and angles of attack on the flow field structure over NACA0015 airfoil.
- 2- To investigate the noise emitted over NACA0015 airfoil at different angles of attack and a moderate Reynolds number.
- 3- To determine the effect of flow control techniques on the aerodynamic and flow field characteristics.
- 4- To evaluate effective noise-reducing methods for airfoil tonal noise based on passive techniques.

#### **1.6. RESEARCH SCOPE**

The study focuses on examining the link between the physics of flow and the generation of tonal noise over a NACA0015 airfoil as relatively little experimental and numerical

analysis has been undertaken at moderate Reynolds numbers and various angles of attack, which have more practical applications. Additionally, the NACA 0015 airfoil is preferred due to its utilization as a symmetric airfoil with increased thickness compared to the more frequently employed NACA 0012 airfoil. The purpose is to better understand the tonal noise mechanism and discover efficient reduction methods. Furthermore, this thesis focuses on a specific range of conditions for analysis. In the 2D analysis, the scope encompasses relatively low Reynolds numbers (ranging from  $8.4 \times 10^4$  to  $1.7 \times 10^5$ ) and moderate angles of attack (ranging from 0 to 6 degrees). For 3D analysis, the chosen parameters are a moderate Reynolds number of  $1.6 \times 10^5$  and a zero Angle of attack, driven by available published data. The experimental tests further emphasize a moderate Reynolds number of  $1.7 \times 10^5$ , with variations in angles of attack spanning from 0 to 12 degrees.

To comprehensively understand the issue, the research will apply a multi-disciplinary strategy combining flow visualization experiments with computational fluid dynamics (CFD) simulations. The measurement of the flow structure and flow visualization experiments will be undertaken by applying the Particle Image Velocimetry (PIV) technique to the flow over an airfoil at moderate Reynolds number and varied angles of attack in a wind tunnel setup.

In addition, the research will also use CFD models to support the experimental data. The simulations will include 2D analysis using the SST turbulence model and 3D analysis with the Large Eddy Simulation (LES) method. These simulations will give more insights into the fundamental physics of flow and tone noise creation across the airfoil. Moreover, the research intends to analyze the influence of passive flow control strategies on the airfoil's noise emission and flow structure. This element of the study is significant as it will assist in evaluating if flow control measures can be employed to minimize both tonal and broadband noise while still maintaining or enhancing the aerodynamic efficiency of the airfoil.

In conclusion, the research scope of this study is aimed at offering significant insights into the generation of airfoil tonal noise and the possibility of its reduction

through flow control methods. The findings of this research will lead to the development of effective and efficient noise-reducing techniques for practical applications.

### **1.7. LIMITATIONS OF THE STUDY**

The constraints of this study are mostly concentrated upon the fabrication, computational fluid dynamics (CFD), and particle image velocimetry (PIV) parts of the research. The fabrication process provides obstacles in creating tiny holes in poro-serrated models and sharp edges in serration, comb, and comb-serrated models, leading to modifications in the original designs. The restrictions in the computational fluid dynamics (CFD) part of the study are mostly connected to the availability of high-performance computer resources. Each simulation demands a great amount of time, requiring around one and a half months, due to using finer and more complex meshes and implementing of the large eddy simulation (LES) computational model. Finally, the challenges with PIV, particularly surface light reflections, provide a considerable hurdle to producing correct findings.

### **1.8. SIGNIFICANCE OF THE STUDY**

The research contributes to the field by:

1. Providing valuable insights that will assist in developing effective and efficient noise-reducing innovations for practical applications.
2. Adding new insights into the influence of numerous passive flow control systems on the airfoil's noise emission and flow structure.
3. The work contributes to current knowledge by presenting new information on using Musou black paint in the particle image velocimetry (PIV) system, which has not been previously explored. Musou Black Paint is used for mitigating light reflections and enhancing precision in PIV results, enriching our methodology with a novel technique. This notable improvement becomes evident when contrasting the outcomes achieved with this paint against those yielded by the conventional flat-black paint commonly employed in similar studies, as illustrated in Figure 3.19.

4. The research offers a comprehensive model (comb-serrated) that considers the effects of both serrated and combed trailing edges on flow and noise. These new techniques offer additional noise reduction and a further understanding of the flow field.

## **1.9. THESIS STRUCTURE**

This thesis is composed of six chapters. The first chapter is an introduction that comprises a general overview, background information, research objectives, a problem statement, and the scope of the study. The second review of the preceding research concerning the noise mechanism, flow characteristics at low Reynolds numbers, and several flow and noise control approaches. Additionally, the chapter provides a comprehensive explanation of the numerical analysis. The third chapter explains the methods utilized in the research, including an in-depth discussion of the particle image velocimetry, wind tunnel, and experimental models, as well as the preparation and setup of the equipment. Furthermore, the chapter details the computational fluid dynamics approach employed in this work. The fourth and fifth chapter summarizes the outcomes of the investigation, including the flow structure, and aeroacoustics findings respectively. Finally, the sixth chapter summarizes the analysis and outlines the important contributions and recommendations.

## CHAPTER TWO

### LITERATURE REVIEW

#### 2.1. OVERVIEW

The research of self-generated noise derives inspiration from the amazing quiet flying of owls, attributable to their unique airfoil and feather properties. Characteristics such as fringes and downy airfoil surfaces have been demonstrated to dramatically minimize noise in the auditory range of their prey and the owl. Further in-depth physical investigation is essential for a greater understanding of these systems. Nevertheless, a comprehensive investigation is required, given the complicated interplay of numerous traits and behaviours in owl flying. The findings of this study may ultimately lead to a clearer grasp of the processes underpinning silent flying. Therefore, this section discusses a comprehensive review of previous research and relevant literature on noise mechanisms, flow characteristics at low Reynolds numbers, and various flow and noise control strategies. Additionally, an overview of the basic principles of particle image velocimetry and numerical analysis provides a comprehensive understanding of the field.

#### 2.2. FLOW STRUCTURE AT LOW REYNOLD'S NUMBER

The research on low Reynolds numbers ( $Re < 10^6$ ) has demonstrated significant improvement because of technological progress (Kurelek et al., 2021). For example, the rapid advancement of the unmanned aerial vehicles often used in everyday operations has sparked the attention of many researchers, but the topic is a great challenge, especially in understanding the flow phenomena owing to the intricacies of the flow field (Kurelek et al., 2021; Singh, 2019).

Adverse pressure gradient forces the laminar boundary layer (LBL) to separate on the airfoil upper surface at a relatively low Reynolds number, promoting the development of a separated shear layer (Carmichael, 1981; ElJack, 2017; Alam &



Sandham, 2000; Miozzi et al., 2019). Likewise, in situations with a considerable adverse pressure gradient combined with low momentum, the flow will continue to separate, giving rise to a substantial wake (Council & Boulama, 2013). Furthermore, the instability of a separated shear layer to disturbances facilitates the swift development of vortices (Borgmann et al., 2021). The formation and evolution of vortices play a vital role in shaping the flow and significantly impact the development of separation bubbles (Kurelek et al., 2021). The initial instabilities that trigger the formation of vortices are created by upstream disturbances occurring prior to the separation point (Kurelek et al., 2021). Therefore, the behavior of the flow should be carefully analyzed, considering the impact of these factors on the flow mechanism.

In addition, flow separation may disrupt the boundary layer (BL), leading to the emergence of hydrodynamic instabilities. The resulting instabilities undergo non-uniform breakdown, leading to a chaotic flow pattern (Borgmann et al., 2021; Malkiel et al., 1996). Changes in fluid pressure and velocity are intimately linked to the characteristics of the flow. Alternatively, the flow builds momentum and rapidly transitions to a turbulent state (Malkiel et al., 1996; Sandberg et al., 2009). Vortical structures referred to as the “reverse-flow vortex” then cause the reattachment of the turbulent flow (ElJack, 2017; Sandberg et al., 2009). The reattachment of the enhanced shear layer on the surface generates a confined recirculation area, commonly referred to as a laminar separation bubble (LSB) (Malkiel & Mayle, 1996; ElJack, 2017; Sandberg et al., 2009). Further downstream from the LSB, the turbulent flow may undergo separation again or reattach to the trailing edge of the surface (Council & Boulama, 2013).

In the low Reynolds number range, the laminar separation bubbles are commonly observed. These bubbles can be categorized into two forms, namely short and long bubbles. At a displacement thickness  $\delta s^*$  and chord length  $C$ , observations have shown that the length of short bubbles ranges from  $0.1C$  and  $102\delta s^*$  to  $103\delta s^*$ . Alternatively, the extent of the long bubbles is of the order of  $104\delta s^*$  (Owen et al., 1953). Additionally, short bubbles tend to impact the external potential flow, while long bubbles can affect the pressure distribution across a surface (Sandberg et al., 2009). A small variation of Reynolds number and Angle of attack affects the formation,

breakdown, or disappearance of laminar separation bubbles (Mcgranahan & Selig, 2003). Moreover, short bubbles may rupture and form larger bubbles that reattach far downstream or fail to reattach at a moderate Angle of attack. Below the stall angle, the bubble governs the transition process, while the bubble's bursting determines the stall behavior of the model (Borgmann et al., 2021; Sandberg et al., 2009). Additionally, the characteristics of the bubble, including bursting, can influence the aerodynamic performance. Bubbles can increase lift, enhance unsteadiness, and decrease the drag coefficient (Bernardos et al., 2019; Borgmann et al., 2021; Uthra & Antony, 2020). In addition to Reynolds number and Angle of attack, the wake characteristics are also influenced by turbulence intensity and airfoil geometry. These factors may affect the generated vortex's size, rotational direction, and shedding frequency (Council & Boulama, 2011). Also, the factors that govern the bursting of bubbles, along with a potential semi-empirical approach for analyzing bubble growth, were described (Gaster, 1963, 1969; Horton, 1967). It is noteworthy to mention that in identical experiments conducted at different facilities, the size, location, and structure of LSB may vary (Mcauliffe et al., 2005).

As the Angle of attack increases, the BL separation gradually diminishes, resulting in a reduction in the size and length of LSB on the bottom side of the airfoil (Figure 2.1). Moreover, as the Angle of attack increases, the laminar separation points on the upper surface shift rapidly from the trailing edge towards the mid-chord, finally reaching the leading edge (Kim & Chang, 2014). As a consequence, the transition of the flow on the airfoil upper side advances towards the upstream direction. In contrast, the BL on the bottom side remains laminar and extends closer to the TE before separating to form a LSB (Plogmann et al., 2013). Additionally, the airfoil's profile and thickness also impact the LSB's size. Altering the Angle of attack was observed to have a notable impact on both the flow structure and the aerodynamic performance (Maet al., 2015).

Numerous investigations have indicated that the aerodynamic characteristics of airfoils are highly dependent on the flow features at low Reynolds numbers (Council & Boulama, 2013). For instance, a slight alteration in the airfoil profile can significantly influence the lift coefficient, separation point, and stalling (Selig et al., 1996). In low

Reynolds number conditions, separation of the flow and subsequent stalling can harm vehicle's aerodynamic performance and structural load (Lissaman, 1983). Due to their susceptibility to separation and stalling, there is a growing interest in developing effective control methods to improve the aerodynamic and acoustic performance of airfoils at low Reynolds numbers. A thorough understanding of laminar separation bubbles is crucial to achieve this goal. Previous studies have shown that both angles of attack and Reynolds number influence these bubble's development, length, and position. They can significantly impact airfoil aerodynamic characteristics and contribute to airfoil tonal noise. Flow visualization experiments are performed to examine the physical flow features to investigate the mechanisms underlying airfoil tonal noise.

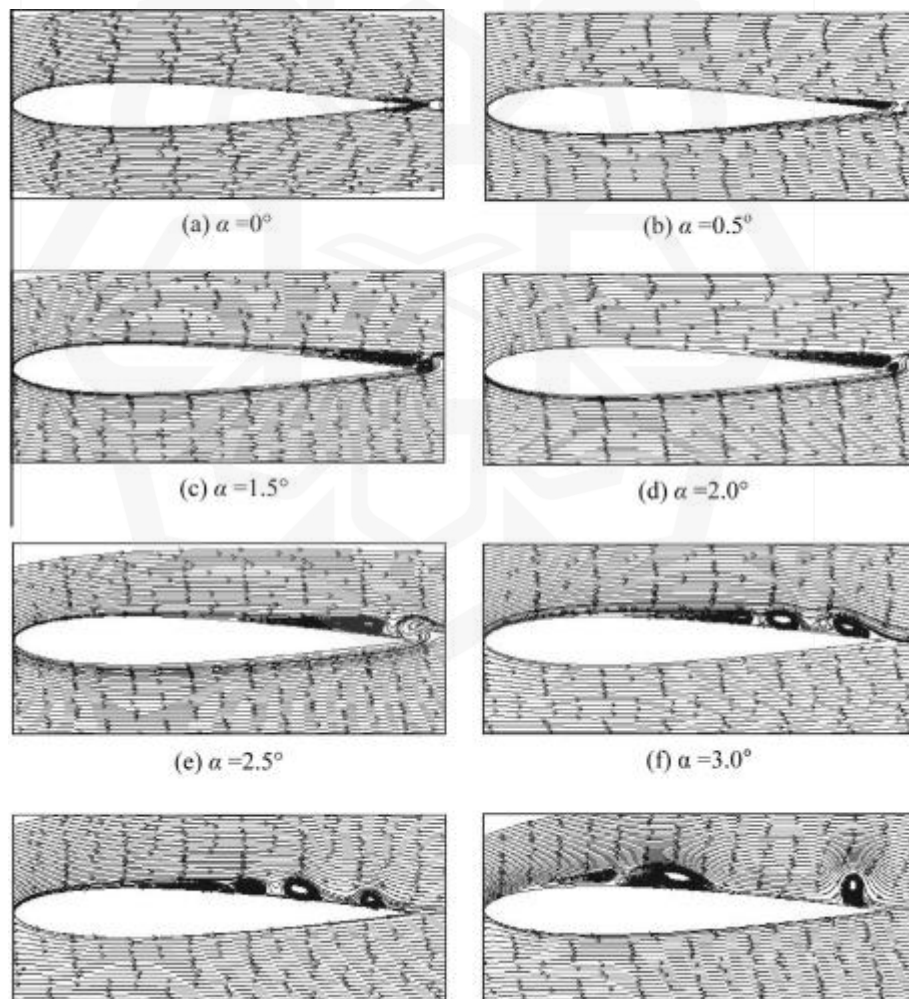


Figure 2.1 Effect of Angle of attack on separation bubble

(Lei et al., 2013)

## 2.3. NOISE MECHANISMS

### 2.3.1. Types of Noise

The generated sound can be classified as mechanical or aeroacoustic noise (Barone, 2011). Mechanical noise can be reduced by isolating mechanical vibrations and using materials that absorb sound (Crivellini et al., 2014). However, aeroacoustic noises are more prevalent and challenging to reduce (Jakobsen, 1993). Aeroacoustic noise is classified into: airfoil self-noise and turbulent inflow noise (Barone, 2011). Airfoil self-noise is categorized into several types, including Turbulent Boundary Layer - Trailing-Edge Noise, Laminar Boundary Layer - Vortex-Shedding Noise, Separation-Stall Noise, Trailing Edge Bluntness Vortex-Shedding Noise, and Tip Vortex Formation Noise (Figure 2.2) (Brooks et al., 1989). These noises are associated with conditions below the speed of sound. When the Reynolds number is relatively low, instabilities within the laminar boundary layer (LBL) interact with the trailing edge, resulting in noise. At higher Reynolds numbers, noise is produced through the interaction of the turbulence layer with the trailing edge. At angles of attack greater than zero, flow separation occurs from the surface, causing acoustic waves to be emitted due to stall and reverse flow. Finally, acoustic signals are also generated by vortices created at the trailing edge and near the airfoil tip. Turbulent Boundary Layer - Trailing-Edge Noise is the primary source of noise in various applications (Brooks et al., 1989; Guo & Thomas, 2019), although its impacts were initially overlooked (Guo & Thomas, 2019). Turbulent Boundary Layer - Trailing-Edge Noise is generated when turbulence oscillations within the BL at the trailing edge scatter, resulting in noise radiation (Barone, 2011). However, In another study, a well-explained equation and concept that help to understand how the intensity of the sound pressure that leads to the TE noise is related to various flow features is provided (Brooks et al., 1989).

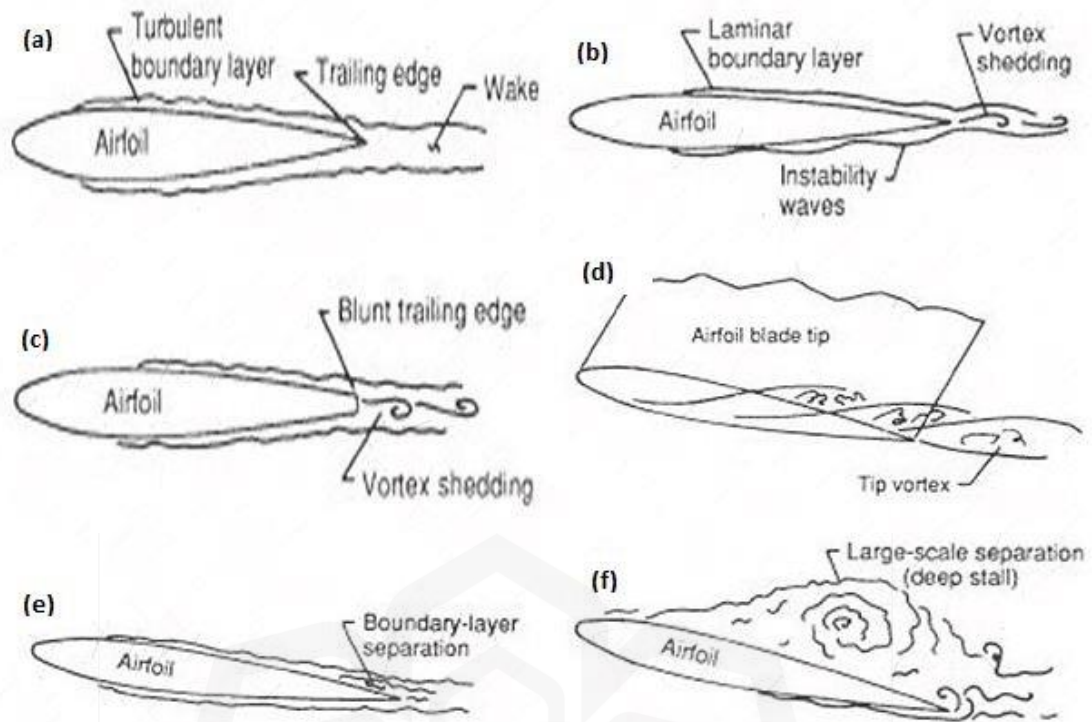


Figure 2.2 Types of airfoil self-noise (Brooks et al., 1989)

Airfoils operating within the low to moderate Reynolds numbers emit tonal noise that resembles a whistle (Andan & Lee, 2019). Whistle-like tonal noise can be observed in structures with blunt or airfoil shapes, namely: turbines, buildings, and airfoils. A distinct sound with a specific frequency emanated from sharp trailing edges and was first detected in isolated airfoils operating at moderate Reynolds numbers (Alan et al., 1971; Smith et al., 1970; Glark, 1971). At low to moderate Reynolds numbers, typically encountered in micro-wind turbines, small UAVs, compressors, and cooling fans, airfoils can generate tonal and broadband noises near the trailing edge. The sources of broadband noise include the interaction of BL turbulence with the TE, incoming turbulence and LE interaction, and vortex-related features (Casalino, 2021). However, discrete and multiple tones were observed in the spectrum (Arbey & Bataille, 1983; Paterson et al., 1973; Williams & Hall, 1970). The noise spectra that are produced indicate the presence of a primary tone ( $fn, max$ ) as well as a group of secondary tones ( $fn$ ). Additionally, there is a broadband hump ( $fs$ ) which is the center frequency of the broadband components (Arcondoulis et al., 2005), as depicted in Figure 1.1. Another study revealed that airfoil tonal noise consists of both broadband noise with a central

frequency and a combination of distinct tonal noise (Schumacher et al., 2014). Whenever the peak frequency of the noise reaches a level of at least 40dB, a noticeable tone is produced (Andan & Lee, 2019).

### **2.3.2. Noise Generation Mechanism**

The production of recognizable airfoil tonal noise is believed to result from the magnification of naturally occurring LBL instability by the LSB at the TE of the airfoil. Nonetheless, this circumstance could not be the sole cause of airfoil tonal noise. Tonal noise initiates from relatively small instabilities referred to as Tollmien-Schlichting (TS) waves that occur naturally within the LSB on the airfoil bottom side. The LSB near the trailing edge amplifies the TS-wave instabilities significantly (Park & Park, 2013). As a result, passing these amplified instabilities over the airfoil's trailing edge generates noise, frequently observed at low-to-moderate Reynolds numbers (Andan & Lee, 2019). In a different research, the flow structure shows the presence of a laminar boundary layer, which is later disturbed by unsteady fluctuations in the form of TS-waves that cause the transition to turbulence. Depending on the flow conditions, the boundary layer may also separate, leading to the fluctuations of the shear layers. Eventually, the unsteady flows from the upper and bottom sides of the airfoil link at the TE, forming a complex wake (Sandberg et al., 2009). Airfoil noise is caused by the shedding of vortices at a location close to the trailing edge (Paterson et al., 1973). The primary contributors to airfoil self-noise are the shedding of vortices resulting from LBL instabilities and blunt trailing edges (Jakobsen, 1993). Additionally, the airfoil tonal noise was linked to the interaction between the wake and boundary layers (Ramírez & Wolf, 2016). On the other hand, the discrete tones observed at the TE are related to the LBL present on the bottom surface of the airfoil (Fink, 1975).

Minor disturbances in the form of acoustic waves (known as TS-waves) emerge from the sharp TE of the airfoil and travel along the wake. When these disturbances grow in intensity, they create transverse fluctuations in the wake, leading to the generation of acoustic signals. Some of this sound energy travels upstream towards the bottom side of the airfoil close to the trailing edge, causing oscillations in the BL and completing a feedback loop (Tam, 1974). Similarly, a hydrodynamic and acoustic

feedback loop is completed as acoustic waves propagate upstream. The starting point of the feedback loop is where the BL instabilities on the airfoil profile originate (Schlinker, 1976). Another study suggests a different explanation, which proposes that hydrodynamic oscillations travel upstream to where they originate in the LBL, where the flow velocity is at its maximum. If the frequencies of the hydrodynamic fluctuations and sound waves are in phase, the hydrodynamic fluctuations will be amplified. This process leads to the propagation of hydrodynamic instabilities downstream to complete the feedback loop (Arbey & Bataille, 1983). As the BL becomes unstable, T-S waves develop and propagate along the airfoil towards the trailing edge, eventually rolling into a vortex. This results in a source oscillating at an equal frequency as the T-S waves, advancing upstream to about the mid-chord length of the airfoil, generating narrow-band tones. This indicates that the feedback process is centered on the development and growth of vortex shedding (Lowson et al., 1997). The periodic formation of a vortex is caused by periodic velocity variations in the separating region, which results in upwash and downwash. Tonal noise occurs when there is a slight adverse pressure gradient that allows instability waves to slowly grow and propagate upstream towards the point of BL instability, which initiates a feedback loop (Nakano et al., 2006).

Furthermore, it has been established that for an airfoil to exhibit a distinctive whistle-like tonal noise, a set of requirements must be fulfilled. As illustrated in Figure 2.3 (Desquesnes et al., 2007), these requirements include:

1. TS-waves are massively amplified by the LSB around the TE.
2. LSB must remain closed to the TE and the tonal noise is less effective as the LSB moves away from the trailing edge.
3. The adverse pressure gradient near the TE must not be too firm to hinder flow reattachment.

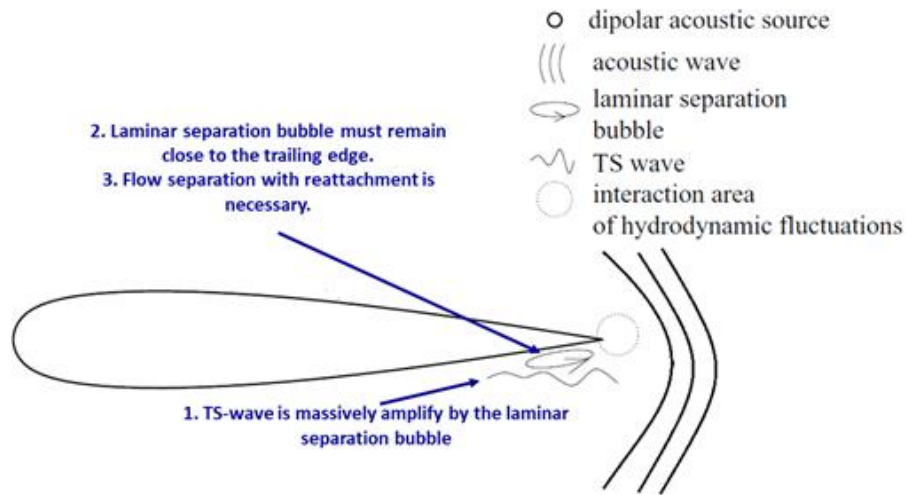


Figure 2.3 Necessary criterion for whistle noise emission (Desquesnes et al., 2007)

Trailing edge noise production is a complex phenomenon that requires ongoing investigation and development. The mechanisms behind the formation of turbulence and its influence on noise emission, and the development of accurate models for predicting noise levels are still topics of active investigation. Additionally, the impact of aeroelasticity in noise generation remains a topic of interest, and additional research is needed to examine its potential for generating novel noise reduction measures.

### 2.3.3. Factors Affecting Airfoil Noise

At a moderate Reynolds number, a slight rise in velocity can cause a change in the main tonal frequency by  $U^{0.8}$  for a symmetrical NACA airfoil. Additionally, the primary tone frequency can instantaneously jump to a higher frequency at a particular speed, resulting in a ladder-like structure with a 0.8 power relationship. The  $U^{0.8}$  curves differ depending on Reynolds's number and angles of attack. The frequency-tone relationship follows a  $U^{1.5}$  curve, and the overall frequency of the main tone can be expressed as in equation (2.1) (Paterson et al., 1973).

$$f_s = \frac{0.011U^{1.5}}{\sqrt{c\nu}} \quad (2.1)$$



Changing the Reynolds number also impacts both the quantity and amplitude of the main tone. Specifically, increasing the Reynolds number at zero angles of attack results in a drop of the primary tone amplitude (Arbey & Bataille, 1983). As the freestream velocity increases at low Reynolds numbers, a higher intensity centered frequency ( $f_s$ ) is observed along with more distinct secondary discrete tonal noise of frequency ( $f_n$ ) (Andan & Lee, 2019). At moderate Reynolds number, a broadband hump is generated with multiple tones (Ramírez & Wolf, 2016). Another proclaimed results are that higher Mach numbers result in an increase in both the amplitude and frequency of the tone.

For a non-zero Angle of attack (AOA), the flow structure becomes asymmetric, causing the BL to grow at different rates on the upper and bottom sides of the airfoil. As contrast to the bottom side, which maintains relatively smooth flow even for smaller angles of attack, the upper side separates initially due to the unsteady features of the flow (Ramírez & Wolf, 2016). The tonal noise reduces slightly as the Angle of attack rose from  $\alpha = 0^\circ$  and disappears after  $\alpha = 5^\circ$  (Andan & Lee, 2019). One possible explanation for this is that the pressure side experiences a delayed transition to turbulence while the suction side separates early, resulting in a predominantly turbulent flow.

Thinner NACA 0012 airfoils do not exhibit the reverse flow region (Sandberg et al., 2009). This demonstrates the impact of airfoil thickness on the characteristics of the flow. Likewise, raising the airfoil thickness would lead to a rise in low-frequency noise on both the upper and bottom sides of the airfoil (Lee, 2019). Furthermore, a cambered airfoil raises low-frequency sound on the top side and lessens the acoustic sound on the bottom surface of the airfoil (Lee, 2019). At the same velocity, thicker blunt trailing edges would have a lower tonal frequency (Tam & Ju, 2011). Moreover, higher amplitude is produced by thicker airfoils, and higher frequency tones are produced by thinner ones (Ramírez & Wolf, 2016). According to experimental results, noise increases up to an 8 bevel angle. At greater angles, though, the noise eventually reduces. Above  $20^\circ$ , the noise decreases below the baseline of  $0^\circ$  (Celik et al., 2020).

Trailing edge noise is a complicated phenomenon due to many factors that affect its generation and propagation, including but not limited to the airfoil geometry, Angle of attack and free-stream velocity. The influence of airfoil geometry on noise production, particularly its relationship with design factors such as lift coefficient, needs further investigation to optimize airfoil geometries for optimal noise reduction. Furthermore, the impact of the Reynolds number on trailing edge noise generation has yet to be entirely known, necessitating ongoing research to understand the underlying causes.

## **2.4. FLOW AND NOISE CONTROL**

### **2.4.1. Flow Control**

Laminar Flow Control (LFC) is one of the techniques used to push a particular amount of energy into the flow (Joslin, 1998) as well as introducing disturbance (Tillman & Hwang, 1999). Because the laminar flow is unstable, strengthening might improve its resilience on the model. Natural Laminar Flow (NLF) is another method of minimizing drag (Joslin, 1998). This technique deploys a favourable pressure gradient to halt transition (Joslin, 1998) by realigning the flow structure (Tillman & Hwang, 1999). This is intended to lower the momentum of the flow, hence changing the transition location. This method is passively employed compared to active Laminar Flow Control. However, it is applying NLF in practical areas is difficult because of the unrealistic pressure drag related to it (Tillman & Hwang, 1999).

NLF becomes inefficient, particularly when evaluating a three-dimensional model. Boundary layer instability, known as crossflow vortex, causes the condition at the airfoil LE to be turbulent. However, it is claimed that the contemporary NLF method may avoid this problem by lowering the LE dimensions. Consequently, lowering the streamwise length of the crossflow area allows a much quicker flow around the airfoil surfaces. It has also been stated that NLF endures bug contamination and ice adhesion to the system when used in practical scenarios (Joslin, 1998).

Hybrid Laminar Flow Control (HLFC) is another key step achieved in advancing LFC techniques. LFC is a sophisticated technique incorporating a suction approach, using ducts, flutes, and pump sources throughout the airfoil length. HLFC incorporates the ideas of NLF with LFC to reduce suction needs and minimise system complexity (Joslin, 1998).

#### **2.4.2. Influence on Aerodynamic Performance**

Another standard procedure employed and explored with LFC is suction and blowing. Nevertheless, unblown holes frequently impart roughness on the surface. Skin roughness could also be induced by numerous causes, namely contaminations, production restrictions, and coatings. Moreover, LFC offers a skin friction drop of roughly 75% compared to a baseline surface; additionally, this decreases overall skin reduction to about 1-2%, notably on the engine (Tillman & Hwang, 1999). This decrease corresponds to reduced engine power demand, consequently decreasing pollutants and the sound produced.

Furthermore, a unique notion related to porous material is micro-blowing technology (MBT). Not blown porous plate is defined as MBT, if the proportion of its skin friction compared to the solid surface is less than 1.1, implying a 10% rise in the drag relative to the baseline plate (Hwang, 2004). This indicates that a porous material generally has higher drag when compared to the baseline plate. Despite 8% porous regarded as aerodynamically smooth, it still has a drag value more significant than the baseline model (Wilkinson et al., 1983). Three variables have been evaluated separately from each other to illustrate the influence from each variable independently. The variables are aperture diameter, a depth-to-diameter ratio, and void fraction of the material. From the assessment, the lowest skin friction ratio is attained at Reynolds number dependent on the aperture diameter of approximately 400, depth-to-diameter ratio of around 6, and a void fraction of about 13 to 23% (Hwang, 2004). Moreover, extending the cavity depth would raise the drag values. Tiny and tightly packed pores would also elevate the drag coefficient due to the vortex interaction in the pores (Wilkinson et al., 1983). Additionally, it is noted that blowing diminishes aerodynamic efficiency, whereas suction enhances the aerodynamic performance on the upper side

of the airfoil (Atzori et al., 2019). The researchers also agreed that blowing enhances the aerodynamic performance on the bottom side of the airfoil. Subsequently, blowing distorts the BL, whereas suction strengthens it (Liu et al., 2006).

Roughness noise is created owing to the rough surfaces. One feature used to define surface roughness is roughness height and density. Roughness height and density have been proven to impact noise generated, with roughness height having a higher influence (Liu et al., 2006). On the contrary, a rise in the noise (Thomas et al., 2010a; Liu et al., 2006) and overall SPL (Liu et al., 2006) at high frequency is linked to surface roughness noise. Surface roughness noise is more prominent at this frequency range than the baseline plate. For instance, roughness noise is seen to exceed the TE noise at high frequencies (Liu et al., 2006). Roughness enhances the acoustic signals at higher frequencies. Therefore, this causes the energy in the BL to be scattered, thus radiating acoustic signals away (Liu et al., 2006). This indicates that skin roughness must be regarded in the investigations and modelling of the geometries.

### **2.4.3. Noise Control**

Trailing-edge noise prediction techniques proposed and developed are based on analytical and semi-analytical methods (Amiet, 1976; Brooks & Hodgson, 1981; Chase, 1975; Gruber et al., 2010; Howe, 1978, 1999; Lyu et al., 2016; Stalnov et al., 2016; Williams & Hall, 1970). Analytical models were based upon physical geometry only whereas semi-analytical depended on extra features such as boundary layer parameters and unsteady surface pressure fluctuations (Avallone et al., 2018). However, complex flow field contributes to the arguable prediction of radiated noise around the serrated trailing-edge (Arce et al., 2016a; Avallone et al., 2016; Jones & Sandberg, 2012). The initial model proposed to analyze noise generated by a semi-infinite flat plate with serrated TE was based on the assumptions of effective frozen boundary layer turbulence (Howe, 1999). The method predicted that the noise radiated in the presence of serrated trailing-edge at high frequency is less by approximately  $10 \log_{10}[1 + (4h/\lambda)^2]$  dB compared to the unserrated (straight) trailing-edge. The trailing-edge noise prediction is dependent on serration amplitude ( $2h$ ) and spanwise wavelength of the serration ( $\lambda$ ) as shown by Figure 2.4. Nevertheless, several researchers (León et al., 2016b; Avallone

et al., 2017a; Chong & Vathylakis, 2015; Gruber, 2012; Gruber et al., 2011a; Moreau & Doolan, 2013a; Oerlemans et al., 2009a; Parchen, 1996a) pointed-out that the model does not give accurate solutions when compared with the measurements, it over-projects highest noise reduction and does not show increase of the sound beyond cross-over frequency (León et al., 2016a; Avallone et al., 2017b; Jaworski & Peake, 2019; Moreau & Doolan, 2013b; Oerlemans et al., 2009b; Parchen, 1996b) On the other hand, for more noise reduction to be achieved, another comprehensive study proposed that serration height has to be greater than boundary layer thickness at the trailing-edge ( $2h \gtrsim \delta$ ) where  $\delta$  is the boundary layer thickness (Jaworski & Peake, 2019). In spite of the differences shown above, (Jaworski & Peake, 2019) still acknowledged Howe’s model in that narrower sawtooth is more essential for maximum noise reduction. Moreover, (Geyer et al., 2010) has proposed a new model that is more realistic and consistent with experimental work.

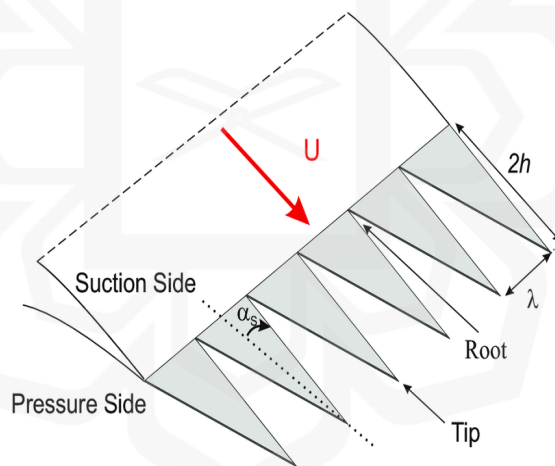


Figure 2.4 Sketch of a serrated trailing-edge incorporating the investigated dimensions of  $h$  and  $\lambda$  (Gruber et al., 2011a)

Following the nature of the Owls, the use of serration geometries as a passive tool has been widely investigated by several researchers (Gruber et al., 2011b; Jones & Sandberg, 2012; Lyu et al., 2016). Indeed, earlier attempts by several experimental studies have shown that trailing-edge serration is one of the promising passive control techniques to decrease trailing-edge noise. One of the studies that was performed at a

high Reynolds number (1.6 Million) showed that noise can be reduced by about 6 dB. Moreover, when applied to the full-scale wind turbine blades, the noise was successfully decreased by approximately 3 dB at a frequency below 1 kHz and increased above 1kHz without significantly affecting the aerodynamic performance (Tze et al., 2016). However, in another work, an investigation at a relatively low Reynolds number (200,000 – 830,000) found that noise can be reduced by about 7 dB at a frequency below 2 kHz and an increase in the noise level above this frequency. In addition, the Strouhal number based on boundary-layer thickness that delimits noise increase and decrease was determined to be roughly 1 (Szoke et al., 2020). Some of the investigation has shown that cutting serration connected to the main body compared to the flat plate inserts have higher broadband noises due to bluntness. However, they have also observed that increasing noise at high frequency can be reduced with cutting serration linked to the main body (Herr & Reichenberger, 2011).

Furthermore, those broadband noises can be reduced by introducing a mesh screen that covers the serration surfaces (Herr & Reichenberger, 2011). In recent years, application of a modified trailing-edge such as serration has been demonstrated experimentally (Tze et al., 2013; Gruber et al., 2010; Moreau et al., 2011; Oerlemans et al., 2001; Parchen, 1996b; Sandberg et al., 2009) and numerically (Jones & Sandberg, 2010; Sandberg & Jones, 2011) that it can minimize noise generated at trailing-edge. However, in most cases, these serrations are made into thin flat plates and inserted into the main body of the airfoil (Chong et al., 2013). Theoretically, the geometry of the serration destructs the coherence structure between the acoustic waves thus alters the acoustic radiation along the span. After that, noise reduction is achieved due to the interference of acoustics at the source (Howe, (1999); Lyu et al., 2016). On the contrary, an experimental work examined the wall pressure power spectral density as well as the coherence structure along the serration edges, they found that the flow-field is almost the same. Nevertheless, they have also observed vortices along the serration edges, thus affecting the momentum and turbulence energy distribution (Tze et al., 2015). The vortices near the serration trailing edges will affect the acoustic radiation, which will reduce in the trailing edge noise (Chaitanya et al., 2018). Based on other studies (Chaitanya et al., 2018; Lau et al., 2013; Lyu & Azarpeyvand, 2017), serration affects the flow-field structure, that is reducing the amplitude of the unsteady pressure

fluctuations along the span and hence at times referred to as source cut-off effect. Following one of the studies (Lau et al., 2013), the unsteady pressure fluctuations at the source have a direct influence on the sound generated. Therefore, reducing the pressure oscillations at the source affects the overall noise generated.

Additionally, the comb-type design shows that while the flexibility of the comb design is advantageous, it is not necessary to obtain noise reduction. In addition to the minimum extent of the device, the decisive design parameter is the slit width. The study finds that an almost zero spacing of the comb fibers ( $<0.1$  mm) produces the most favorable results, leading to the assumption that the noise reduction is mainly due to the viscous damping of turbulent flow pressure amplitudes in the comb area (Herr, 2007a). In another study, the obstruction of a gap due to shear layer diffusion at the edges of a comb-like plate at low Reynolds numbers resulted in an increase in the plate's effective surface area and changes to the formation of vortices near the LE and TE. The study found that a plate with a tiny space might generate aerodynamic force as effectively in the starting step as in the quasi-steady phase. However, a large gap size significantly drops in aerodynamic force as the diffusion of growing shear layers cannot obstruct the gap (Lee et al., 2017). Another study confirms that combed-sawtooth serrations are more advantageous than conventional sawtooth serrations in lowering noise for the low and moderate frequency range. The research reveals that the introduction of combs impacts the strength of the emitted sound. However, it does not affect the frequency range for acoustic signal elimination. Surface pressure fluctuations exhibit a decreasing intensity from the root to the tip for both configurations, and the primary sources of noise are situated at the serrations' root for the considerably lower and moderate frequency regime (Avallone et al., 2018). Combining of comb-like ridges results in a more consistent distribution of acoustic signals along the edges than the conventional serration. Implementing combs minimizes the impact between the airfoil's two sides at the TE and suppresses the formation of a turbulent wake in the gap between the ridges. This, in turn, reduces the internal (from serration edge to centerline) and external (from serration centerline to edge) flow movements arising from the presence of the teeth (Avallone et al., 2018; van der Velden et al., 2017).

Another exceptional technique that is incorporated with serration design is porosity. This approach reduces noise (Vathylakis et al., 2015). Different researchers use different terminology to define the porous material. Porosity, permeability, resistivity, constant of porosity, dimensionless permeability, flow control severity, and tortuosity are some of the commonly used parameters. Porosity represents the measurement of the empty gap present on a surface. Permeability defines the capability of a substance to transport fluid via its empty spaces. Resistivity refers to a substance's capacity to resist fluid passage through its empty areas. The noise produced at the TE is mainly linked to several factors, including the sound speed, fluid density, kinetic viscosity, chord, span length, Angle of attack, airfoil shape, incoming velocity, void fraction, distance between the viewer and the object, frequency, flow resistivity, BL thickness, and tortuosity (Sarradj & Geyer, 2013). Eleven dimensionless quantities have been defined from the aforementioned properties. These include normalized mean square sound pressure, Reynolds number based on chord, Strouhal number based on chord, Mach number, acoustical Rayleigh number, void fraction, tortuosity, extent ratios, and Angle of attack (Sarradj & Geyer, 2013). Moreover, materials can be characterized through airflow resistivity, volume porosity, tortuosity, thermal permeability, characteristic viscous dimension, and thermal characteristic dimension (Geyer, 2011). The author stated that airflow resistivity and volume porosity have the most significant impact on the noise generated around the airfoil among the listed properties.

Pores in a material promote the development of crossflow and vortex shedding, with the intensity being determined by the characteristics of the hole parameters. This, in turn, impacts the turbulence structures (Bernicke et al., 2019). To reduce the noise produced, using porous materials with smaller pore sizes, sub-millimeter diameters, medium to large void fraction, and tiny void coverage is recommended. Such factors allow the flow to pass across the porous medium, thus affecting with the BL and reducing the scattered sound at the TE (Zhang & Chong, 2020). The primary source of noise is located close to the TE, and reducing the size of pores can help to suppress both vortex shedding noise and turbulent noise in that area (Zhang & Chong, 2020). Sub-millimeter pores reduce high-frequency noise near the trailing edge (Zhang & Chong, 2020). Additionally, porous materials can generate noise at the transition between the



solid and porous parts, with higher permeability leading to more noise (Bernicke et al., 2019). Other factors that contribute to extra noise include roughness of the surface, low void fraction, and vibration of the TE (Thomas et al., 2019). It should be noted that some porous materials, such as foams, generate less noise than solid ones (Thomas et al., 2019).

According to (Frink et al., 2003), the height of the porous layer should be more than the hole diameter to achieve an aspect ratio greater than one. Furthermore, the hole diameter should be smaller than the BL thickness (Frink et al., 2003; Thomas et al., 2019). Sharp and broadened noise is produced when the height is at least twice the typical BL thickness (Zhang & Chong, 2020). (Lilley, 1998) explained that the sound produced around the surface is exactly proportional to the volume of turbulence via the TE, enhancing the efficiency of the porous portion. Moreover, (Zhang & Chong, 2020) found that sharp tones dominate when the ratio of the gap between apertures and the apertures diameter is less than/equal to 1.5, while broadened tones dominate when the ratio is greater than 1.5. According to (Herr, 2007b), the airfoil TE is considered sharp when the aperture diameter to the BL displacement thickness ratio is less than 0.3, and blunt when higher than that value.

Regarding noise reduction, moderate permeability is considered optimal based on studies conducted by (Bae & Moon, 2011; Zhang & Chong, 2020). Higher permeability results in negligible resistance, effectively shortening the chord, while lower permeability behaves similarly to a solid surface, producing similar results to the solid model (Bae & Moon, 2011; Geyer et al., 2010). Moreover, noise reduction at low to medium frequencies is observed by increasing material resistivity. In contrast, high frequency noise is observed in surface roughness noise, that is pronounced more than in the baseline surface (Geyer et al., 2010b).

In a study on partially porous airfoils, it was found that increasing the resistivity of the material while reducing the porous region can lead to an increase in lift coefficient and a decrease in drag coefficient (Geyer & Sarradj, 2018; Geyer & Sarradj, 2019). However, enhancing the length of the porous part from the TE towards the LE can result in increased turbulence intensity and boundary layer thickness, leading to more wake

deficit after the trailing edge and a reduction in lift coefficient (Geyer & Sarradj, 2014). Also, extending of the void area would lower the lift values around the airfoil (Aldheeb et al., 2018). Another study implied that smaller porous sections of a considerable 3.7% coverage (Zhang & Chong, 2020) presented a decrease in noise over the airfoil (Khorrami & Choudhari, 2003). Nevertheless, a small extent of porous coverage on the airfoil surface can reduce in noise radiation, with sub-millimeter pores having the most significant effect (Zhang & Chong, 2020). Material selection is also important in reducing noise (Geyer & Sarradj, 2019). It was discovered that precise positioning of the void zone on the surface might limit the swirling of the eddies. This, in turn decreases pressure oscillation and peak rotational velocity, resulting in decreased produced noise (Revell et al., 1997). Moreover, a uniform porous pattern helps to minimize rapid changes in sound impedance, which is the principal source of TE noise (Barone, 2011). Raising flow control severity has the potential to expand the viscous region while lowering the logarithmic part, and the best noise reduction of roughly 5dB is observed at a flow control severity of 6 and suction angle of  $70^\circ$  (Szóke et al., 2019).

There is still much to learn about optimizing the design of serrated and porous trailing edges for maximum noise reduction. Additionally, the effects of aeroelasticity on trailing edge noise production still need to be fully understood, and further examination is needed to investigate the underlying mechanisms and potential for developing new noise reduction strategies. Incorporating the flexibility of the structure into the noise control analysis could provide valuable new information. Although active noise control has shown promise in reducing noise levels in the cabin or cockpit of an aircraft, there are more practical solutions for large-scale noise reduction. Therefore, research efforts are needed to develop effective passive noise reduction strategies. One area of investigation is porous materials, which have effectively reduced noise levels by absorbing or attenuating sound waves. Moreover, the combined impact of serrated and comb designs on airfoil performance must be more adequately explored. It is important to note that any noise reduction strategy must consider the durability and cost implications of using advanced materials or other techniques.

## **2.5. PARAMETRIC DESIGNS OF THE PRESENT MODELS**

### **2.5.1. Design Based on Skin Friction**

The study examined the impact of three different parameters on their own: hole diameter, aspect ratio, and material porosity. The aspect ratio represents the ratio of the skin height to the aperture diameter. At the same time, porosity indicates the proportion of the empty space to the space occupied by the voids. Additionally, the term "Reynolds number" was employed in the research depending on the hole diameter, which serves as the reference length that is confined to the flow. These parameters were studied separately from each other to determine their individual effects.

According to the analysis, the skin friction ratio is at its lowest when the Reynolds number is approximately 400 based on the hole diameter. Above this value, the skin friction ratio increases significantly, while there is only a slight increase below this value. A depth-to-diameter ratio of 6 results in the most minor skin friction ratio, with an increase observed above and below this value. On the other hand, porosity ranging from 13% to 23% yields the least skin friction ratio, whereas a rise in the ratio is observed when the porosity is above 25%. Figures 2.5, 2.6, and 2.7 present the findings mentioned above.

Among the three variables, aperture shapes, sizes, and their patterns can be manipulated to minimize the impact of skin friction. It is also important to note that skin roughness can increase noise levels at high frequencies (Geyer et al., 2010b). However, meeting all requirements during the design process can be challenging due to factors such as manufacturing limitations and study objectives. Therefore, parameter optimization based on study goals and constraints is necessary. Ultimately, these parameters are crucial components in developing of porous sizes and patterns.

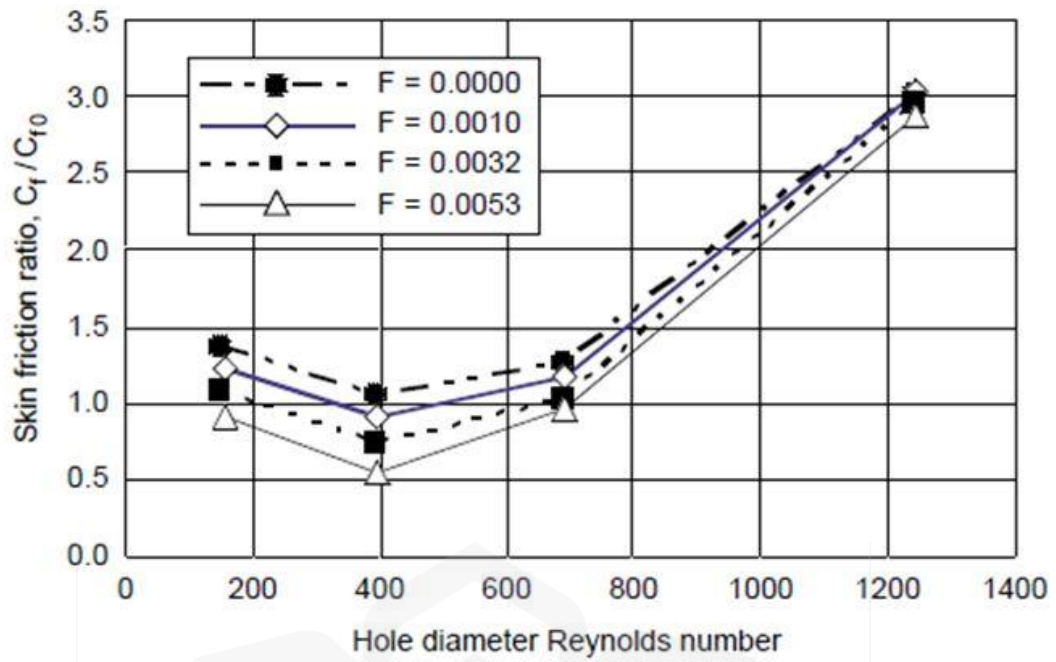


Figure 2.5 Relationship between skin friction ratio and Reynolds number based on aperture diameter (Hwang, 2004)

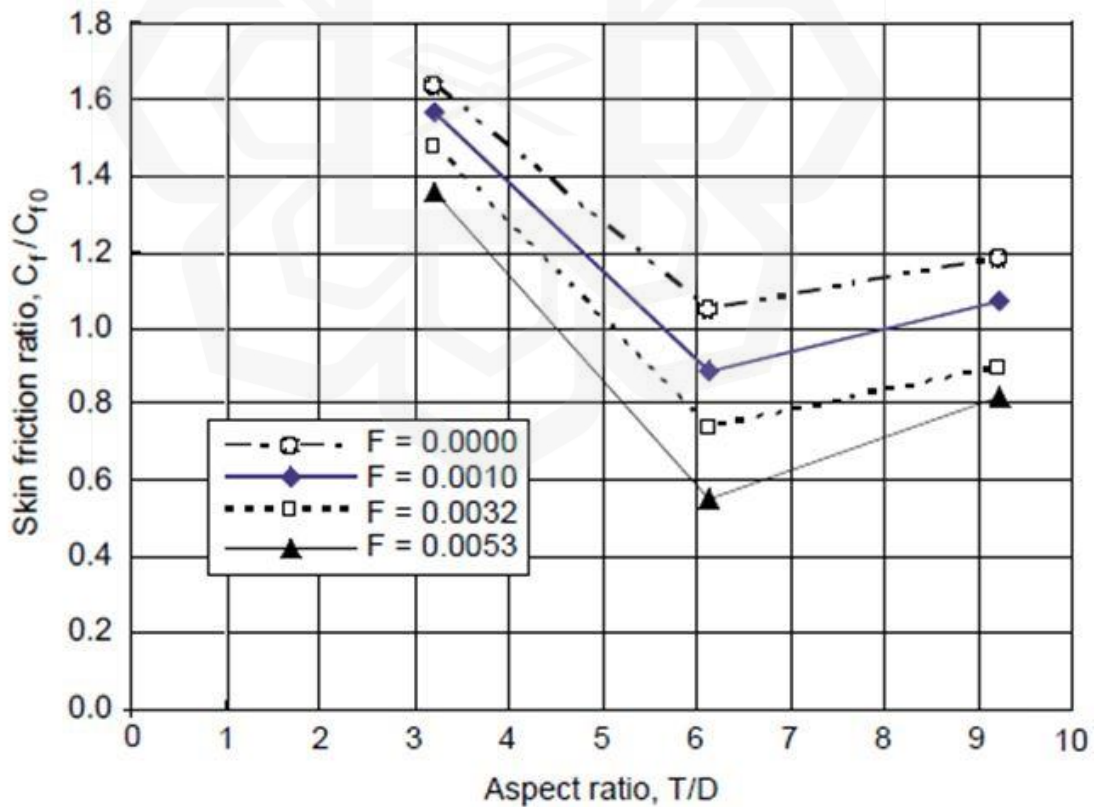


Figure 2.6 Relationship between skin friction ratio and depth-to-diameter ratio (Hwang, 2004)

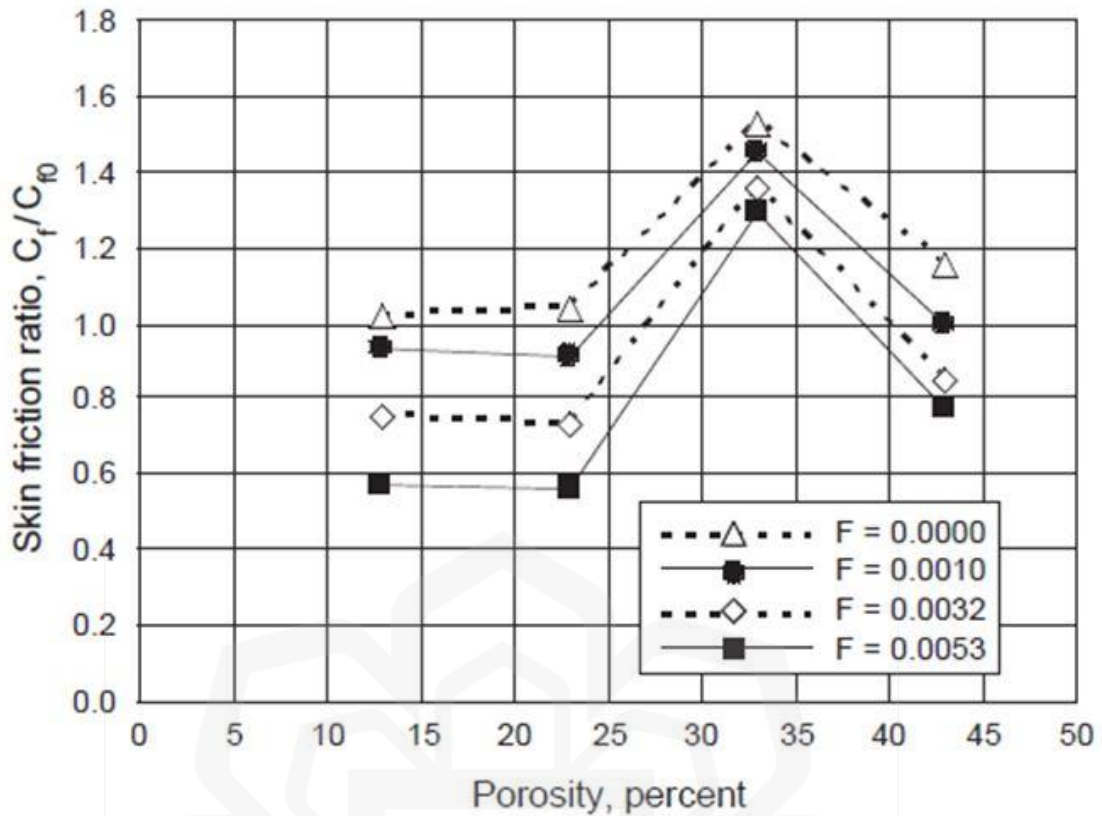


Figure 2.7 Relationship between skin friction ratio against void fraction (Hwang, 2004)

### 2.5.2. Design Based on Aperture Parameters

Howe's theory (Howe, 1979) involves several assumptions, including the disregard of viscous effects, the assumption that the flow is independent of porosity, a low Mach number and the length of the eddies being more significant than the aperture diameter. The theory establishes a relationship between the non-dimensional pore variable and the radiated TE noise as stated in equation (2.2)

$$\lambda = 8/\pi^2 \varepsilon l/R \quad (2.2)$$

where  $\lambda$  is the dimensionless hole variable,  $\varepsilon$  is the porosity calculated by dividing the opening's area by the total void space,  $l$  is the length of the void space from the TE, and  $R$  is the radius of the hole.

Howe investigated two instances, one with a consistent pattern of apertures across the porous surface and the other with apertures increasing linearly towards the trailing edge. Based on his analysis, he determined that the optimal non-dimensional pore variable values for case 1 and case 2 are 0.89 and 1.25, respectively. These values offer considerable noise reduction, with case 1 having a succession of high-frequency noise reduction peaks and case 2 exhibiting constant noise reduction. However, experiments must be conducted cautiously when turbulence in the boundary layer is affected, as it may generate various noise sources.

### 2.5.3. Design Based on Flow Characteristics

Equation (2.3) as defined by (Joslin, 1998) outlines an equation for the boundary condition that creates disturbances through a hole using suction and blower.

$$V = f(x) \exp(-i\omega t) \quad (2.3)$$

where  $\omega$  the frequency of the oscillations,  $f(x)$  describes the form of the suction and blowing set-up, and  $V$  defines the resultant normal velocity at the wall.

The speed of suction and blower, as well as the size and orientation of the hole, determine the regulation of suction and blowing. Solving certain applications can be challenging, but it is possible to simplify the problem by breaking it down into basic algebraic equations that relate the aperture shape to the normal velocity.

### 2.5.4. Design Based on Sawtooth Parameters

Based on several parameters, the serration, comb and comb-serrated configuration is modelled (Gruber, 2012). The expressions proposed are as follows.

$$\lambda/h \leq 4 \quad (2.4)$$

$$\alpha_s < 45^\circ \quad (2.5)$$

where  $\lambda$  the wavelength of the sawtooth,  $2h$  is the height of the ridges and  $\alpha_s$  is the inclination of the ridges relative to the flow direction. The dimensions are illustrated clearly by Figure 2.4.

According to equation (2.4), optimal noise reduction occurs when the ratio approaches zero or is less than 4, indicating that greater noise reduction is achieved with sharper serrations. Additionally, equation (2.5) suggests that a reduction in noise is maximized when the angle is below  $45^\circ$ .

### **2.5.5. Future Studies**

Further investigation is required on the specific geometry of serrations and porous materials, including their size, shape, and spacing. The design of trailing edges is a complex process driven by various aspects that require careful thought. It is vital to create suitable optimized parameters that can improve both noise reduction and flow characteristics. For instance, it is worth mentioning that a deeper serration depth can contribute to improved noise reduction; however, it can also result in increased drag and potential lift drop. On the other hand, establishing a consistent link between permeability and noise reduction is crucial as it has yet to be well known. In addition, the interaction between the porous material and other elements involved, such as the airfoil shape, can alter its noise reduction capabilities, but this relationship is poorly understood. Therefore, throughout this study, careful consideration was given to selecting appropriate models based on the review of relevant literature, as shown in Table 2.1. Considering the existing designs and their associated limitations, several adjustments have been suggested. These include incorporating detachable trailing edges with a curved tip and optimizing the height-to-width ratio for serrated, combed, and comb-serrated designs. For poro-serrated trailing edges, additional improvements involve increasing the porous space and employing sub-millimeter holes to achieve maximum effectiveness.

Table 2.1 Comparison of previous trailing edge designs, limitations, and proposed present study design.

| Designs  | Types  | Setbacks   | Proposed   | References   |
|----------|--|--|--|--|
| Serrated | <ul style="list-style-type: none"> <li>• Flat Plate</li> <li>• Cuttings inserted to the main body</li> </ul> | <ul style="list-style-type: none"> <li>• Not fitting the exact shape of the profile</li> </ul> | <ul style="list-style-type: none"> <li>• Detachable TE</li> <li>• Curved Tip of TE</li> <li>• Used appropriate height to wavelength ratio</li> </ul> | [León, 2016]<br>[Gruber, 2012]<br>[Moreau & Doolan, 2013a]<br>[Oerlemans et al., 2009]<br>[Parchen, 1996a]<br>[Jones & Sandberg, 2012]<br>[Szoke et al., |
| Combed   |  |  |  | [Lee, et al., 2017]<br>[Avallone et al., 2018]   |
| Porous   |  |  |  | <ul style="list-style-type: none"> <li>• Detachable TE</li> <li>• Curved Tip of TE</li> <li>• Increasing the porous part towards the TE.</li> </ul>      |

## 2.6. NUMERICAL ANALYSIS

In the disciplines of Aerodynamics and Aeroacoustics, there are three methodologies for predicting aerodynamic performance and defining noise generating mechanisms: mathematical modelling, numerical simulation, and experimental testing. Mathematical modelling applies mathematical representations to handle specific challenges, whereas



numerical simulation has the power to answer complicated problems, although at the cost of substantial computational resources.

The use of computational fluid dynamics (CFD) enables a comprehensive analysis of the setup, offers affordable solutions, facilitates the examination of the flow field, allows for easy extraction of data, and eliminates equipment inconsistencies in the investigation of low Reynolds number (Carmichael, 1981; Derksen et al., 2008; Fujii, 2005; Ol et al., 2005; Yarusevych et al., 2008). The simulation of LSB is more complicated than that of simple channel flows. Consequently, it is crucial to have a precise solution for the reattached TBL and the transition of the separated flow. Although Direct Numerical Simulation (DNS) can provide high resolution in space and time scales, it requires significant computing power (Wang et al., 2010). Thus, it is prohibitively expensive for users (Alam et al., 2011). Similarly, due to the three-dimensional nature of eddies, Large Eddy Simulation (LES) is computationally costly for complicated unsteady flow structures, as noted by Faridul et al. (2011) and Wang et al. (2010). Unfortunately, economical and feasible CFD solutions are not commonly available for low-Reynolds-number flows, as stated by (Counsil & Boulama, 2013).

Most turbulence models utilized for aerodynamic efficiency evaluation at lower Reynolds numbers, such as Spalart-Allmaras,  $K-\epsilon$ , and  $K-\omega$ , were developed under the assumption of fully turbulent flow, resulting in unreliable results compared to experimental data (Lee & Baeder, 2021; Wang et al., 2010). Additionally, fully turbulent models may not account for laminar separation near the airfoil's LE, leading to incorrect turbulent flow predictions and laminar separation bubble predictions (Wang et al., 2010).

The use of fully turbulent Reynolds-Averaged Navier-Stokes (RANS) models must accurately calculate the transition features (Counsil & Boulama, 2011; Lee & Baeder, 2021; Rumsey & Greenblatt, 2009). As in the case of low-Reynolds number turbulence models, which cannot detect the transition and reattachment locations even after settling the viscous sublayer adequately (Zheng et al., 1998). Meanwhile, the tripping method with URANS models needs attention to transition patterns, which may lead to unreliable outcomes (Suluksna & Juntasaro, 2008). On the other hand, the eN

method, which is based on linear stability theory, provides an unclear physical interpretation of 3-D flows (Galbraith & Visbal, 2010). Furthermore, Intermittency coupled with the transition process gives appropriate and less expensive data (Chen et al., 2020; Lee & Baeder, 2021; Lodefier et al., 2003; Suluksna & Juntasaro, 2008). However, the models are limited to 2-D flow computation and rely on global variables, ignoring transition features (Langtry & Menter, 2009). It is recommended to use LES or DNS to simulate the flow field accurately, as these methods consider the flow's three-dimensional nature, making them suitable for analyzing complex phenomena detached from the surface. Accordingly, LES is used to simulate aerodynamic data of the transient flow field. This enables well-resolved and detail information on the unsteady flow to be generated around the airfoil (Wagner et al., 2007). LES resolves the energy-containing eddies (large-scale eddies) directly and makes use of the sub-grid scale (SGS) to analyze the effect of small-scale eddies (Wagner et al., 2007). These large-scale eddies are considered the most contributor to the acoustic source (Wang & Moin, 2000).

The propagation of acoustic wave analysis depends on the model of the acoustic source (Zhu et al., 2018). This can be either a single point, moving or a time and space-dependent source (Zhao, 2019). For instance, the semi-empirical source can be modelled from computational parameters coupled with empirical relationships (Wagner et al., 2007; Zhao, 2019). However, the accuracy of the pressure fluctuation at the source needs detailed aerodynamic analysis (Zhao, 2019). After the source prediction, the pressure spectrum is propagated by one of the transport methods to the far-field. This can be done computationally or analytically (Wagner et al., 2007). Computational transport methods resolve partial differential equations in the entire volume up to the observer, whereas analytical transport techniques solve an integrated form of a specific acoustic propagation equation. This can be Kirchhoff's surface integral or the Ffowcs Williams–Hawkings (FW–H) equation (Wagner et al., 2007). Lighthill pioneered of the acoustic propagation model (Lighthill, 1952, 1954). The formulation was based on an inhomogeneous wave equation derived from compressible Navier-Stokes equations. Following the interpretation of the stress terms, it is assumed that acoustic fluctuations do not have significant interference in the fluid flow, the noise source is fixed, and acoustic waves are radiated into the free space. Nevertheless, the flow is not affected by

fluctuations at low Reynolds numbers (Zhao, 2019). In addition, at low Mach numbers, Lighthill's analogy can further be simplified into an expression of pressure fluctuations. This is possible because the ambient density is assumed to be constant (Zhao, 2019).

Ffowcs-Williams and Hawkings (FW-H) analogy is formulated to describe the effects of non-stationary control surface and control volume. They used an integration technique in computational aeroacoustics (CAA) based on the analogy of Lighthill. This is attained by employing a generalized function known as surface distribution (Wagner et al., 2007). This acoustic analogy can be applied to a rotating body, such as a wind turbine and fan blades. Therefore, the FW-H acoustic analogy can be utilized to compute the pressure spectrum at an observer location at a particular location in time for any moving surfaces. An exceptionally accurate source solution is required, which can be achieved by utilizing Green's function tailored to the geometry (Goldstein, 1976; Zhao, 2019).

The current empirical models have limitations when predicting airfoil-self noise at low Reynolds numbers and different angles of attack (Andan & Lee, 2019). To comprehend the generation of the airfoil whistle noise, measuring and visualizing the flow field over the airfoil surfaces is important. Subsequently, with these, it may not be possible to provide a detailed explanation of the measured results. Another approach that has recently gained interest is the computation of dynamic behavior such as the oscillations of the TE (Moreau et al., 2016), which has been shown to have a significant effect on the noise generated (Manela, 2013; Zhou et al., 2019).

Table 2.2 Comprehensive Analysis of Numerical Models

| <b>Models</b> | <b>Suitable</b>   | <b>Setbacks</b>  | <b>References</b>          |
|---------------|---|--|----------------------------|
| Xfoil         | <ul style="list-style-type: none"> <li>• Flow is incompressible and viscous effect is neglected</li> <li>• Initial design tool</li> </ul> | <ul style="list-style-type: none"> <li>• Unclear physical Interpretation as a result of its linear-stability theory</li> </ul> | [Galbraith & Visbal, 2010] |

|  |   |   |   |
|--|---|---|---|
| SA,<br>K-epsilon<br>(k-ε) and<br>k-omega<br>(k-ω)<br>Model | <ul style="list-style-type: none"> <li>Moderate to high turbulence intensity</li> </ul>   | <ul style="list-style-type: none"> <li>Unreliable results such as LSB prediction</li> <li>Even after tripping, the transition pattern is neglected</li> </ul> | <p>[Lee &amp; Baeder, 2021]</p> <p>[Wang et al., 2010]</p> <p>[Council &amp; Boulama, 2011]</p>                                   |
| SST $\gamma$ –<br>$Re\theta$ Model                         | <ul style="list-style-type: none"> <li>Capture the transition process and provide more accurate predictions for boundary layer flows with less expensive data</li> </ul>                                  | <ul style="list-style-type: none"> <li>Limited to 2d analysis</li> <li>Rely on global variables hence ignoring the transition features</li> </ul>             | <p>[Chen et al., 2020]</p> <p>[Lee &amp; Baeder, 2021]</p> <p>[Lodefier et al., 2003]</p> <p>[Suluksna &amp; Juntasaro, 2008]</p> |
| LES Model  | <ul style="list-style-type: none"> <li>Flow with large-scale coherent structures</li> <li>For capturing turbulent flow features e.g. vortex shedding, separation and flow instabilities</li> </ul>        | <ul style="list-style-type: none"> <li>High computationally time</li> <li>High computational power</li> </ul>   | <p>[Alam et al., 2011]</p> <p>[Wang et al., 2010]</p> <p>[Wagner et al., 2007]</p> <p>[Zhao, 2019]</p>                            |
| DNS  | <ul style="list-style-type: none"> <li>Provides a highly accurate representation of the flow physics, capturing the complete dynamics and interaction of vortices, eddies, and other turbulent</li> </ul> |   | <p>[Wagner et al., 2007]</p> <p>[Wang et al., 2010]</p> <p>[Alam et al., 2011]</p>  |

The field of aeroacoustics simulation requires further investigation and development to improve the accuracy of numerical simulations and understanding of the interaction between flow structures and noise generation. Additionally, there is a need to understand the impacts of flow vortices and the interaction between sound

waves and the flow, particularly in complex geometries. Computational aeroacoustics methods must be made more efficient and accurate to facilitate practical application in industry. After conducting a literature review, the numerical methods employed in this study were carefully selected based on the suitability and limitations of various computational methods as displayed in Table 2.2. The SST  $\gamma - Re\theta$  model was used for 2D flow analysis to ensure reliable results with computational efficiency. This model is renowned for its accuracy in predicting flow behavior while being computationally economical. However, a 3D analysis was performed using the LES (Large Eddy Simulation) model for more precise capture of unsteady flow dynamics and accurate prediction of noise signals.

## **2.7. SUMMARY**

A thorough examination of the literature reveals that a comprehensive experimental investigation of the flow structure of modified trailing-edges has yet to adequately describe flow patterns at moderate Reynolds numbers, as most studies have focused on low Reynolds numbers. Additionally, the combined impact of serrated and comb designs on airfoil performance must be more adequately explored. Moreover, while tonal noise emission from airfoils is associated with amplification of laminar boundary layer instabilities, it is emphasized that the presence of these instabilities does not invariably lead to tonal noise; rather, the characteristics and positioning of laminar separation bubbles also significantly influence this phenomenon. Despite the viability of several previous works, the fundamental physical reasons causing airfoil tonal noise still need to be understood. Therefore, it is necessary to strive to provide a thorough understanding of the tonal noise process and related physical phenomena by conducting wind tunnel tests and CFD simulations, evaluating the flow structure and tonal noise over an airfoil impacted by whistle tonal noise and comparing it with the past literature.

## **CHAPTER THREE**

### **METHODOLOGY**

#### **3.1. INTRODUCTION**

The research methodology section comprehensively evaluates the study's critical flow, including the methods and strategies employed to fulfil the research objectives. The experimental component of the investigation was carried out in an open-loop UPNM low-speed wind tunnel. The experimental work aimed to examine the flow field behaviour over the baseline and modified configurations. Several airfoil models were designed, and the flow over them was assessed through Particle Image Velocimetry (PIV) measurements. PIV is a commonly used measuring method that enables the study of flow field behaviour by capturing images of tracer particles in a fluid and estimating their velocity vectors. In addition to the experimental investigations, the research also included computational fluid dynamics (CFD) simulations, which were calculated using Ansys Fluent. CFD simulations are extensively used in fluid mechanics research to simulate and evaluate complicated flow fields. The CFD simulations were done when applicable and within the capability of the simulation model. Multiple models were developed and studied in both approaches to compare the findings of the experimental and CFD studies. The results of the numerical and experimental tests were then compared and reviewed to uncover any differences and to verify the reliability of the CFD models. Additionally, the impact of Musou black, a paint proclaimed the blackest in the world, is presented and contrasted to the regularly used flat black paint. In summary, this chapter fully describes the methodology and models used in the research, including the experimental and CFD components, the models used, and the measurements employed. The procedures are discussed in depth in the following sections, providing a complete description of the research methodology as displayed in Figure 3.1.

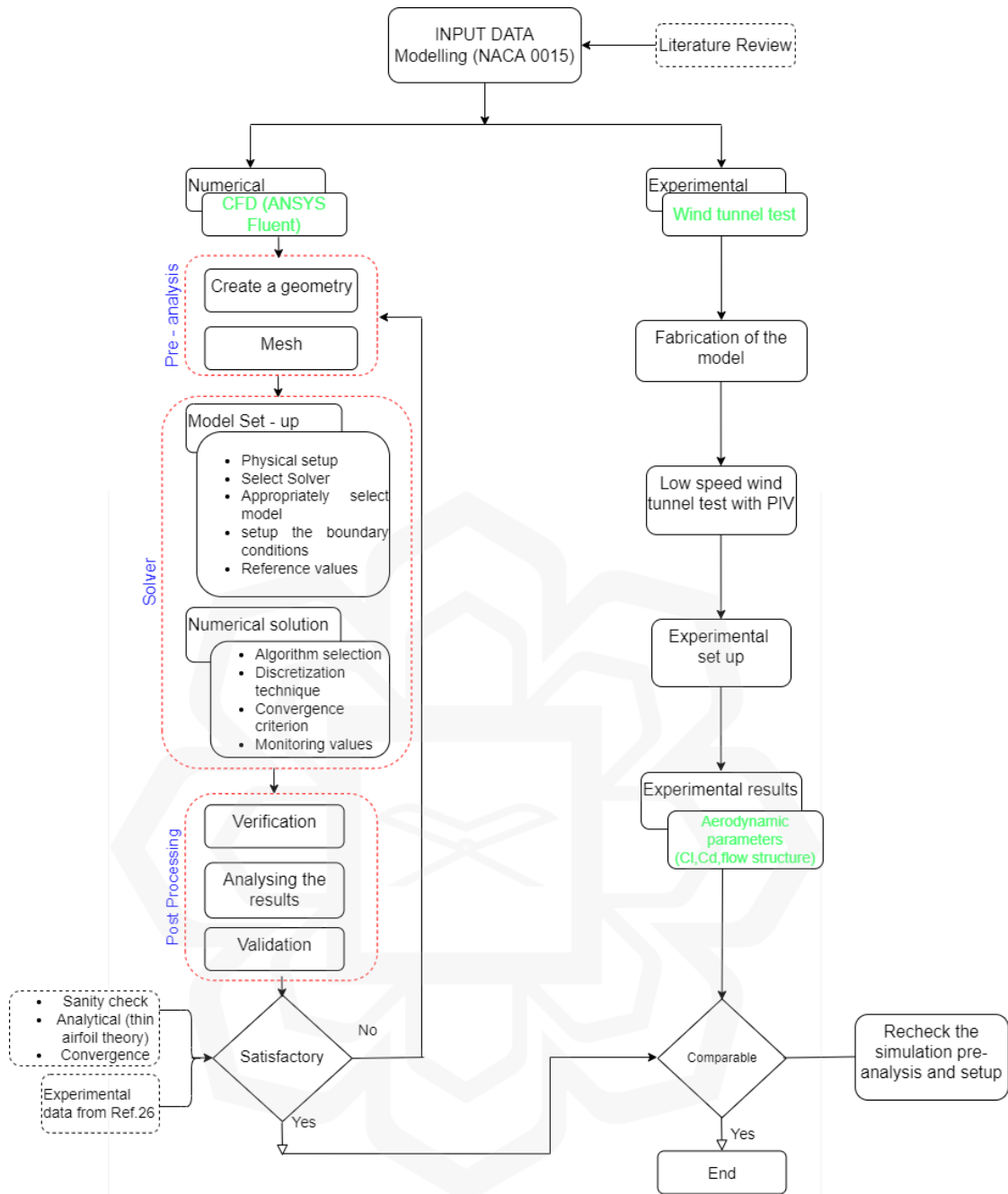


Figure 3.1 Flowchart of the methodology

### 3.2. MODEL DESCRIPTIONS

This study focuses on the aerodynamic and aeroacoustics analysis of a NACA0015 airfoil with a chord length of 150 mm, 22.5 mm maximum thickness and span length of 296 mm. The selection of these dimensions is driven by the need for a symmetrical profile, alignment with the wind tunnel's span dimensions, and a customized chord

length that not only adheres to the tunnel's speed limitations but also attains a specific Reynolds number target of approximately 160,000. The airfoil design was such that it extended across the entire test section of the wind tunnel, as shown in Figure 3.2. The design of the trailing edge was intentionally kept blunt to alleviate the complexity in meshing for the computational model, and to address the limitations posed by sharp trailing edges in manufacturing. The fabrication of sharp trailing edges often presents difficulties, so a blunt shape was deemed a more feasible solution.

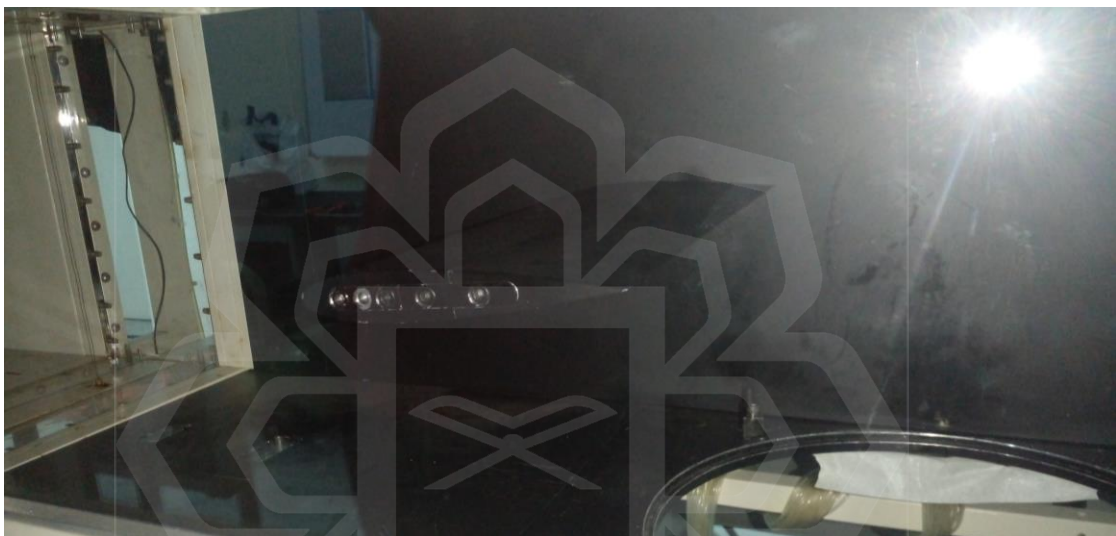


Figure 3.2 Side view of the airfoil inside test section

### 3.2.1. Baseline Model

The baseline airfoil model was designed and built with a chord length of 150mm and a span of 296 mm, as indicated in Figure 3.3-3.4. The design was determined to have a straight and symmetric form, revealing a consistent cross-sectional shape over the whole span. The trailing edge of the baseline model was chosen to have a blunt shape with a thickness of roughly 0.15 mm. Based on these observations, the baseline design was selected as the reference model for examining the impacts of modifications on the airfoil's flow structure and aeroacoustics response. Using a baseline design enabled a systematic and controlled assessment of the effect of modifications on the performance and behaviour of the airfoil. This approach contributes to a deeper understanding of the



links between design changes and flow topology and enables for a more extensive study of the consequences of changes.

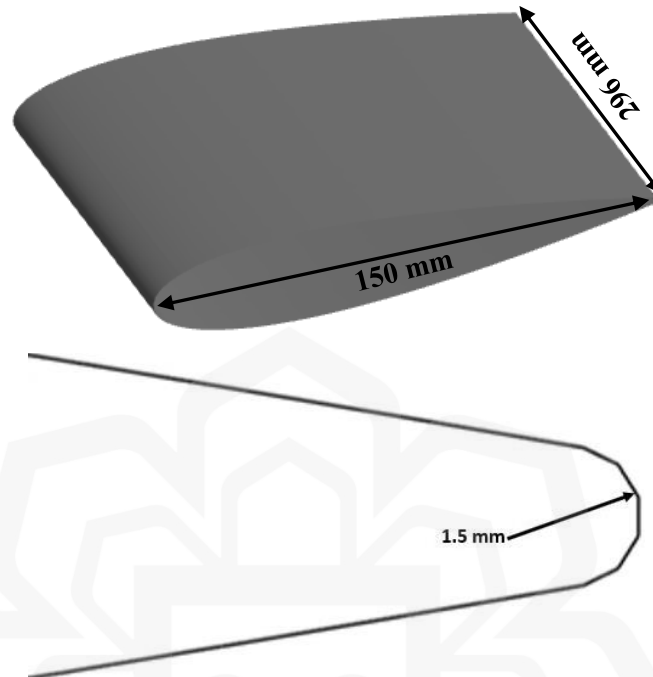


Figure 3.3 Geometry of NACA0015 airfoil used in this research.



Figure 3.4 Top view of the baseline airfoil model

### 3.2.2. Serrated Trailing-edge Configuration

The research also analyses various trailing-edge shapes, including the serrated model, as seen in Figure 3.5. The serrated trailing edge airfoil model was selected because it reduces the acoustic signal's scattering, as discussed in section 2.4.3. These configurations result from changes made to the trailing-edge surface of the airfoil,

positioned roughly 30% from the trailing edge. These specifications were meticulously selected to ensure that the modified trailing edges effectively encompass the area primarily affected by laminar bubble separation. Specifically, the serrated model was designed and constructed by integrating sawtooth-like projections into the airfoil surface. The projections have serration specifications, including a height of 38.55 mm, a wavelength of 8 mm, and an angle of 6 degrees, as shown in Figure 3.6. These specific values were chosen to align precisely with the criteria stipulated in Table 2.1.

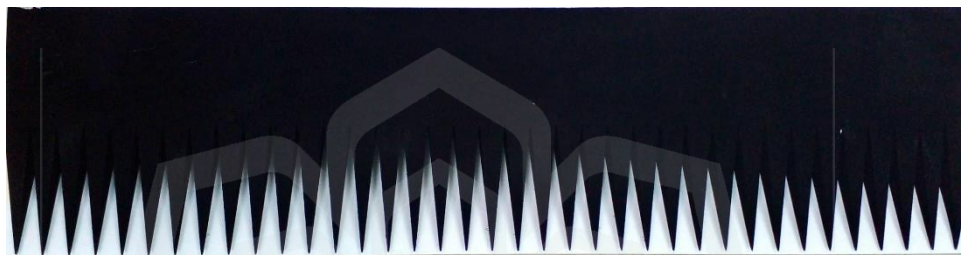


Figure 3.5 Top view of the serrated model

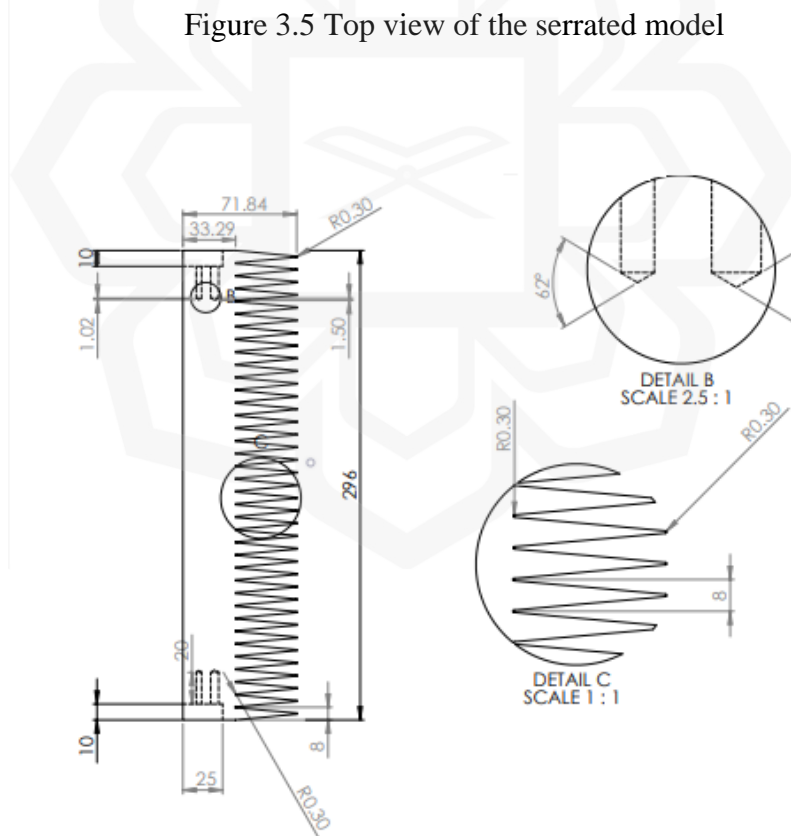


Figure 3.6 Top view of the serrated model

### 3.2.3. Combed Trailing-edge Type

The study also examined the comb modification, which consisted of adding parallel ridges to the airfoil surface, as displayed in Figure 3.7. Similarly, it is positioned roughly 30% from the trailing edge. The comb modification was designed with specific parameters, including a comb height of 38.55 mm and a comb spacing of 5 mm, as depicted in Figure 3.8. These specific values were chosen to align precisely with the criteria stipulated in Table 2.1. The comb modification represented a variation in the trailing-edge surface of the airfoil, and the results of this study allowed for a comprehensive analysis of the effects of such modifications on the aircraft.

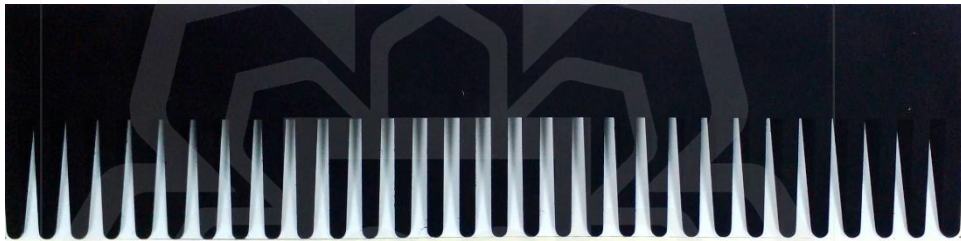


Figure 3.7 Top view of the comb configuration

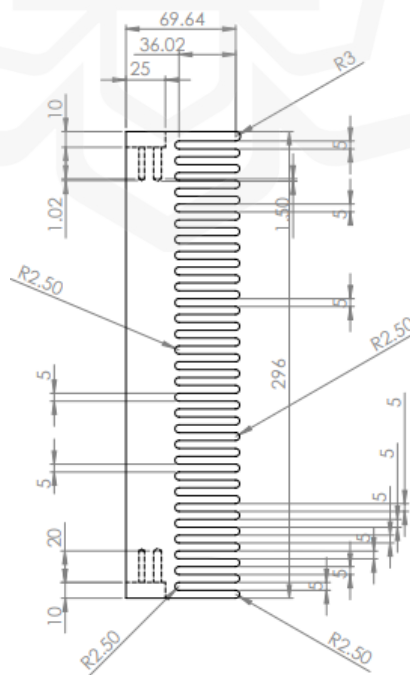


Figure 3.8 Top view of the comb configuration

### 3.2.4. Comb-Serrated Trailing-edge Model

The study also included investigation of the comb-serrated configuration, which is a combination of the serrated and comb forms. This airfoil layout was specified by the parameters of serration height (38.55 mm), serration wavelength (6.5 mm), comb height (38.55 mm), and comb spacing (1 mm), as illustrated in Figure 3.9-3.10. These specific values were chosen to align precisely with the criteria stipulated in Table 2.1. The purpose of the comb-serrated design was to assess the influence of this particular modification on the flow structure and aeroacoustics behaviour of the airfoil, relative to the baseline NACA0015 airfoil and other airfoil configurations explored. The comb-serrated structure constituted a unique combination of modifications to the airfoil surface, and the results of this study allowed for a thorough insight of the impacts of such adjustments.

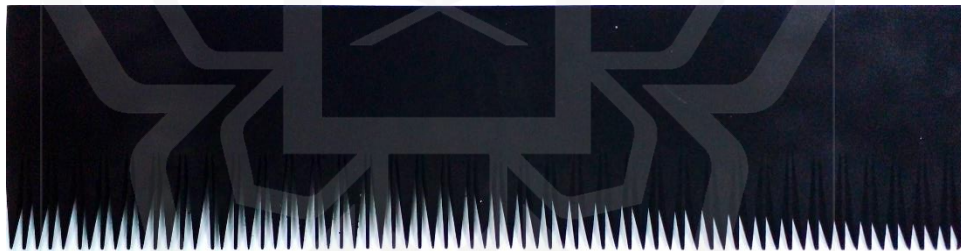


Figure 3.9 Top view of the comb-serrated model

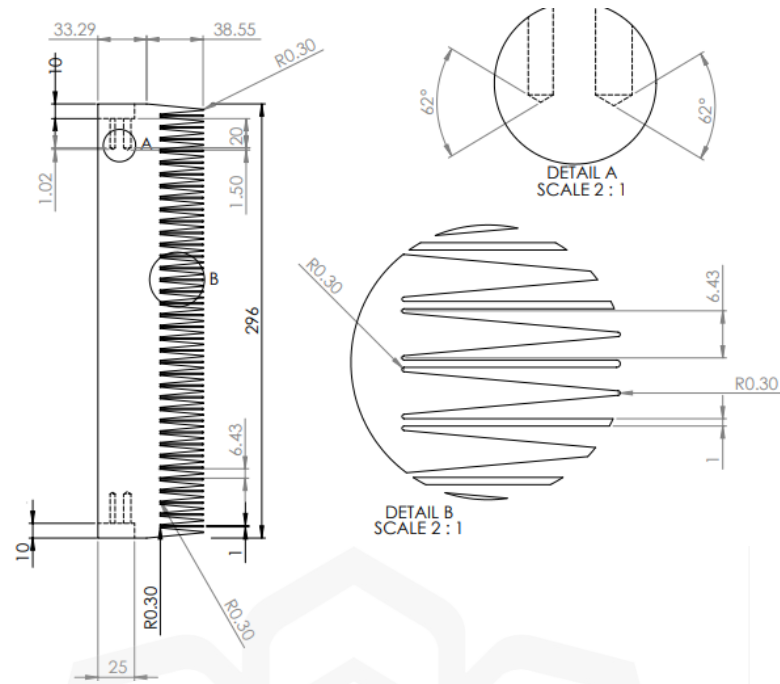


Figure 3.10 Top view of the comb-serrated configuration

### 3.2.5. Poro-Serrated Trailing-edge Configuration

The study also investigates the poro-serrated trailing-edge design, which offers a new approach to redesigning the airfoil surface. The configuration required the integration of multiple holes into the airfoil surface. It was determined by particular characteristics, such as a pore size of 1mm and a porosity value of roughly 43%, as displayed in Figure 3.11-3.12. These specific values were chosen to align precisely with the criteria stipulated in Table 2.1. Porosity refers to the percentage of void space in a material to its overall volume. It measures the degree to which a substance is permeable or porous and is frequently represented as a percentage. The findings of this investigation would give significant insight into the impacts of incorporating porous materials into the airfoil surface and contribute to the progress of aerodynamic design and optimization procedures.

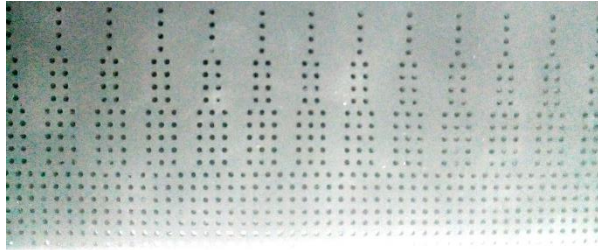


Figure 3.11 Top view of the poro-serrated model

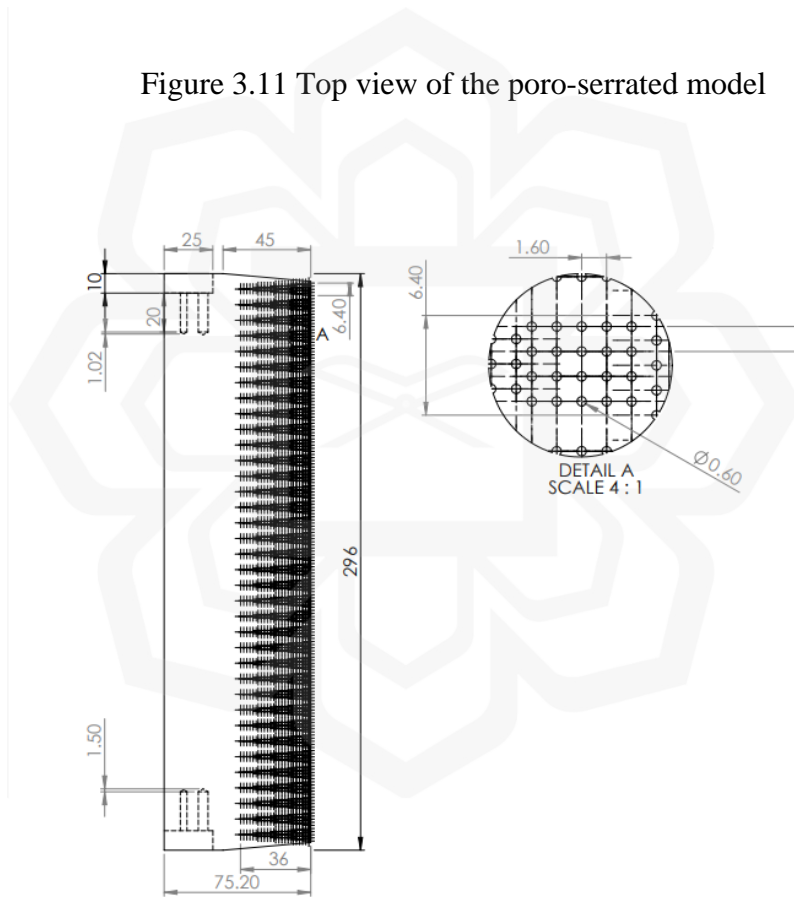


Figure 3.12 Top view of the poro-serrated configuration

### 3.3. NUMERICAL METHOD

### 3.3.1. Computational Domain and Boundary Conditions

The study simulated a 2D NACA0015 airfoil with a chord length of 150 mm and thickness of 22.5 mm, featuring a sharp trailing edge to facilitate meshing. The computational domain (Figure 3.13) was extended 30 times the chord length measured from the airfoil surfaces to ensure accuracy, except in the downstream direction, where an extension of 60 times the chord length was included. The downstream double extension is necessary to capture the wake region and ensure consistent inlet freestream conditions. The C-shaped shape part was selected as the inlet, whereas the rightmost part of the domain was chosen as the outlet. The selection of a C-shaped part as the inlet and the rightmost section of the domain as the outlet is to leverage the inlet geometry for controlled flow direction while allowing natural dissipation of disturbances through an unobstructed outlet, enhancing the accuracy and relevance of the computational analysis. The domain was chosen based on a published study (Council & Boulama, 2013) that analyzed the NACA0012 airfoil at a relatively moderate Reynolds number of  $10^5$ .

As for the 3D simulation, the computational domain (Figure 3.14) used to investigate the flow field numerically was about 15 airfoil chords measured from the airfoil surfaces except of 30 airfoil chords in the downstream direction, this was considered to reduce the impact of spanwise periodic boundary conditions (Manni et al., 2016). Similarly, the left side, top and bottom were considered as the inlet, whereas the right side of the domain was chosen as the outlet. In the context of a 3D domain, adopting the left side, top, and bottom as the inlet while designating the right side of the domain as the outlet ensures a coherent and streamlined flow pattern, facilitating accurate simulation results by minimizing potential flow disturbances from the outlet region. The reference pressure value used for each case was 101325 Pa.

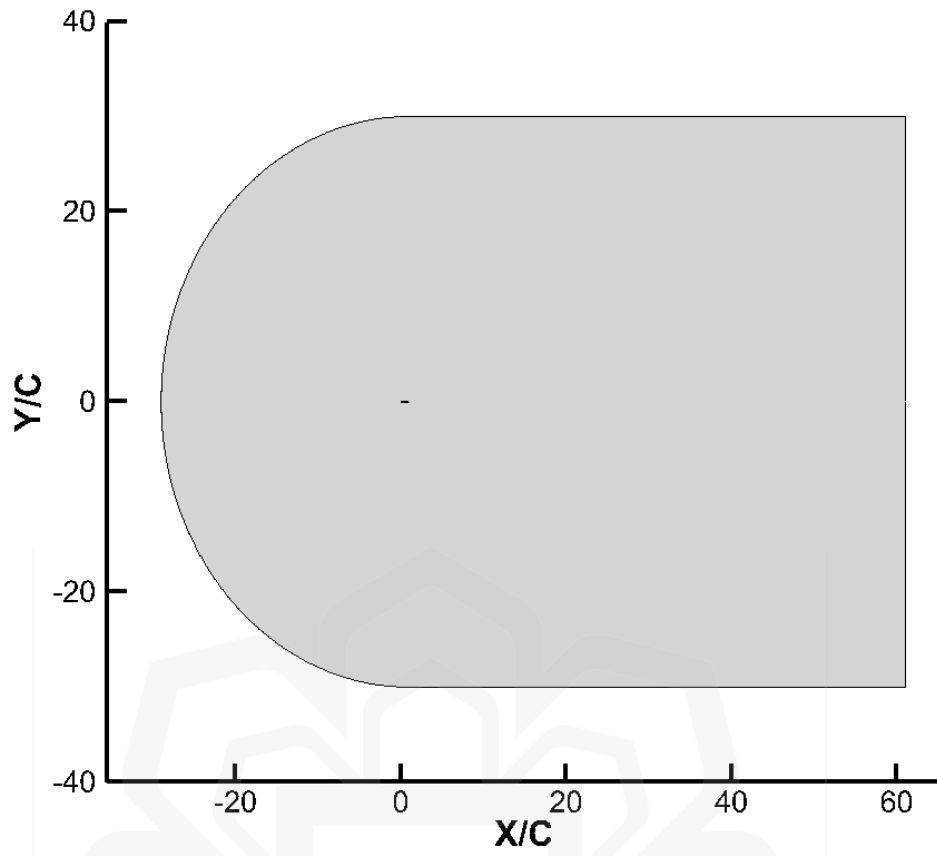


Figure 3.13 Boundaries and dimensions of 2D analysis domain.

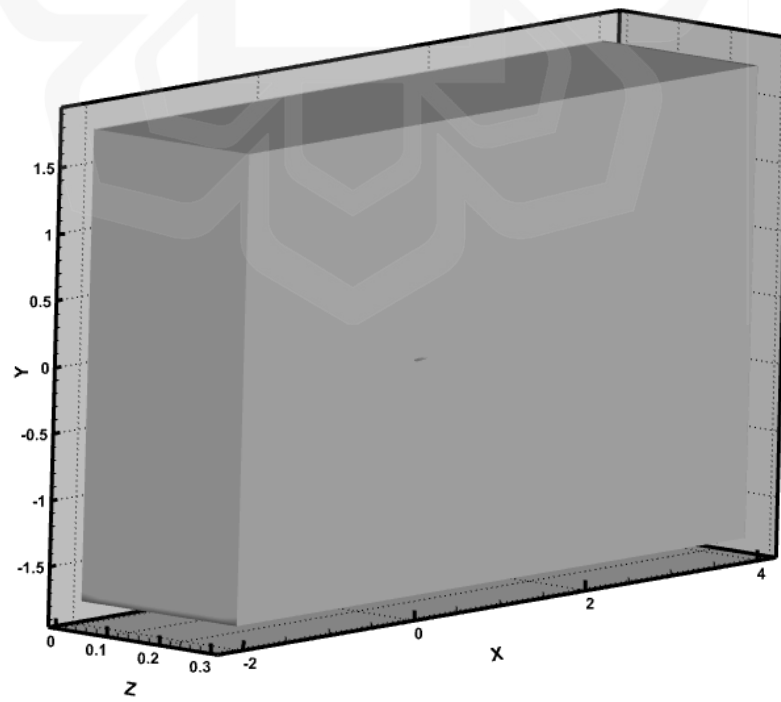


Figure 3.14 Boundaries and dimensions of 3D analysis domain.



### 3.3.2. Spatial Grid

A mesh consisting of six parts was used to conduct the 2D analysis. The first part, located closest to the airfoil walls, was designed with the finest mesh to resolve the boundary layer region better. The subsequent parts were subdivided adjacent to the first shell to provide an evenly distributed grid. The structured C-H grid was chosen for this purpose, as elaborated in Figure 3.15.

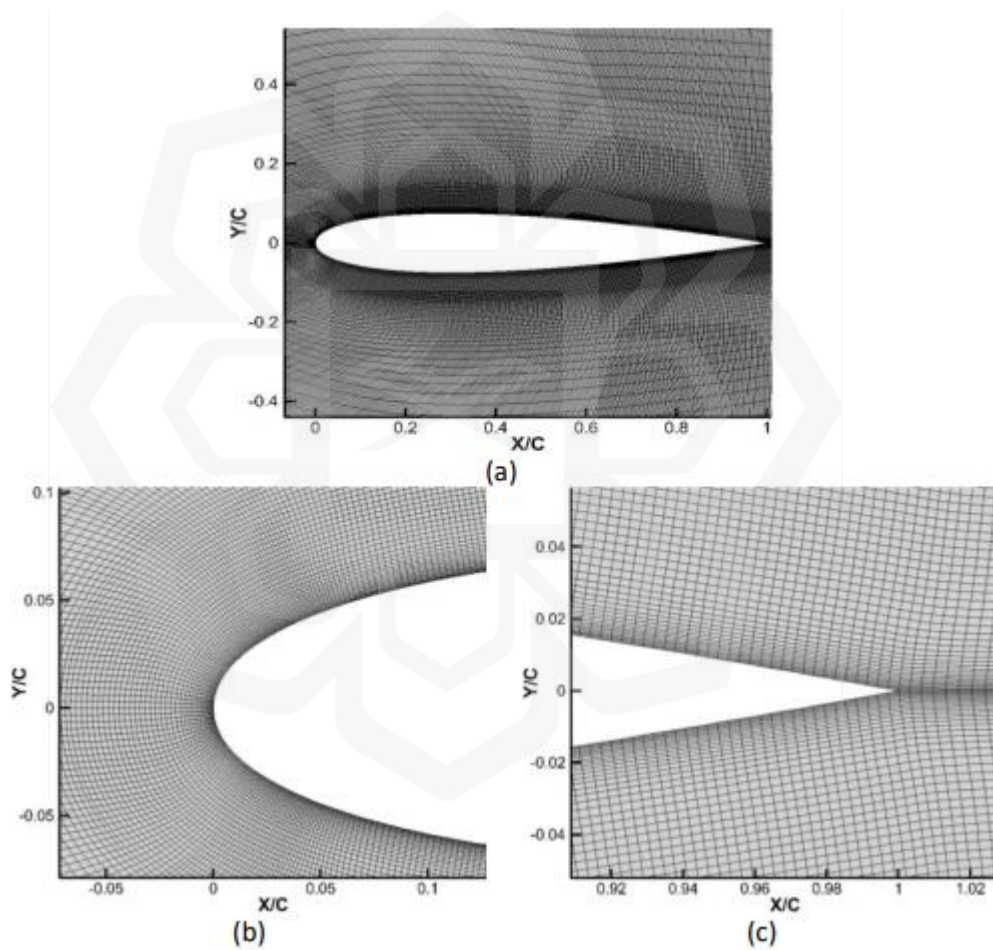


Figure 3.15 (a) C-type grid topology (b) Detailed view of the LE (c) Detailed view of the TE.

Several simulations were conducted with varying grid numbers, as illustrated in Figure 3.16. Case 1 utilized 72 220 grids, while Case 2 and Case 3 employed 144 440

and 288 880 grids, respectively. Among the cases, Case 3 had the finest resolution, while Case 2 had a better resolution than Case 1, achieved by doubling the mesh. The distance between the first row of cells and the airfoil wall was set as 0.8, with a wall grid expansion of 1.2, yielding a  $y^+$  of 0.8, less than 1, as required by the SST  $\gamma - Re\theta$  model. This configuration provides improved resolution near the airfoil walls, thus enabling adequate representation of laminar and transition boundary layers. Generally, the analysis in Figure 3.16 indicates that Case 2 and Case 3 are both suitable for analysing flow characteristics. However, Case 2 is more appropriate because it requires less computational time and produces nearly identical results to the finest mesh.

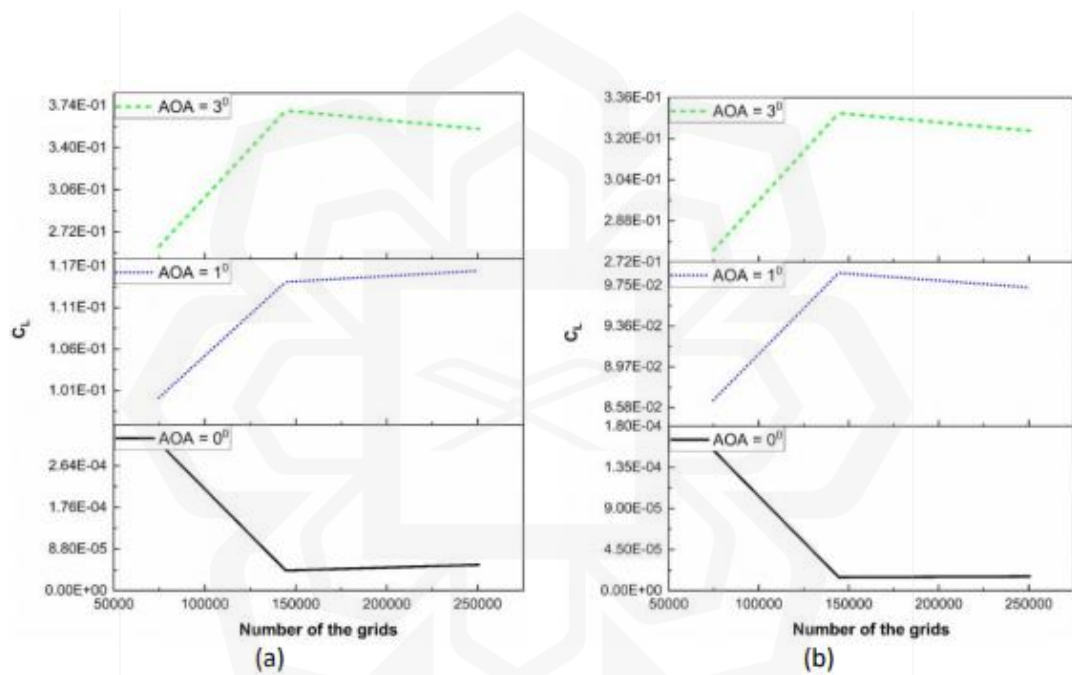


Figure 3.16 (a) Mesh convergence analysis at  $Re = 8.4 \times 10^4$  (b) Mesh convergence analysis at  $Re = 1.7 \times 10^5$

A mesh consisting of three parts was utilized to conduct the 3D analysis . The initial part was dedicated to the finest mesh near the airfoil walls due to its proximity to the boundary layer area, which aids in achieving boundary layer resolution. The other shells were subdivided adjacent to the first shell. This division strategy facilitated the creation of a well-distributed and finer mesh in the area of focus. An unstructured C-H grid was selected (Figure 3.17). The  $y^+$  value was computed and found to be

approximately 0.9. This value defines the wall resolution, in that the boundary layer effects are captured well, especially near the viscous sub-layer.

Considering the main focus points are the airfoil surfaces the cell sizes are reduced to about 2mm. A relatively finer grid at those locations enhances the accuracy of the computational outputs. Likewise, finer mesh allows the spectrum of high frequencies to be captured. Similarly, the computational mesh for a serrated, comb, or comb-serrated model typically employs an unstructured grid approach. The mesh refinement is done in areas near the TE due to the complex geometry and boundaries of the physical domain. This allows the grid to accurately capture important geometric and flow features such as sharp edges, narrow gaps, or high gradients. For instance, in a serrated configuration, a sawtooth-like triangular shape is positioned between the serration surfaces to represent the complex geometry of the trailing-edge. This approach ensures a more precise representation and computational results.

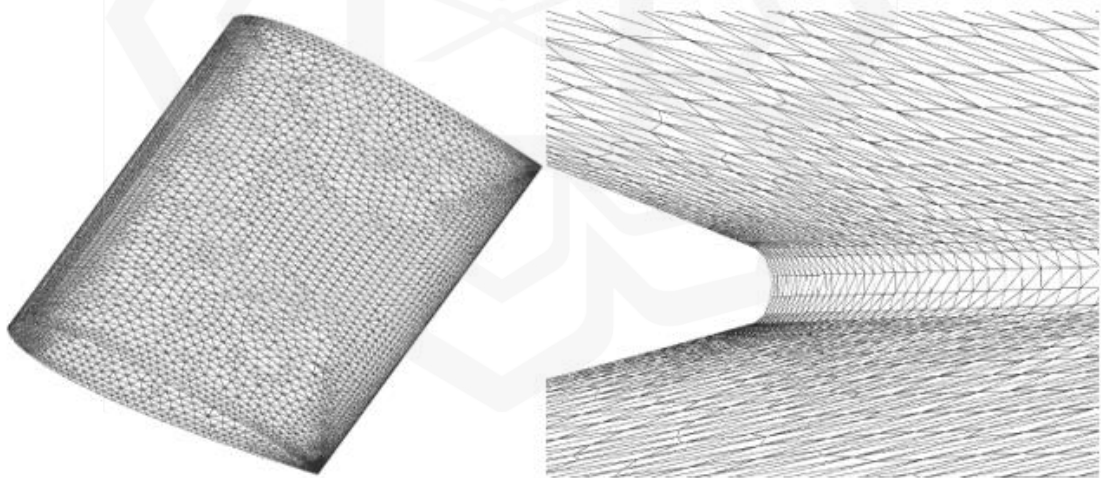


Figure 3.17 Detailed view of the mesh around the airfoil and at the TE.

### 3.3.3. Numerical Scheme

The 2D case analysis utilized a coupled pressure-velocity integrating scheme with least-squares cell method for gradient calculation. An upwind discretization scheme of

second-order was used to solve equations, and a bounded second-order implicit scheme was selected for a suitable time-dependent formulation. A fixed time-stepping scheme of  $5.0 \times 10^{-5}$  was deemed sufficient for various cases and was verified with drag and lift coefficient graphs. Double precision was chosen to minimize truncation error, and residual for all calculations was set to none to ensure simulation results suits experimental data. The convergence criteria for the computational analysis were determined based on the residual, with a threshold set at approximately  $10^{-6}$ , ensuring the solution's stability and accuracy. Furthermore, automated journal codes were implemented to ensure a smooth and uninterrupted continuation of the simulation process, as depicted in the appendix section. The numerical simulation employed the shear-stress transport (SST)  $\gamma - Re\theta$  model to analyze unsteady, laminar-turbulent flow around the airfoil (ANSYS, 2013; Langtry & Menter, 2009) as shown by equation 3.1 – 3.6.

$$\frac{\partial(\rho\gamma)}{\partial t} + \frac{\partial(\rho U_j \gamma)}{\partial x_j} = P_{\gamma 1} - E_{\gamma 1} + P_{\gamma 2} - E_{\gamma 2} + \frac{\partial}{\partial x} \left[ \left( \mu + \frac{\mu_\tau}{\sigma_f} \right) \frac{\partial \gamma}{\partial x_j} \right] \quad (3.1)$$

The sources for intermittency transport equation are defined as:

$$P_{\gamma 1} = F_{length} \rho S [\gamma F_{onset}]^{C_{a1}} \quad (3.2)$$

$$E_{\gamma 1} = C_{e1} P_{\gamma 1} \gamma \quad (3.3)$$

Where S defines the rate of deformation magnitude,  $F_{onset}$  is a function of vorticity Reynolds number and is used to trigger the intermittency production,  $F_{length}$  is an experimental correlation that defines the extent of the transition region.  $Re_{\theta C}$  is the Reynolds number where the intermittency initially starts to rise in the flow near a bounded surface, and it happens ahead of the transition Reynolds number ( $Re_{\theta t}$ ).  $Re_{\theta C}$  is related to  $F_{onset}$ .

The transport equation for the  $\widetilde{Re}_{\theta t}$  is based on the following equation:

$$\frac{\partial(\rho\bar{Re}_{\theta t})}{\partial t} + \frac{\partial(\rho U_j \bar{Re}_{\theta t})}{\partial x_j} = P_{\theta t} + \frac{\partial}{\partial x_j} [\sigma_{\theta t} (\mu + \mu_t) \frac{\partial \bar{Re}_{\theta t}}{\partial x_j}] \quad (3.4)$$

This equation (3.4) helps to pass the freestream values to the boundary layer using only a local formulation.  $Re_{\theta t}$  relies on the attack variables such as turbulence intensity and pressure gradient.

The source term is defined as:

$$P_{\theta t} = c_{\theta t} \frac{\rho}{t} (Re_{\theta t} - \bar{Re}_{\theta t}) (1.0 - F_{\theta t}) \quad (3.5)$$

$$P_{\theta t} = \frac{500\mu}{\rho U^2} \quad (3.6)$$

where  $t$  is a time scale,  $F_{\theta t}$  is employed to disable the source term in the BL and allow  $\bar{Re}_{\theta t}$  to disseminate into the BL from the freestream.  $F_{\theta t}$  is assigned 0 in the freestream and 1 in the boundary layer.  $\bar{Re}_{\theta t}$  is the transmitted scalar value of  $Re_{\theta t}$  to the boundary value, zero flux is assigned at the wall.

In 3D investigation the Simplec pressure-velocity integration scheme was employed, with gradients evaluated using the Green-Gauss node-based technique. A second-order upwind discretization scheme was employed to solve all equations. A bounded second-order implicit method was chosen to establish a suitable time-dependent solution formulation. The simulation was carried out using a fixed time-stepping scheme. After evaluating various time intervals, it was determined that incoming velocity and airfoil chord-based dimensionless time of 160 was sufficient for all cases. This was confirmed by examining both instantaneous and averaged lift (Cl) and Drag coefficients (Cd). The total simulation time was originally calculated using a method known as "hydraulic retention time." However, the estimated flow time was doubled to ensure that the flow had sufficient time to traverse the domain twice. Furthermore, double precision was enabled in order to decrease the truncation error. On the other hand, the convergence criteria for the simulation were defined by monitoring the fluctuations in velocity and lift coefficient; convergence was considered achieved when these values stabilized over time. The residual criterion was not utilized due to

the inherently highly fluctuating nature of the flow, which rendered it unsuitable as a reliable indicator of convergence.

The large-eddy simulation model was used to analyze the unsteady fluid flow within the computational domain. The sub-grid viscosity values were computed based on the dynamic Smagorinsky model (DSM). Thus, the Smagorinsky constant will be a local value. The governing equations employed in the analysis were described in detail according to equations 3.7 through 3.10, providing a comprehensive mathematical foundation for the computational framework. These equations enhance the accuracy of the results, specifically near the wall compared to the original Smagorinsky model, which uses a single value for all the cases.

Filtered Navier–Stokes equation and continuity equations for incompressible flow can be written as (Kim, 2004):

$$\frac{\partial}{\partial t}(\rho \bar{u}_i) + \frac{\partial}{\partial x_j}(\rho \bar{u}_i \bar{u}_j) = \frac{\partial}{\partial x_j}(\sigma_{ij}) - \frac{\partial \bar{p}}{\partial x_i} - \frac{\partial \tau_{ij}}{\partial x_j} \quad (3.7)$$

$$\frac{\partial \rho}{\partial t} + \frac{\partial}{\partial x_i}(\rho \bar{u}_i) = 0 \quad (3.8)$$

where  $\sigma_{ij}$  is the stress tensor, it is interpreted as follows

$$\sigma_{ij} = \left[ \mu \left( \frac{\partial \bar{u}_i}{\partial x_j} + \frac{\partial \bar{u}_j}{\partial x_i} \right) \right] - \frac{2}{3} \mu \frac{\partial \bar{u}_i}{\partial x_i} \delta_{ij} \quad (3.9)$$

And  $\tau_{ij}$  is the subgrid-scale (SGS) stress tensor illustrated as

$$\tau_{ij} = \rho \bar{u}_i \bar{u}_j - \rho \bar{u}_i \bar{u}_j \quad (3.10)$$

Nonetheless, the subgrid-scale stress tensor is unknown and thus modelled based on isotropic assumptions as shown by Eqn. (3.11)

$$\tau_{ij} - \frac{1}{3} \tau_{kk} \delta_{ij} = -2\nu_{sgs} \bar{S}_{ij} \quad (3.11)$$

where  $\nu_{sgs}$  is the subgrid-scale kinematic viscosity and  $\bar{S}_{ij}$  is the strain rate from the smallest resolved eddies. The rate of strain tensor is defined as

$$\bar{S}_{ij} = \frac{1}{2} \left( \frac{\partial \bar{u}_i}{\partial x_j} + \frac{\partial \bar{u}_j}{\partial x_i} \right) \quad (3.12)$$

In addition, the subgrid-scale kinematic viscosity is undetermined and thus becomes the variable to be evaluated. Based on original Smagorinsky method (Smagorinsky, 1963), SGS viscosity is computed as follows

$$\nu_{sgs} = C_s \bar{\Delta}^2 |\bar{S}| \quad (3.13)$$

where  $C_s$  is the model constant, also referred to as Smagorinsky coefficient. It describes the ratio of the cell size that gives the average eddy in a cell, it has a value ranging from 0 to 1 because it is expected to be less than the cell size. The second term on the right side of equation (7) ( $\bar{\Delta}$ ) is the subgrid filter width, this defines the mesh size. Lastly,  $|\bar{S}|$  is the modulus of strain rate tensor and it is equivalent to  $\sqrt{2\bar{S}_{ij}\bar{S}_{ij}}$ .

Following the computation of subgrid-scale kinematic viscosity, subgrid-scale stress tensor can now be presented as shown by equation (3.14)

$$\tau_{ij} - \frac{1}{3} \tau_{kk} \delta_{ij} = -2C_s \bar{\Delta}^2 |\bar{S}| \bar{S}_{ij} \quad (3.14)$$

However, the optimum  $C_s$  value varies for each part of the flow and must be reduced near solid walls in order to minimize the numerical dissipation introduced by the sub-grid scale model, this is particularly the case for wind turbine blades where the surface fluctuations are assumed to be the main acoustic sources. Therefore, the dynamic Smagorinsky method can be used (Germano et al., 1991).

In this model an extra filter level known as the test filter ( $\tilde{\Delta}$ ) is used in combination with sub-grid scale filter level, in order to estimate a value of  $C_{s,new}$ , which is a function

of time and space (Zhao, 2019). Following Germano's (Germano et al., 1991) evaluation, the two filters were compared as follows;

$$\tilde{L}_{ij} = \overline{\tilde{u}_i \tilde{u}_j} - \tilde{u}_i \tilde{u}_j \quad (3.15)$$

where  $\tilde{L}_{ij}$  can be computed using resolved eddies in a cell as shown by Eqn. (3.16)

$$\tilde{L}_{ij} = 2C_{s,new} \bar{\Delta} M_{ij} \quad (3.16)$$

where  $M_{ij}$  is defined as

$$M_{ij} = (\tilde{\Delta}/\bar{\Delta})^2 |\tilde{S}| \tilde{S}_{ij} \quad (3.17)$$

Moreover, the new model constant ( $C_{s,new}$ ) that provide stable solution during the analysis is presented by equation (3.18)

$$C_{s,new} \bar{\Delta}^2 = \frac{L_{ij} M_{ij}}{M_{ij} M_{ij}} \quad (3.18)$$

The acoustic noise calculations were formulated by an integral-form solution of Ffowcs Williams and Hawkings as presented by Eqn. 3.19 – 3.22.

The Ffowcs Williams and Hawkings equation can be written as (Williams & Hawkings, 1969):

$$\frac{1}{c_0^2} \frac{\partial^2 p'}{\partial t^2} - \nabla^2 p' = \frac{\partial^2}{\partial x_i \partial x_j} \{T_{ij} H(f)\} - \frac{\partial}{\partial x_i} \{ [P_{ij} n_j + \rho u_i (u_n - v_n)] \delta(f) \} + \frac{\partial}{\partial t} \{ [\rho_0 v_n + \rho (u_n - v_n)] \delta(f) \} \quad (3.19)$$

where  $f$  describes the non-stationary surfaces ( $f < 0$  inside part,  $f = 0$  on the surface and  $f > 0$  outside part),  $\delta(f)$  is the Dirac delta function and  $H(f)$  is the Heaviside function.  $u_n$  and  $v_n$  are the fluid and surface velocity normal to the surface.  $p'$  is the pressure fluctuation at the far-field observer location.



The three expressions on the right side of equation 3.19 can be defined as additional acoustic sources. The first term describes the quadrupole source with four lobes, it is related to the velocity fluctuation outside of the surface. This source has very little contribution at low Reynolds number and thus can be neglected. The second term defines dipole source with two lobes of directivity. These sources are generated due to the forces acting on the surface of the body and for this reason, it is also referred to as loading noise. The last term is monopole with a single lobe of directivity. These sources are related to the geometry of the model such as thickness of the wing hence known as thickness noise (Zhao, 2019).

Acoustic pressure fluctuations at any receiver location can be evaluated by the combination of loading ( $p'_L$ ) and thickness noise ( $p'_T$ ). Considering low flow velocity, the quadrupole sources are neglected from equation 3.19. Loading and thickness noises are computed as shown by equations 3.21 and 3.22.

$$p' = p'_L + p'_T \quad (3.20)$$

$$4\pi p'_L(x, t) = \frac{1}{c_0} \int_{f=0} \left[ \frac{\dot{L}_r}{r(1-M_r)^2} \right]_{ret} ds + \int_{f=0} \left[ \frac{L_r - L_M}{r^2(1-M_r)^2} \right]_{ret} ds + \frac{1}{c_0} \int_{f=0} \left[ \frac{L_r \{rM_r + C_0(M_r - M^2)\}}{r^2(1-M_r)^3} \right]_{ret} ds \quad (3.21)$$

$$4\pi p'_T(x, t) = \int_{f=0} \left[ \frac{\rho_0(\dot{U}_n + U_n)}{r(1-M_r)^2} \right]_{ret} ds + \frac{1}{c_0} \int_{f=0} \left[ \frac{\rho_0 U_n \{rM_r + C_0(M_r - M^2)\}}{r^2(1-M_r)^3} \right]_{ret} ds \quad (3.22)$$

where  $U_i$  and  $L_i$  are defined as

$$U_i = v_i + \frac{\rho}{\rho_0} (u_i - v_i) \quad (3.23)$$

$$L_i = P_{ij} \delta_{ij} n_j + \rho u_i (u_n - v_n) \quad (3.24)$$

The airfoil surface was identified as the source of the acoustic wave, and four receiver locations were chosen: one located upstream of the leading edge (8c), one above the suction side (8c), one below the pressure side (8c), and one downstream of

the trailing edge (8c) as shown by Figure 3.18. All the observer positions were measured relative to the center of the airfoil.

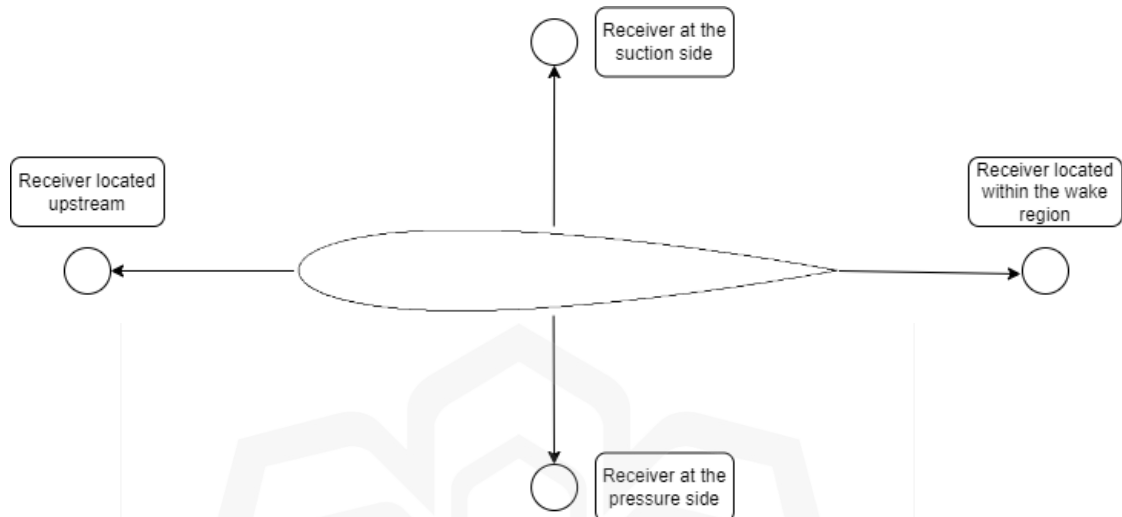


Figure 3.18 Schematic diagram illustrating the receiver locations.

### 3.3.4. Data Validation

Validation is a critical aspect of the study that is important to the results' reliability. This study's validation procedure was undertaken to ensure the accuracy and reliability of the data acquired from the 2D and 3D analyses. It was validated against other experimental data on lift coefficient and demonstrated satisfactory agreement to confirm the 2D analysis,. Furthermore, the 3D analysis was confirmed by comparisons with existing work in literature. In the aerodynamic aspect, the mean lift coefficient values and lift fluctuation values were compared with published work, and the findings revealed a remarkable degree of agreement. Additionally, the acoustic results, especially pressure fluctuations, were verified against published work in the literature, giving further confidence in the findings obtained. The complete validation approach, carried out in this work, highlights the necessity of validation and raises the assurance in the results reached from the analysis.

### **3.4. EXPERIMENTAL SET-UP**

#### **3.4.1. Flow Facility**

A test facility is a crucial component of every experimental setup. It offers the environment, equipment, and infrastructure essential to perform experiments and gather data. The test facility can range from simple equipment to a comprehensive facility with specialized equipment, instruments, and facilities for testing. The selection and design of a test facility may considerably affect the success of an experiment; hence it is vital to carefully analyze each experiment's individual needs and specifications of each experiment when choosing a test facility.

The Open Loop Wind Tunnel at Universiti Pertahanan Nasional Malaysia (UPNM) was used in our study as a specialized facility for examining flow structure in a controlled airflow. With a mean turbulence intensity of 0.04% (UPNM, 2022), the tunnel provided a continuously steady testing environment, enabling us to acquire precise and reliable data as shown in Figure 3.19. The low turbulence intensity resulted in a highly smooth incoming flow, assuring flow quality. Moreover, The maximum solid blockage was evaluated and found around 7.4%. Therefore, no blockage corrections were applied to the recorded data. The versatile speed capabilities of the wind tunnel, ranging from 0 to 100 meters per second, allowed us to conduct a range of aerodynamic experiments. The 300 by 300 millimeters test section offered adequate area for small-scale aerodynamic testing and study. The overview of the wind tunnel may be seen in Figure 3.20.

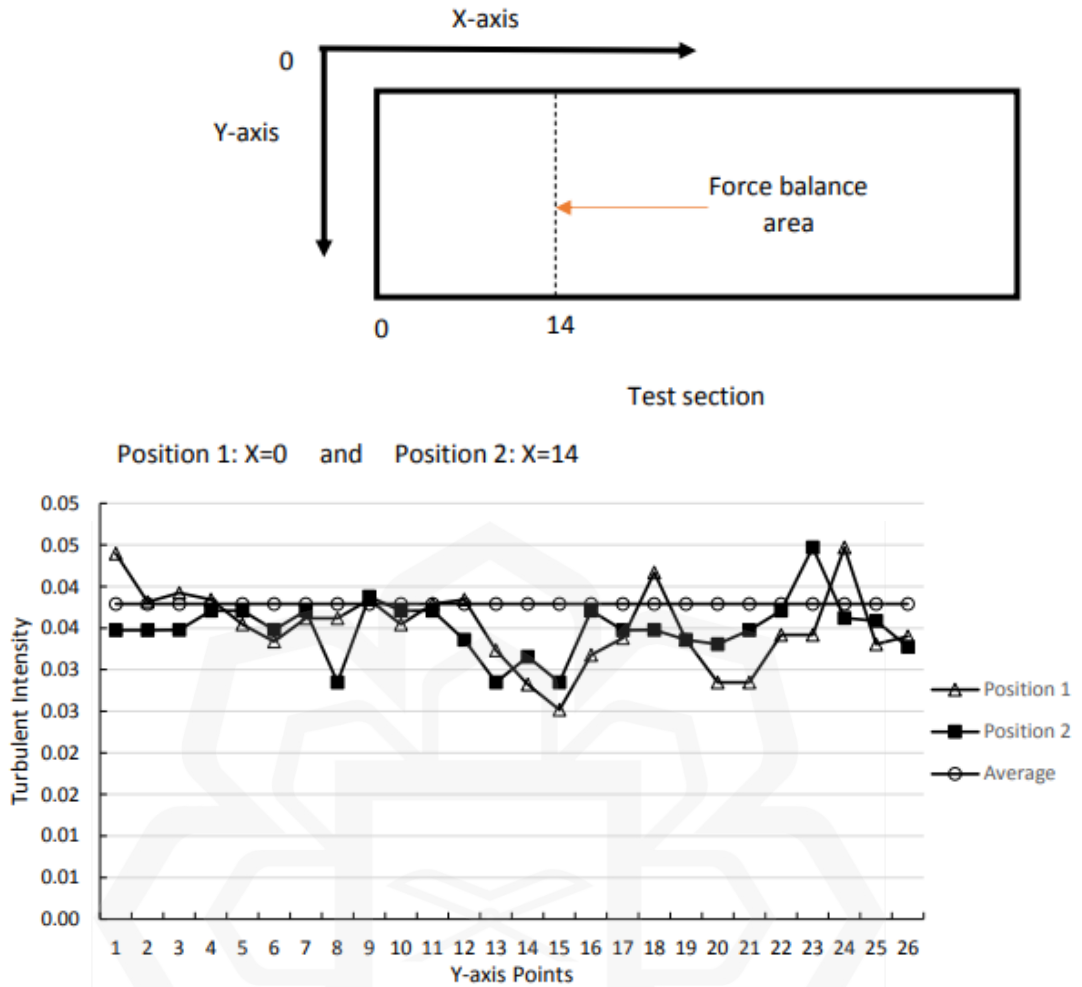


Figure 3.19 Turbulence intensity as a function of the vertical distance (UPNM, 2022)

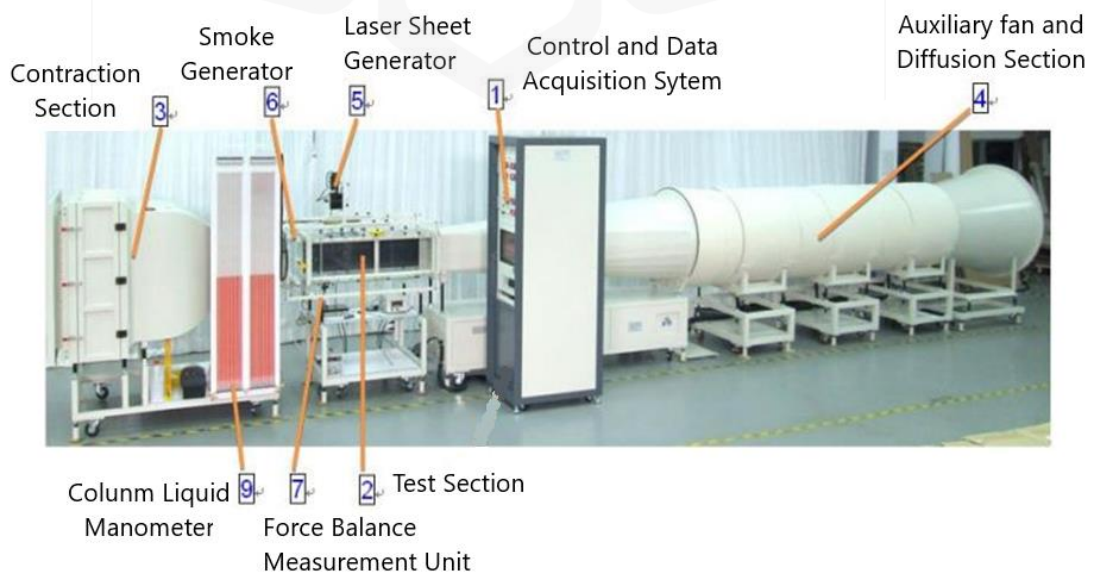


Figure 3.20 Schematic of UPNM open loop wind tunnel (UPNM, 2014)

### 3.4.2. Particle Image Velocimetry (PIV)

The 2D Particle Image Velocimetry (PIV) system was performed in a plane perpendicular to the flow direction using the configurations depicted in Figure 3.21. In order to improve particle visibility, the flow was seeded with Di-ethyl-hexyl-sebacat (DEHS) particles with an average diameter of  $1\ \mu\text{m}$ . The seeding is employed since it has low vapour pressure, it is non-toxic and is readily dispersible in the flow due to its low density. On top of that, the seeding material was illuminated by a laser sheet produced by a dual-pulsed Nd: YAG laser with a pulse energy of 200 MJ, frequency of 15 Hz, and wavelength of 532 nm. The laser beam was introduced into the test section through the top wall and conditioned into a thin sheet with an estimated thickness of 1 millimeter. The laser was calibrated by utilizing two rulers at both ends of the laser sheet to ensure the perpendicularity of the laser sheet in the flow direction, as shown in Figure 3.21.

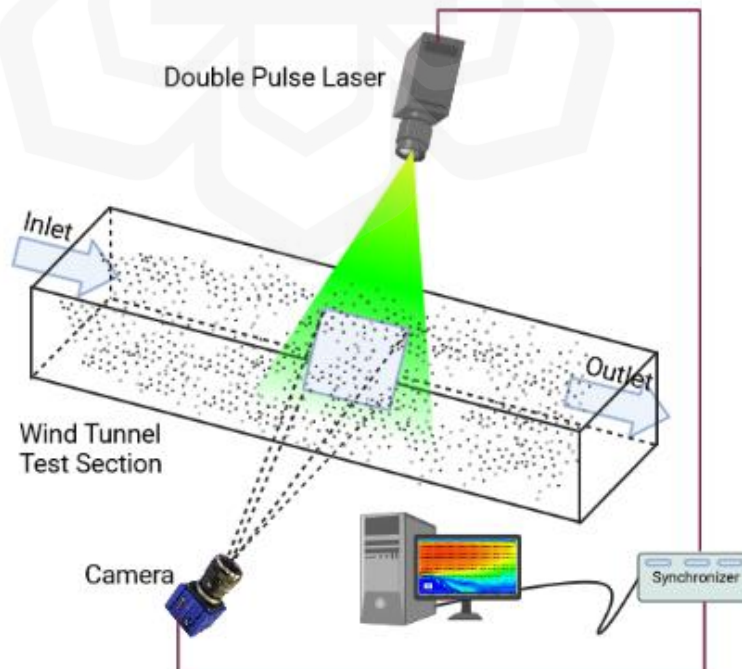


Figure 3.21 Schematic of PIV setup in the wind tunnel

Furthermore, the particle image velocity (PIV) data was recorded by a high-speed camera equipped with a 50 mm lens and a 2752 x 2200 pixels resolution. The camera was synchronized with the laser pulses through a programmable timing unit (PTU) utilizing DaVis 10.0 software. The camera was calibrated with a standard calibration target to determine its intrinsic parameters, such as vertical and horizontal orientation to the field of view. The field of view was carefully chosen to provide a clear and comprehensive view of both the upstream and downstream flow regions. This was achieved by ensuring that the field of view was appropriately sized to capture all relevant flow information, providing a comprehensive understanding of the flow dynamics in the test section. The flow field was calibrated using tracer particles. In addition, the images were acquired using a dual-frame PIV approach with a sampling rate of 12.95 Hz, and an exposure time of 50  $\mu$ s per frame. Moreover, the camera used in the experiment was originally set to have a relative aperture setting of f/1.8. This parameter was used to concentrate the particles in the flow field effectively. However, to improve the focus of the acquired images, the hole size was increased to f/2.8, which reduced the quantity of light and provided sharper images.

A substantial number of 500 images were recorded and processed using a cross-correlation algorithm. The Particle Image Velocimetry (PIV) measurements were captured three times and averaged to enhance accuracy and reliability, mitigating the impact of random errors and transient flow variations. The final interrogation window size was 32 by 32 pixels with 75% image overlap, with each window having ten particles on average. The particle displacements and time difference between the two frames were used to calculate the velocity field, which was then statistically analyzed and visualized using vector plots and contour plots. The accuracy of the results was limited by factors such as the reflection from the surface, particle image resolution, laser light intensity, camera exposure time, and the presence of flow structures such as vortices and wakes. Moreover, to enhance the experiment's precision and minimize the impact of surface reflection on the results, the models were coated with a specialized paint named Musuo black. This paint has been carefully selected based on its optical

properties and ability to reduce surface reflection, thereby improving the accuracy of The experiment. the measurements were repeated multiple times to ensure the quality of the results,. Table 3.1 summarizes the parameters for the PIV experiments.

Table 3.1 Parameters used in 2D Particle Image Velocimetry (PIV) measurements.

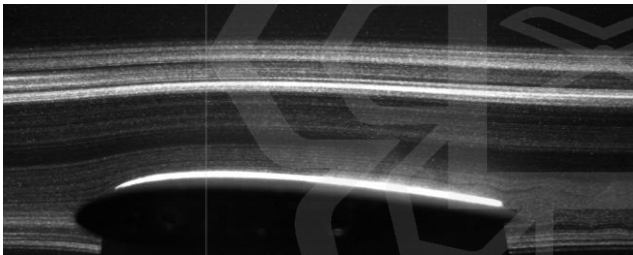
| <b>Parameters</b>    | <b>Units</b>    | <b>Symbols</b> | <b>Data</b>       |
|----------------------|-----------------|----------------|-------------------|
| Focal length         | mm              |                | 50                |
| Aperture number      |                 | f/             | 2.8               |
| Field of view        | mm <sup>2</sup> | FoV            | 160 x 160         |
| Imaging resolution   | pixels          | S              | 2752 x 2200       |
| Interrogation window | pixels          |                | 32 by 32          |
| Sampling frequency   | Hz              | f <sub>s</sub> | 12.95             |
| PIV frame mode       |                 |                | Double frame mode |
| Exposure time        | μs              | Δt             | 50                |
| Freestream           | pixels          | Δx             | 10                |

### 3.4.3. Surface Reflection

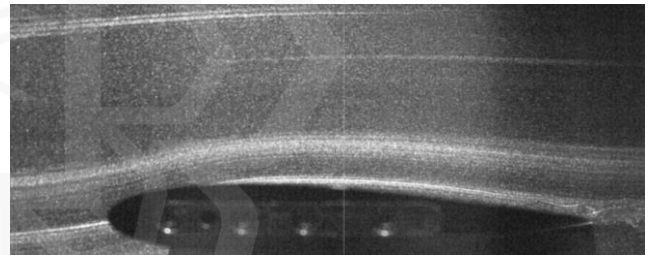
Musou Black paint is created from ultra-fine carbon particles known as nitrogen-doped graphene, which equips it with a deep and robust black colour. This paint has the potential to absorb virtually all the light that strikes its surface, leaving it an incredibly dark substance. The absorption rate of Musou Black paint is believed to be close to 99.965%, yielding to an unusually low reflectivity. As a result, it is suited for usage in optical applications such as experiments on Particle Image Velocimetry (PIV).

Because of the qualities above and considering the absence of prior research employing Musou Black paint in PIV measurement, this study intends to compare it with the conventional Flat black paint. The two types of paint differ significantly in terms of their light absorption capabilities. Flat black paint has an absorption rate close to 80%. Given these numbers, it is evident that Musou Black has a larger light absorption capability than to Flat Black paint. The results provided in Figure 3.22

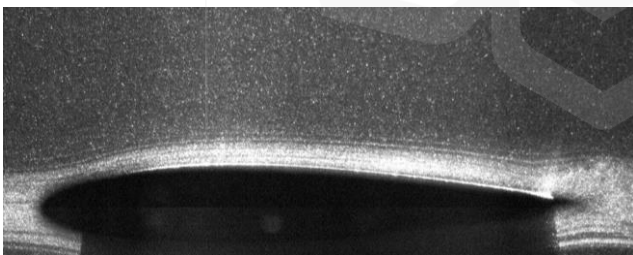
demonstrate that Musou Black paint surpasses Flat Black paint in the baseline, serration, and comb models when it comes to light reflection from the surface. Specifically, Musou Black demonstrated reduced reflection of light from these models when compared to Flat Black. However, the situation is flipped with the poro-serrated type, where flat black exhibits less reflection. The variation in light reflection between the two paints is probably related to the existence of holes in the poro-serrated model. The perforations may make the light to scatter differently, resulting in a distinct reflection pattern. Additionally, the unique pigments employed in the composition of Musou Black paint may contribute to the disparity in reflection. These pigments may influence how the paint interacts with light, resulting in differences in reflection between the two types of paint. Therefore, for all the other models, such as the baseline, serration, comb, and comb-serrated models, Musou Black paint is the recommended option. As a result, it is commonly used to paint these models, whereas the poro-serrated model is painted with flat black paint.



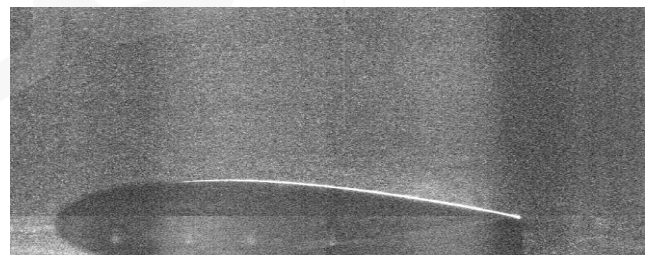
(a) Flat Black, Baseline airfoil at  $\alpha = 0$



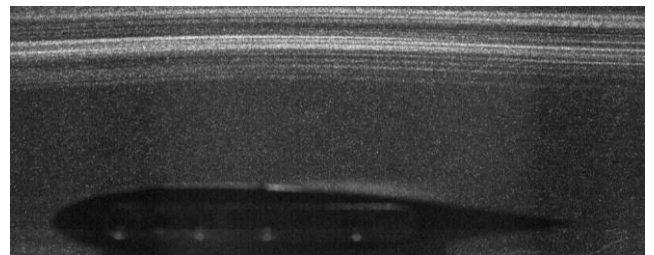
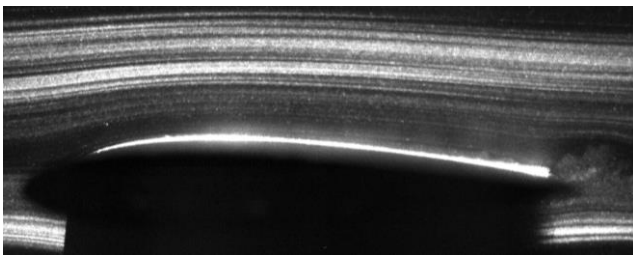
(b) Musou Black, Baseline airfoil at  $\alpha = 0$



(c) Flat Black, Serrated TE airfoil at  $\alpha = 0$

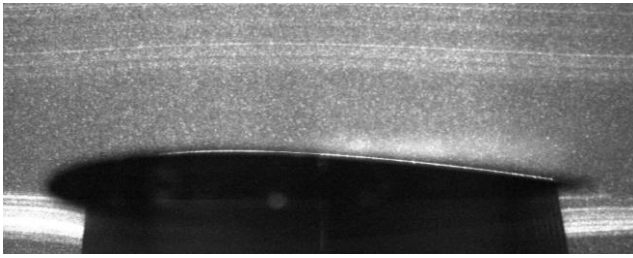


(d) Musou Black, Serrated TE airfoil at  $\alpha = 0$

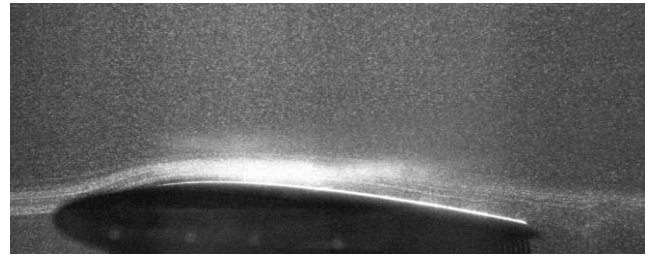




(e) Flat Black, Comb TE airofoil at  $\alpha = 0$



(f) Musou Black, Comb TE at  $\alpha = 0$



(g) Flat Black, Poro-Serrated airfoil at  $\alpha = 0$

(h) Musou Black, Poro-Serrated airfoil at  $\alpha = 0$

Figure 3.22 Surface reflection from Musou and Flat black painted surface at  $\alpha = 0^\circ$ .

### 3.5. SUMMARY

This chapter outlines the experimental and computational methods employed in this research study. The low-speed wind tunnel at Universiti Pertahanan Nasional Malaysia (UPNM) was equipped with Particle Image Velocimetry (PIV) systems, which were used to conduct flow visualization experiments on the baseline and modified models. In addition, computational fluid dynamics simulations were performed using the Ansys Fluent package in order to analyze the flow topology and aeroacoustics of the various models under study.

## CHAPTER FOUR

### AERODYNAMIC AND FLOW FIELD INVESTIGATIONS

#### 4.1. INTRODUCTION

This chapter investigates the flow field structure of both the baseline and modified models. The study combines numerical calculations by using Ansys Fluent software with experimental work carried out in the UPNM low-speed wind tunnel. The findings of the computational analysis are reported in both two-dimensional (2D) and three-dimensional (3D) cases. The two-dimensional (2D) study was done across a range of relatively low Reynolds numbers, which varied from  $8.4 \times 10^4$  to  $1.7 \times 10^5$ , and at moderate angles of attack from 0 to 6 degrees. In contrast, the three-dimensional (3D) analysis was performed at a Reynolds number of  $1.6 \times 10^5$  and a single Angle of attack of 0 degrees due to computational restrictions.

In addition to the numerical analysis, experimental measurements were carried out utilizing PIV. The findings of the experimental measurements were utilized to validate the simulation work at an Angle of attack of 0 degrees and to offer a more complete understanding of the flow structure at a moderate Reynolds number of  $1.6 \times 10^5$  and various angles of attack ranging from 0 to 10 degrees.

In Chapter 3, the models under consideration are presented orderly and comprehensively, with their distinctive features and characteristics highlighted in depth. The models comprise the physical dimensions of each model, as well as their precise layouts and geometries, which play a key role in defining their aerodynamic performance. The configurations of these models are clearly described in Figures 3.1-3.10, offering a diagram of the models for further clarity. This information is necessary for the reader to understand better of the models being researched and the basis for their aerodynamic analysis.

A complete review of the computational and experimental results is presented In Chapter 4. The computational analysis is separated into 2D and 3D analysis, with an

entire verification of each section provided in a clear and simple manner. The results of the computational study are then described in depth, highlighting significant findings and insights. Based on PIV, the experimental study is also discussed in this chapter, with some of its results employed to validate the 3D analysis. The flow structure results from PIV are also explored in detail, offering a deeper insight into the flow behaviour around the models. The chapter finishes with a summary of the main points from each part, offering a concise overview of the significant conclusions from the aerodynamic study. This chapter is provided first to complement the subsequent acoustic results and enable a smooth grasp of the content.

## **4.2. COMPUTATIONAL SIMULATION**

### **4.2.1. Two-Dimensional Numerical Simulation**

This study, selected the NACA0015 airfoil with a chord length of 0.15 m as the model. The airfoil was designed with a sharp trailing edge to improve the mesh structure,. Two-dimensional analysis was chosen as many previous studies have used this approach, allowing for easy comparison of results. Additionally, 2D analysis produces reasonably accurate results while requiring less computational time compared to 3D analysis.

#### ***4.2.1.1 Comparison with other study***

The lift ( $C_l$ ) and drag coefficients ( $C_d$ ) obtained from the present study were compared with those from previous experimental data (Jacobs and Sherman, 1939; Miley, 1982) and presented in Figures 4.1-4.2. The results presented reasonable agreement between the current research and the experimental work. However, the turbulence viscosity ratio used in the experiment work was not provided in the previous work (Jacobs and Sherman, 1939; Miley, 1982). In the present research, a turbulent intensity of 2% was used, which was consistent with the experimental work by (Miley, 1982). The experimental results were obtained at lower Reynolds number ( $Re = 1.66 \times 10^5$ ) compared to the present study and the other experimental work ( $Re = 1.7 \times 10^5$ ) (Jacobs and Sherman, 1939; Miley, 1982). However, all were reported at  $Re = 8.4 \times 10^4$ .

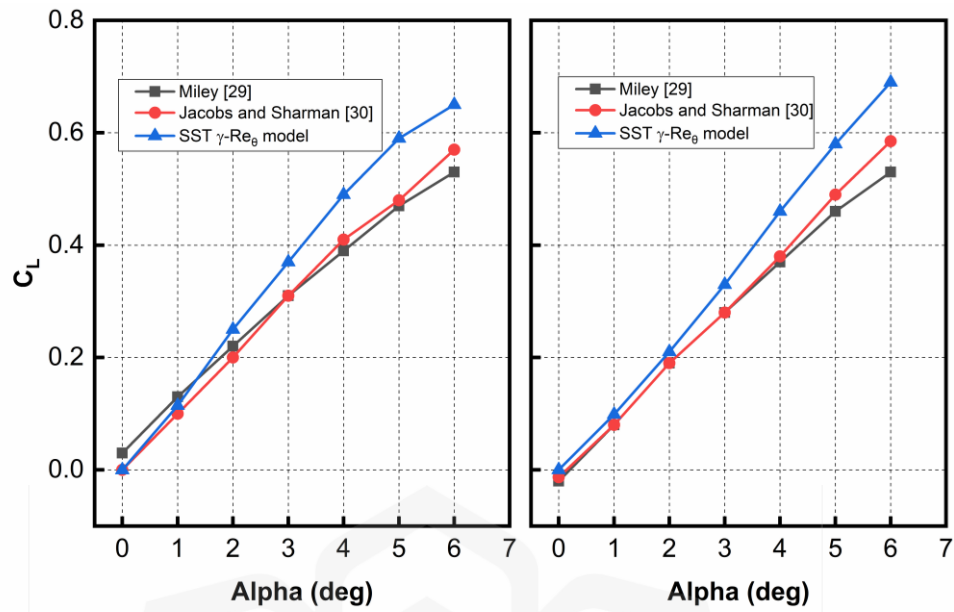


Figure 4.1 Comparison of  $C_L$  at different Reynolds numbers

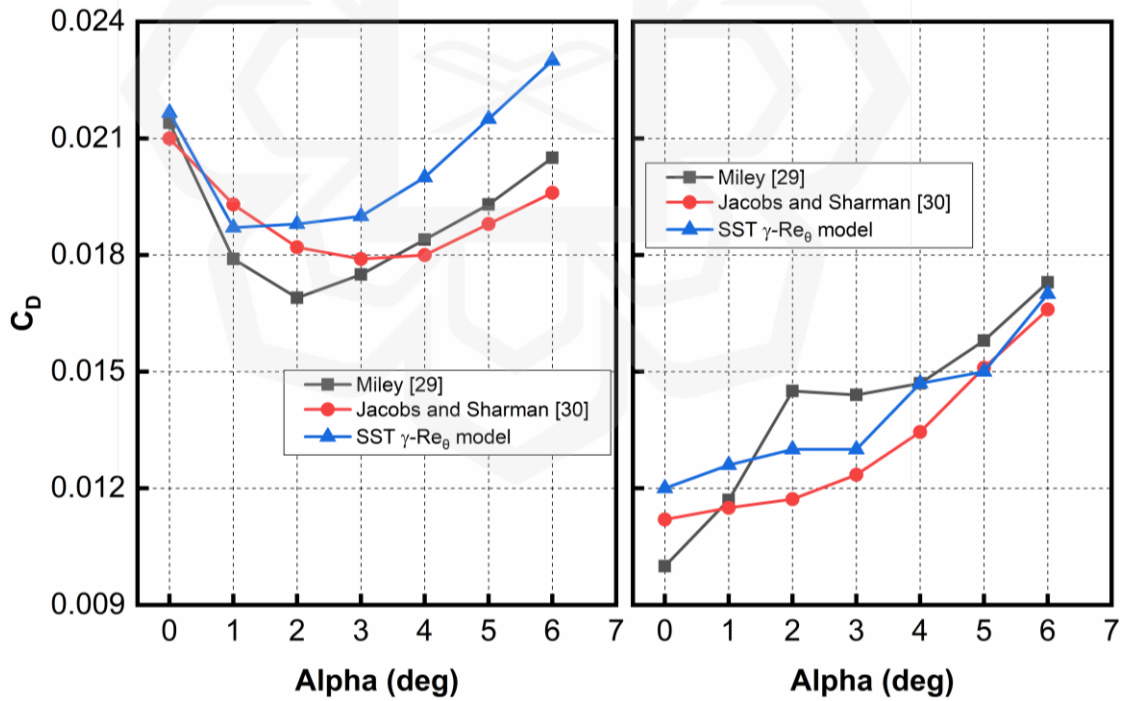


Figure 4.2 Comparison of  $C_D$  at different Reynolds numbers

The lift and drag coefficients exhibit an acceptable trend through all angles of attack for both  $Re = 8.4 \times 10^4$  and  $Re = 1.7 \times 10^5$ . The results agree well, particularly at

low angles of attack between 0 and 2 degrees, with some small fluctuations observed throughout the experimental result. Both the SST  $\gamma - Re\theta$  model and experimental data demonstrate a drop in the drag coefficient value as Reynolds number increases from  $8.4 \times 10^4$  to  $1.7 \times 10^5$ . As the Reynolds number increases, the dominance of inertial forces over viscosity leads to the formation of a more chaotic flow beyond it, reducing the overall impact of viscosity on the flow and consequently causing a decrease in the drag coefficient. Additionally, for  $Re = 1.7 \times 10^5$ , the drag coefficient increased with Angle of attack. In contrast, both the present work and the experiments illustrated an increase in the lift coefficient with an increase in both Reynolds number and Angle of attack. Furthermore, the examination of the data unveils a clear pattern in the Lift coefficient's percentage error, showing a consistent increase from 0 degrees. There is an approximately 12% error progressively climbing to 19% at a 6-degree angle compared to the experimental findings. In contrast, the Drag coefficient demonstrates an opposite trend. The percentage error starts at about 9% when the angle is 0 degrees and gradually decreases to 2% at a 6-degree angle relative to the experimental outcomes. In general, the SST  $\gamma - Re\theta$  model effectively estimates lift and drag values trends. Other researchers (Lee & Baeder, 2021; Rezaeiha et al., 2019) have also observed good agreement between experimental and numerical results. Therefore, the numerical model can be considered adequate for studying the flow characteristics and features of the NACA0015 airfoil at relatively lower Reynolds numbers.

#### ***4.2.1.2 Mean Aerodynamic Characteristics***

The flow around the LE of the airfoil is mostly laminar and separates downstream due to the inherent instability in the BL. As the flow progresses, flow separation and reattachment occur, forming LSB. The size of this bubble can vary depending on the flow conditions across the surface of the airfoil. A thorough analysis of the low Reynolds number regime is necessary to understand the complex flow phenomena fully.

In this investigation, the SST  $\gamma - Re\theta$  model was used to analyze case 2 as shown by Figure 3.16, which consisted of a mesh with 144440 grids. The study focused on various Reynolds numbers and angles of attack ranging from 0 to 3 degrees, and flow direction moved from left to right in each image. The results were presented with

symbols to show separation points ('S'), transition ('T') and reattachment ('R') points, along with a skin friction coefficient ( $C_f$ ) plot to verify these points. The separation and reattachment locations were anticipated by the intersection of the skin friction curve with the x-axis line, while the negative peak of the curve indicated the transition location. These results were obtained in accordance with the findings presented in Chapter 3.

The position of the separation point on the suction side (top side of the airfoil surface) moved slightly upstream with an increase in Reynolds number from  $8.4 \times 10^4$  to  $1.7 \times 10^5$ , as shown in Figure 4.3-4.4. Another researcher has also observed this trend (Park et al., 2020). The LSB in the adverse pressure gradient can be classified into two types, namely short and long bubbles. The LSB shown in Figure 4.5 belongs to the long type, covering around 35% to 50% of the chord size. The negative part of the skin friction curve shows the reversed flow regime and the extent of the bubble is measured between the intersection points with the x-axis line (Figure 4.4). In general, the flow meets at the TE on the suction side of the airfoil. Therefore, fully turbulent flow is not sufficiently seen on the upper side, which is evident at  $0^\circ \leq \alpha \leq 3^\circ$  (Figure 4.5(b) to Figure 4.5(h)).

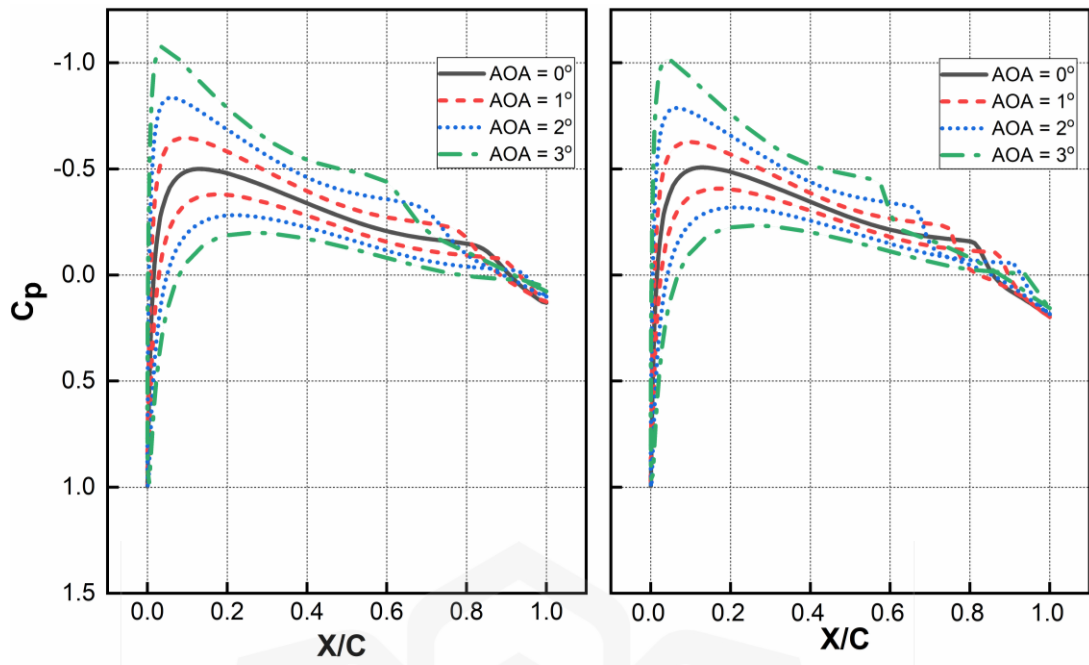


Figure 4.3 Pressure Coefficient at different Reynolds numbers

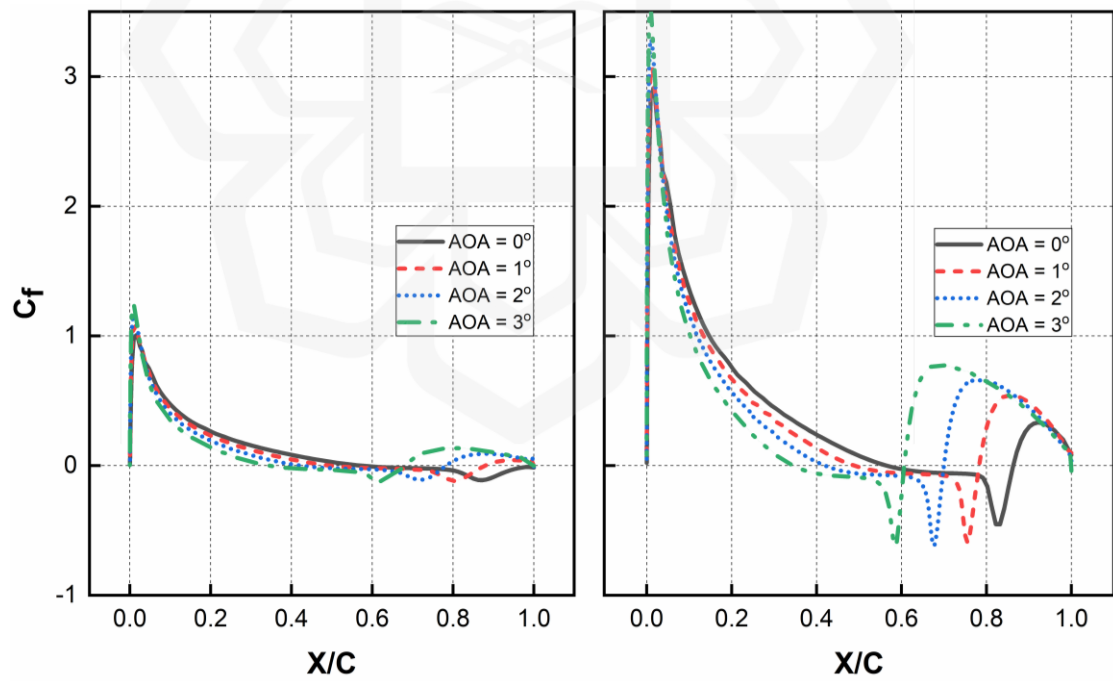
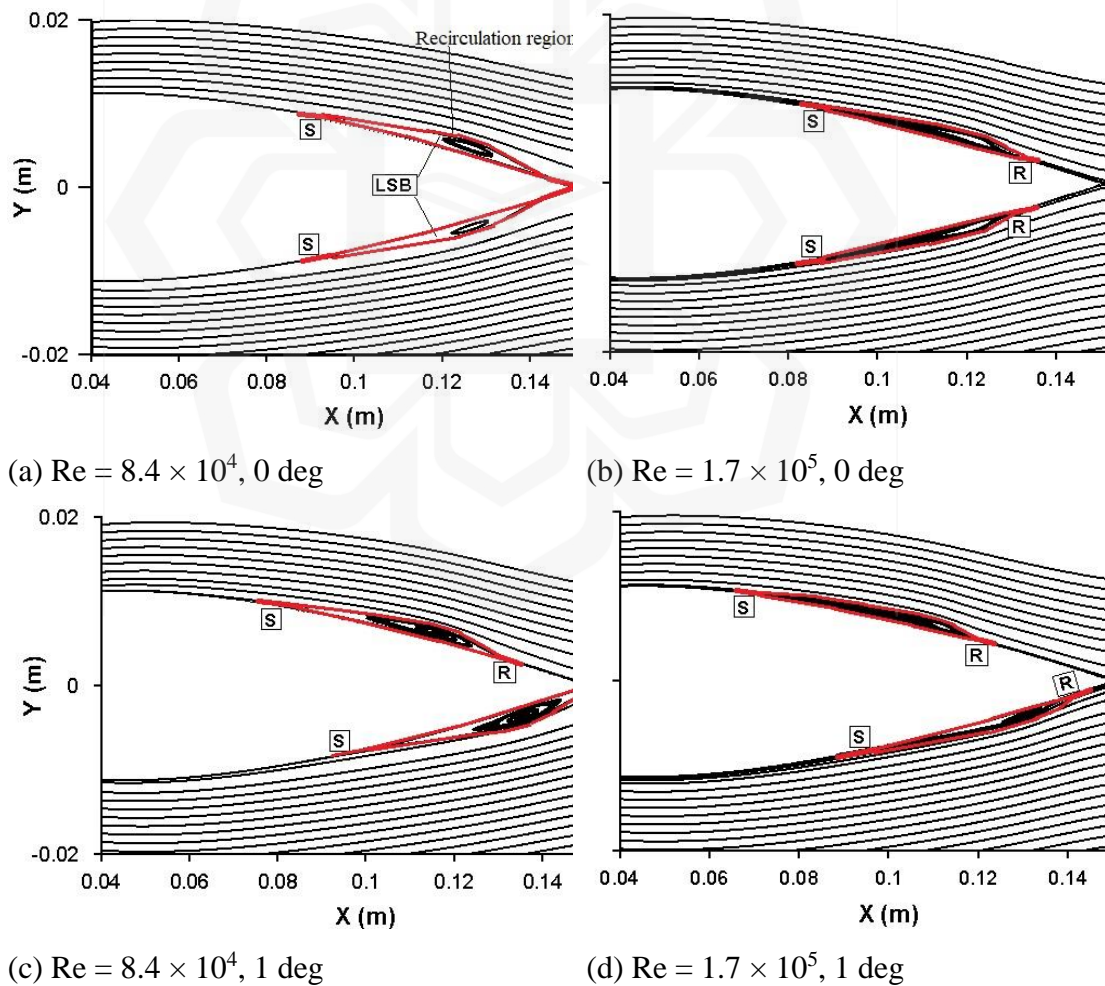


Figure 4.4 Skin friction coefficient at different Reynolds numbers

In contrast, the separation location is unchanged at  $\alpha = 3^\circ$  (as depicted in Figure 4.5(g) and Figure 4.5(h)). Moreover, an increase in the Angle of attack was observed to shift the separation, transition, and reattachment locations closer to the LE. At  $\alpha = 1^\circ$  (as shown in Figure 4.5(a) and 4.6), the flow separated at around  $0.498c$ . However, at  $\alpha = 3^\circ$ , the separation location shifted to approximately  $0.345c$ . Several other authors also reported these patterns (Guerra, 2021; Lee & Baeder, 2021; Miozzi et al., 2019). A LSB is created when the flow reattaches to the surface after separating. The development of such LSB on the upper side of the airfoil was observed at both  $Re = 8.4 \times 10^4$  and  $1.7 \times 10^5$  (as depicted in Figure 4.5(b) to Figure 4.5(h)). However, at  $Re = 8.4 \times 10^4$  (as shown in Figure 4.5(a)), the flow experienced separation without reattachment.





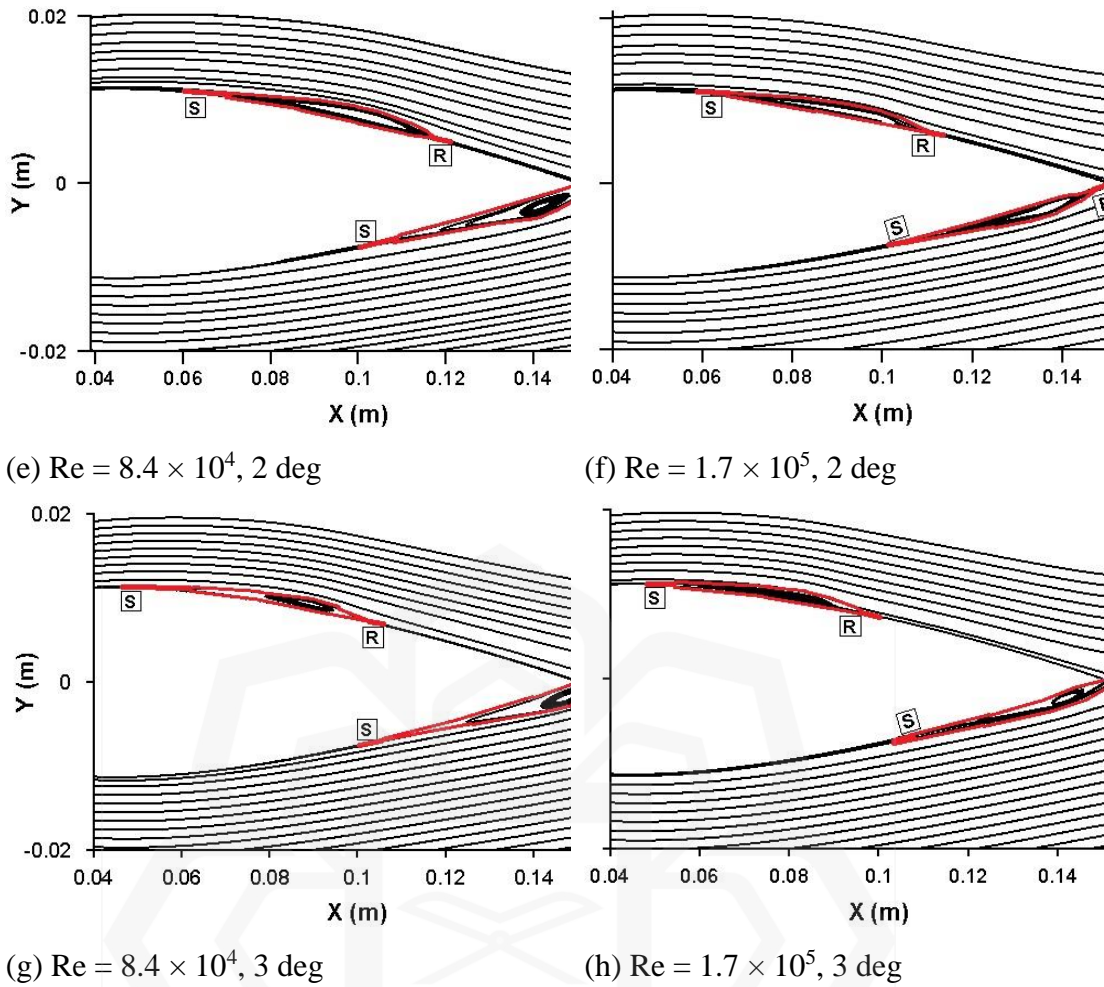


Figure 4.5 Mean Streamlines at different Reynolds numbers

Figures 4.5 and 4.6 show that as the Angle of attack increases, the laminar bubble on the pressure side moves towards the TE while maintaining a relatively constant size. Specifically, at  $\alpha = 0^\circ$  and  $\alpha = 3^\circ$ , the separation point on the pressure side shifted from  $0.57c$  to  $0.723c$ . At  $Re = 1.7 \times 10^5$ , a LSB was observed on the bottom side of the airfoil, except at  $\alpha = 3^\circ$ . On the other hand, at  $Re = 8.4 \times 10^4$ , the flow undergoes separation without reattachment throughout all angles of attack, as shown in Figure 4.5(a), Figure 4.5(c), Figure 4.5(e), and Figure 4.5(g).

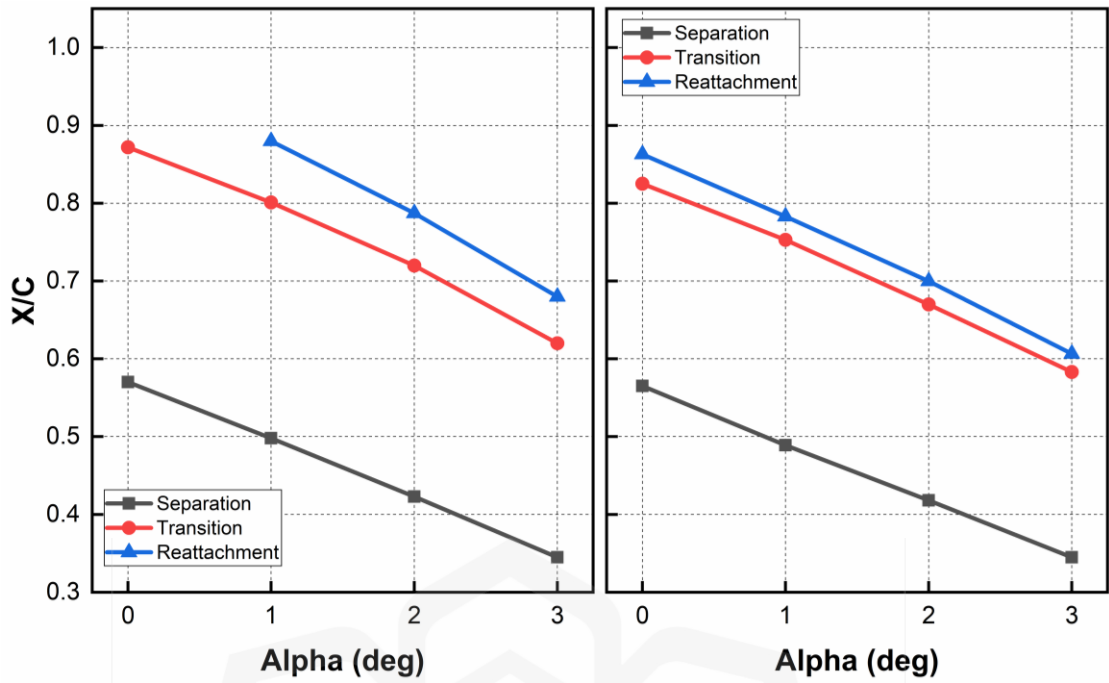


Figure 4.6 Movement of laminar separation bubble on the suction side

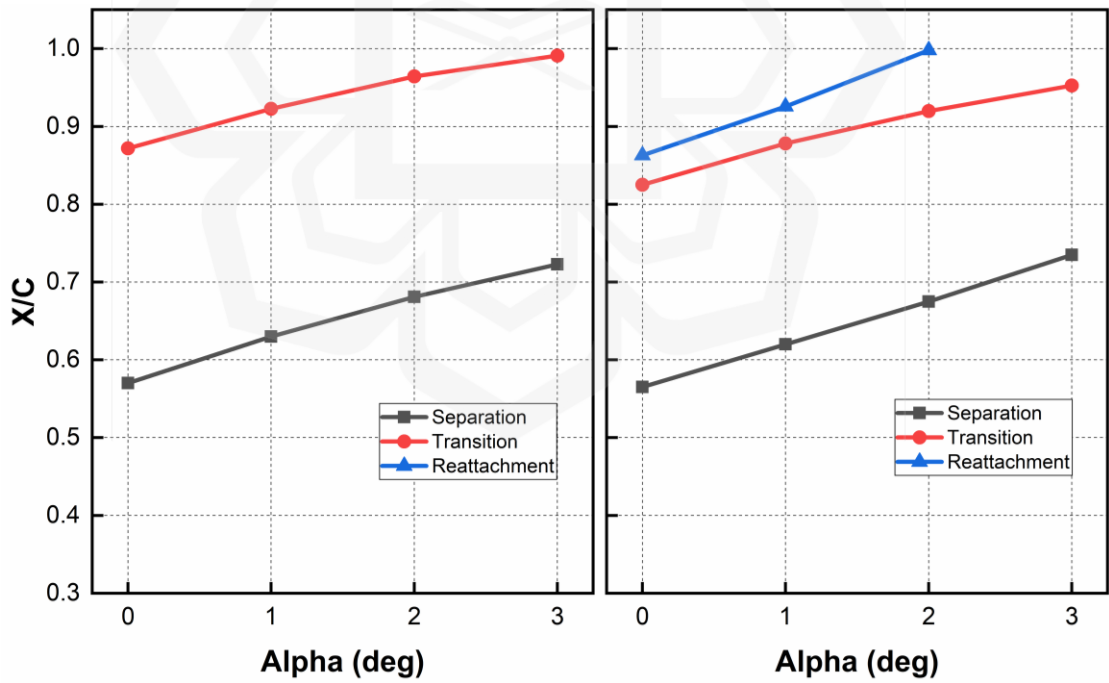


Figure 4.7 Movement of laminar separation bubble on the pressure side

Figure 4.4 illustrates an area of flow reversal immediately following the separation point, which moves upstream as the Angle of attack increases. This part encompasses the inner portion of the LSB and arises from an adverse pressure gradient. When the pressure gradient exceeds the momentum from the incoming flow, the flow is compelled to travel against the incident stream, resulting in a reversed flow. This section of the LSB is unstable and may transition to turbulence. The average velocity profiles in Figure 4.8-4.9 further elucidate this. At  $\alpha = 3^\circ$  (Figure 4.5(a)), the vortices are created by the rolling-up vortex combined with the flow near the bottom side, resulting in a more complicated swirling structure at the TE (wake region).

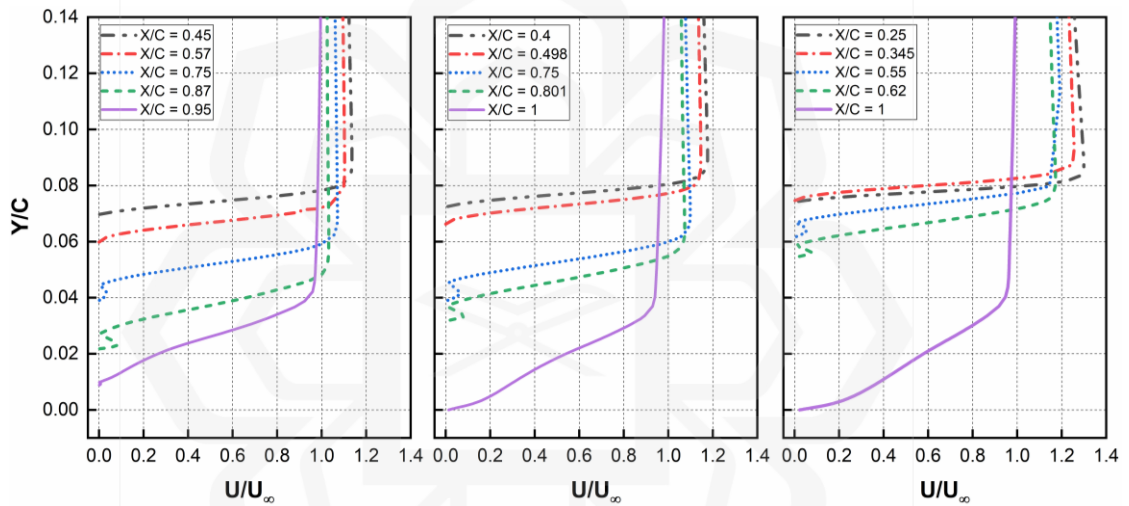


Figure 4.8 Average velocity profiles on the pressure side

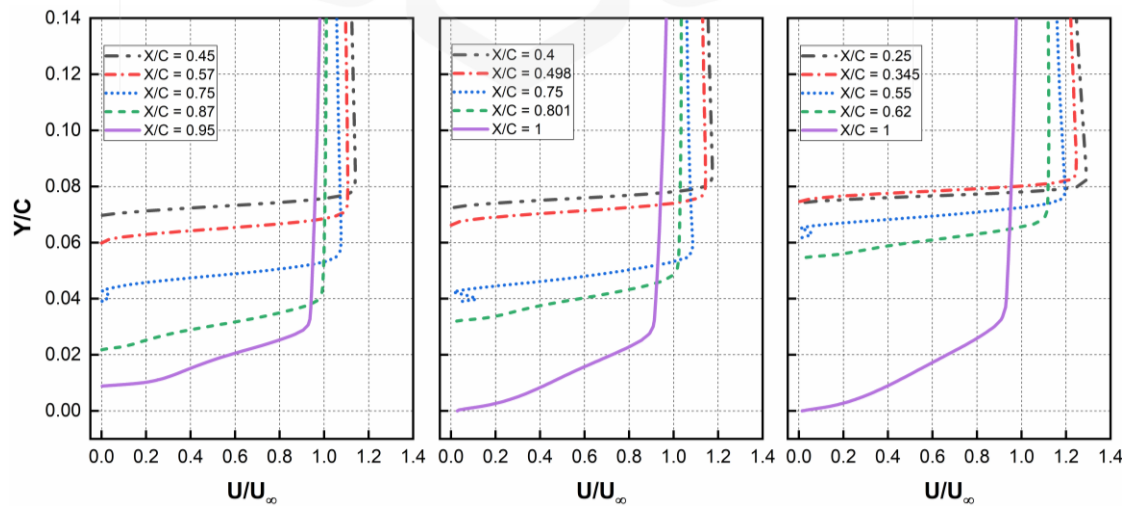


Figure 4.9 Average velocity profiles on the suction side

The flow's shear-layer patterns are well-demonstrated in Figure 4.8-4.9, indicating the bubble's position and size on the airfoil surface. The abrupt zero velocity slope near the wall surface denotes the separation point, while the curving of the profile near the wall depicts flow reversal. The velocity profile offered for five chordwise points across the airfoil upper side illustrates the different stages of flow development. As the Angle of attack increases, the velocity profiles move closer to the LE, confirming the AoA's impact .

Hence, the findings from the suction side reveal that as the Reynolds number and Angle of attack increase, the LSB moves towards the LE, resulting in an earlier transition and reattachment in some cases. On the other hand, for the pressure side, as the Angle of attack rises, the separation location moves closer to the TE (Wauters et al., 2019). Generally, bubbles are present on the top and bottom sides of the airfoil for  $Re = 1.7 \times 10^5$  except at  $\alpha = 3^\circ$  (Figure 4.5(h)). However, no LSB was detected on the bottom side for  $Re = 8.4 \times 10^4$  at all angles of attack between  $0^\circ$  and  $3^\circ$ . Furthermore, the impact of the Angle of attack on the LSB characteristics is greater than that of the Reynolds number.

#### **4.2.2. Three-Dimensional Numerical Simulation**

In this subsection, the findings of the three-dimensional (3D) simulation are studied to assess the influence of the modified models on the flow structure compared to the baseline model. The findings from this study were then compared with other relevant studies published in the area, in order to validate the research result and to provide a better insight into the results. A three-dimensional analysis was deemed necessary to understand the complexity of the flow structure and its interactions with the airfoil models. Flow structures can display significant variations in three dimensions, and a complete evaluation would need a proper representation of the flow field. Moreover, the notion of conducting a 3D study was prompted by the necessity for accurate pressure fluctuation data over the surface, which is vital for the subsequent analysis of acoustic results. The computational domain and mesh utilized in the research were described in Chapter 3. This information is necessary for understanding the parameters and assumptions applied in the analysis, and for interpreting the results meaningfully.

#### 4.2.2.1 Validation of the computational method

Several validations of the results have been carried out in the present study. Amongst valid resolution check is to compare the lift coefficient of the present study with another study (Shen et al., 2009) of similar parameters. Compared to a study with the same airfoil profile (NACA0015) but slightly different bluntness at the trailing edge, the time-history result of lift coefficients is shown in Figure 4.10. The airfoil bluntness used in this study is 1.5 mm, whereas the other study has a bluntness of about 1.3 mm. The lift-coefficient time variations after convergence are seen with minor fluctuations in the present work and slightly higher fluctuations in the other study. The observed differences in the magnitude of oscillations might be due to the variation of airfoil bluntness or different numerical techniques used. However, they oscillate around a mean lift coefficient value of about 0.43. The periodic lift coefficients occur because of vortices propagating through various regions on the airfoil surface such as the unsteadiness within the wake locations.

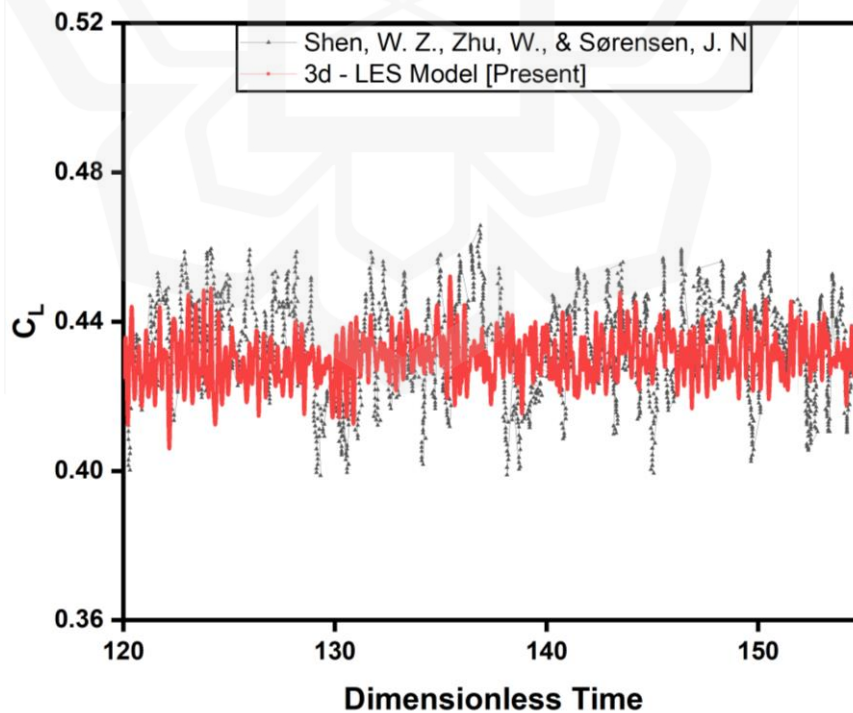


Figure 4.10 Comparison of the present work with a numerical study.

Figure 4.11 shows the average lift coefficients of NACA 0015 measured using the present numerical model, with a comparison to a published study (Ibren et al., 2021) and experimental work (Jacobs and Sherman, 1939; Miley, 1982). The three-dimensional analysis was limited to a maximum Angle of attack of 2 degrees due to both computational constraints and the focus on investigating the range where tonal noise predominates, which primarily at smaller angles of attack. The lift coefficient pattern is entirely satisfactory at all angles of attack. The analysis reveals that the error percentage of the lift coefficient remains consistently below 1% across all angles of attack. The model sufficiently predicts an increase in the mean lift coefficient value as the Angle of attack increases. However, the SST  $\gamma - Re\theta$  model based on two-dimensional analysis displayed a slight over-prediction of the mean lift coefficient value above an Angle of attack of  $2^\circ$ . Moreover, the same pattern is observed as the Angle of attack increases. In general, a good agreement between the present work and the experimental results is observed for all angles of attack.

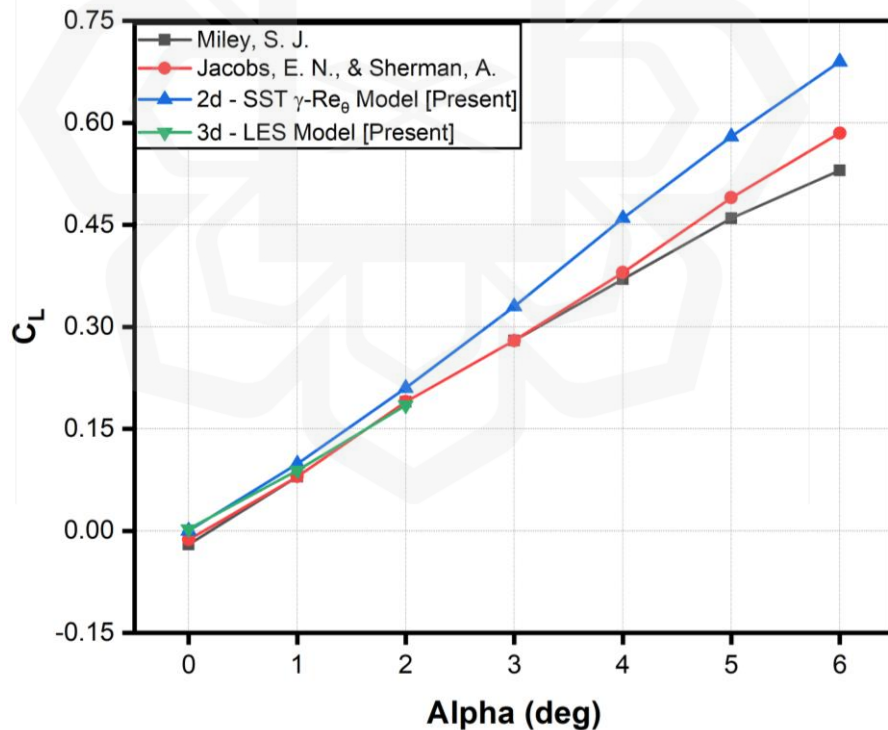


Figure 4.11 Validation of the predicted values with the experimental data.

The validation of computational findings is reviewed using experimental data. The x-velocity component of the numerical analysis and experimental test results is



displayed in Figure 4.12. The validation of the x-velocity component in both simulation and experimental data was undertaken to examine the accuracy and reliability of the numerical analysis. The measurements were performed at various angles of attack; however, 0-degree measurement was utilized to evaluate if the numerical results properly conform with the experiment work. The comparison of the numerical results with the corresponding experimental data indicated a remarkable level of agreement between the two. The results demonstrated a consistent flow field pattern without any separation along the surface. Additionally, a drop in flow velocity was noted in the upstream and downstream regions, whereas an increase was noticed on the suction and pressure sides. This was consistent with lowering the streamwise velocity towards the trailing-edge tip due to bluntness. Furthermore, both the numerical and experimental findings revealed a symmetrical pattern, further supporting the validity of the numerical model and its ability to produce accurate predictions of flow behavior. These findings support the accuracy and precision of the numerical simulations and their ability to offer accurate predictions of the flow behavior.

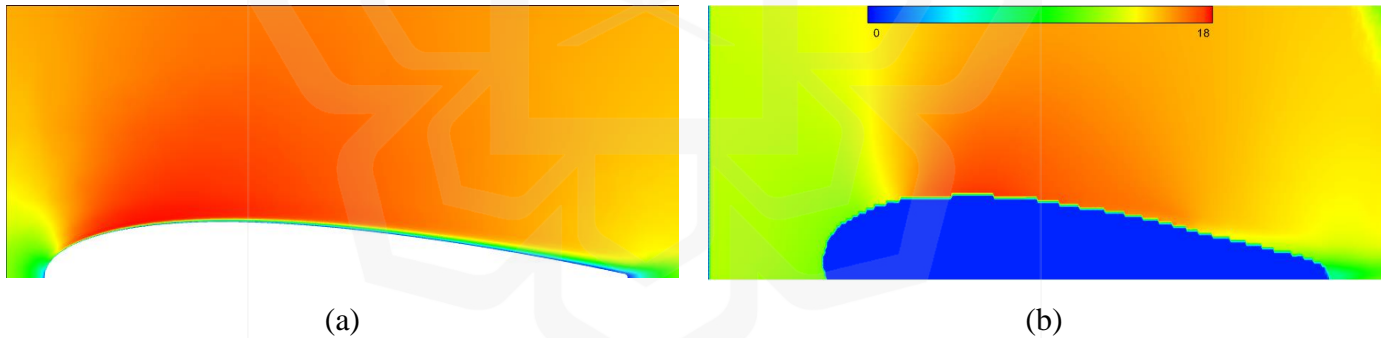


Figure 4.12 Validation of numerical result (a) with the experimental work (b) at  $\alpha = 0^0$

Figure 4.13 displays the velocity profile adopted to confirm the simulation findings by comparison with experimental observations on the suction side of the airfoil. To confirm the effectiveness of the numerical model in predicting the velocity distribution in this critical airfoil region. The results indicate that the numerical predictions were closely aligned with the actual velocity distribution, with a mean absolute error that was assessed to be minimal. However, a slight disparity was detected around the leading edge. This mismatch might be traced to the reflection of light, which

can alter the estimation of the cross-correlation and, therefore, affect the velocity field results. The experimental results indicate the presence of a separation zone in the wake region. Despite this, the overall combined results give great confidence regarding the accuracy and reliability of the computation model in its ability to predict fluid flow behavior on the suction side of the airfoil.

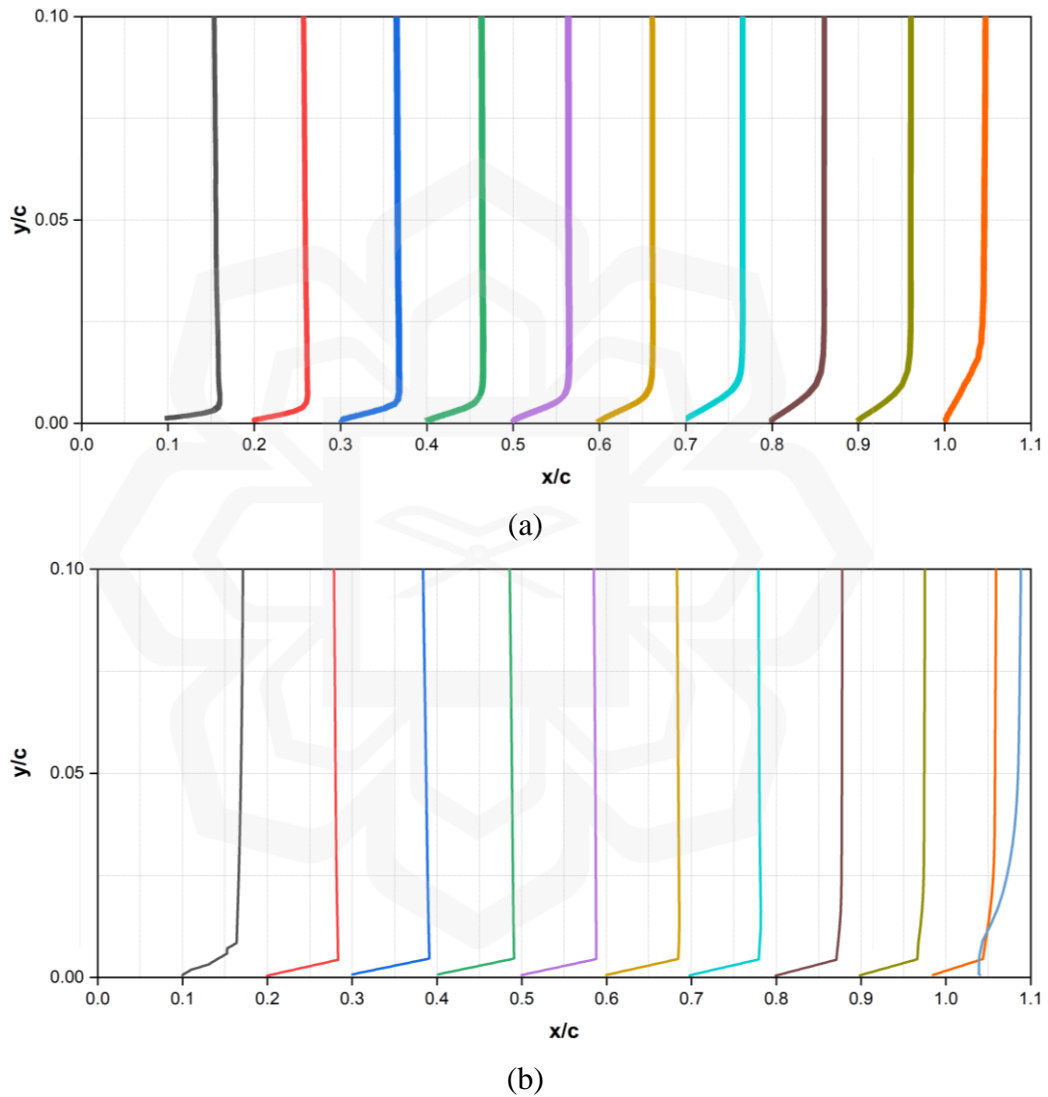


Figure 4.13 Validation of numerical result (a) with the experimental work (b) at  $\alpha = 0^\circ$

#### 4.2.2.2 Baseline Flow Field

Figure 4.14 exhibits the variation of pressure and skin friction coefficient distribution over the surface of the NACA0015 airfoil at a zero Angle of attack. The pressure



coefficient graph showed a symmetrical distribution of the pressure along the surface of the airfoil. The pressure coefficient graph shows a symmetrical distribution of the pressure along the surface of the airfoil. The maximum pressure is detected along the leading edge as anticipated due to the flow slowing down towards this region. Moreover, a smooth pressure gradient is evident along the surface with a higher change towards the leading edge and a progressive drop in the pressure towards the trailing edge. On the other hand, the skin friction coefficient reconfirmed the absence of a separation zone over the surface of the airfoil, except for the tip part of the trailing edge, which is shown by the negative values of the skin friction coefficient. Moreover, the graph shows decreasing from the leading to the trailing edge, with the highest value at the leading edge. The figure indicated that the surface suffers comparatively modest low skin friction drag force.

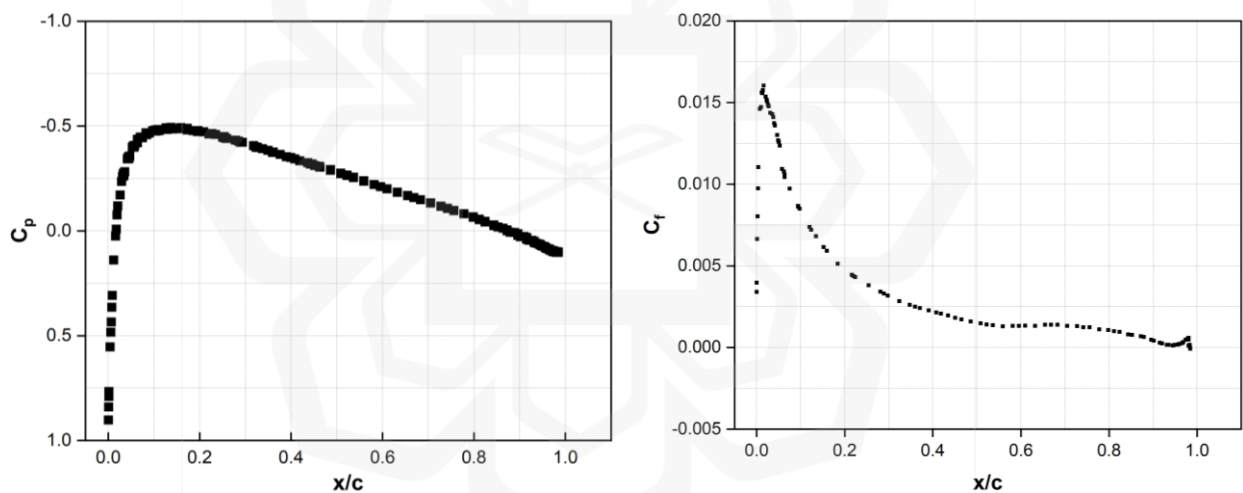


Figure 4.14 Pressure and skin friction coefficient of the baseline airfoil at  $\alpha = 0^\circ$ .

The mean x-velocity contour in Figure 4.15 demonstrates the symmetrical flow pattern found at a zero Angle of attack which is underlined by the uniform velocity magnitude present on the airfoil's top and lower surfaces. As one advances away from the leading edge, the velocity progressively increases until reaching a maximum near the mid-chord. The velocity then declines until reaching roughly zero at the trailing edge, as seen by the detailed picture of the trailing edge. This phenomenon is aligned with the rules of fluid mechanics, which suggest that the velocity of a fluid rises in regions with decreasing pressure. Additionally, due to the airfoil's blunt design, the flow

is distinguished by its smoothness and absence of separation along the surface until after the tip of the trailing edge. The streamlines are also observed to be straight and parallel, resulting in a steady and uniform velocity distribution.

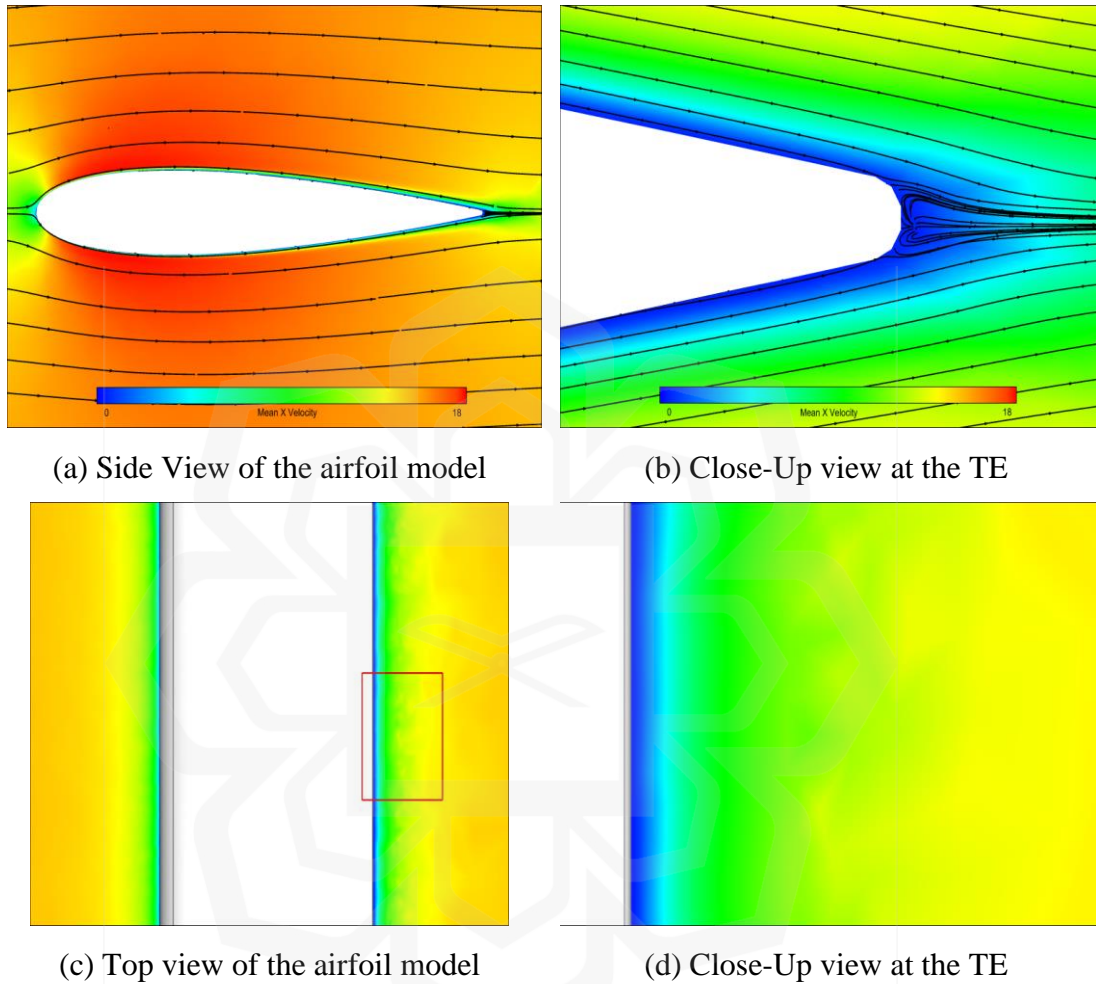


Figure 4.15 x-velocity magnitude of the baseline airfoil at  $\alpha = 0^0$ .

The velocity profile of an airfoil at a zero Angle of attack plays a crucial role in defining the overall aerodynamic performance of the airfoil. The baseline airfoil has a well-defined velocity profile at a zero Angle of attack, which is represented in Figure 4.16. The velocity profile plot illustrates a smooth and consistent distribution of velocities throughout the airfoil's chord. The observed distribution can be due to the symmetrical and stable flow conditions occurring across the airfoil surface at zero Angle of attack. Furthermore, following the observation of the velocity profile gradient, it can

be noted that the velocity magnitudes increase as one approaches away from the leading edge. Lastly, the velocity profiles of the baseline airfoil at zero Angle of attack do not display any signs of flow separation, indicated by the lack of a rapid change in the velocity gradient and a region of reversed flow. These imply a regular and well-behaved flow, leading to the best aerodynamic efficiency.

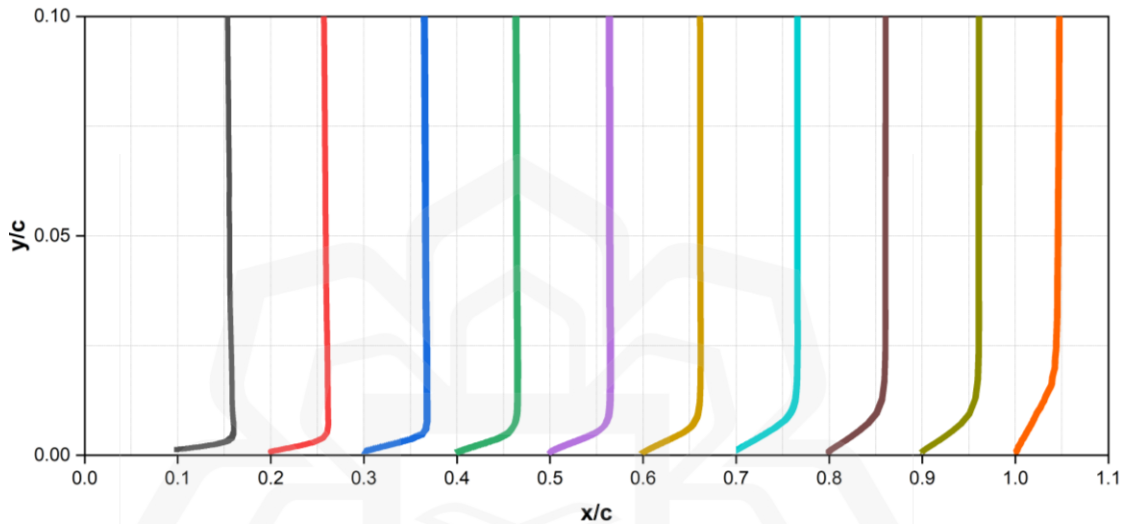


Figure 4.16 Velocity Profile of the baseline airfoil at  $\alpha = 0^{\circ}$

#### 4.2.2.3 Modified Trailing-Edge Flow Field

The pressure coefficient graph used to analyze the influence of serration, comb, and comb-serrated modifications on the trailing edge, is displayed in Figure 4.17. This graph gives vital information on the distribution of pressure throughout the airfoil's surface and enables for a complete evaluation of the flow characteristics impact of these adjustments. It is shown that all modifications result in an early negative pressure zone near the trailing edge when compared to the baseline airfoil, with the earliest detected in the serration and comb models and a later occurrence in the comb-serrated model. These adjustments are known to redistribute the flow over the surface of the airfoil, resulting in changed flow structures. Despite this, identical levels of pressure are seen at the leading edge, which results from the adjustments being positioned near the trailing edge rather than the leading edge. Similar to the baseline airfoil, the pressure rises

dramatically near the leading edge and progressively declines. The skin friction coefficient graph for the serration, comb, and comb-serrated trailing edge modifications at a zero Angle of attack is provided in Figure 4.18. The comparison between the baseline airfoil and the modified trailing edges is visible in this graph. The serrated trailing edge reveals a separated flow, resulting in a tiny separation bubble at the trailing edge, as evidenced by a negative zone in the skin friction coefficient plot. On the other hand, the comb structure demonstrates a lower variability in skin friction compared to the baseline airfoil. This can be due to the comb structure that alters the fluid flow towards the trailing edge, thereby decreasing turbulence and providing a more uniform flow. All the modified models, however, still display an uneven flow with greater skin friction values near the trailing edge. The interaction between the flow and the redesigned trailing edges, generating turbulence and enhancing the fluid's momentum transmitted to the airfoil's surface.

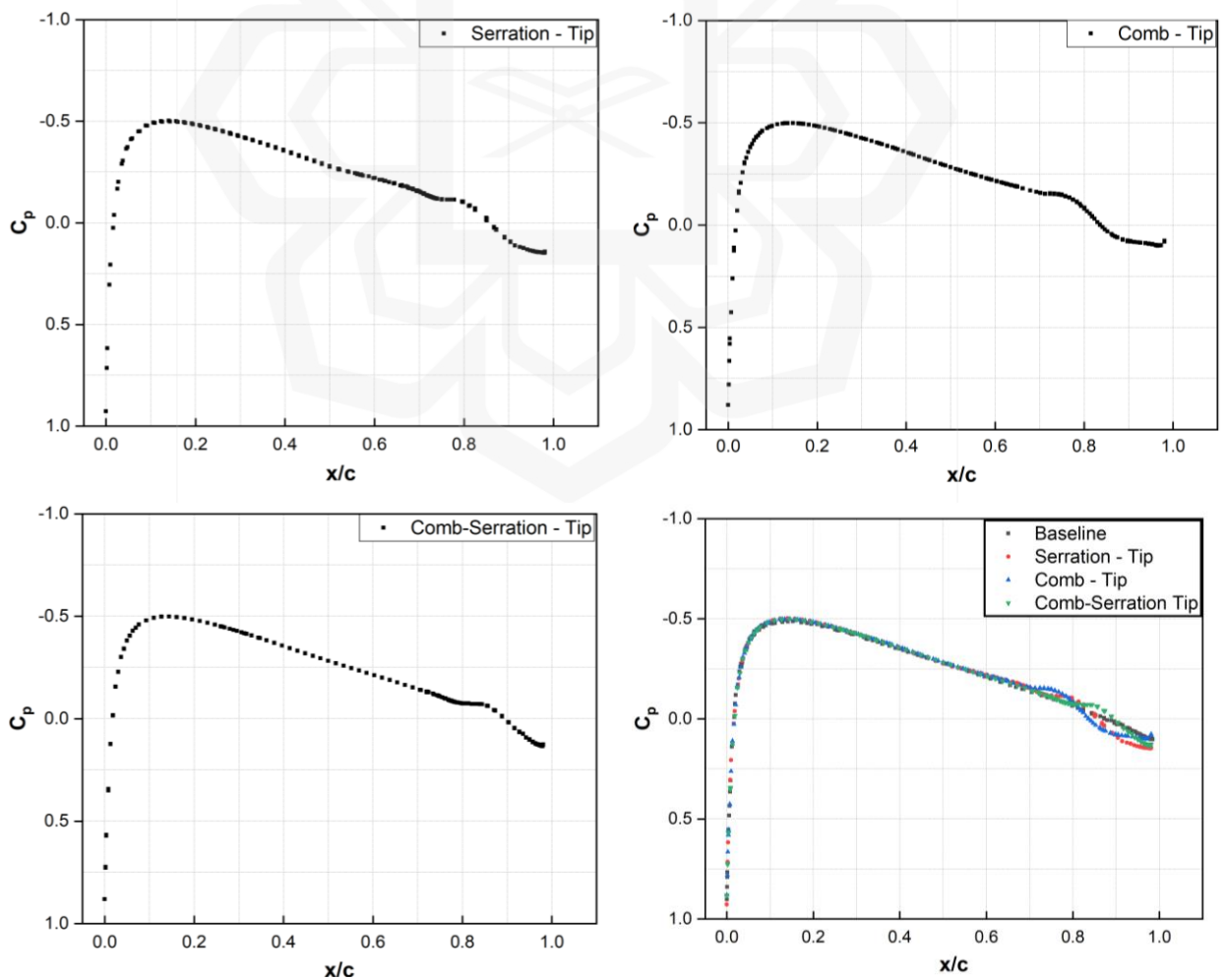


Figure 4.17 Pressure coefficient of the modified models at  $\alpha = 0^\circ$ .

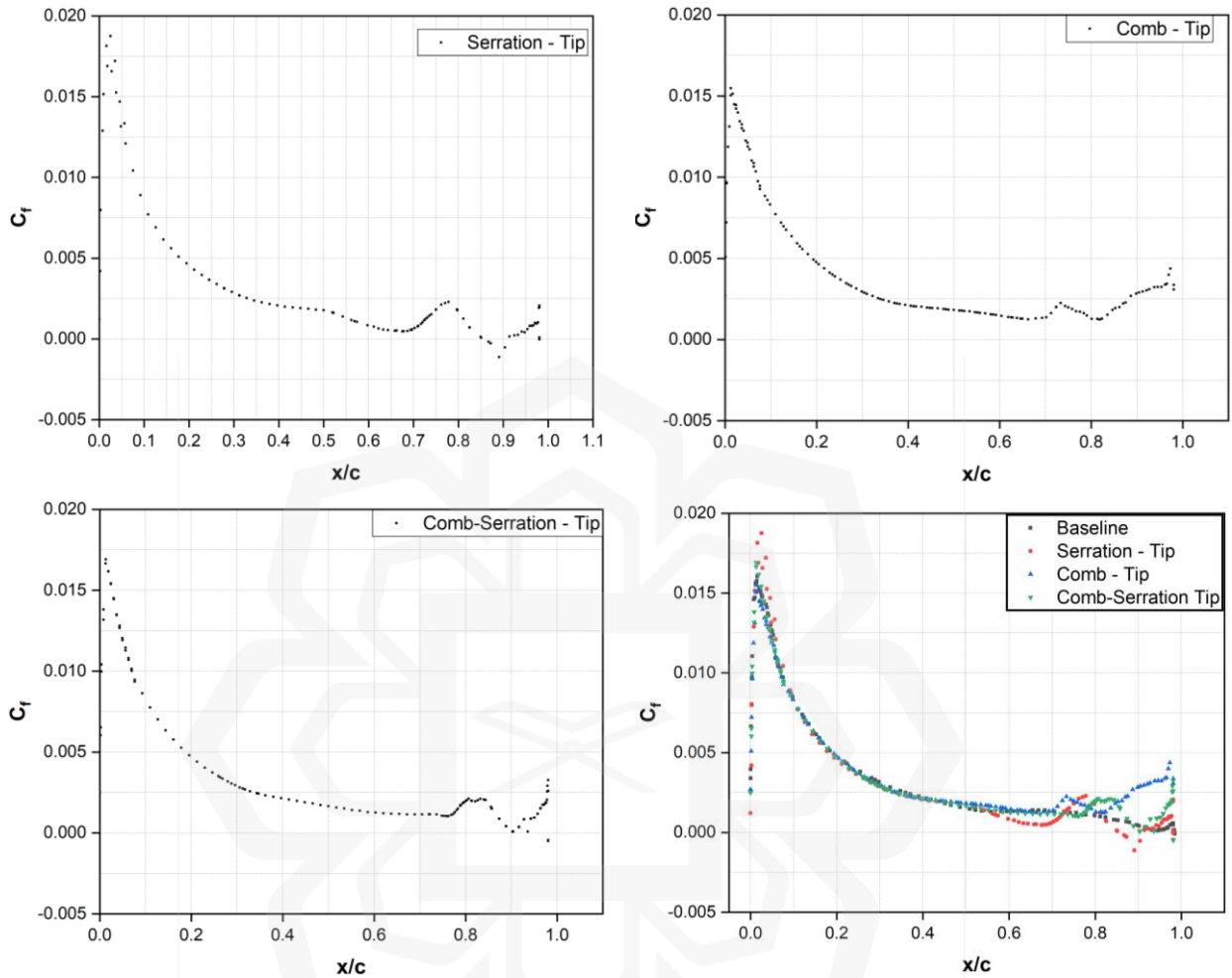
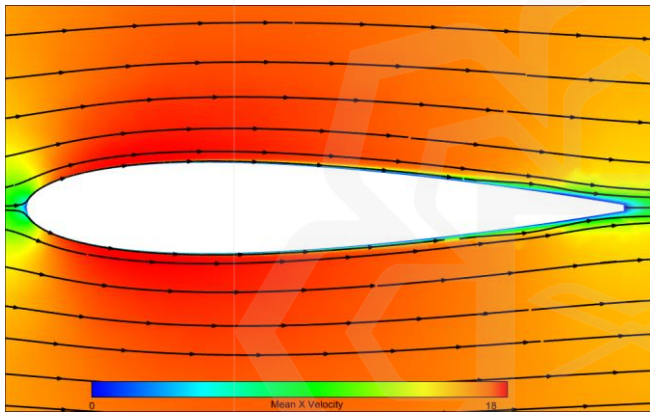


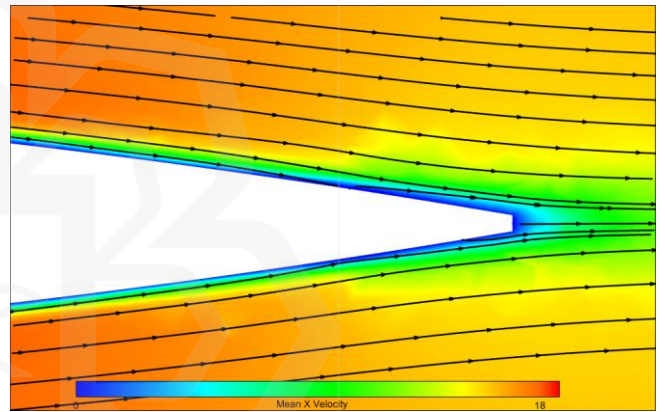
Figure 4.18 Skin friction coefficient of the modified models at  $\alpha = 0^\circ$ .

The x-velocity contours of serration, comb, and comb-serrated designs at a zero Angle of attack are presented in Figure 4.19-4.21. This analysis gives additional insight into the influence of these adjustments on aerodynamic characteristics. At a zero Angle of attack, it is noticed that the flow separates at the tip and root regions of the modified trailing edges, which is ascribed to the existence of surface structures that perturb the boundary layer and cause it to separate from the surface. On the other hand, the comb structure does not display any separation of the flow due to its perpendicular alignment with the surface, which helps maintain a smooth flow. The comb-serrated layout,

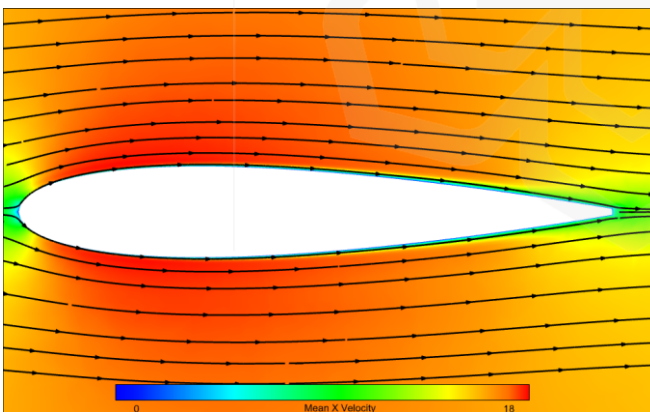
however, is seen to retain a somewhat regular flow efficiently and demonstrate flow separation, showing that the alteration effectively incorporates the effects of both the serrated and comb configurations. Additionally, a thorough analysis of Figure 4.20 indicates that the flow separates significantly along the roots of the serrated and comb models, whereas only a slight separation is noted for the comb-serrated design. This separation is a consequence of the bluntness present along the root of the trailing edge. Furthermore, Figure 4.21 gives a complete illustration of the flow patterns of the models, revealing that the comb slows down the flow more severely near the root of its trailing edge, followed by serration and, eventually, the comb-serrated arrangement.



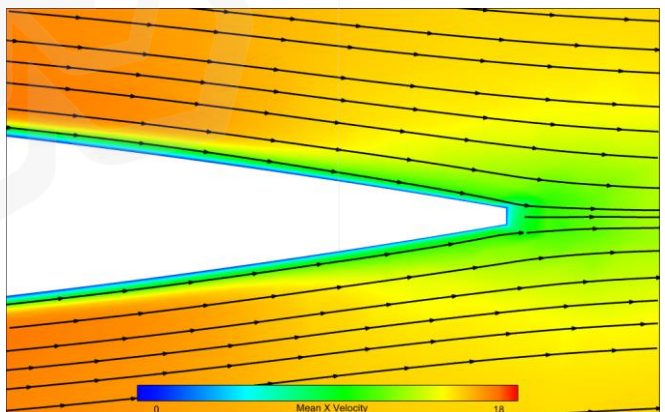
(a) Serrated TE model (Tip)



(b) Close-Up view at the tip

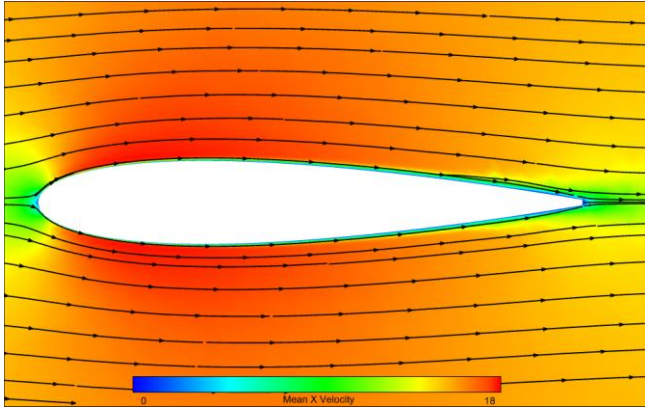


(e) Combed TE model (Tip)

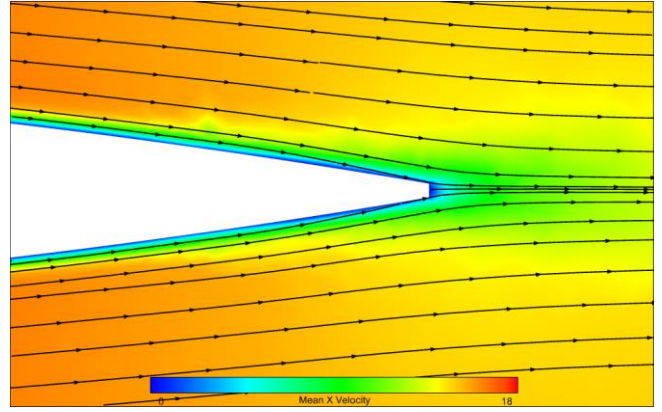


(f) Close-Up view at the tip



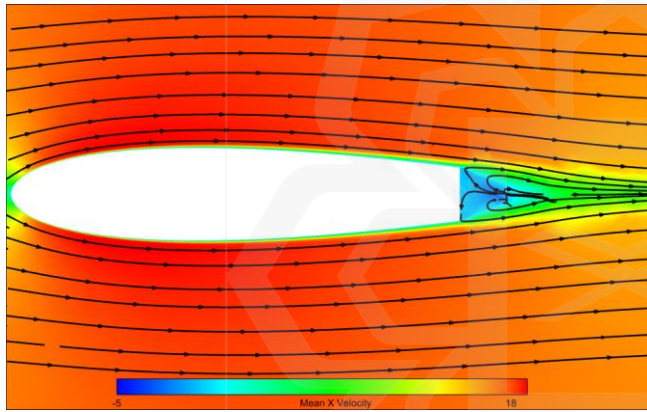


(e) Comb-Serrated TE model (Tip)

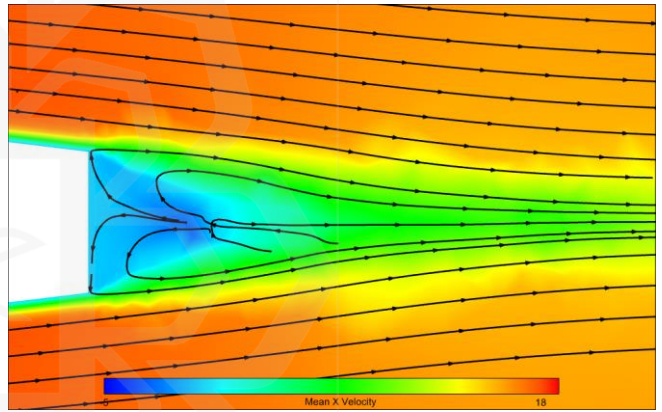


(f) Close-Up view at the tip

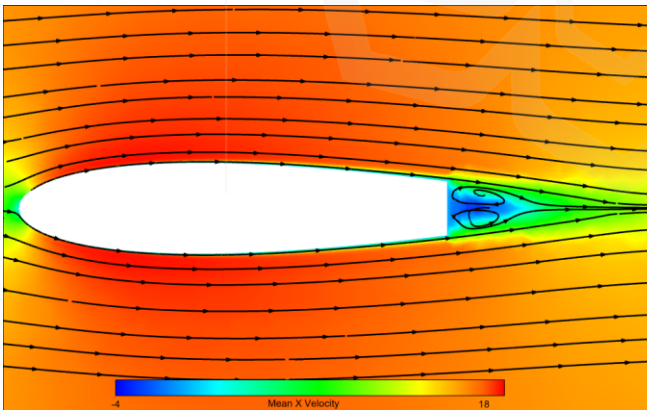
Figure 4.19 x-velocity contour at the tip of the modified models ( $\alpha = 0^\circ$ ).



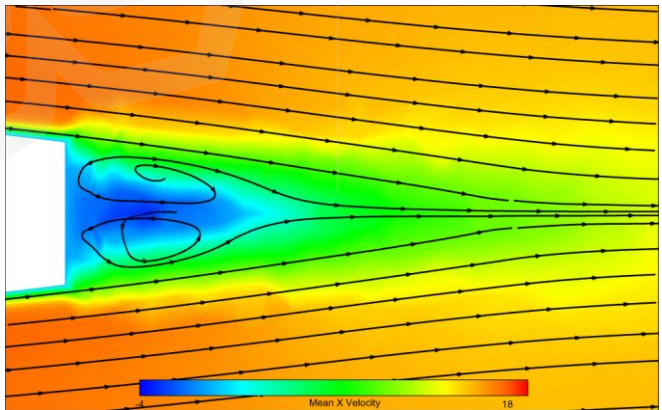
(a) Serrated TE model (Root)



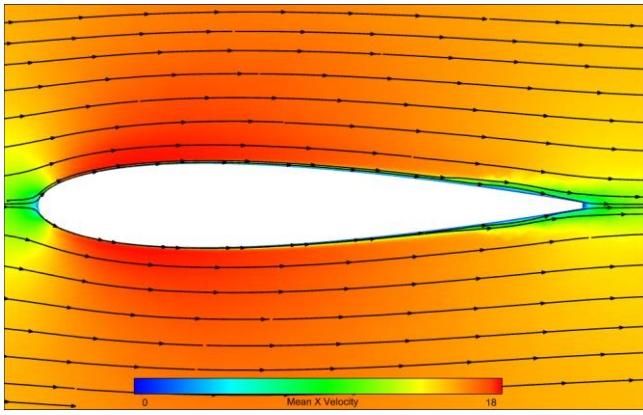
(b) Close-Up view at the root



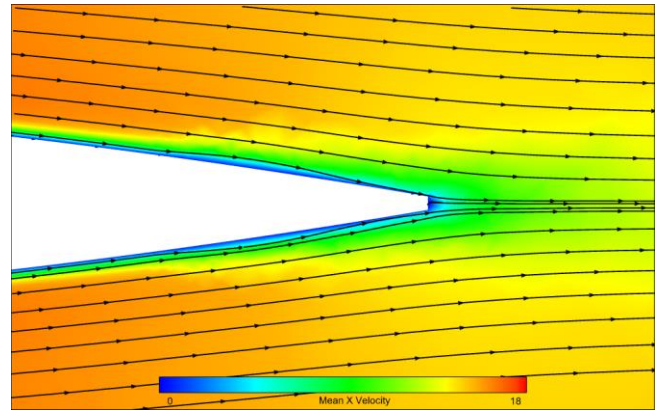
(c) Combed TE model (Root)



(d) Close-Up view at the root

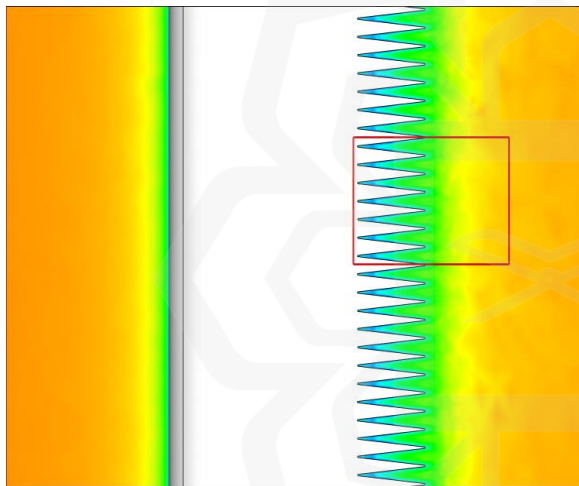


(e) Comb-Serrated TE model (Root)

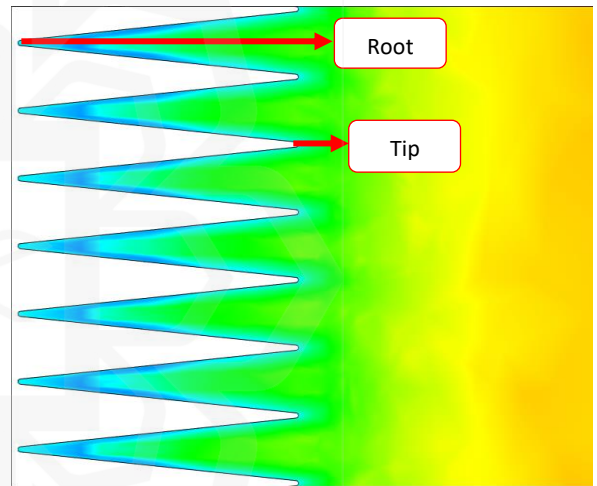


(f) Close-Up view at the root

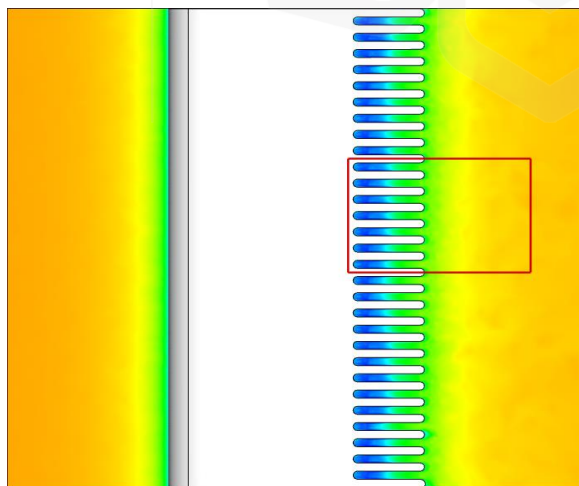
Figure 4.20 x-velocity contour at the root of the modified models ( $\alpha = 0^0$ ).



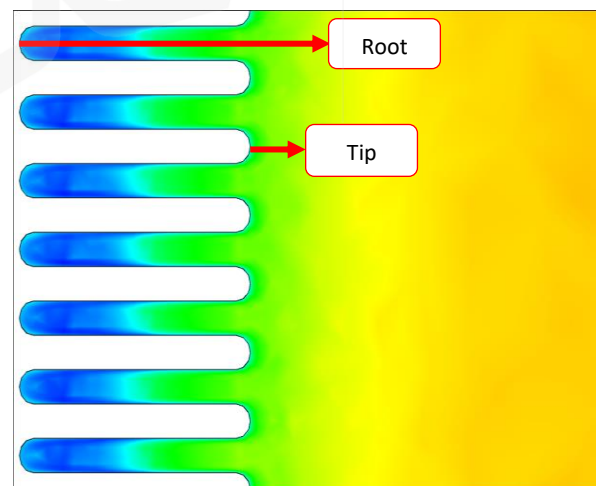
(a) Serrated TE model (Top View)



(b) Close-Up view at the TE



(c) Combed TE model (Top View)



(d) Close-Up view at the TE



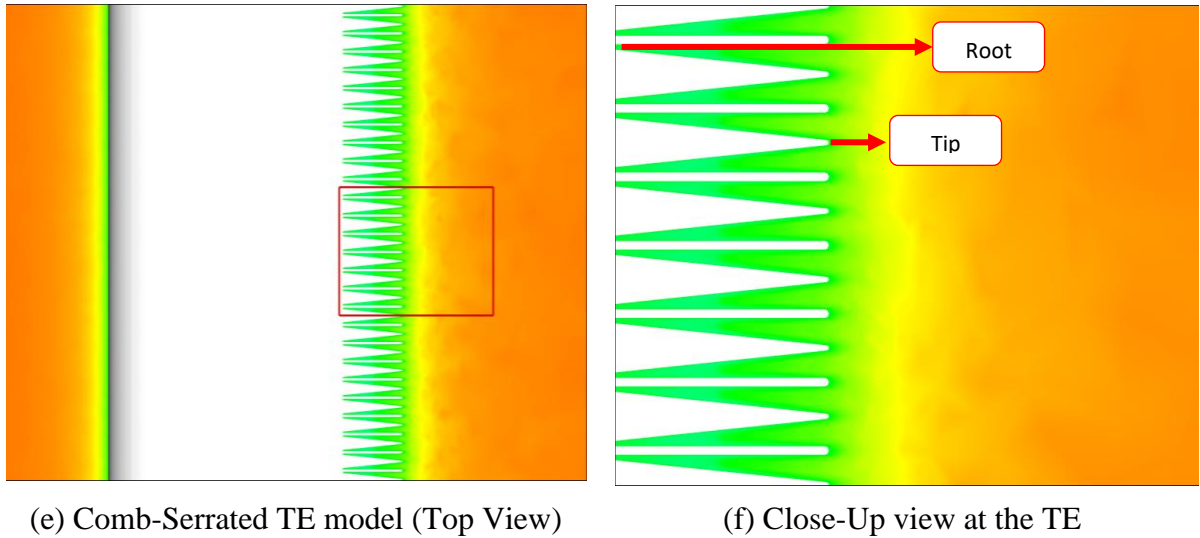


Figure 4.21 Top view contour of x-velocity component for the modified models ( $\alpha = 0^\circ$ ).

The velocity profile graph of serrated, comb, and comb-serrated configurations is provided in Figure 4.22. It offers a thorough illustration of the influence of modified trailing edges on the velocity distribution along the top surface of the airfoil. This graph demonstrates how the distinct property of each arrangement affects fluid flow. As represented in the velocity profile graph, the serrated trailing edge identifies an increase in fluid velocity away from the leading edge. At the tip and root of the trailing edge, the onset of separation and the development of vortices in the flow are noted at roughly  $0.8c$  and  $0.7c$ , respectively. This leads to a drop in overall pressure levels on the serrated trailing edge, as illustrated clearly in Figure 4.17. The combed trailing edge, on the other hand, does not demonstrate any separation along the tip. However, a separation zone of roughly  $0.7c$  is noted along the root of the trailing edge, as illustrated in Figure 4.17-4.18. As seen in the velocity profile graph, the comb-serrated model exhibits no separation zone along either the sawtooth-like or comb-like section. This is shown by a lack of sudden changes in the velocity gradient, which suggests continuous fluid flow along the surface of the airfoil.

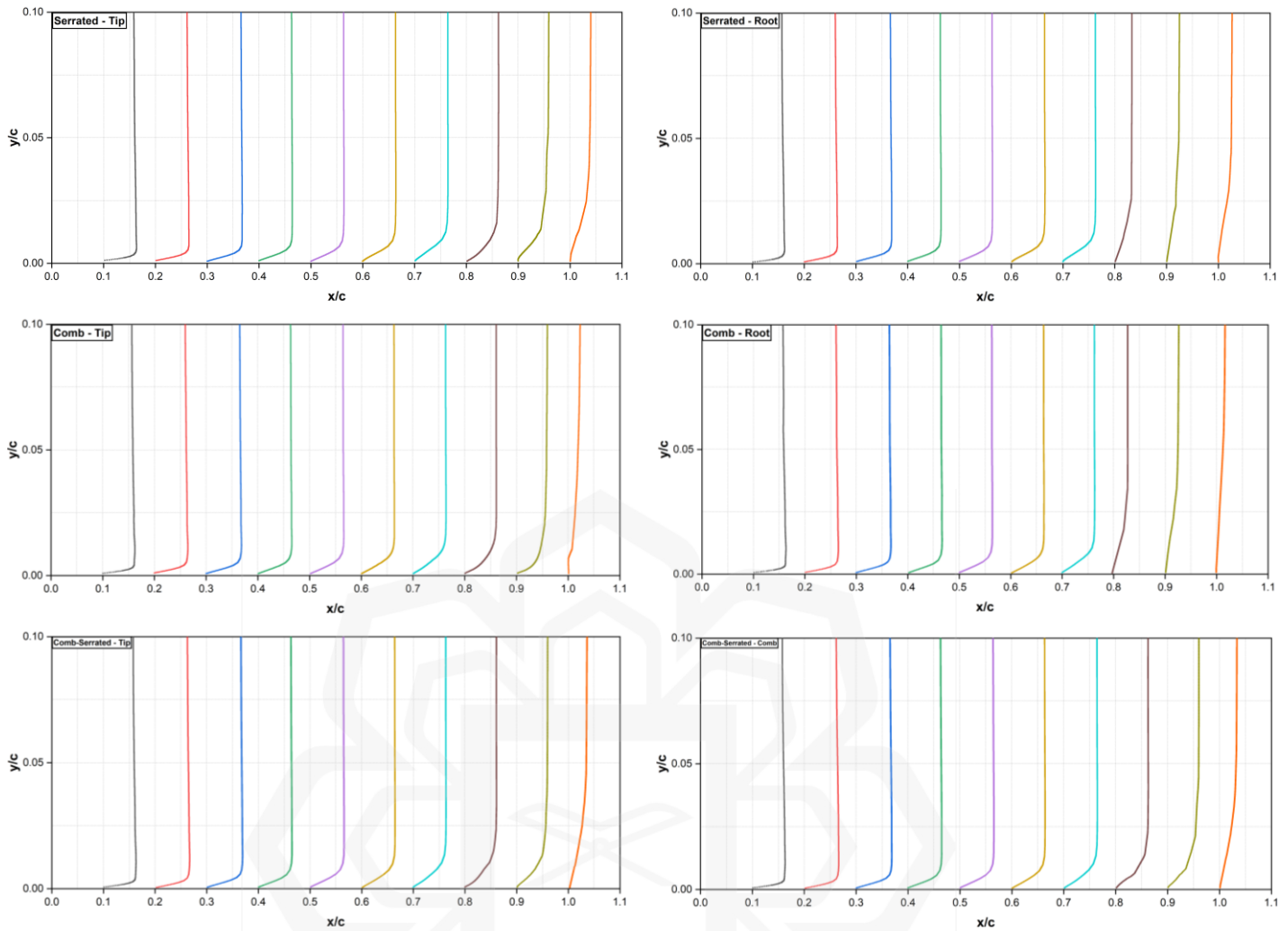


Figure 4.22 Velocity Profile of the modified airfoil models at  $\alpha = 0^0$ .

### 4.2.3. Summary of the Numerical Simulation

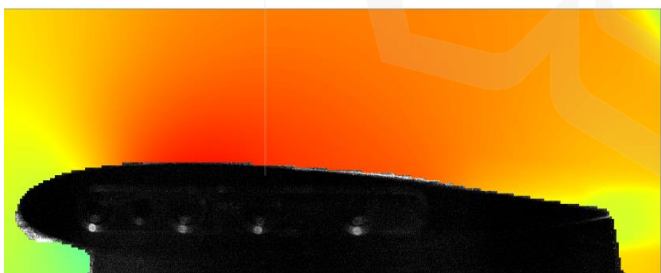
In conclusion, the findings of the 2D analysis demonstrate that the position and size of the laminar separation bubble on the suction side are impacted by the Reynolds number and Angle of attack, with the bubble moving upstream and shrinking as the Angle of attack increases. On the pressure side, the laminar bubble advances towards the trailing edge at a roughly constant size with an increasing Angle of attack. The influence of the Angle of attack is found to be more prominent than that of the Reynolds number on the features of the laminar separation bubble. The reattachment points were reported to be negligible within the range of angles of attack investigated. The findings of the 3D research reveal that the serrated, comb, and comb-serrated airfoil designs each have a

distinct influence on fluid flow. The serrated trailing edge increases in fluid velocity and pressure drop; the combed trailing edge has separation at the root; and the comb-serrated design maintains a continuous fluid flow over the airfoil's surface.

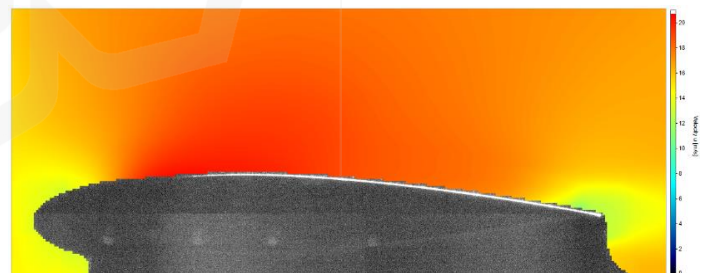
### 4.3. EXPERIMENTAL RESULTS

#### 4.3.1. Streamwise Velocity Field

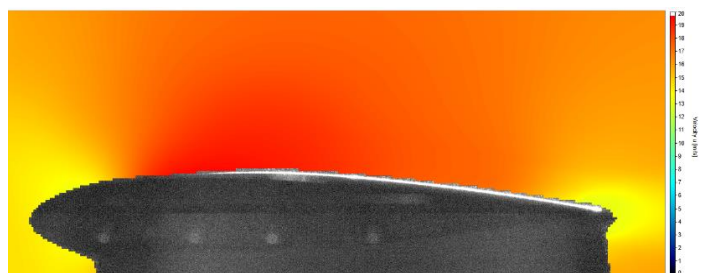
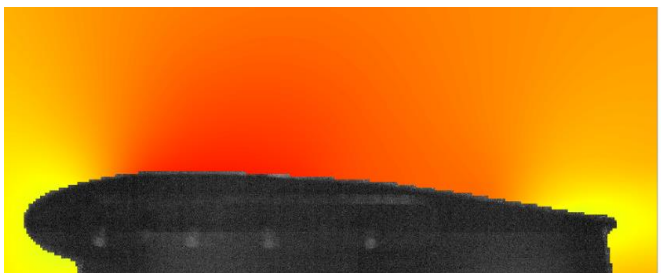
At a zero Angle of attack, as represented in Figure 4.23, the baseline airfoil presents a pattern consistent with the numerical results. Its symmetry and uniformity define the flow, without any visible perturbations. The velocity of the flow rises as one goes away from the leading edge, with the maximum velocity measured towards the mid-chord position of the airfoil. This velocity steadily decreases towards the trailing edge. As the Angle of attack increases, the flow over the airfoil gets progressively disturbed, resulting in variations in the x-velocity contour, as seen in Figure 4.24-4.28. For example, at an Angle of attack of 6 degrees, the flow is observed to first separate from the surface of the airfoil, forming a laminar separation bubble. This bubble continues to move upstream as the Angle of attack increases to 10 degrees, and its size grows with the rising Angle of attack.



(a) Baseline airfoil

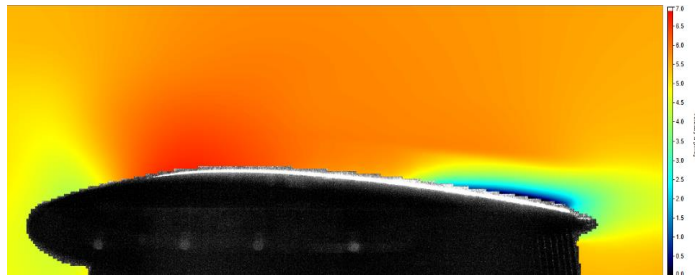


(b) Serrated TE airfoil



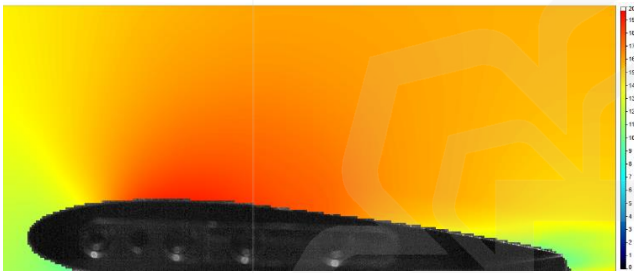
(c) Combed TE airfoil

(d) Comb-Serrated TE airfoil

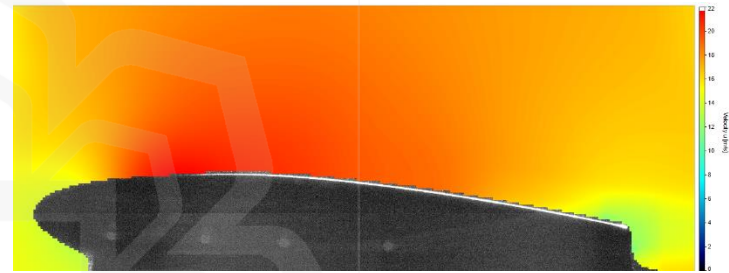


(e) Poro-Serrated TE airfoil

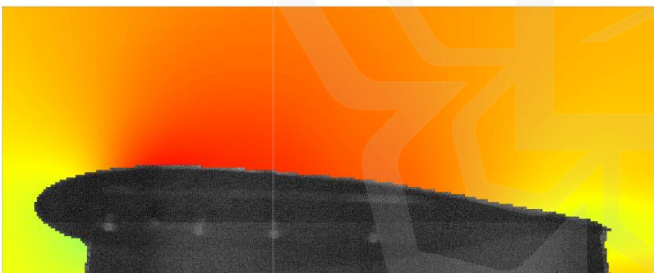
Figure 4.23 Streamwise velocity component at  $\alpha = 0^\circ$ .



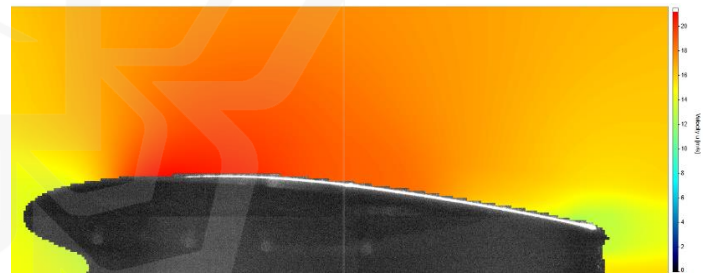
(a) Baseline airfoil



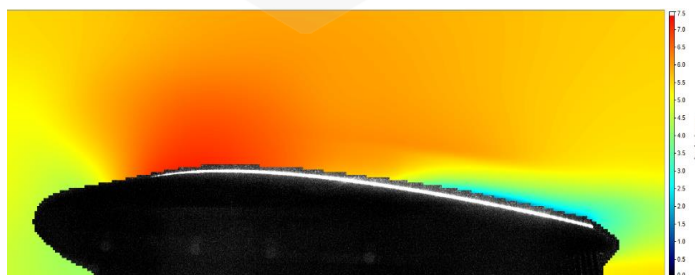
(b) Serrated TE airfoil



(c) Combed TE airfoil



(d) Comb-Serrated TE airfoil



(e) Poro-Serrated TE airfoil

Figure 4.24 Streamwise velocity component at  $\alpha = 2^\circ$ .

The x-velocity contour of the serrated trailing edge airfoil demonstrates distinct behaviour compared to the baseline airfoil. The flow remains attached to the surface of the airfoil until an Angle of attack of 8 degrees, where a tiny separation bubble is formed. As the Angle of attack increases to 10 degrees, the size of the separation bubble grows. This can be due to the sawteeth on the trailing edge, which increases the flow's momentum and enhances its stability as it passes over the trailing edge. The separation bubble is observed to move upstream when the Angle of attack increases to 10 degrees, resulting from the enhanced stability of the flow. Furthermore, the x-velocity contour of the combed airfoil model reveals a smooth and uniform flow pattern as the Angle of attack increases from 0 degrees to 6 degrees. At an Angle of attack of 8 degrees, the flow separates and forms a separation bubble that is considerably smaller in size compared to the baseline and serrated airfoil models. As the Angle of attack continues to grow, the size of the separation bubble expands and shifts upstream along the flow. The comb-like structure on the airfoil's trailing edge aligns the flow and decreases the disturbances caused by the discontinuity present in the baseline airfoil. This results in a steadier flow pattern and a reduction in the size of the separation bubble.

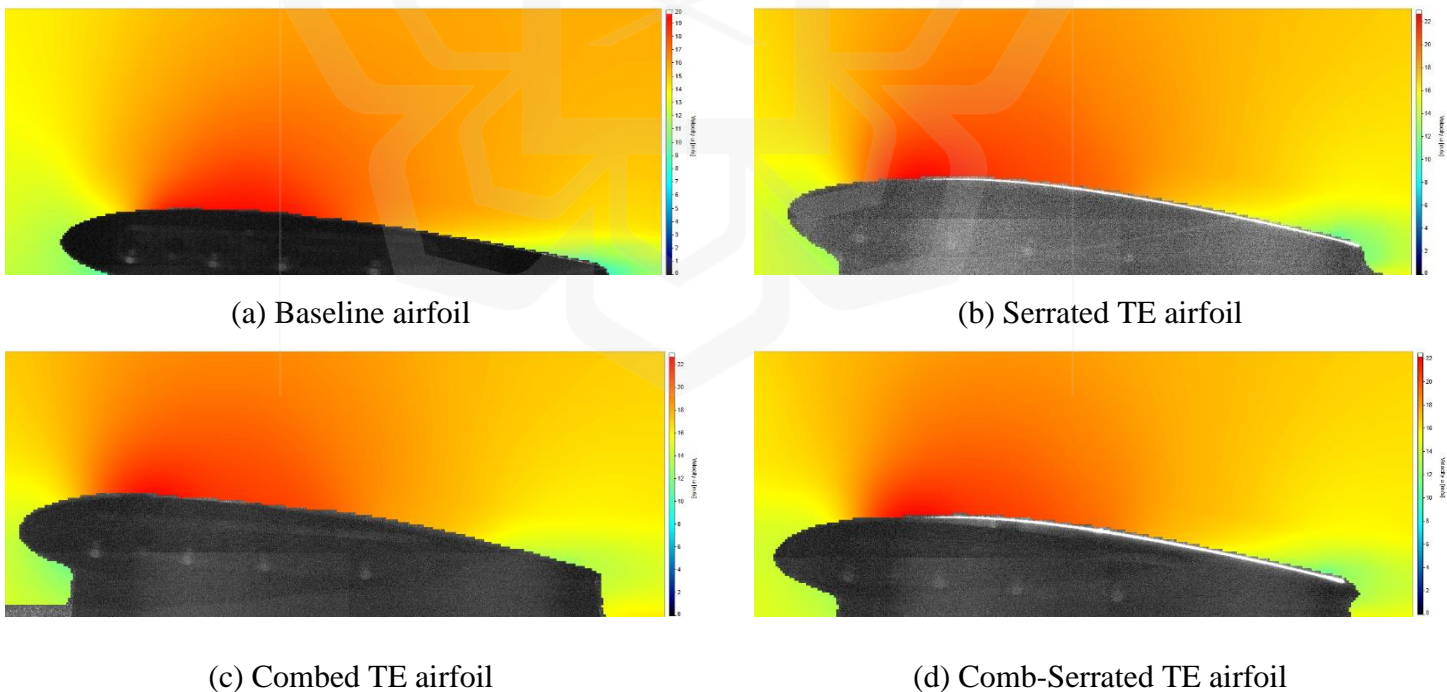


Figure 4.25 Streamwise velocity component at  $\alpha = 3^\circ$ .



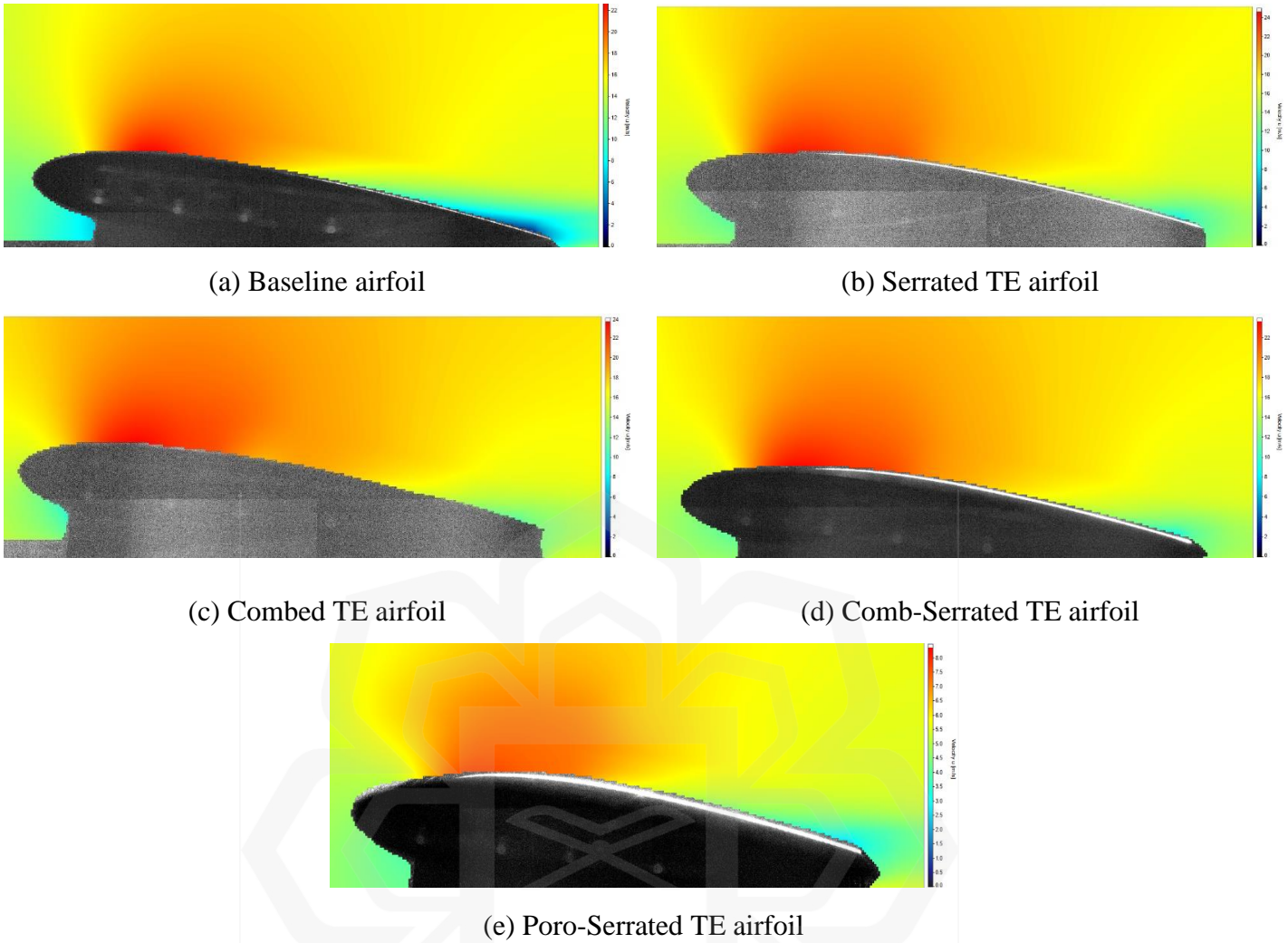


Figure 4.26 Streamwise velocity component at  $\alpha = 6^\circ$ .

On the other hand, the comb-serrated airfoil model displays a similar pattern to that of the other models, with the flow remaining attached to the surface until an Angle of attack of 8 degrees is attained. At this Angle of attack, the flow separates and forms a separation bubble that is even smaller in size than the comb-airfoil model. As the Angle of attack increases to 10 degrees, a visible separation bubble is detected, which has moved slightly upstream and grown in size compared to the bubble formed at 8 degrees. This study reveals that this model has a smaller separation bubble and a more stable flow pattern compared to the other models. Finally, a poro-serrated airfoil model exhibits a radically different flow pattern than previous designs. Unlike the other models, this airfoil type shows a laminar separation bubble at a zero Angle of attack, a phenomenon not observed in other airfoil forms. This may be linked to the porous nature

of the airfoil, which enables air to pass through both sides, disturbing the flow and resulting in the flow's separation. At an Angle of attack of 2 degrees, however, no separating bubble is detected, a poorly understood phenomenon. Furthermore, when the Angle of attack increases from 6 degrees, another separating bubble is formed. Similarly, this bubble is observed to grow in size and move upstream as the Angle of attack rises. The model's flow pattern is more disturbed than the other modified airfoil models, as evident by the variations in the x-velocity contour. Studying the x-velocity contour of different airfoil configurations gives essential insights into the flow and separation behaviour of airfoils, which can guide the design of more efficient and sophisticated airfoils in the future.

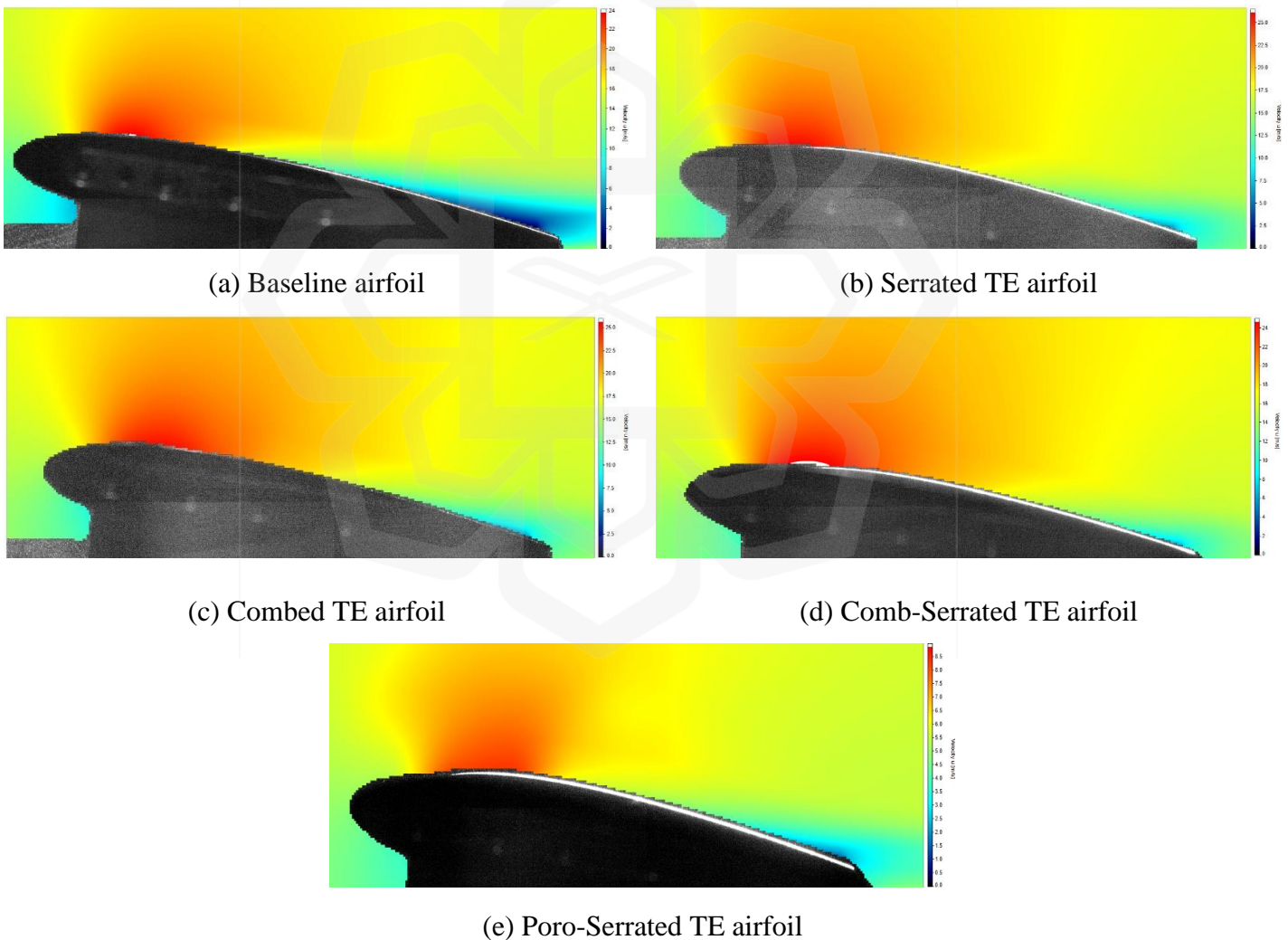
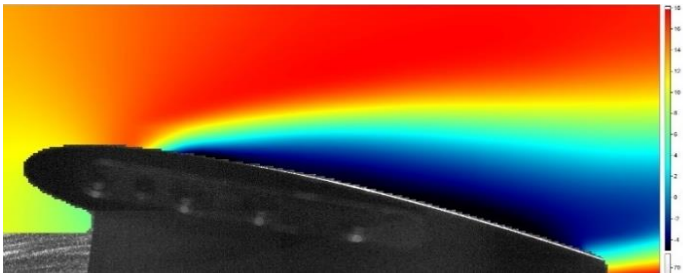
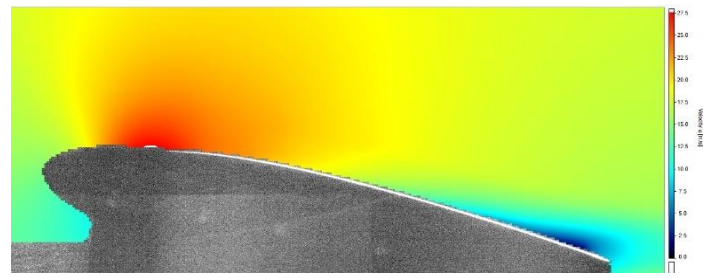


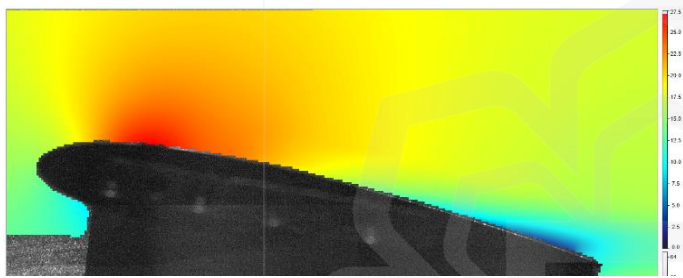
Figure 4.27 Streamwise velocity component at  $\alpha = 8^\circ$ .



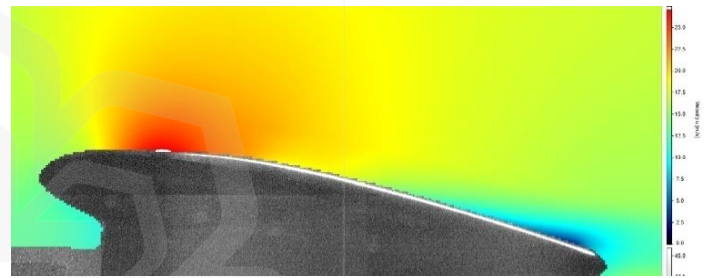
(a) Baseline airfoil



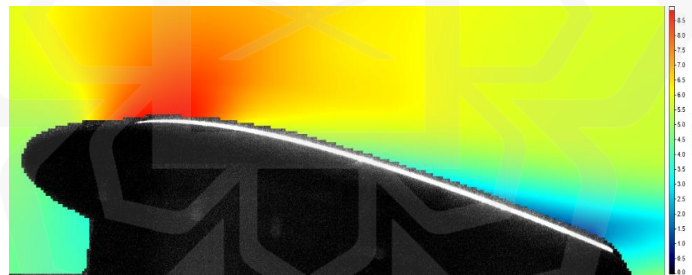
(b) Serrated TE airfoil



(c) Combed TE airfoil



(d) Comb-Serrated TE airfoil



(e) Poro-Serrated TE airfoil

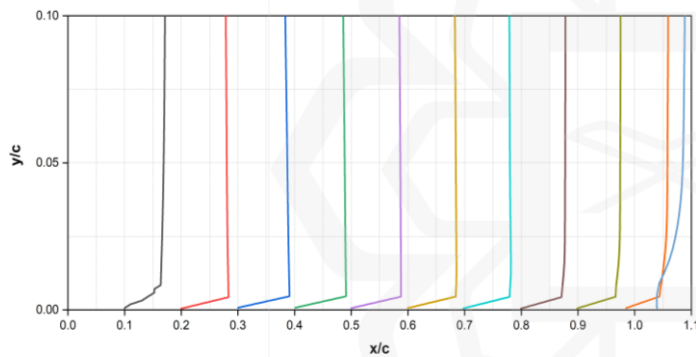
Figure 4.28 Streamwise velocity component at  $\alpha = 10^0$ .

### 4.3.2. Flow Velocity Distribution

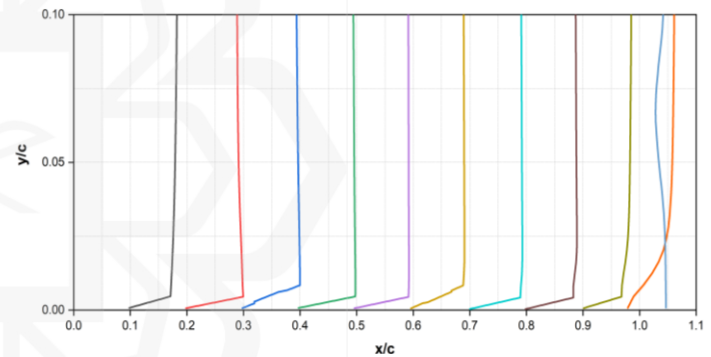
The experimental measurements of the velocity profile graphs of several designs, including serrated, comb, comb-serrated, and poro-serrated, are provided in Figure 4.29-4.34. These graphs offer a detailed explanation of the influence of modified trailing edges on the velocity distribution over the top surface of the airfoil at various angles of attack. The baseline airfoil displays a smooth and continuous flow at a zero Angle of



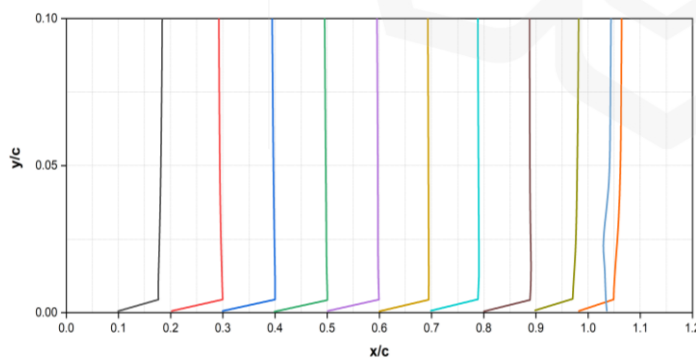
attack, as demonstrated by the slope of the figure. This feature maintains across the spectrum of angles of attack till 8 degrees. However, at an Angle of attack of 8 degrees, the velocity profile encounters a sharper gradient and a reversed flow towards the trailing edge. This separation area eventually advances upstream of the flow and reaches roughly  $0.3c$  at an Angle of attack of 10 degrees. The graphs indicate that the serration model has considerably smoother flow until an Angle of attack of 6 degrees, where the flow becomes erratic. However, approximately at 8 degrees, the flow becomes unpredictable and separates from the surface at roughly  $0.9c$ . At an Angle of attack of 10 degrees, the separation area is found to have moved to around  $0.8c$ . This implies that the size of the separation zone is less than 20% of the chord length, which is much less than the baseline model, where the size of the separation region is around 70% of the chord length at 10 degrees.



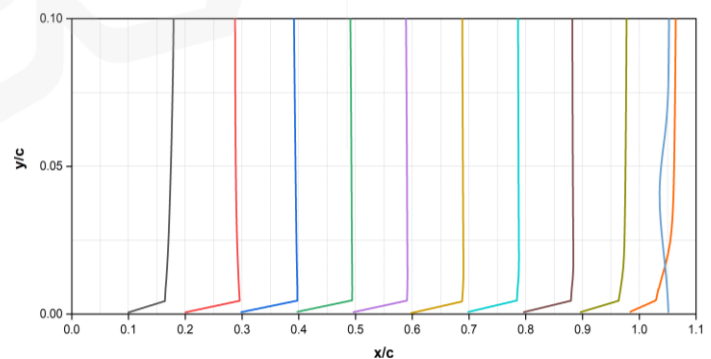
(a) Baseline airfoil



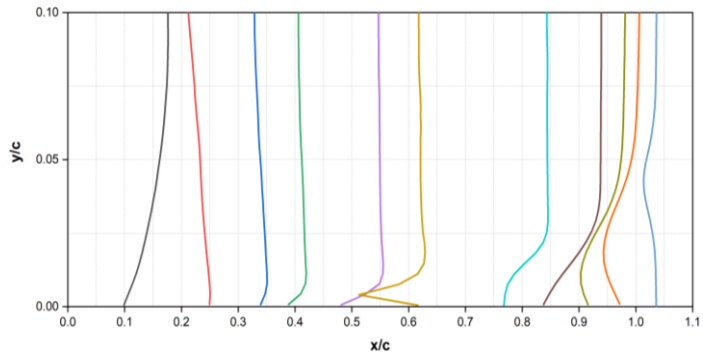
(b) Serrated TE airfoil



(c) Combed TE airfoil

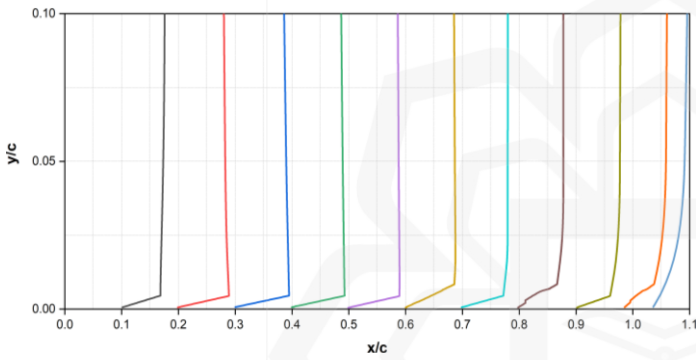


(d) Comb-Serrated TE airfoil

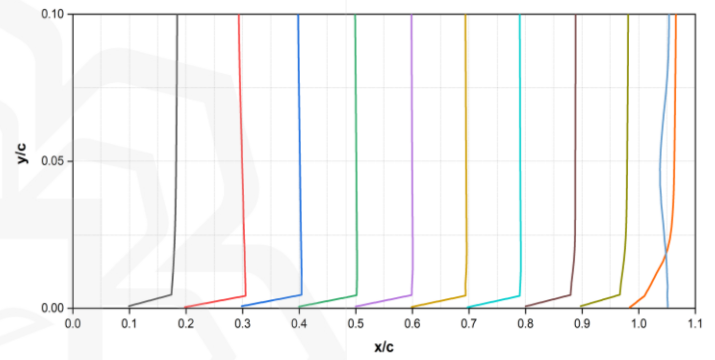


(e) Poro-Serrated TE airfoil

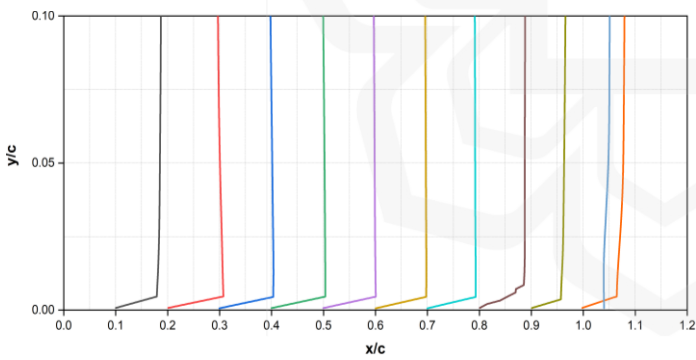
Figure 4.29 Velocity Profile at  $\alpha = 0^\circ$ .



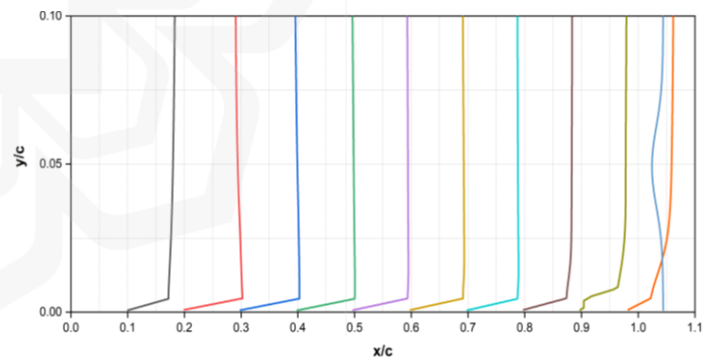
(a) Baseline airfoil



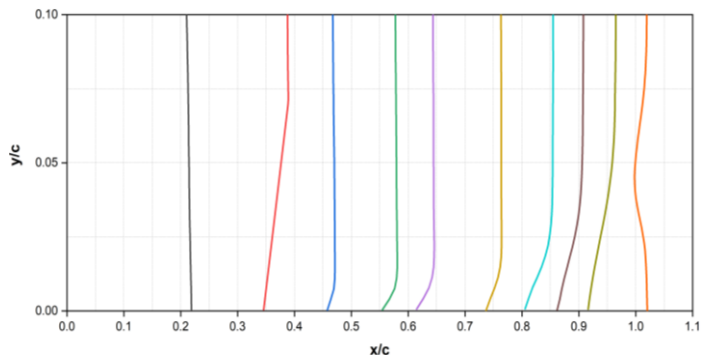
(b) Serrated TE airfoil



(c) Combed TE airfoil



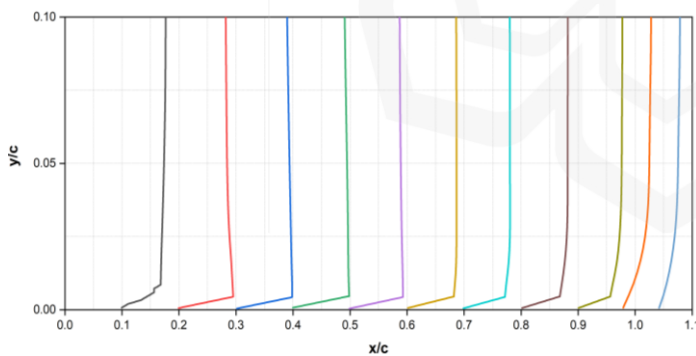
(d) Comb-Serrated TE airfoil



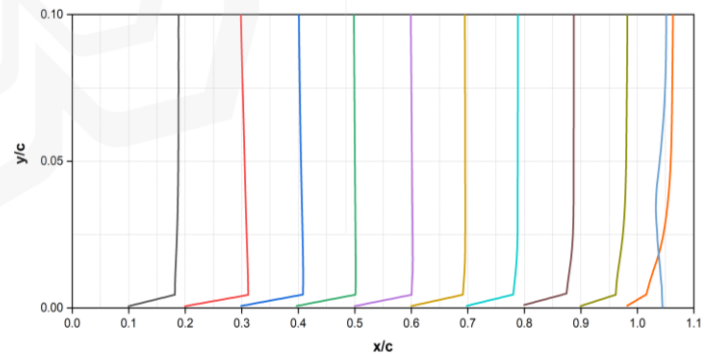
(e) Poro-Serrated TE airfoil

Figure 4.30 Velocity Profile at  $\alpha = 2^\circ$ .

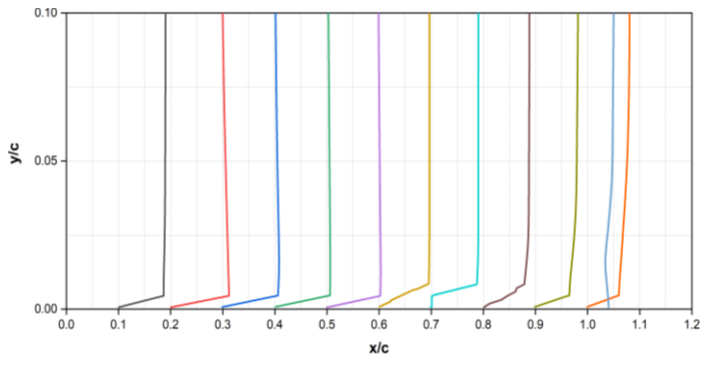
Furthermore, the velocity profile graphs give insight into the flow characteristics of the combed-airfoil and the comb-serrated models. The combed-airfoil model demonstrates a continuous flow from a zero Angle of attack to 8 degrees. However, when the Angle of attack increases from 8 to 10 degrees, a minor disruption in the flow along the trailing edge is seen. The flow separation is seen to occur at roughly  $0.98c$  and  $0.9c$  for angles of attack of 8 degrees and 10 degrees, respectively, resulting in a separation zone that is less than 10% of the chord length. The x-velocity contour further verifies this observation. Similarly, the comb-serrated model reveals flow patterns comparable to the combed-airfoil model. The flow through this model is shown to be laminar, starting from a zero Angle of attack till 8 degrees. Even at high angles of attack of 10 degrees, the flow only separates along the trailing edge, resulting in a minimum separation part of less than 5% of the chord length. These findings show the potential of the comb-serrated model to sustain laminar flow over a vast range of angles of attack, resulting in a smaller separation zone.



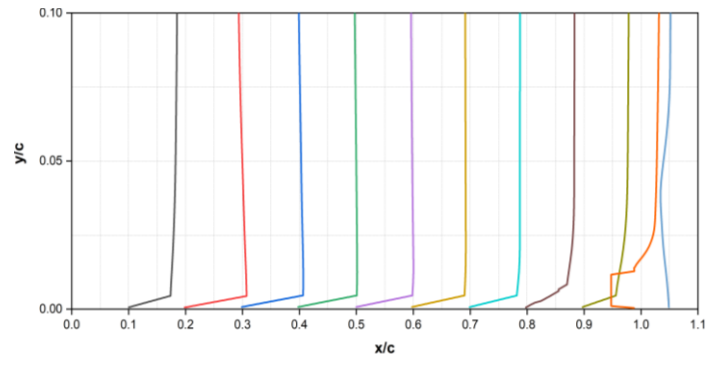
(a) Baseline airfoil



(b) Serrated TE airfoil

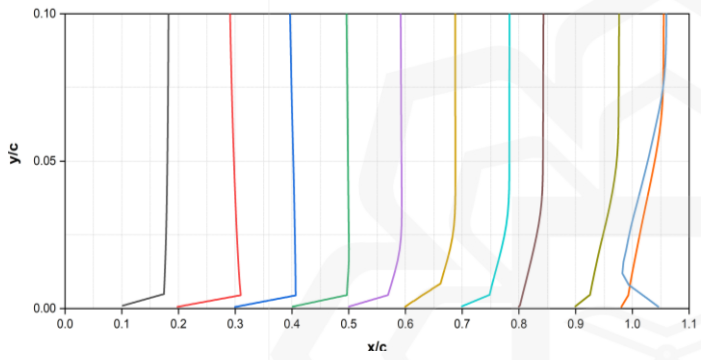


(c) Combed TE airfoil

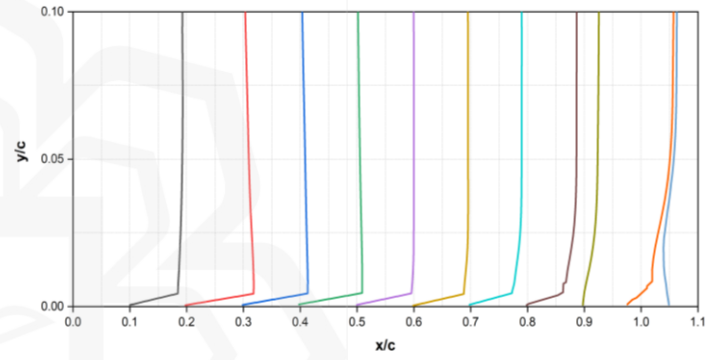


(d) Comb-Serrated TE airfoil

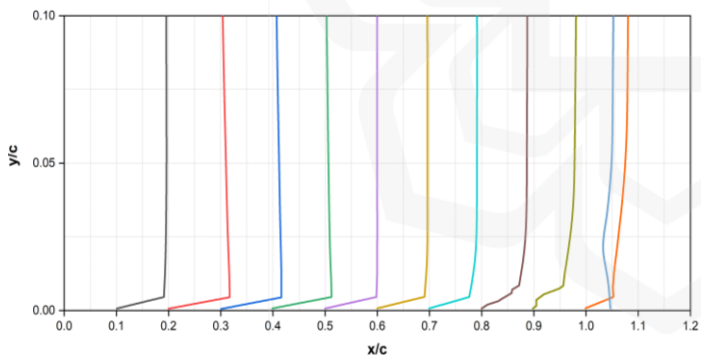
Figure 4.31 Velocity Profile at  $\alpha = 3^\circ$ .



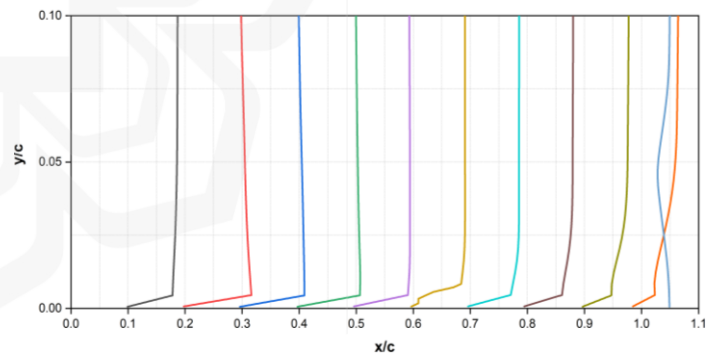
(a) Baseline airfoil



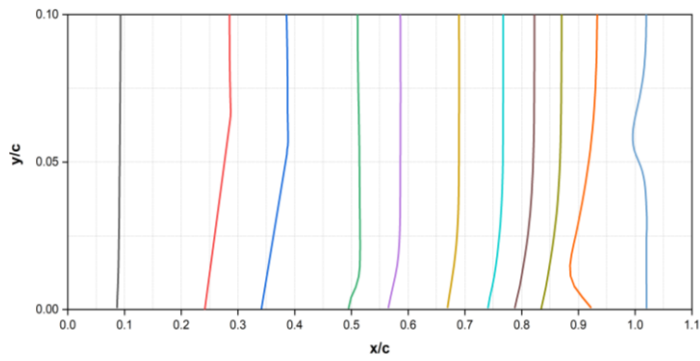
(b) Serrated TE airfoil



(c) Combed TE airfoil



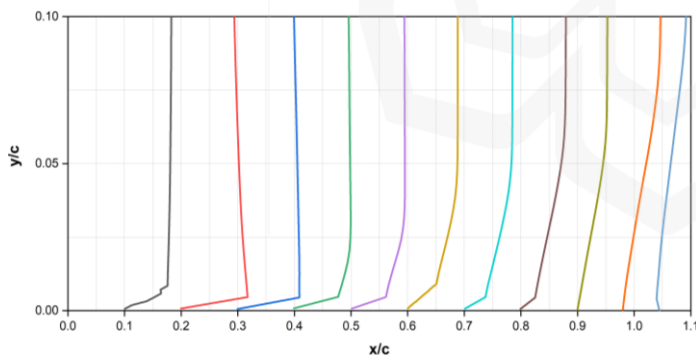
(d) Comb-Serrated TE airfoil



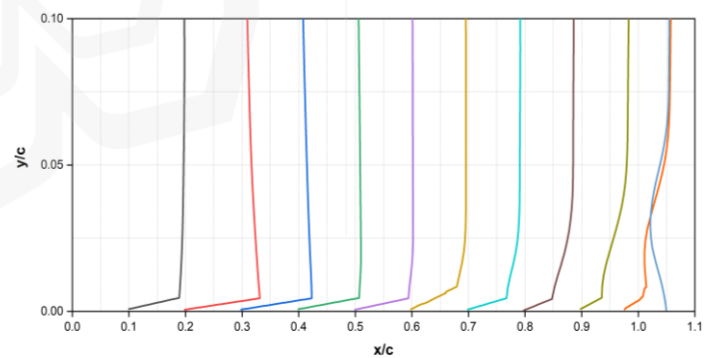
(e) Poro-Serrated TE airfoil

Figure 4.32 Velocity Profile at  $\alpha = 6^\circ$ .

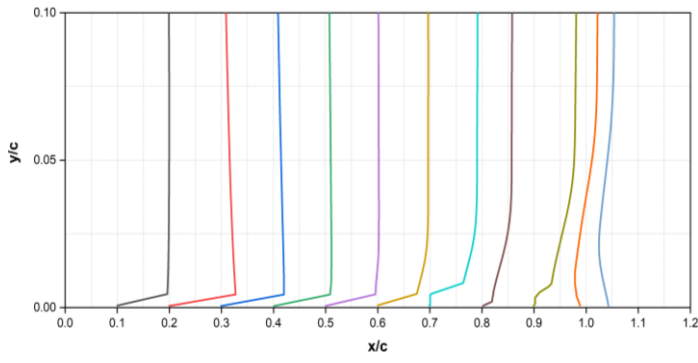
From the velocity profile graph, the poro-serrated model separates at around 0.6c at zero Angle of attack. This flow reattaches with the surface towards the trailing edge, forming a laminar separation bubble roughly 40% of the chord length. As the Angle of attack is adjusted to 6, 8 and 10 degrees, the flow is found to separate at around 0.93c, 0.9c and 0.85c, respectively. The result demonstrates that the separation point moves upstream as the Angle of attack increases. The flow separation occurs without reattachment, resulting in no separation bubble development. However, the size of the separation region, measured from the separation point, may be expected to be larger than 7%, 10% and 15% for angles of attack of 6, 8 and 10 degrees, respectively. The poro-serrated model displays unusual flow characteristics as opposed to the other models due to its ability to enable air to pass beyond its porous region. This characteristics results in a distinctive separation pattern, which offers insight into the efficiency of the poro-serrated design in changing the flow field across an airfoil surface.



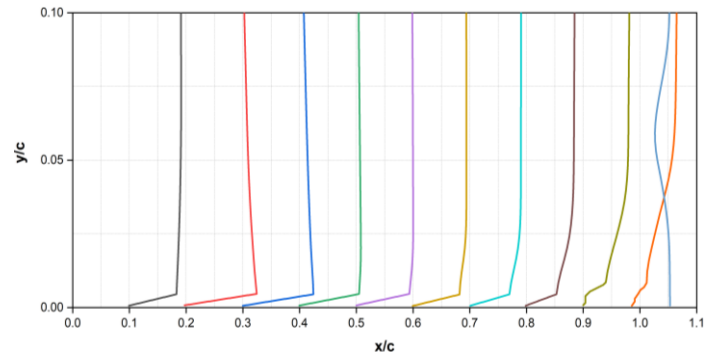
(a) Baseline airfoil



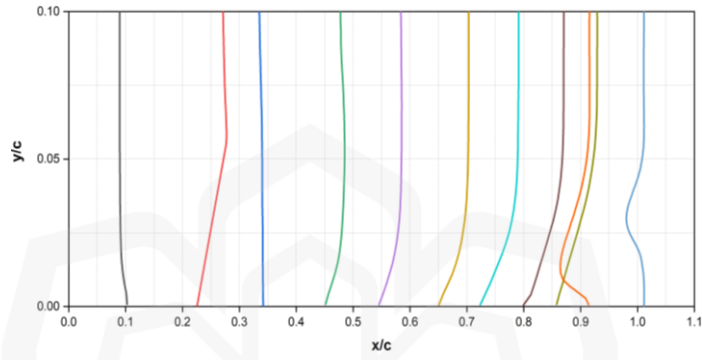
(b) Serrated TE airfoil



(c) Combed TE airfoil

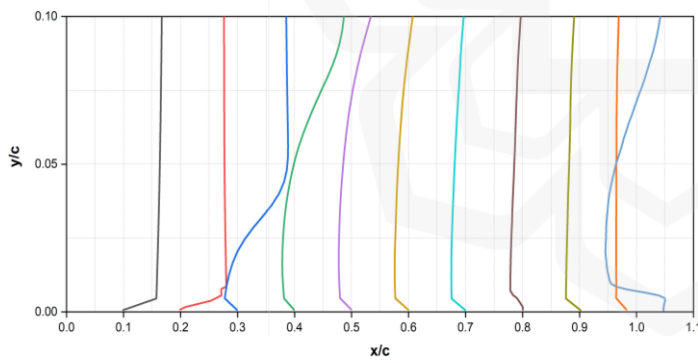


(d) Comb-Serrated TE airfoil

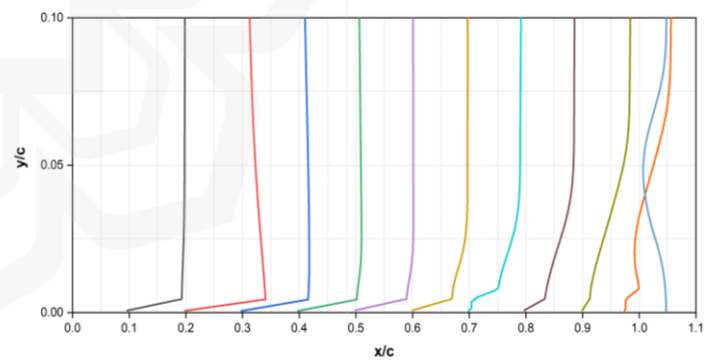


(e) Poro-Serrated TE airfoil

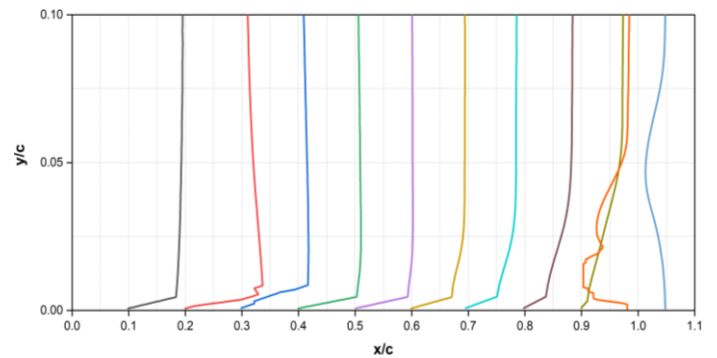
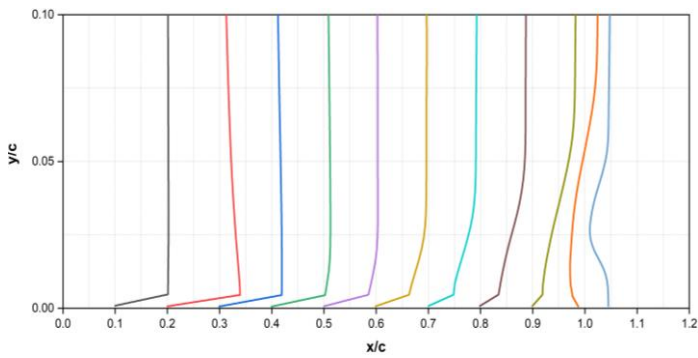
Figure 4.33 Velocity Profile at  $\alpha = 8^\circ$ .



(a) Baseline airfoil

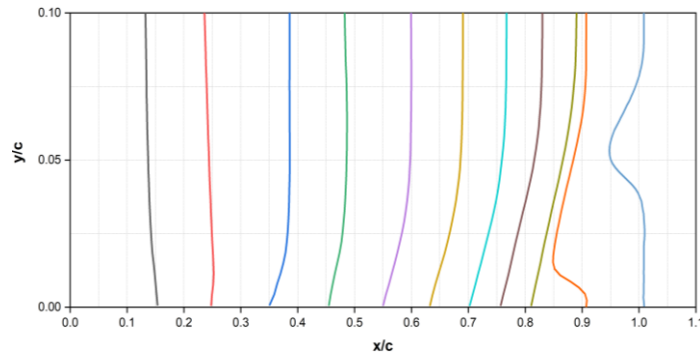


(b) Serrated TE airfoil



(c) Combed TE airfoil

(d) Comb-Serrated TE airfoil



(e) Poro-Serrated TE airfoil

Figure 4.34 Velocity Profile at  $\alpha = 10^\circ$ .

### 4.3.3. Spanwise Vorticity

Figure 4.35-4.40 possess distinctive information that helps to visually and thoroughly understand the three-dimensional flow structure, such as vortices and eddies. Vorticity defines the rotational movement of fluid elements within a fluid flow. To determine the velocity vector, the displacement of tracer particles is analyzed across consecutive images and then divided by the time elapsed. The computation of the curl applied to these velocity vectors reveals vorticity vectors, indicating the local rotational motion of fluid elements. Each vector component represents the rate of rotation around a specific axis. The spanwise vorticity plots for several models are provided and compared to clearly illustrate the causes for their discrepancies.

At a zero Angle of attack, the vorticity is seen to vary at the trailing edge with the exception at the root of the combed-type trailing edge. The poro-serrated model displays unsteadiness throughout the trailing edge, starting at  $0.6c$  and extending until near the tip of the trailing edge. This finding reveals the rolling of the shear layers after separation, generating a recirculation zone that reattaches with the surface towards the tip of the trailing edge. The serration design also displays a recirculation zone at the near end of the trailing edge. These findings give an additional knowledge of the flow structures and their behaviour in diverse models and combinations. As the Angle of attack is raised from 0 to 2 degrees, the behaviour of the spanwise vorticity differs for

different models. In general, the spanwise vorticity behaviour at an Angle of attack of 2 degrees was consistent with observations conducted at a zero Angle of attack. The poro-serrated and serrated models continued to display greater unsteadiness than other models. However, it was noticed that the unsteadiness in these designs had substantially diminished as the Angle of attack increased. This reduction in unsteadiness illustrates the sensitivity of the flow structures to changes in the Angle of attack. In contrast, the other models indicated a slight increase in the spanwise vorticity. This rise, however, could have been higher. In particular, the poro-serrated model revealed a considerable shift in the flow patterns. The unsteadiness, which was previously found at the trailing edge, was noted to have shifted upstream. This variation in behaviour reveals it's flow system' complex and dynamic character. The comb model demonstrated a distinctive behaviour in the spanwise vorticity as the Angle of attack increased from 0 to 2 degrees. Unlike the serrated and poro-serrated models, which indicated separation of the flow and formation of a bubble, the flow along the root of the comb model was shown to have shifted further away from the trailing edge.

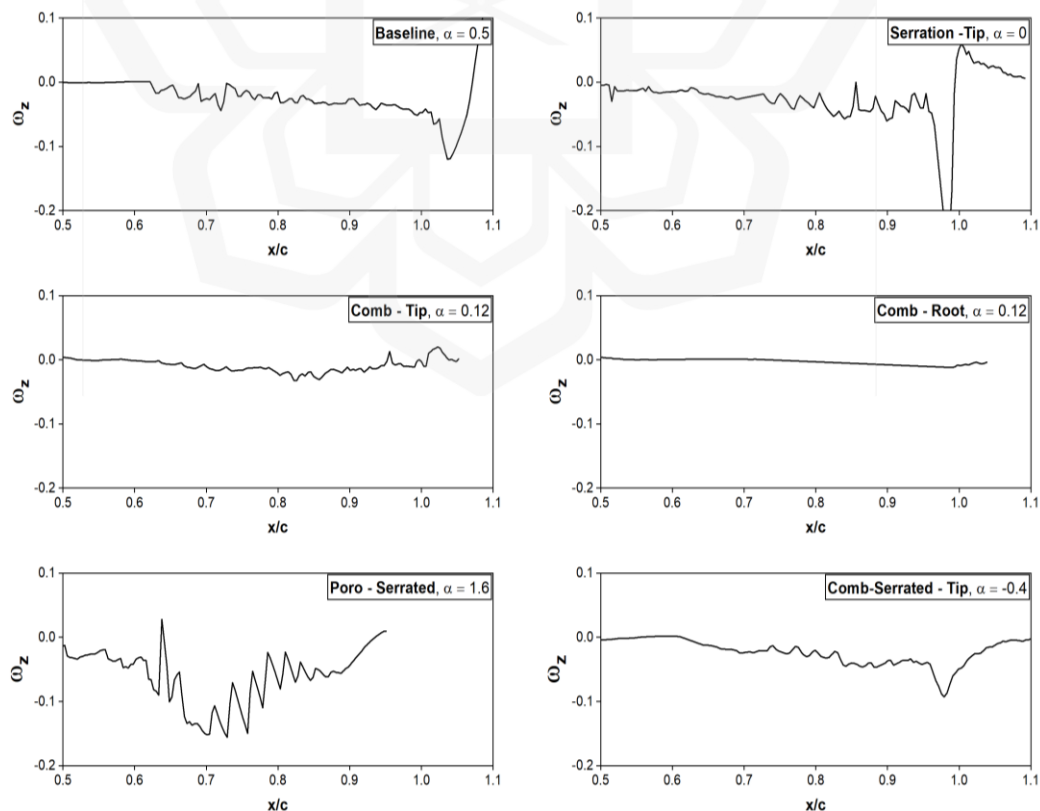


Figure 4.35 Spanwise Vorticity at  $\alpha = 0^\circ$ .



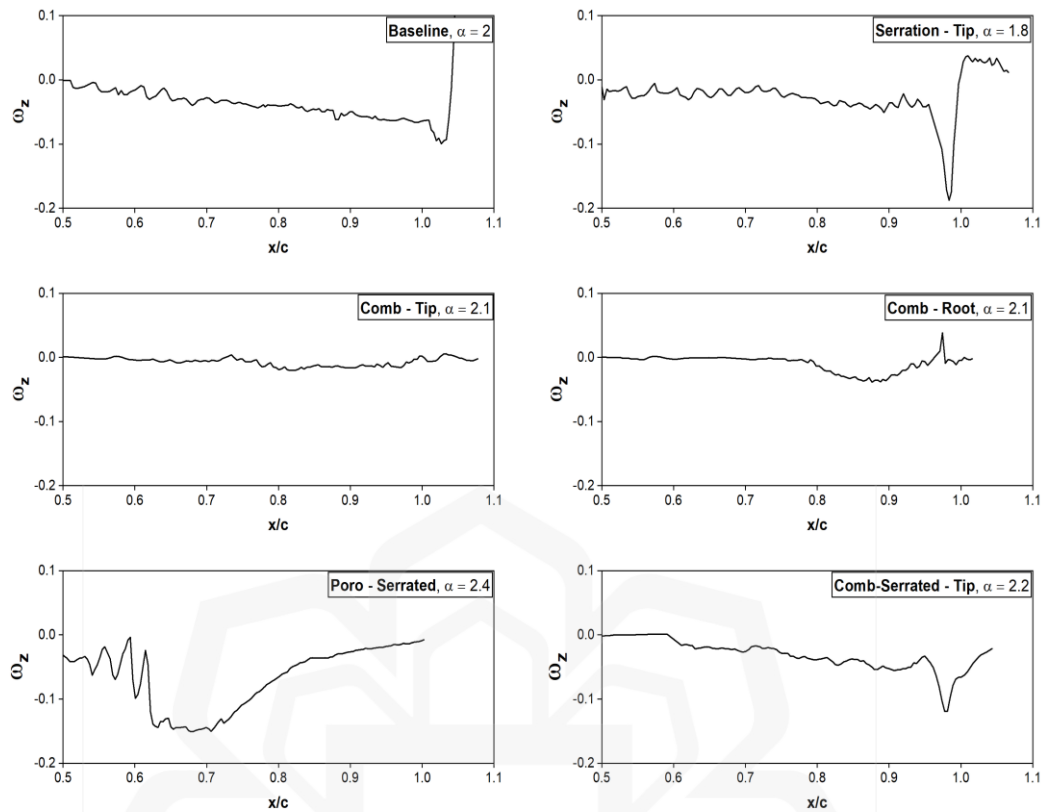


Figure 4.36 Spanwise Vorticity at  $\alpha = 2^{\circ}$ .

At an Angle of attack of 3 degrees, the spanwise vorticity over the baseline model gradually increases compared to the results at 2 degrees, as demonstrated by the decline in the amplitude of vortices over the baseline model. In the case of the serration design, the flow continues to demonstrate a rolling and separating behaviour near the end of the trailing edge as it advances into the wake zone without reattaching to the surface. At this Angle of attack, the root section of the serration displays a higher amount of unsteadiness than the tip component. The root section displays significant oscillations in the spanwise vorticity as contrasted to the tip, which is observed to detach more swiftly. This implies that the flow is getting increasingly more unstable towards the root of the serration as the Angle of attack increases from 2 to 3 degrees. Meanwhile, the comb design displays a pattern similar to the one observed at 2 degrees, with the flow moving away from the trailing edge and forming a more streamlined structure. The comb design continues to display a smooth flow over the surface without any evidence of separation.

On the other side, the spanwise vorticity values of the comb-serrated model reveal higher unsteadiness around the tip of the trailing edge than the other regions. The tip area displays the maximum level of unsteadiness, followed by the comb-like section, and the least amount of unsteadiness is detected along the root. This trend shows that the serration and comb configurations impact the flow in distinct ways, and the resulting spanwise vorticity values reflect these changes. Furthermore, as the Angle of attack is increased from 3 to 6 degrees, a further rise in unsteadiness is noted in the spanwise vorticity of the baseline model. This rise is characterized by the development of a rolling structure and the growth of a laminar separation bubble without reattachment. In the serrated model, the unsteadiness along the tip intensifies, with a decrease in the amplitude of the sudden disturbance noticed at the end of the trailing edge. The comb structure shows a sharp unsteadiness towards the tip of its geometry is comparable to the serration characteristic and ascribed to the bluntness of the trailing edge. However, the root component of the comb structure demonstrates less unsteadiness compared to the Angle of attack of 3 degrees. In contrast, the poro-serrated model depicts a smooth flow with minor disruptions, which can be due to the change in momentum from the airflow passing through the porous zone. Meanwhile, the comb-serrated model exhibits minimal variation compared to the Angle of attack of 3 degrees, with minor disruptions noted around the tip, root, and comb-like section of the trailing edge.

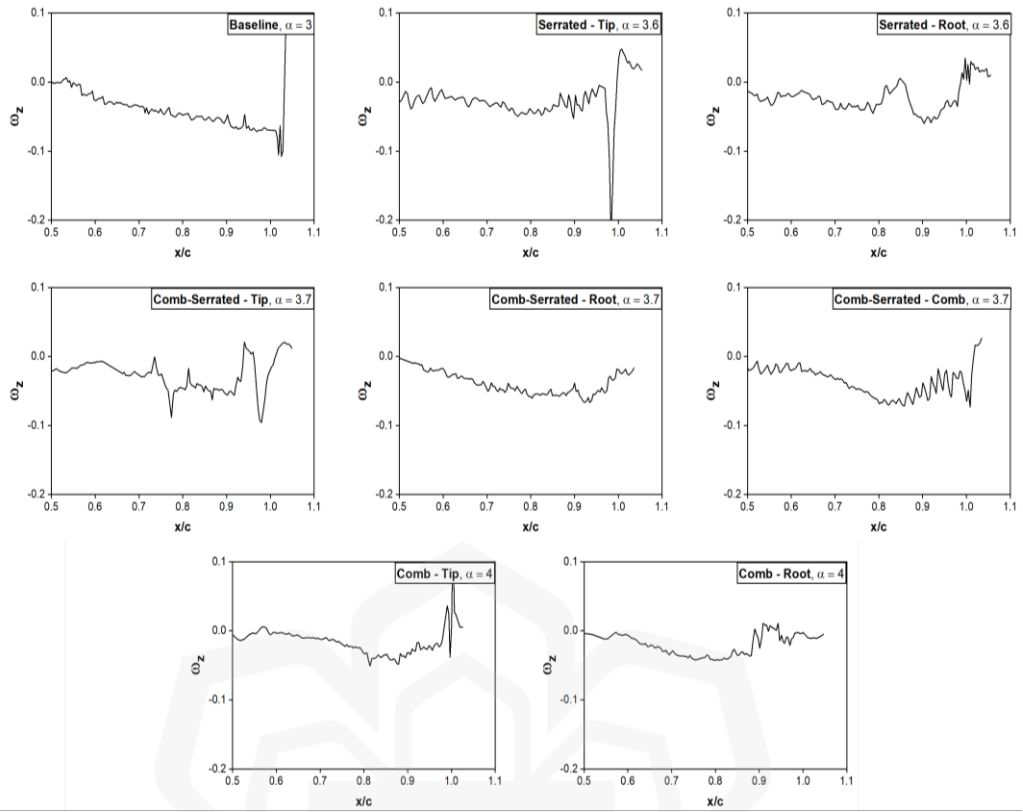


Figure 4.37 Spanwise Vorticity at  $\alpha = 3^\circ$ .

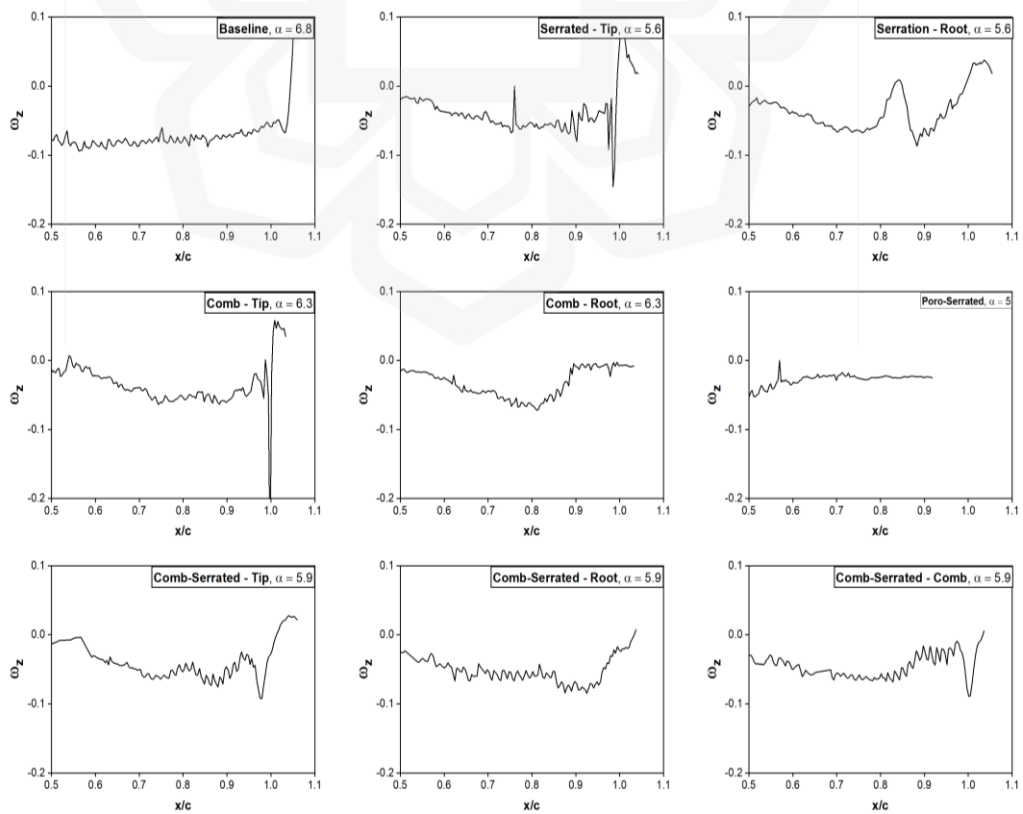


Figure 4.38 Spanwise Vorticity at  $\alpha = 6^\circ$ .

The results presented in Figure 4.39 reveal that as the Angle of attack is raised from 6 to 8 degrees, the spanwise vorticity in the baseline model undergoes a further upsurge in unsteadiness. This increase is evident by disturbances being monitored even in the wake region. The serration model likewise displays an increase in unsteadiness, with both the root and tip sections experiencing greater levels of unsteadiness. Unlike the Angle of attack of 6 degrees, the rapid disruption noted at the end of the trailing edge at the tip section is no longer present. Nonetheless, both the baseline and serration models demonstrate that the flow separates and reattaches near the end of the trailing edge, resulting in the development of a separation bubble.

Similarly, the comb model demonstrates separation at the end of the trailing edge and forms separation bubbles at both the tip and root sections. The disturbance is more prominent near the end of the trailing edge in the root section, whereas the tip part sees a somewhat less disturbed flow.

In contrast, the poro-serrated model displays a smooth flow with little perturbation. However, the flow is observed to detach, forming of a tiny separation bubble after reattaching to the surface. On the other hand, the comb-serrated model demonstrates increasing disturbance levels along all sections. Unlike the root component, the tip and comb-like part reattach to the surface after separation. The root and comb segments generate larger amounts of unsteadiness in the flow, than the other types. With the Angle of attack of 10 degrees, as shown in Figure 4.40, the flow across the baseline surface experiences a breakdown due to the excessive intensity of the nonlinear interaction. This pattern leads to the fast shedding of vortices downstream, clearly visible in Figure 4.28. However, due to the high downstream flow, the vortices are not clearly apparent. The spanwise vorticity of the serration model displays characteristics comparable to those found at an Angle of attack of 8 degrees at the tip section. Despite this, the root section suffers a decrease in disturbance, marked by visible vortices. The flow separates and reattaches at a location roughly 0.98 chords from the leading edge, forming of a separation bubble in both cases. The comb model

reveals patterns comparable to those found at an Angle of attack of 8 degrees for both the tip and root sections. In contrast, the poro-serrated model demonstrates increased disturbance throughout the trailing edge surface, with separation visible throughout. Similarly, the comb-serrated model displays feature comparable to those seen at an Angle of attack of 8 degrees, with a minor increase in unsteadiness along the root section.

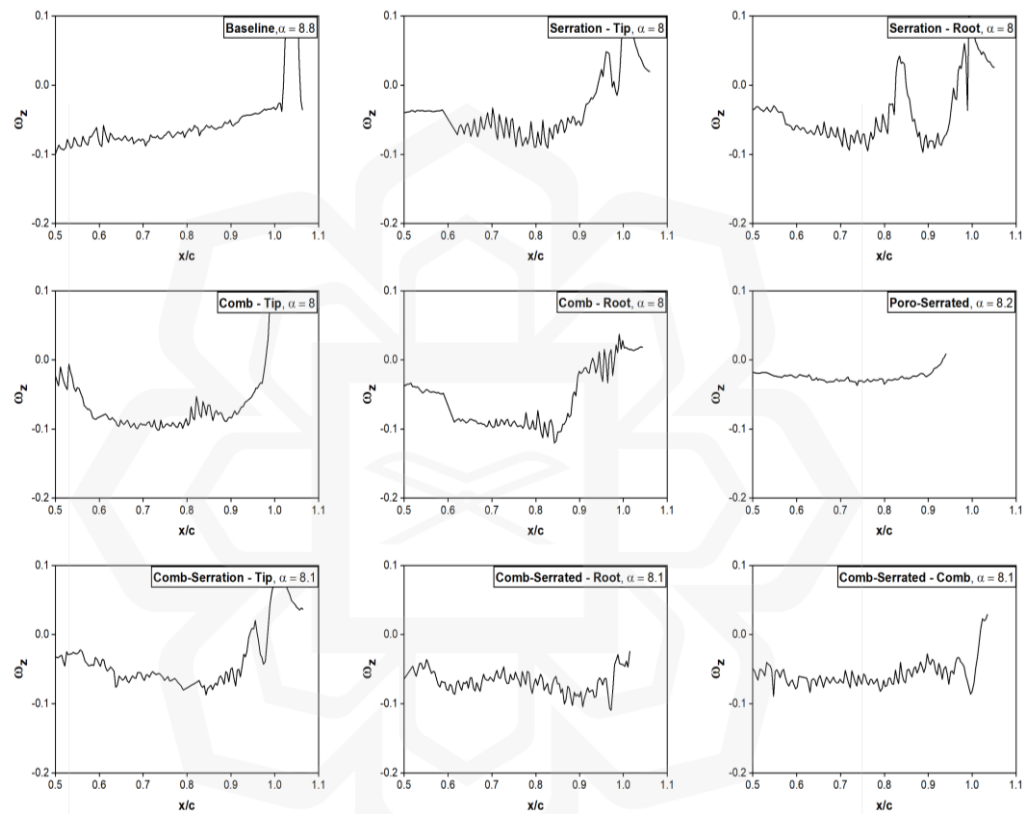


Figure 4.39 Spanwise Vorticity at  $\alpha = 8^{\circ}$ .

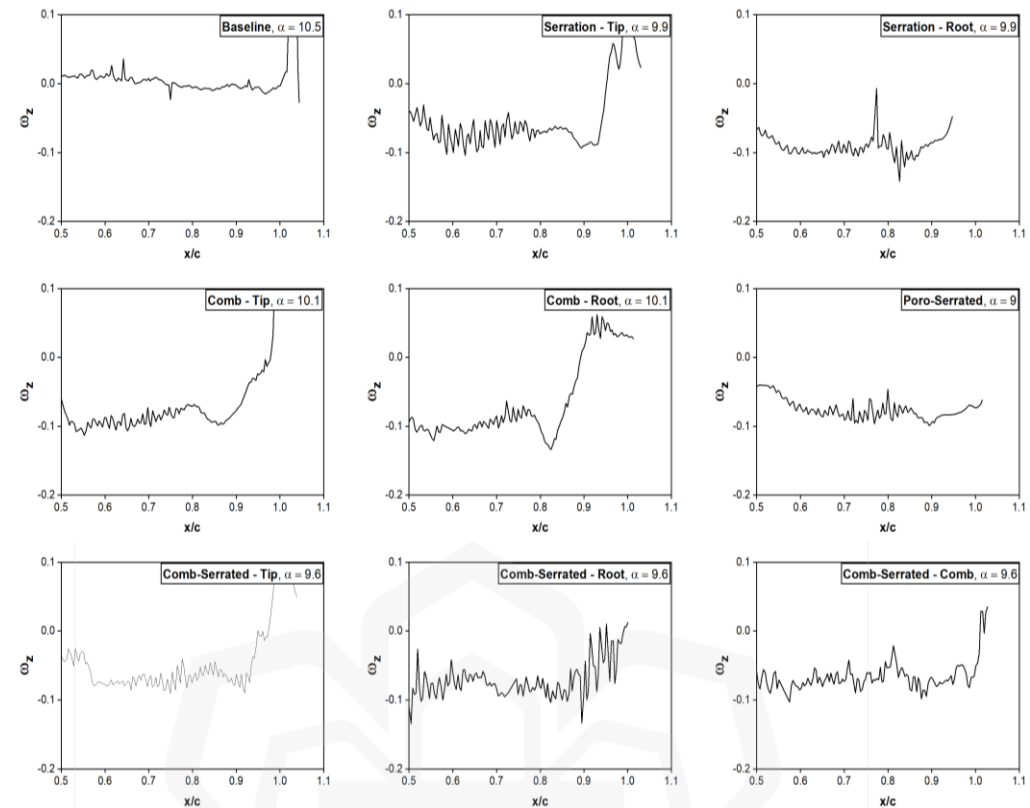


Figure 4.40 Spanwise Vorticity at  $\alpha = 10^\circ$ .

#### 4.3.4. Summary of the Experimental Work

From the experimental studies, the results of the x-velocity contour and spanwise vorticity analysis reveal that the serrated, combed, and comb-serrated airfoil models have more stable flow patterns and shorter separation bubbles than the baseline airfoil. The poro-serrated airfoil revealed a more disordered flow pattern with a laminar separation bubble that moves upstream as the Angle of attack increases. At zero Angle of attack, the poro-serrated model demonstrated unsteadiness throughout of its trailing edge, although a decrease was noted at a 2-degree Angle of attack. The other models indicated a slight rise in spanwise vorticity, with the comb model showing a distinct trend. As the Angle of attack rose from 6 to 8 degrees, the baseline and serration models demonstrated higher instability with flow separation, whereas the comb and poro-serrated models indicated minor disruption. At 10 degrees Angle of attack, the baseline model exhibited a breakdown of its shear layer, while the poro-serrated model showed increased disturbance with separation throughout. The comb-serrated and serration

models revealed features comparable to those reported at 8 degrees Angle of attack, with a minor increase in unsteadiness.

#### **4.4. SUMMARY**

In conclusion, the research findings showed the following:

- The findings of the 2D numerical simulation demonstrated that the position and size of the laminar separation bubble on the suction side of the airfoil are affected by both the Reynolds number and the Angle of attack, with the effect of Angle of attack being more pronounced than Reynolds number.
- On the other hand, the outcome of the 3D investigations reveals that the serrated, combed, and comb-serrated airfoil designs have distinct impacts on fluid flow, with the serrated trailing edge creating higher velocity and pressure drop, combed trailing edge inducing separation at the root, and comb-serrated design maintaining a continuous fluid flow.
- The experimental results showed that the serrated, combed, and comb-serrated models have more stable flow patterns and fewer separation bubbles compared to the baseline airfoil. The poro-serrated model had a more distorted flow pattern and an upstream-moving laminar separation bubble.
- At zero Angle of attack, the poro-serrated model showed unsteadiness along its trailing edge, while the other models indicated a minor rise in spanwise vorticity, with the comb model exhibiting a significant trend.
- As the Angle of attack increased, the baseline and serration models showed significant instability with flow separation, while the comb and poro-serrated models showed minor disruption. At 10 degrees Angle of attack, the baseline model had a disintegration of its shear layer, while the poro-serrated model showed increasing disturbance and separation. The comb-serrated and serration models showed traits comparable to those at an 8 degrees Angle of attack.

## **CHAPTER FIVE**

### **AEROACOUSTIC SIMULATIONS**

#### **5.1. INTRODUCTION**

This chapter investigates the aeroacoustics of both the baseline and modified models. The study performs numerical calculations by using Ansys Fluent software. The findings of the computational analysis are evaluated in a three-dimensional (3D) case. In this section, the three-dimensional (3D) analysis was performed at a Reynolds number of  $1.6 \times 10^5$  and various angles of attack ranging from -2 to 2 degrees.

In Chapter 3, the models under consideration are presented orderly and comprehensively, with their distinctive features and characteristics highlighted in depth. The models comprise the physical dimensions of each model, as well as their precise layouts and geometries, which play a key role in defining their aerodynamic performance. The configurations of these models are clearly described in Figures 3.1-3.10, offering a diagram of the models for further clarity. This information is necessary for the reader to understand better the models being researched and the basis for their aerodynamic analysis.

A complete review of the 3D computational results is presented in Chapter 4. The computational analysis is verified with another published study to validate the 3D analysis. Therefore, this result complements the subsequent acoustic results. The results of the computational study are then described in depth, highlighting significant findings and insights. The chapter finishes with a summary of the main points, offering a concise overview of the significant conclusions from the acoustic analysis.

#### **5.2. COMPARISON WITH OTHER STUDY**

The ability to compare results from multiple simulations or observations is made feasible by normalizing the pressure variations. These differences can result in the emission of sound, and the size of the pressure fluctuations can be used to anticipate the



resulting noise levels. Therefore, it is vital to compare the normalized pressure fluctuations from the current research with those from another numerical result to identify noise levels appropriately. The airfoil bluntness employed in this study is 1.5 mm, whereas the other study had a bluntness of roughly 1.3 mm (Shen et al., 2009).

A comprehensive assessment of the normalized pressure variations was carried out at specific locations within the flow domain. This plot illustrates the fluctuation pattern observed on the normalized pressure fluctuation plot and relates it to another study. As illustrated in Figure 5.1, the surface pressure signals computed using the present numerical model were examined at two points: one centered about 50% of the chord length on the suction side ( $90^\circ$ ) and another one upstream ( $0^\circ$ ). These positions are situated at a distance of 12 chords from the airfoil's upper surface and the leading edge. The plot of the pressure variations at the suction side displays a unique pattern with a comparatively low amplitude of 0.00015 compared to a reference value.

On the other hand, the changes on the upstream side are small since the reference pressure utilized is the ambient pressure of 101,325 Pa on the upstream side of the flow. The data reveal that the pressure differences are modest, proving the pressure measurements' accuracy. However, it is worth emphasizing that the major purpose of this research is to compare the average pressure value between the present work and the numerical study. The mean value for the point placed on the suction side for both is roughly -0.00022, while for the upstream scenario, it is around 0.0001.

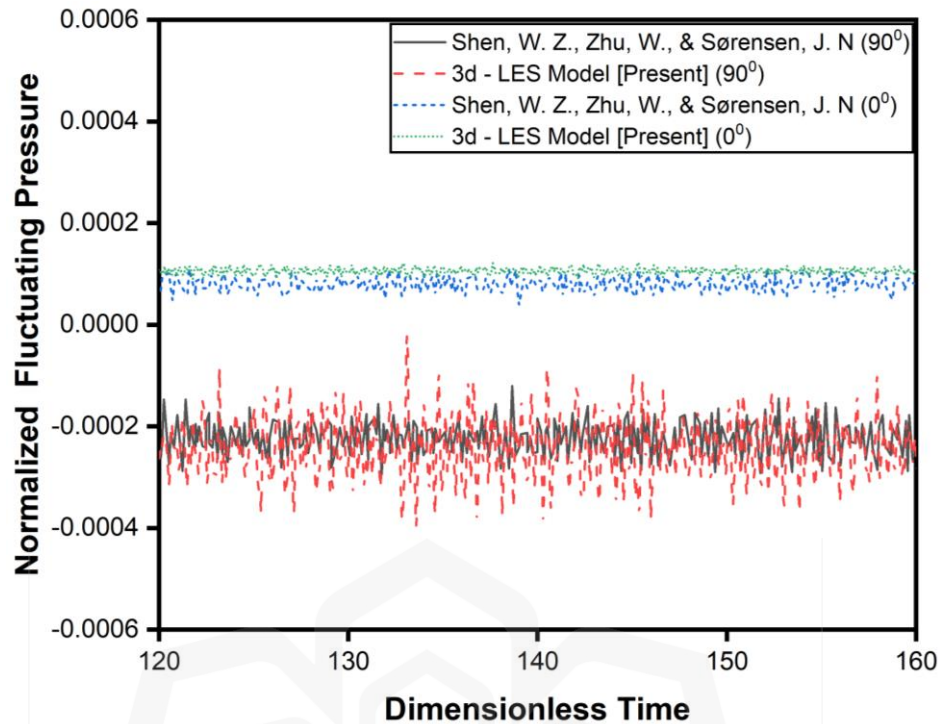


Figure 5.1 Normalized Surface Pressure Fluctuations at  $\alpha = 4^\circ$

### 5.3. FAR-FIELD NOISE PREDICTION

In this simulation, a trimmed mesh with 3.5 million cells is used. The mesh has 20 prism layers with a stretching growth rate of 1.2 to resolve the near wall flow.

#### 5.3.1. Surface Pressure Fluctuations

Examining wall pressure signals is particularly crucial for finding low-frequency noise due to surface pressure variations along the airfoil surfaces. The interaction between the airflow and the surface of an airfoil leads to variations in pressure distribution, which in turn gives rise to different types of noise, primarily aerodynamic noise and turbulent boundary layer noise. As the airflow speeds up over the airfoil's upper surface and decelerates along the lower surface, vortices are shed at the trailing edge. These vortices interact with the trailing edge and create pressure fluctuations, resulting in sound waves being radiated into the far-field as noise. The situation gets more complicated when paired with additional phenomena, such as flow separation and an unfavorable pressure gradient. Therefore, knowing the surface pressure fluctuation on the airfoil surface is

particularly significant for the design and performance of airplanes and other aerodynamic systems.

The graphs in Figure 5.2-5.6 show the results of a pressure-time evaluation that was undertaken at two separate positions: one positioned at about 50% of the chord length on the suction side of the airfoil ( $90^{\circ}$ ) and the other placed at about 50% of the chord length on the pressure side of the airfoil ( $270^{\circ}$ ) as shown by Figure 3.18. This analysis was done at various angles of attack ranging from  $-2$  degrees to  $2$  degrees. Additionally, the study was done on four distinct configurations: the baseline airfoil, an airfoil with serrations on the trailing edge, an airfoil with a comb-shaped trailing edge, and an airfoil with both serrations and a comb-shaped (Comb-serration) trailing edge. The findings of the research were then compared to understand the influence of these distinct geometries on surface pressure fluctuation.

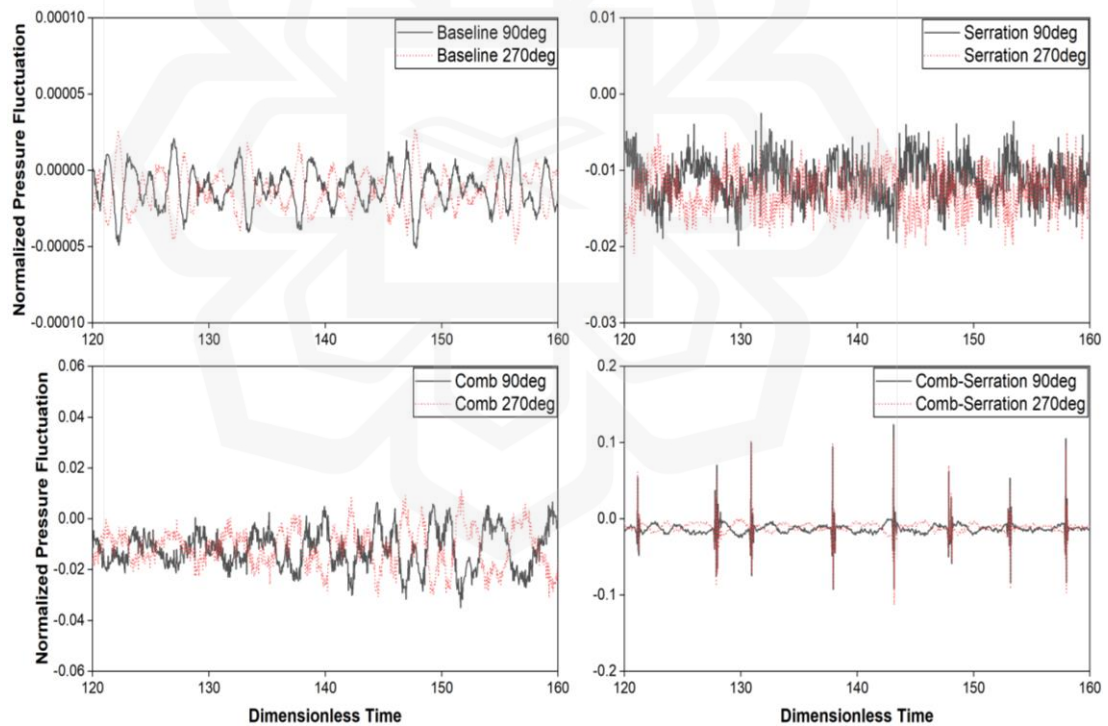


Figure 5.2 Time histories of the normalized wall pressure at  $\alpha = 0^{\circ}$ .

Figure 5.2, shows that the baseline design's surface pressure fluctuation displays a more sinusoidal pattern of pressure fluctuations, with an amplitude of about  $0.000003$  Pa. This trend shows that the airfoil surface receives some form of regular change in

pressure as it passes through the air. Moreover, the variations both at the suction side (90 deg) and the pressure side (270 deg) have a mean value of roughly 0 Pa as the airfoil is symmetric and at zero Angle of attack. When evaluating the trend of the surface pressure fluctuation for the serration configuration compared to the baseline configuration, it can be noted that there is an increase in the pressure fluctuation amplitude, with a value of roughly 0.005 Pa. This trend indicates that the serrated trailing edge enhances the amplitude of the surface pressure variation, resulting in a greater pressure distribution throughout the airfoil surface. Additionally, the model anticipated a mean value of roughly -0.0115 Pa for suction and pressure. The surface pressure fluctuation for the comb trailing edge reveals a pattern with several peaks and troughs, showing that the comb structure results in a more turbulent pressure distribution over the airfoil surface. As for the surface pressure fluctuation of the comb-serration structure, a more complicated pattern of pressure fluctuation is seen. Overall, this finding elaborates on the possible influence of varied trailing edges on the surface pressure fluctuation and the relevance of knowing the pressure distribution throughout the airfoil surface for noise reduction.

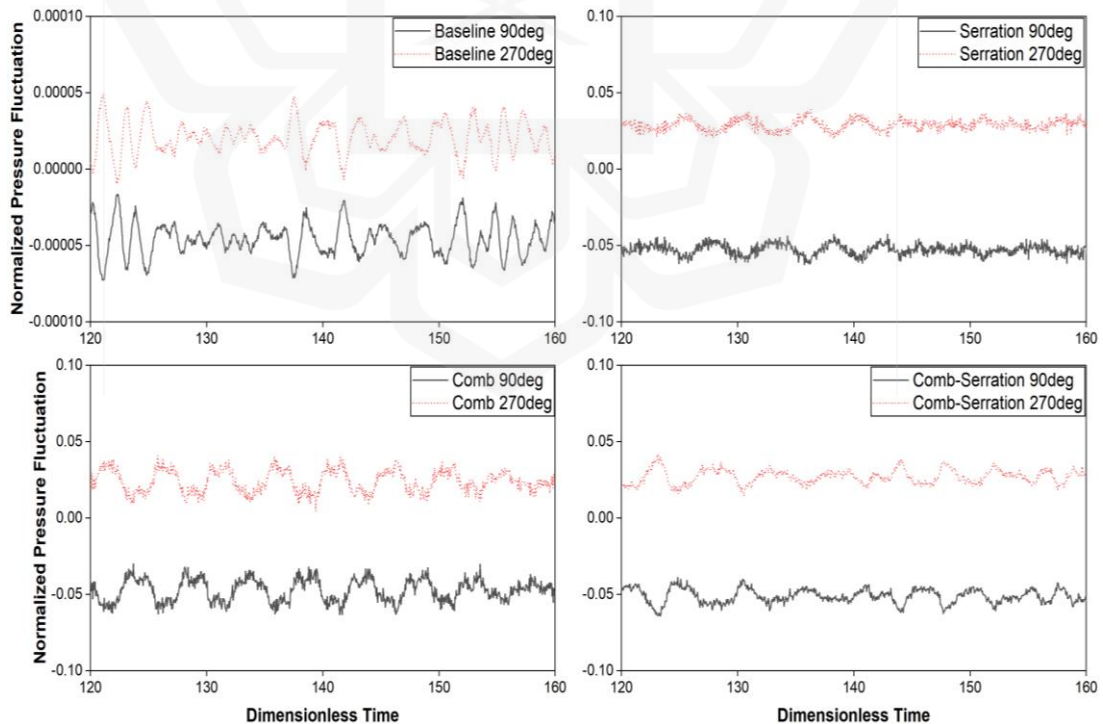


Figure 5.3 Time histories of the normalized wall pressure at  $\alpha = 1^\circ$ .

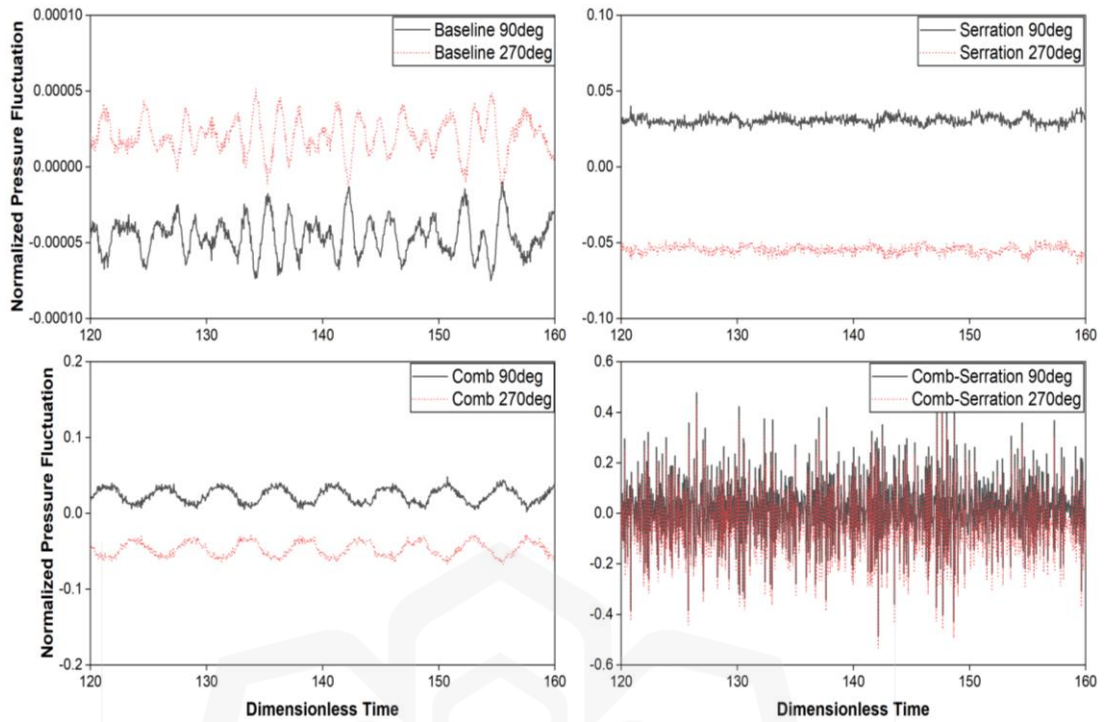


Figure 5.4 Time histories of the normalized wall pressure at  $\alpha = -1^\circ$ .

It can be observed from Figure 5.3 and Figure 5.4 that the baseline design of the airfoil surface presents a characteristic pattern of pressure fluctuation, with a mean value of roughly 0.000025 Pa at the pressure side and a smaller value of about -0.00005 Pa at the suction side. Furthermore, it can be noted that when the Angle of attack increases from 0 degrees to 1 degrees, the amplitude of the pressure fluctuation likewise increases by 0.000012 Pa, suggesting that the pressure fluctuation on the airfoil surface increases with the Angle of attack. On the other hand, the serrated trailing edge displays a similar trend, with an increase in the mean pressure fluctuation on the pressure side and a reduction on the suction side; nevertheless, the amplitude stays unchanged. However, the comb trailing-edge design produces a more sinusoidal-like pattern, with an amplitude of around 0.0136 Pa compared to the complicated pattern at 0 degree. Furthermore, the comb arrangement displays a more complicated pattern of pressure fluctuation, with an increase in amplitude and many peaks and troughs in the pressure fluctuation. The comb-serration configuration demonstrates a mix of the characteristics identified for the serration and comb configurations, with a drop in amplitude and a more complicated pattern of pressure fluctuation. It may be noticed that all three configurations, serration, comb, and comb-serration, predict comparable mean values of roughly 0.025 Pa on the pressure side and -0.05 on the suction side.

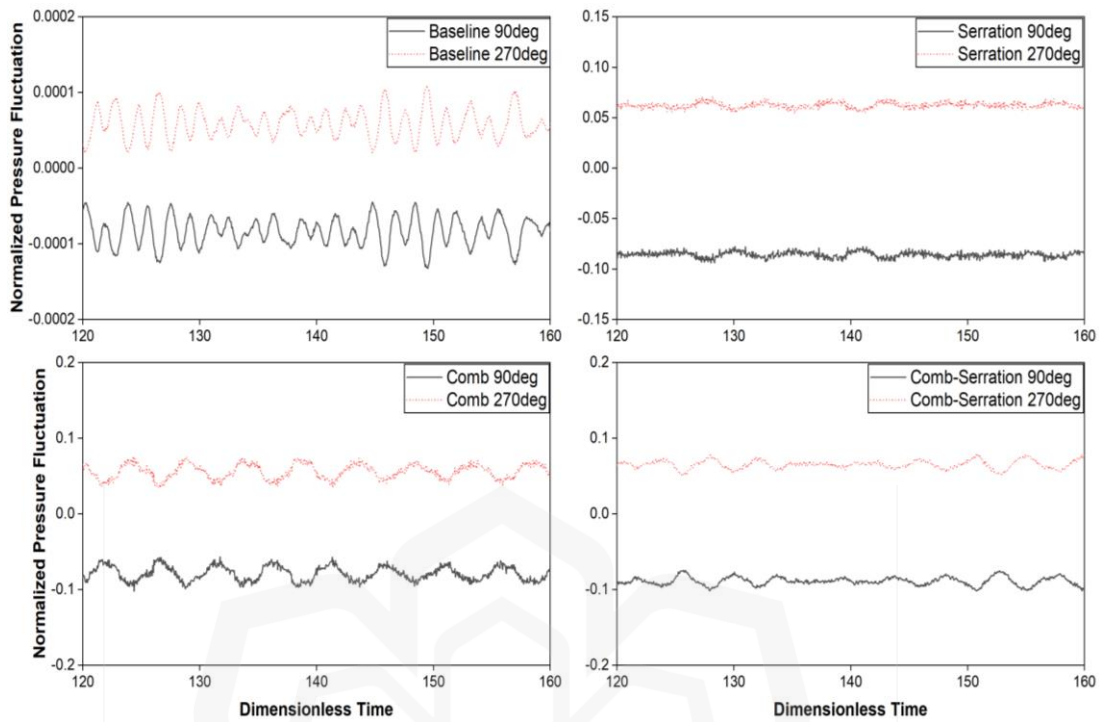


Figure 5.5 Time histories of the normalized wall pressure at  $\alpha = 2^\circ$ .

Figure 5.5 and Figure 5.6 demonstrate that the baseline configuration of the airfoil surface presents a distinct pattern of pressure fluctuation as compared to 0 and 1 degree, with a mean value of around 0.00005 Pa at the pressure side and a low value of about -0.00008 Pa at the suction side. Furthermore, it can be noted that when the Angle of attack increases from 1 degree to 2 degrees, the magnitude of the pressure fluctuation remains virtually the same. The serration arrangement demonstrates a similar tendency, with an increase in the mean pressure fluctuation on the pressure side and a reduction on the suction side; however, the amplitude stays unchanged. The comb trailing-edge design presents a more sinusoidal-like pattern, with an amplitude of roughly 0.02 Pa compared to 1 degree. Furthermore, the comb arrangement displays a more complicated pattern of pressure fluctuation, with an increase in amplitude and many peaks and troughs in the pressure fluctuation. The comb-serration configuration demonstrates a mix of the characteristics identified for the serration and comb configurations, with a drop in amplitude and a more complicated pattern of pressure fluctuation. It may be noticed that all three configurations, serration, comb, and comb-serration, anticipate



comparable mean values of roughly 0.064 Pa on the pressure side and -0.085 on the suction side.

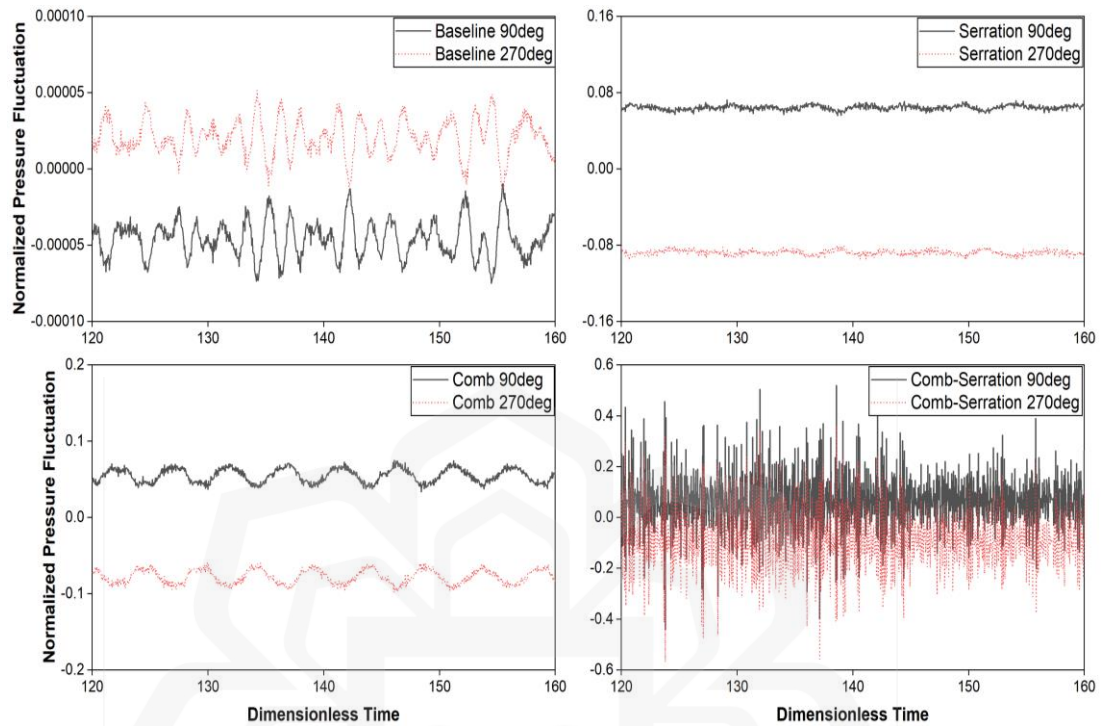


Figure 5.6 Time histories of the normalized wall pressure at  $\alpha = -2^\circ$ .

### 5.3.2. Sound Pressure Level

The Sound Pressure Level (SPL) is a crucial method for assessing the loudness of sounds in various environments. It offers a quantitative measurement of sound loudness and enables comparisons between different sounds. Sound pressure level can also be employed to evaluate the efficiency of noise reduction techniques such as trailing edge configurations. The results of the SPL analysis can be used to identify noise sources and develop strategies for reducing noise levels. Moreover, SPL analysis can also be used to evaluate the compliance of a particular technique with regulations and standards related to noise pollution.

In this investigation, the acoustic field was computed using the Ffowcs, Williams, and Hawkings model based on the unsteady aerodynamic flow field acquired

from large-eddy simulation. The whole surface of the airfoil has been selected as the source of the radiated signals because it provides a comprehensive understanding of the noise created by the airfoil throughout its operation. For this study, the acoustic receivers were strategically placed 8 chord lengths apart from the top ( $90^\circ$ ) and bottom ( $270^\circ$ ) surfaces as well as downstream ( $180^\circ$ ) of the flow. This location facilitates the prediction of pure acoustic signals as less fluctuation is encountered further away from the surfaces. By monitoring the sound pressure level at these different points, it is possible to discover which parts of the airfoil are the primary producers of noise and how the noise is spread throughout the whole surface of the airfoil. Overall, this strategic arrangement of the receivers provides a thorough understanding of the noise-generating process and its dispersion. The observers are positioned on the mid-span plane of the airfoil, since it is an optimal place for recording the noise emitted by the airfoil. The mid-span plane is placed halfway along the length of the airfoil and separates the geometry into two halves. This symmetry enables capturing the noise on both the top and lower surfaces of the airfoil, providing a thorough understanding of the noise created by the airfoil and its distribution. In addition, acoustic signals were acquired at every time step, equivalent to a sample frequency of 20 kHz. This selection permits the detection of sound pressure levels up to a maximum frequency of 10 kHz, which is suited for the current analysis as it focuses on low-frequency noise analysis.

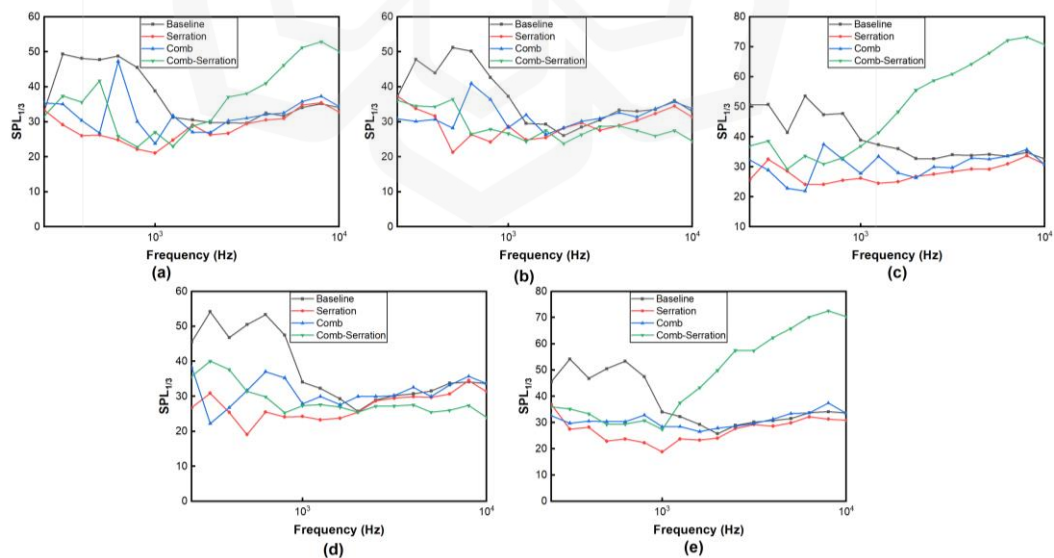


Figure 5.7 Sound pressure level as a function of frequency at the suction side (a)  $\alpha = 0^\circ$  (b)  $\alpha = 1^\circ$  (c)  $\alpha = -1^\circ$  (d)  $\alpha = 2^\circ$  and (e)  $\alpha = -2^\circ$ .



This study gives sound pressure level (SPL) as the primary measure employed to quantify and compare noise sources at different angles of attack ( $-2 \leq \alpha \leq 2$  deg). By calculating the Fast Fourier Transform (FFT) on the wall pressure signals at the four observer locations, the third-octave sound pressure level as a function of frequency is produced and depicted in Figure 5.7-5.9. The figures demonstrate how the SPL fluctuates with frequency, demonstrating which frequencies contribute more to the overall noise level. Based on Figure 5.7, the graph shows the noise level as a function of frequency for various trailing edge configurations of the airfoil. The trend of the noise level for the baseline configuration demonstrates that the noise level increases dramatically at lower frequencies and afterwards diminishes towards the higher frequencies. This pattern is consistent across all the angles of attack indicated on the graph. The fact that the noise level is more significant at lower frequencies shows that the noise source creates more low-frequency noise, consistent with prior research at low to moderate Reynolds numbers. When comparing the trend of the noise level for the serrated design to that of the baseline configuration, it can be observed that there is a drop in the noise level over the entire frequency range displayed on the graph. This decrease is more noticeable at frequencies below 1.6 kHz, where the decrease is roughly 21 dB, demonstrating that the serrated structure is more successful in suppressing low-frequency noise.

Similarly, the trend of the noise level for the comb design indicates a reduction of about 14 dB in the low-frequency noise level compared to the baseline configuration. However, the drop in serration configuration is less significant. Finally, the SPL frequency analysis for the comb-serration arrangement demonstrates a reduction in low-frequency noise levels and an increase in high-frequency noise levels in most situations. The comb-serration model demonstrates a substantial increase of approximately 17 dB in the high-frequency range for angles of attack at 0, -1, and -2 degrees. However, as compared to the baseline configuration, the comb-serration arrangement displays the best reduction in high-frequency noise levels at attack angles of 1 degree and 2 degrees, achieving a reduction of approximately 9 dB.

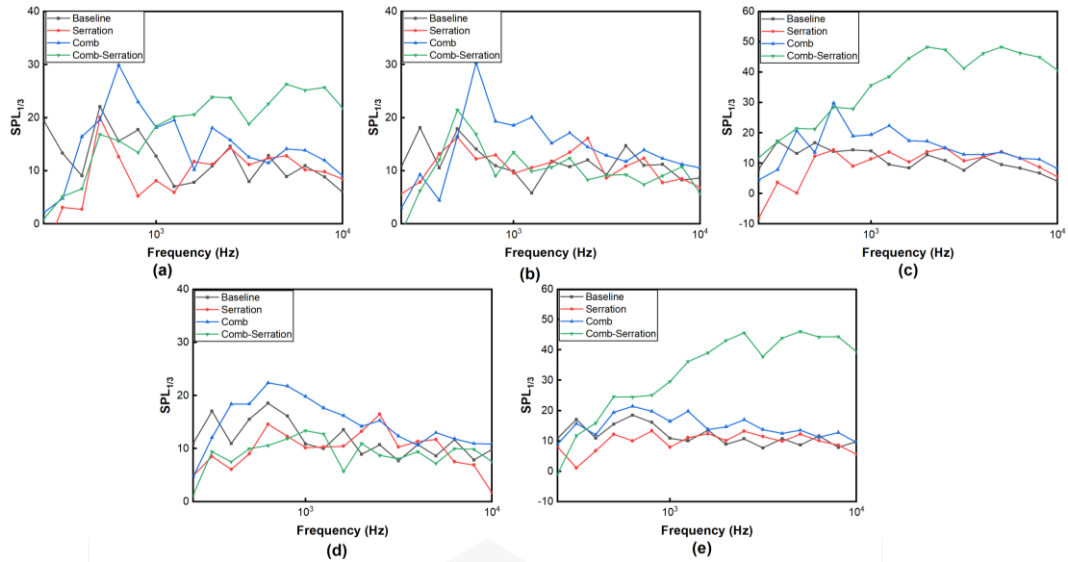


Figure 5.8 Sound pressure level as a function of frequency at the wake region (a)  $\alpha = 0^\circ$  (b)  $\alpha = 1^\circ$  (c)  $\alpha = -1^\circ$  (d)  $\alpha = 2^\circ$  and (e)  $\alpha = -2^\circ$ .

The graph in Figure 5.8 displays the sound pressure level as a function of frequency for various trailing edge designs of the airfoil in the wake region. Examining the sound pressure level trend for the baseline configuration suggests a slight rise in noise level at lower frequencies, followed by a slight drop at higher frequencies. This pattern is consistent across all angles of attack displayed on the graph, showing that the noise source emits both low and high-frequency noise. Upon inspection of the sound pressure level trend for the serrated design about the baseline configuration, it can be noticed that the noise levels are relatively consistent over the frequency range, except for a slight difference at the lower end of the frequency spectrum. This pattern illustrates that serration does have a significant impact on the acoustic level in the wake zone. The measurement of the sound pressure level trend for the comb design indicates a high noise level across most of the frequency range when compared to the baseline configuration. On the other hand, the SPL trend for the comb-serration design demonstrates an overall reduction in noise levels across the frequency range, notably at angles of attack of 1 and 2 degrees, when compared to the baseline configuration. Moreover, the comb-serration model demonstrates a substantial increase of approximately 17 dB in the high-frequency range for angles of attack at 0, -1, and -2 degrees.

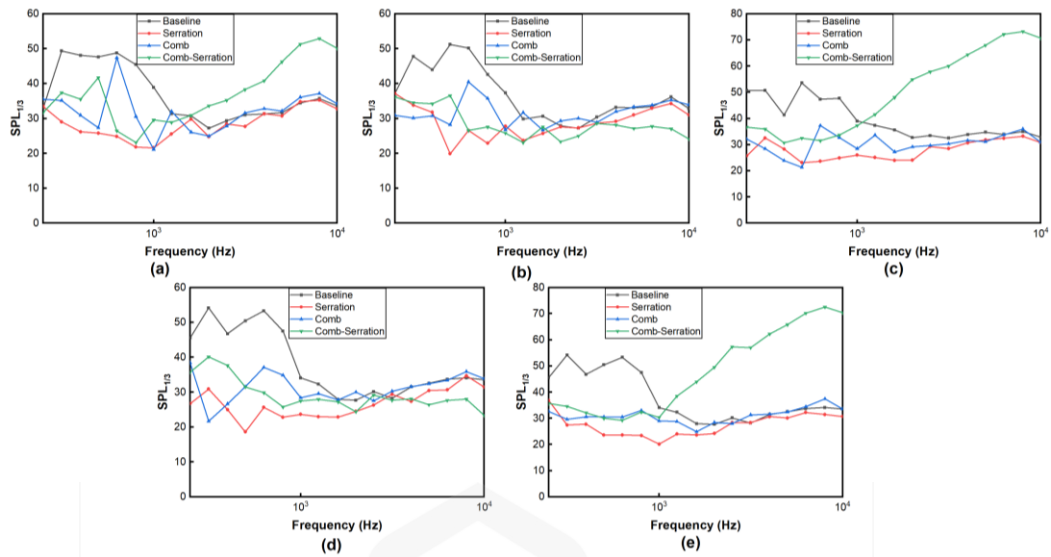


Figure 5.9 Sound pressure level as a function of frequency at the pressure side (a)  $\alpha = 0^\circ$  (b)  $\alpha = 1^\circ$  (c)  $\alpha = -1^\circ$  (d)  $\alpha = 2^\circ$  and (e)  $\alpha = -2^\circ$

The graph in Figure 5.9 illustrates the sound pressure level as a function of frequency for various trailing edge configurations of the airfoil. The trend of the noise level for the baseline design indicates that the noise level increases dramatically at lower frequencies and gradually drops as the frequency increases on the pressure side. This pattern is consistent across all the angles of attack displayed on the graph and implies that the noise source emits low-frequency noise. A similar pattern is seen on the suction side of the airfoil surface. When evaluating the trend of the noise level for the serration configuration compared to the baseline configuration on the pressure side, it can be noted that there is a drop in the noise level across the entire frequency range displayed on the graph. This decline is particularly noticeable at frequencies below 1.6 kHz, showing that the serrated arrangement is more efficient in decreasing low-frequency noise on the pressure side too. Similarly, the trend of the noise level for the comb configuration also reveals a reduction in low-frequency noise level compared to the baseline design on the pressure side; however, the drop is not as significant as that of the serration configuration. Finally, the study for the comb-serration design on the pressure side indicates a reduction in low-frequency noise levels; nevertheless, an increase in high-frequency noise levels is noted in most situations. Nevertheless, as

compared to the baseline configuration on the pressure side, the comb-serration design still displays an overall reduction in high-frequency noise levels at angles of attack of 1 degree and 2 degrees. This pattern shows that the comb-serration design successfully decreases noise levels on the pressure side in the low-frequency region while offering some amount of noise reduction in the high-frequency range for a specified range of angles of attack.

### **5.3.3. Peak Noise Level**

The peak noise level provides information on the highest sound intensity at a particular instant or location, whereas the average noise level offers a better representation of the total noise exposure over a prolonged period, often measured in decibels (dB). In the current research, these data are precious for determining the possible influence of various models on the suction, pressure, and wake region. The trend of the maximum sound pressure level as a function of the Angle of attack for different trailing edge designs of the airfoil is depicted in Figure 5.10. The baseline configuration displays a steady rise in SPL with increasing attack angle, reaching a peak at 2 degrees. This pattern indicates that as the Angle of attack increases, so does the degree of noise emitted by the airfoil surfaces. Notably, it is found that the noise level does not reflect symmetry about the aerodynamic characteristics when comparing negative and positive angles of attack, except for 2 degrees. When comparing the serration configuration to the baseline configuration, it can be noted that there is a rise in the peak SPL throughout the entire range of angles of attack given on the graph, except -2 to -1 degree. The greatest peak SPL of 39.6 dB is seen at around 1 degree, and a little drop is found at 2 degrees, demonstrating that the serrated trailing edge is more successful in suppressing noise levels.

Similarly, the pattern of the highest SPL for the comb arrangement shows a decline until 0 degrees and then a steady rise until 2 degrees, with a maximum peak SPL of around 53 dB. In contrast, the comb-serration design displays a drop in the maximum SPL as the Angle of attack increases, except -2 to -1 degree. The maximum peak SPL of 73 dB is observed at -1 degree. These findings indicate the noise reduction

capabilities of the comb-serration and serration configurations at different angles of attack.

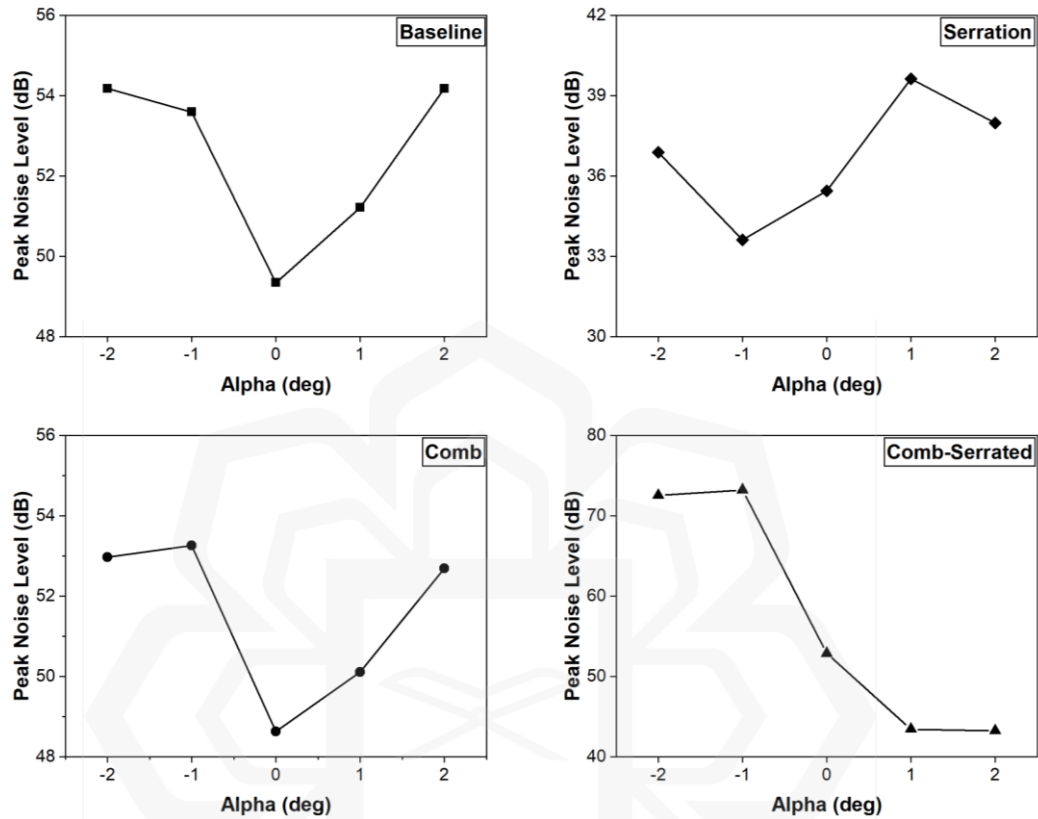


Figure 5.10 The influence of Angle of attack on the maximum noise level on the suction side of the airfoil.

The maximum sound pressure level graph (Figure 5.11) displays varied trailing edge designs in the wake zone. The baseline design demonstrates a variation in SPL, with a fall until -1 degree, an increase up to 0 degree, and then a decrease after that. This pattern implies that when the Angle of attack rises, the degree of noise created by the airfoil surfaces changes at the wake area. Additionally, it is found that the noise level does not display a clear symmetry pattern when comparing negative and positive angles of attack. However, the serrated trailing edge presents an overall rise in noise level until 0 degrees, followed by a drop. This trend suggests that the serrated trailing-edge is less successful in decreasing noise levels in the wake region when the Angle of attack is raised to 2 degrees. A comb structure displays an increase in SPL until -1 degree and

then a continuous rise until 1 degree, followed by a reduction. Lastly, the comb-serration reveals a similar trend to that found on the suction side, with a drop in peak noise level as the Angle of attack increases. Moreover, a serrated trailing edge indicates the possibility of lowering noise level at a low Angle of attack. However, a comb-serrated trailing edge illustrates its potential at a high Angle of attack.

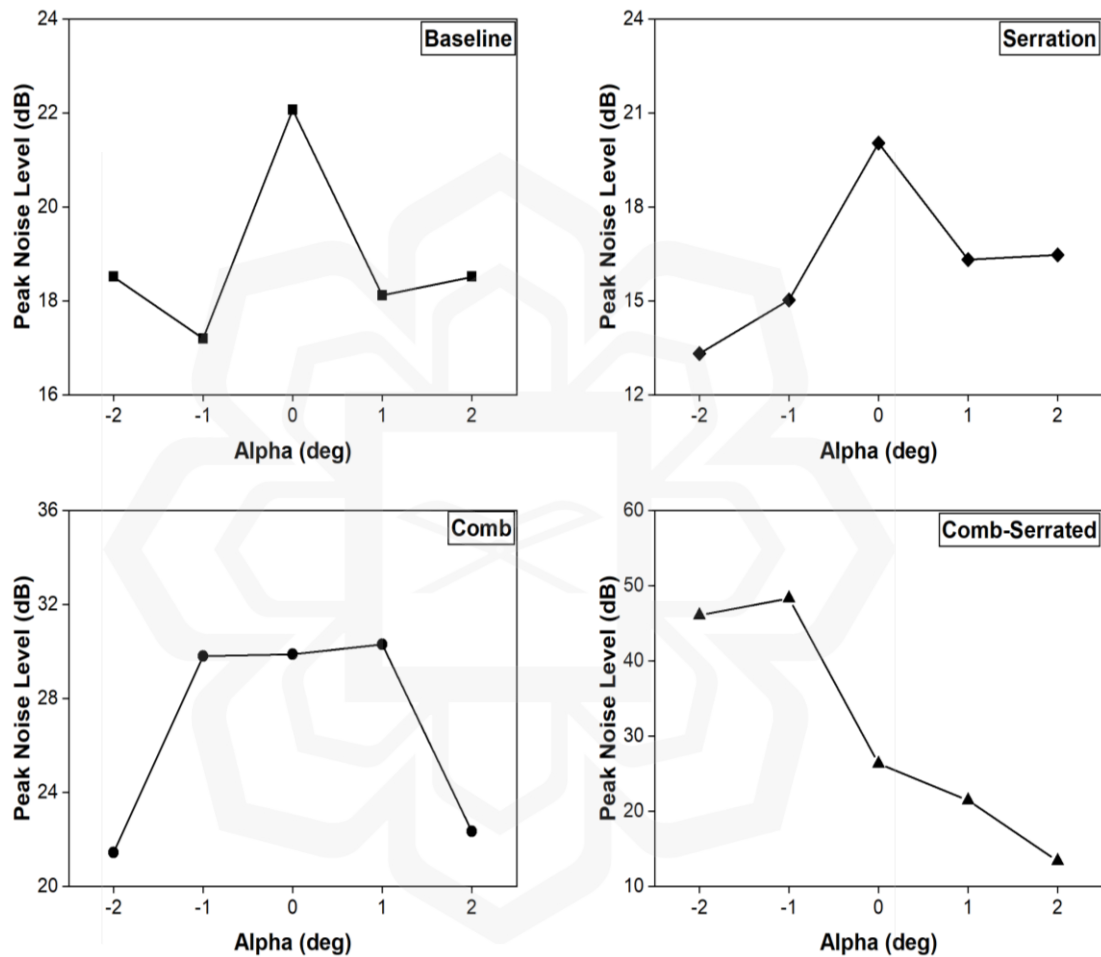


Figure 5.11 The influence of Angle of attack at the wake region of the airfoil.

Figure 5.12 shows the peak sound pressure level fluctuation in proportion to the Angle of attack for various trailing edge designs. Can be seen that the baseline configuration demonstrates a gradual increase in the peak level as the Angle of attack is increased from 0 degrees to 2 degrees, indicating that the noise level generated by the airfoil surfaces increases as the Angle of attack increases, consistent with the trend

observed on the suction side. Additionally, symmetry is exhibited only at 2 degrees, and the noise level does not demonstrate symmetry about the aerodynamic parameters when comparing negative and positive angles of attack. The serration structure similarly demonstrates an increase in the peak noise level throughout most of the angles of attack indicated in the graph, with the highest peak noise level seen at 1 degree. A similar trend is apparent for the comb trailing edge, with a drop in the noise level until 0 degrees and a progressive increase until 2 degrees, with a maximum peak SPL of roughly 53 dB when measured at the pressure side. Moreover, the comb-serration design similarly showed a decline in the most significant noise level as the Angle of attack increases, with the highest peak noise level of 73 dB measured at a -1 degree angle. Overall, these results also demonstrate the possibility for noise reduction when utilizing comb-serration and serration geometries at varied angles of attack.

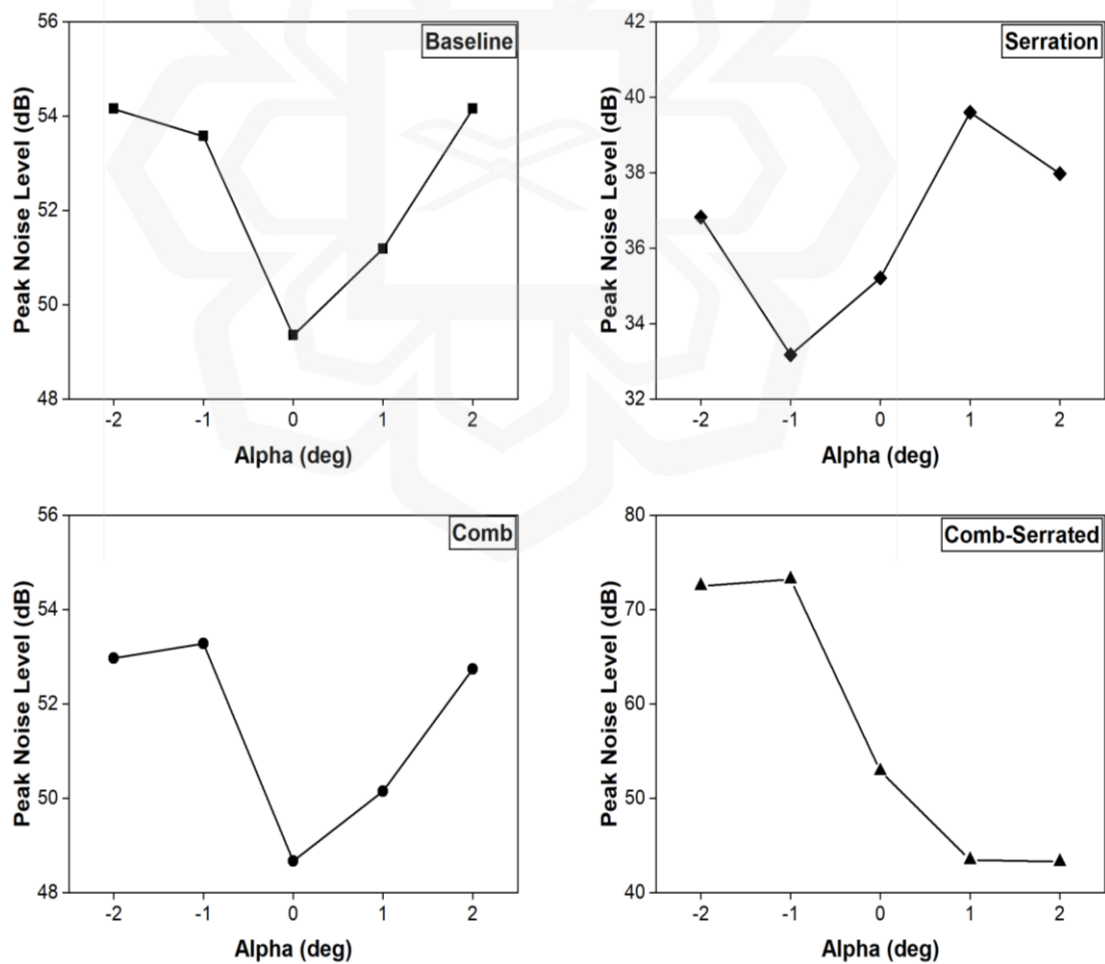


Figure 5.12 The influence of Angle of attack on the maximum noise level recorded on the pressure side of the airfoil.

#### 5.3.4. Peak Frequency

The peak frequency of a sound signal is defined as the frequency at which the sound pressure level or acoustic energy density is greatest. Several things impact it, including the acoustic measuring location's geometry, the sound wave's spectrum composition, and the measurement equipment. Researchers can identify an aerodynamic system's dominant sound-producing mechanism or flow characteristic of by evaluating the peak frequency. In the case of airfoil noise, for example, the peak frequency is associated with the unsteady flow characteristics around the airfoil. Understanding the connection between the peak frequency and the underlying flow characteristics allows researchers to devise ways for mitigating or controlling sound emissions and improving the system's overall acoustic performance. The graph in Figure 5.13 depicts the trend of the peak frequency as a function of the Angle of attack for various trailing edge configurations of the airfoil on the suction side. The baseline design demonstrates a variation in peak frequency as the Angle of attack increases, with an initial increase from -2 degrees to -1 degrees, followed by a reduction up to 0 degrees, an increase up to 1 degree, and then a decrease again. This pattern implies that when the Angle of attack increases, the peak frequency of the noise created by the airfoil surfaces goes to higher frequencies and then returns to lower frequencies.

Furthermore, it is noticed that the peak frequency displays asymmetric behaviour in respect to the aerodynamic parameters when comparing negative and positive angles of attack, unlike the peak noise level plot. When evaluating the trend of the peak frequency for the serration configuration in comparison to the baseline configuration, it can be noted that there is an increase in the peak frequency from -2 degrees to 0 degrees, followed by a reduction after that. This trend illustrates that the serrated trailing edge moves the main frequency towards lower frequencies as the Angle of attack rises to 2 degrees and has minimal influence on the peak frequency between 1 degree and 2 degrees. The trend of the peak frequency for the comb design exhibits slight fluctuation as the Angle of attack increases, showing that it has little influence on



shifting the main frequency. Finally, the peak frequency analysis for the comb-serration arrangement reveals a similar pattern at low angles of attack and a reduction in peak frequency at high angles of attack. This pattern suggests that the comb-serration design successfully shifts the peak frequency to lower frequencies at high angles of attack and has minimal effect at low angles of attack.

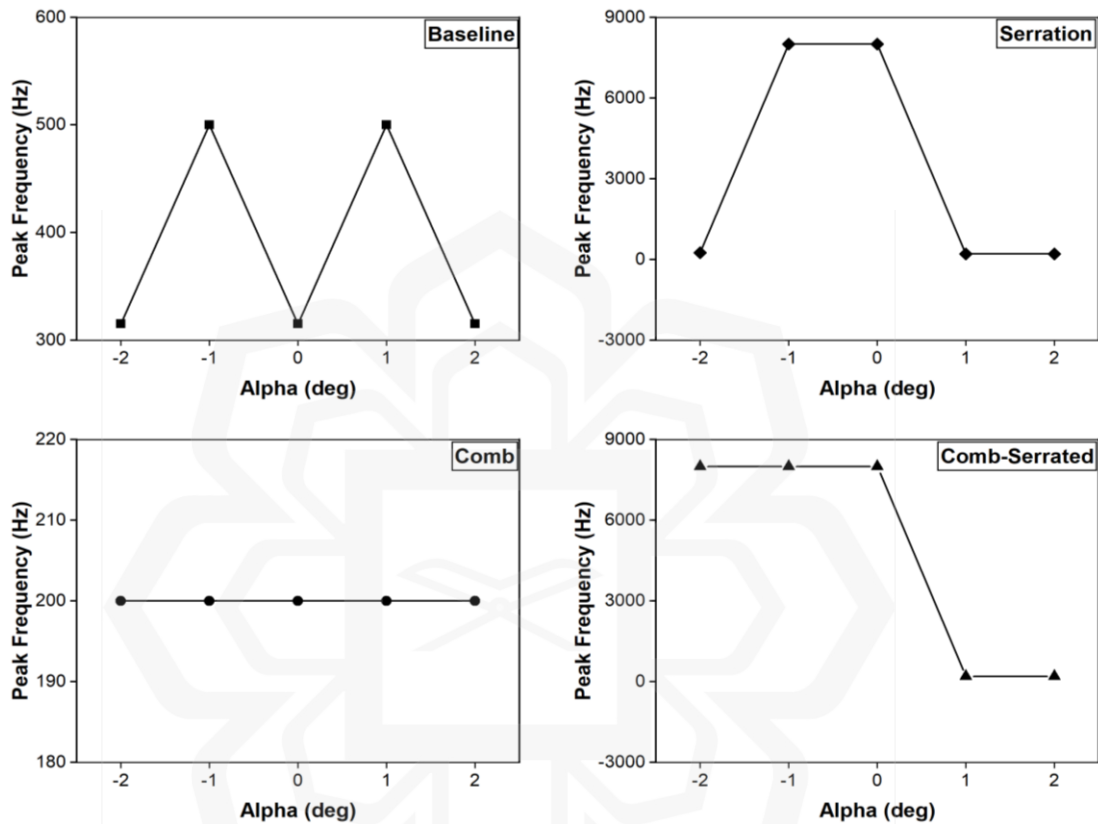
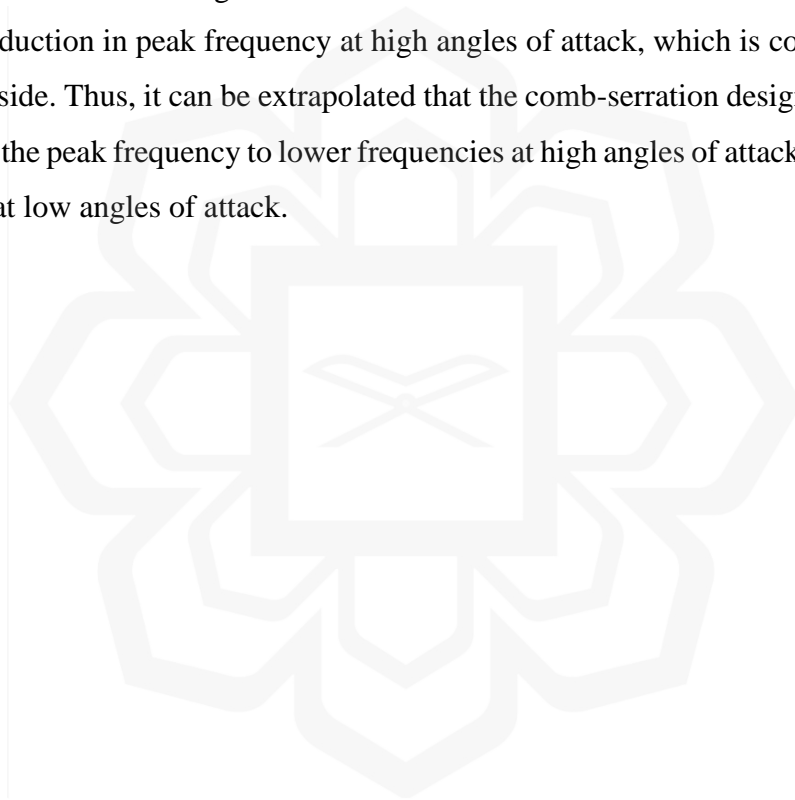


Figure 5.13 The frequency of the highest noise level on the suction side for various angles of attack.

The study of the peak frequency as a function of the Angle of attack for various trailing edge configurations of the airfoil in the wake area is provided in Figure 5.14. The baseline setup demonstrates a variation in the peak frequency when the Angle of attack is varied, described by an initial drop from -2 degrees to -1 degrees, followed by an increase up to 0 degrees, a decrease up to 1 degree, and then an increase again. This pattern implies that when the Angle of attack increases, the peak frequency of the noise created by the airfoil surfaces falls to lower frequencies and then returns to higher frequencies. Furthermore, it is also seen that the peak frequency displays asymmetric

behaviour to the aerodynamic parameters when comparing negative and positive angles of attack, unlike the peak noise level plot. Regarding the serration arrangement, it can be noted that there is a rise in the peak frequency from -2 to -1 degree, followed by a reduction up to 0 degree and then an increase after that. This trend indicates that the serrated trailing edge shifts the main frequency towards higher frequencies as the Angle of attack increases from 0 to 2 degrees, with no influence on the peak frequency between 0 degrees and 1 degrees. Like the suction side, the trend of the peak frequency for the comb design displays slight fluctuation when the Angle of attack increases, showing that it has little influence on shifting the main frequency. The peak frequency study for the comb-serration arrangement likewise reveals a stable trend at low angles of attack and a reduction in peak frequency at high angles of attack, which is consistent with the suction side. Thus, it can be extrapolated that the comb-serration design is successful in shifting the peak frequency to lower frequencies at high angles of attack but has minimal impact at low angles of attack.



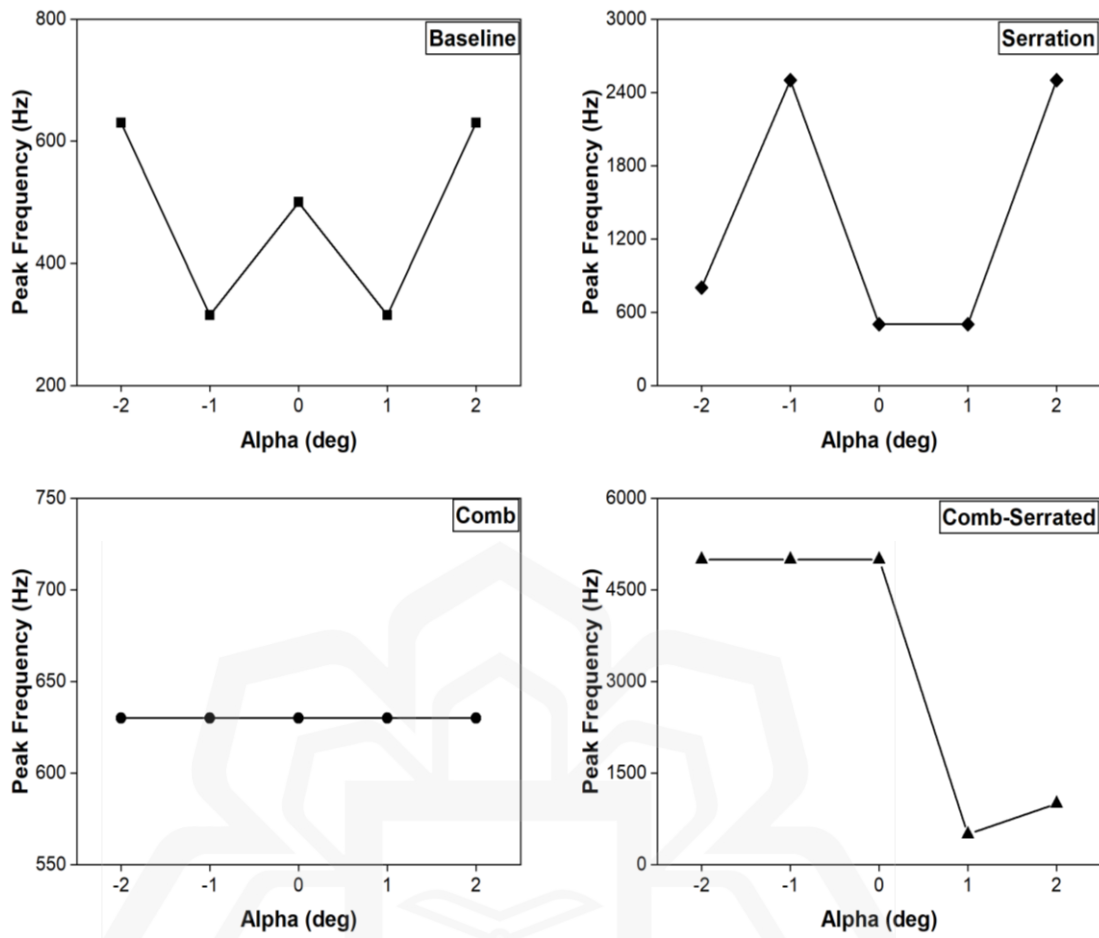


Figure 5.14 The frequency of the highest noise level at the wake region for various angles of attack.

The graph in Figure 5.15 demonstrates the trend of the peak frequency as a function of the Angle of attack for various trailing edge configurations of the airfoil on the pressure side. The trends in this graph are comparable with those reported on the suction side, where similar oscillations in peak frequency are exhibited. The baseline arrangement illustrates that when the Angle of attack increases, the peak frequency of the noise created by the airfoil surfaces goes to higher frequencies and then returns to a lower frequency. It is also noted that the peak frequency displays a symmetric pattern. Similarly, the serrated trailing-edge also indicated the shift of the main frequency towards lower frequencies when the Angle of attack is raised until 2 degrees and no influence on the peak frequency between 1 degree and 2 degrees. Moreover, the comb configuration shows little variability when the Angle of attack varies, indicating that it has little influence on the shifting of the main frequency. Lastly, the comb-serration

design also confirmed its effectiveness in shifting the primary frequency to a lower frequency at high angles of attack and having less effect at low angles of attack. This pattern illustrates the uniformity of the results and the effectiveness of the combination arrangement in decreasing noise levels on the pressure side and suction side.

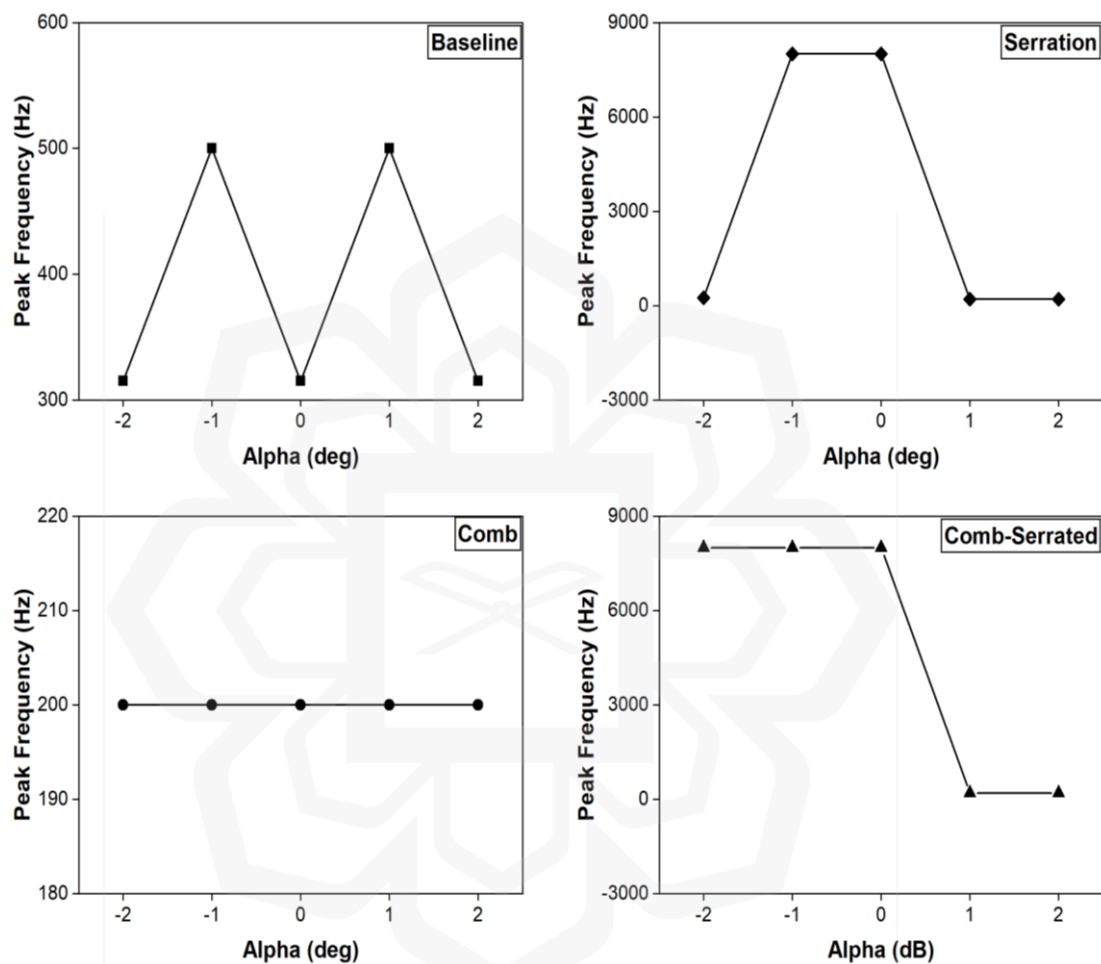


Figure 5.15 The frequency of the highest noise level on the pressure side for various angles of attack.

### 5.3.5. Directivity Pattern

The directivity pattern of an acoustic source defines the directionality of the radiated sound field emitting from the acoustic source. In addition, it also elaborates on the direction with the highest radiated sound pressure, which assists in pointing out the area

of concern. The noise directivity pattern at different angles of attack is often represented by a polar plot, such as that shown in Figure 5.16. From the graph, it can be noted that the directivity pattern of the source is highly directional, with the maximum overall sound level in the direction of 90 degrees and 270 degrees and a minimum level in the direction of 0 degrees and 180 degrees. This pattern is consistent across all models, showing that most of the source's acoustic energy is being emitted in the direction of 90 degrees and 270 degrees and comparatively less energy in the direction of 0 degrees and 180 degrees. This trend also confirms the necessity of monitoring the noise level on the suction and pressure sides of the airfoil surfaces.

Additionally, the directivity pattern reveals a relatively symmetric structure, with a comparable sound pressure level in the directions of 90 and 270 degrees, suggesting that the source is producing energy in a relatively consistent manner in those directions. However, the effect of angles of attack is inconsistent across different configurations. For the baseline, the figure indicates a considerable rise in the noise level when the Angle of attack is raised from 0 to 2 degrees in the region below the airfoil surface. On the suction side, an increase is noted exclusively from 0 to 1 degree with an almost comparable noise level at 2 degrees. On the other hand, upstream and downstream sides exhibit a consistent level of noise across the angles of attack, with a little increase in the upstream direction at 2 deg. The overall noise level rose by roughly 6 dB and 5 dB as the Angle of attack increased from 0 to 1 degree for the suction and pressure sides, respectively. However, a difference of roughly 9 dB and 19 dB is detected as the Angle of attack increases to 2 degrees. The serrated trailing-edge resulted in a greater noise level as the Angle of attack increased from 0 to 2 degrees on the suction and pressure sides; however, a drop in the noise level was seen in the upstream and downstream directions.

Furthermore, the comb model predicts a decrease in the overall noise level as the Angle of attack is increased to 1 degree, followed by an increase when the Angle of attack is increased to 2 degrees on the suction and pressure sides. Both the wake region and upstream side resulted in noise reduction throughout the angles of attack. Nonetheless, the comb-serrated design dramatically dropped the total noise level as the attack angle rose to 2 degrees. Notably, the complete structure of the noise pattern is not

reflected as we employed only four observer positions, but significantly more spots around the airfoil surface are necessary.

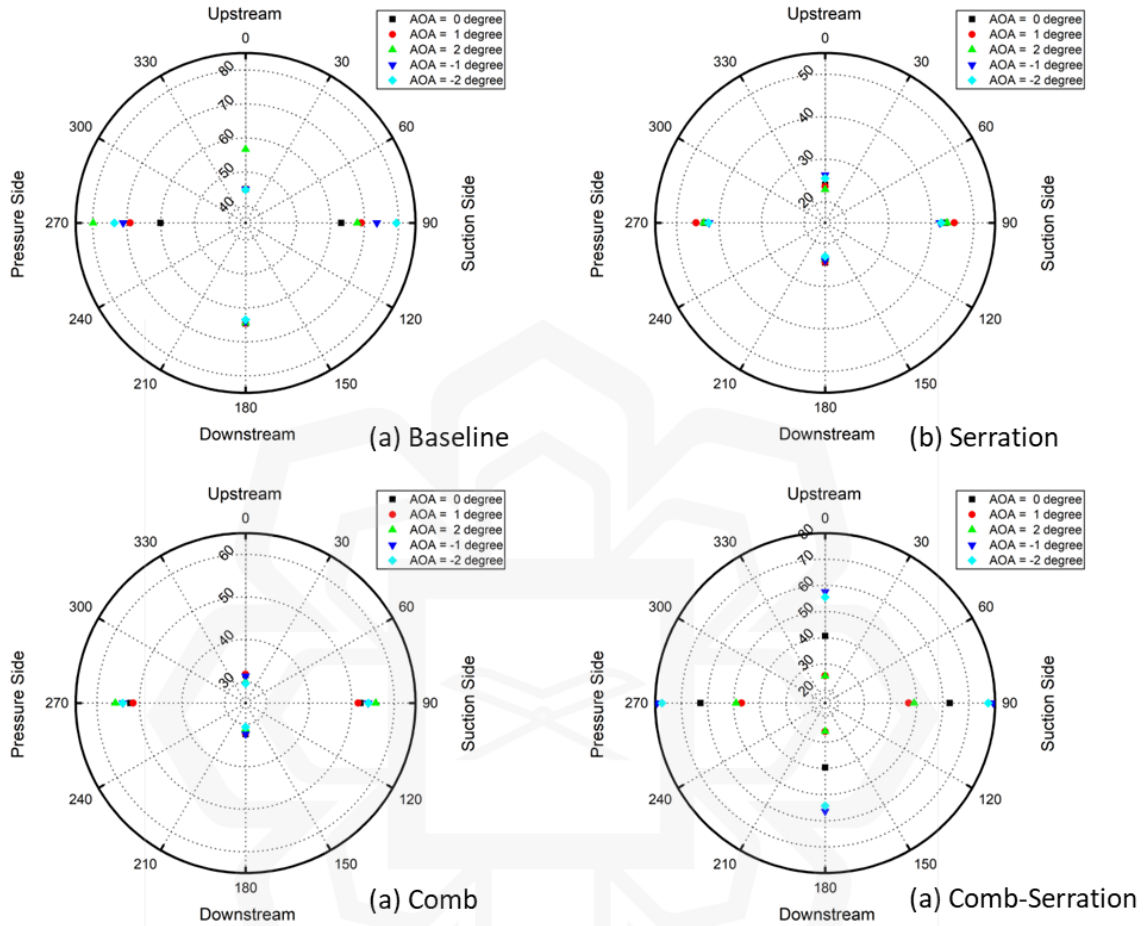


Figure 5.16 The directivity of the acoustic signals measured at a radial distance of 12 chords from the airfoil center.

## 5.4. SUMMARY

In conclusion, the current research aims to predict radiated noise around a NACA0015 airfoil using large-eddy simulation and the Ffowcs-Williams and Hawkings model. The results of the study showed that:

1. The numerical model effectively captures the fluctuations of the lift coefficient, and the comparison with experimental data showed that the lift coefficient pattern is accurate at all angles of attack.

2. The results of the normalized sound pressure are quite comparable with the other study and fluctuation, and average values are consistent.
3. The serrated trailing edge enhances the amplitude of the surface pressure fluctuation and generates a more complicated pressure distribution. The comb-serration design is beneficial in lowering the magnitude of pressure fluctuation.
4. The Angle of attack significantly influences the peak frequency, with the comb design showing a stable value across all the angles of attack. The sound pressure level increases as Angle of attack increases, except for comb-serrated, which reduces considerably.
5. The directivity pattern showed that the maximum noise level radiates at an azimuth angle of around 90 degrees, implying that most of the acoustic energy is emitted on the suction and pressure sides of the airfoil.
6. The results suggest that serration and comb-serration can reduce noise levels at high angles of attack, particularly low-frequency noise for the serration model and high-frequency noise for the comb-serrated model.
7. The analysis shows that knowing the flow behavior is crucial in accurately predicting the acoustic signals.

In conclusion, this study provides insights into the relationship between airfoil design and radiated noise, offering valuable information for the design of low-noise airfoils.

## CHAPTER SIX

### CONCLUSION AND RECOMMENDATIONS

The present research strives to provide an understanding of the tonal noise process and related physical phenomena by conducting wind tunnel tests and CFD simulations. As a result of the limited understanding of the efficiency of trailing-edge fringes, this research effectively elaborates how these models improve the flow structure and noise performance at relatively moderate Reynolds number ( $1.7 \times 10^5$ ) and varying angles of attack ( $-2^\circ \leq \alpha \leq 2^\circ$ ). Furthermore, the combined effects of serrated and comb designs are thoroughly explored and effectively presented via the comb-serration configuration. The selection of the NACA 0015 airfoil facilitates a broader understanding of discrete tonal behaviour across different profiles. Additionally, the intricate features of the laminar separation bubble are elaborated upon, including its influence on airfoil tonal emissions and flow structures. Consequently, we pursued the following research objectives to tackle these issues and push the boundaries of knowledge within our field.

#### 6.1. OBJECTIVE 1 – CONCLUSION 1

A 2D numerical analysis of the flow characteristics of the NACA0015 airfoil was conducted using the shear-stress transport (SST)  $\gamma$ - $Re\theta$  model. The analysis focused on low Reynolds numbers ( $8.4 \times 10^4$  and  $1.7 \times 10^5$ ) and angles of attack ( $0^\circ \leq \alpha \leq 3^\circ$ ). The results showed the presence of long LSB on the suction side of the airfoil at both Re, except at  $\alpha = 0^\circ$ . The LSB affected both the pressure and skin friction distributions of the airfoil. Subsequently, two types of flow were observed, namely, LSB with reattachment and LSB without reattachment and in general, demonstrated that increasing Reynolds number and Angle of attack caused notable shifts in the flow characteristics, resulting in changes to the laminar separation bubble and the onset of flow instability at higher angles of attack.



The 3D simulation results shows a symmetrical distribution of pressure along the surface, with maximum pressure detected at the leading edge due to flow slowing down on a NACA0015 airfoil at zero Angle of attack. The skin friction coefficient graph reaffirms the absence of a separation zone on the airfoil surface, except at the tip of the trailing edge. Moreover, the velocity profiles of the baseline airfoil at zero Angle of attack do not show any signs of flow separation.

The findings of the experimental investigation indicate that the performance of a baseline airfoil is significantly affected by the Angle of attack. However, as the Angle of attack increases, the flow over the airfoil becomes increasingly disturbed, causing variations in the x-velocity contour. The flow separates from the surface of the airfoil, forming a laminar separation bubble that moves upstream and reaches approximately 0.3c at an Angle of attack of 10 degrees. Furthermore, the flow experiences a breakdown, leading to the fast shedding of vortices downstream. Although the vortices are not visible due to the high downstream flow, the results suggest that at high angles of attack, the flow over the baseline airfoil becomes highly nonlinear and unstable. Therefore, understanding the behavior of spanwise vorticity is essential in analyzing airfoil performance at various angles of attack.

## **6.2. OBJECTIVE 2 – CONCLUSION 2**

The current study has been analyzed by large eddy simulation around a NACA0015 airfoil, with the prediction of radiated noise performed using Ffowcs-Williams and Hawkings model. The numerical model was compared with a published study to assess its effectiveness in capturing the fluctuations of the lift coefficient. Similarly, to check the accuracy of the predicted results of the normalized sound pressure, points located upstream and above the airfoil surface are examined, and it appears that the fluctuation, as well as the average values, are quite comparable, thereby verifying the accuracy of the pressure measurements on both sides of the flow. The results also displayed an irregular broadband spectrum with a centered frequency of about 300 – 600 Hz for all cases. On the suction and pressure side, a slight increase in the value of the centered frequency is also seen as the Angle of attack increases. It also appears that the Angle of

attack can significantly affect the noise peak frequency, as it gradually shifts towards a higher frequency and then back to a lower frequency.

The noise level rises by 2 dB and 4.7 dB on the suction and pressure side, respectively. On the other hand, the directivity pattern showed that the maximum noise level predominantly radiates at an azimuth angle of around 90 degrees for all cases, except at 2 degrees, which is dominated by a radiation angle close to 270 degrees. This observation suggests that the broadband noise is highly dependent on the Angle of attack, not only on noise level but also the directivity pattern. This study provides valuable information for developing noise reduction strategies for airfoils.

### **6.3. OBJECTIVE 3 – CONCLUSION 3**

A detailed analysis of the results was undertaken by numerical and experimental approaches to fully understand the results. The numerical model was validated by its accuracy in capturing the aerodynamic parameters and flow structure, as proven by its prediction of lift fluctuations, mean lift coefficient, and flow structure. The outcomes of the 3D research reveal that the serrated, combed, and comb-serrated airfoil designs have a distinct impact on fluid flow. The serrated trailing edge creates higher fluid velocity and pressure drop, while the combed trailing edge induces separation at the root and the comb-serrated design maintains a continuous fluid flow over the airfoil's surface.

From the experimental investigations, the pressure coefficient and skin friction coefficient graphs reveal that all modifications result in an early negative pressure zone and an uneven flow with greater skin friction values near the trailing edge, relative to the baseline wing. This pattern can be ascribed to the interaction between the flow and the redesigned trailing edges, which causes turbulence and boosts the fluid's momentum delivered to the wing's surface. The x-velocity contour and spanwise vorticity analysis results demonstrate that the serrated, combed, and comb-serrated airfoil models have more stable flow patterns and fewer separation bubbles than the baseline airfoil. This trend shows the capability of these models to delay separation, subsequently, reducing the tonal noise generated. The poro-serrated airfoil has a distorted flow pattern and an upstream-moving laminar separation bubble. This observation indicates that poro-

serrated will likely increase the tonal noise as the LSB amplifies the instabilities near the trailing edges.

#### **6.4. OBJECTIVE 4 – CONCLUSION 4**

The noise levels for the baseline are seen higher at lower frequencies, suggesting that the source emits low-frequency noise. However, the Serrated trailing edge model indicated a drop in the noise level over the whole frequency range and was more noticeable at lower frequencies below 1.6 kHz, where the decrease is roughly 21 dB, showing that this design is more successful in decreasing low-frequency noise. Additionally, the combed trailing edge slightly reduced the noise level at low frequencies. Contrarily, the comb-serration model demonstrates a substantial increase of approximately 17 dB in the high-frequency range for angles of attack at 0, -1, and -2 degrees. However, as compared to the baseline configuration, the comb-serration arrangement displays the best reduction in high-frequency noise levels at attack angles of 1 degree and 2 degrees, achieving a reduction of approximately 9 dB. This study implies that serration and comb-serration are key in reducing noise at high angles of attack. On the other hand, the directivity pattern showed that the maximum noise level is observed to predominantly radiate at an azimuth angle of around 90 degrees for all the cases, ranging from 90 to 270 degrees, indicating that the majority of the source's acoustic energy is being emitted on the suction and pressure sides of the wing. These findings imply that broadband noise is highly dependent on the Angle of attack, not only on noise level but also on the directivity pattern.

In conclusion, this study highlights the importance of understanding the flow behavior in effectively predicting acoustic signals. The findings demonstrate that serrated and comb-serrated designs are beneficial in reducing noise levels, particularly at high angles of attack, and that the Angle of attack can significantly impact both the noise level and directivity pattern.

#### **6.5. RECOMMENDATIONS FOR FURTHER STUDIES**

The field of flow structure and aeroacoustics in relation to airfoil applications, including buildings, fans, turbines, and unmanned aerial vehicles (UAVs), remains a vast area for further research. Future research topics in this area can include:

1. Study of the effect of different surface roughness and geometries on the flow structure and aeroacoustics.
2. Exploration of the impact of various flow conditions, such as turbulence and subsonic/supersonic regimes, on the flow structure and aeroacoustics.
3. Investigation into the use of active flow control techniques for reducing noise and improving aerodynamic performance.
4. Development of advanced computational models and simulations for predicting flow structure and aeroacoustics.
5. Study of the interaction between flow structure and structural acoustics in airfoils.
6. Investigation into the use of materials and coatings for reducing noise and improving aerodynamics.
7. Study of the interplay between airfoil design and the environment, including temperature, pressure, and atmospheric composition.
8. Further exploration of the impact of flow separation and reattachment on flow structure and aeroacoustics.

## REFERENCES

- Alan Hersh, B. S., & Hayden, R. E. (1971). Aerodynamic sound radiation from lifting surfaces with and without leading-edge serrations.
- Aldheeb, M., Asrar, W., Sulaeman, E., & Omar, A. A. (2018). Aerodynamics of porous airfoils and wings. *Acta Mechanica*, 229(9), 3915–3933.
- Amiet, R. K. (1976). Noise due to turbulent flow past a trailing edge. *Journal of Sound and Vibration* (Vol. 47).
- Andan, A. D., & Lee, D.-J. (2019). Discrete Tonal Noise of NACA0015 Airfoil at Low Reynolds Number. *Journal of Advanced Research in Fluid Mechanics and Thermal Sciences Journal Homepage*, 53, 129–145.
- ANSYS. (2013). ANSYS Fluent Theory Guide. ANSYS Inc.
- Arbey, H., & Bataille, J. (1983). Noise generated by airfoil profiles placed in a uniform laminar flow. *J. Fluid Mech* (Vol. 134).
- Arce León, C., Merino-Martínez, R., Ragni, D., Avallone, F., & Snellen, M. (2016a). Boundary layer characterization and acoustic measurements of flow-aligned trailing edge serrations. *Experiments in Fluids*, 57(12).
- Arce León, C., Merino-Martínez, R., Ragni, D., Avallone, F., & Snellen, M. (2016b). Boundary layer characterization and acoustic measurements of flow-aligned trailing edge serrations. *Experiments in Fluids*, 57(12).
- Arcondoulis, E., Arcondoulis, E. J. G., Doolan, C. J., & Zander, A. C. (2005). Airfoil noise measurements at various angles of attack and low Reynolds number. *Proceedings of Acoustics 2009*.
- Atzori, M., Gatti, D., Atzori, M., Vinuesa, R., Schlatter, P., Gatti, D., Frohnäpfel, B. (2019). Effects of Uniform Blowing and Suction on Turbulent Wing Boundary Layers.
- Avallone, F., Pröbsting, S., & Ragni, D. (2016). Three-dimensional flow field over a trailing-edge serration and implications on broadband noise. *Physics of Fluids*, 28(11).
- Avallone, F., van der Velden, W. C. P., & Ragni, D. (2017a). Benefits of curved serrations on broadband trailing-edge noise reduction. *Journal of Sound and Vibration*, 400, 167–177.

- Avallone, F., van der Velden, W. C. P., & Ragni, D. (2017b). Benefits of curved serrations on broadband trailing-edge noise reduction. *Journal of Sound and Vibration*, 400, 167–177.
- Avallone, F., van der Velden, W. C. P., Ragni, D., & Casalino, D. (2018). Noise reduction mechanisms of sawtooth and combed-sawtooth trailing-edge serrations. *Journal of Fluid Mechanics*, 848, 560–591.
- B. H. Carmichael. (1981). *Low Reynolds number airfoil survey volume I*.
- Bae, Y., & Moon, Y. J. (2011). Effect of passive porous surface on the trailing-edge noise. *Physics of Fluids*, 23(12).
- Barone, M. F. (2011). Survey of Techniques for Reduction of Wind Turbine Blade Trailing Edge Noise.
- Bernardos, L., Richez, F., & Gleize, V. (2019). Rans modeling of laminar separation bubbles around airfoils at low Reynolds number conditions. In *AIAA Aviation 2019 Forum*. American Institute of Aeronautics and Astronautics Inc, AIAA.
- Bernicke, P., Akkermans, R. A. D., Ananthan, V. B., Ewert, R., Dierke, J., & Rossian, L. (2019). A zonal noise prediction method for trailing-edge noise with a porous model. *International Journal of Heat and Fluid Flow*, 80.
- Borgmann, D., Hosseinverdi, S., Little, J., & Fasel, H. (2021). Investigation of Laminar Separation Bubbles Using Experiments, Theory and DNS. In *AIAA Aviation and Aeronautics Forum and Exposition, AIAA AVIATION Forum 2021*. American Institute of Aeronautics and Astronautics Inc, AIAA.
- Brooks, T F, & Hodgson, T. H. (1981). Trailing edge noise Prediction from measured surface pressure. *Journal of Sound and Vibration* (Vol. 78).
- Brooks, Thomas F, Stuart, D., & Marcolini, M. A. (1989). Airfoil Self-Noise and Prediction.
- Casalino, D., Grande, E., Romani, G., Ragni, D., & Avallone, F. (2021). Towards the definition of a benchmark for low Reynolds number propeller aeroacoustics. In *Journal of Physics: Conference Series* (Vol. 1909). IOP Publishing Ltd.
- Celik, A., Bowen, J. L., & Azarpeyvand, M. (2020). Effect of trailing-edge bevel on the aeroacoustics of a flat-plate. *Physics of Fluids*, 32(10).
- Chaitanya, P., Joseph, P., Narayanan, S., & Kim, J. W. (2018). Aerofoil broadband noise reductions through double-wavelength leading-edge serrations: A new control concept. *Journal of Fluid Mechanics*, 855, 131–151.
- Chase, D. M. (1975). Noise radiated from an edge in turbulent flow. *AIAA Journal*, 13(8), 1041–1047.

- Chen, L., Guo, Z., Deng, X., & Hou, Z. (2020). Aerodynamic performance and transition prediction of low-speed fixed-wing unmanned aerial vehicles in full configuration based on improved  $\gamma$ - $\text{Re}\theta$  model. *Aerospace Science and Technology*, 107.
- Chong, T. P., Joseph, P. F., & Gruber, M. (2013). Airfoil self-noise reduction by non-flat plate type trailing edge serrations. *Applied Acoustics*, 74(4), 607–613.
- Chong, Tze Pei, & Dubois, E. (2016). Optimization of the poro-serrated trailing edges for airfoil broadband noise reduction. *The Journal of the Acoustical Society of America*, 140(2), 1361–1373.
- Chong, Tze Pei, & Joseph, P. F. (2013). An experimental study of airfoil instability tonal noise with trailing edge serrations. *Journal of Sound and Vibration*, 332(24), 6335–6358.
- Chong, Tze Pei, & Vathylakis, A. (2015). On the aeroacoustic and flow structures developed on a flat plate with a serrated sawtooth trailing edge. *Journal of Sound and Vibration*, 354, 65–90.
- Counsil, J. N. N., & Boulama, K. G. (2013). Low-Reynolds-number aerodynamic performances of the NACA 0012 and Selig-Donovan 7003 airfoils. *Journal of Aircraft*, 50(1), 204–216.
- Counsil, J. N. N., & Goni Boulama, K. (2011). Validation of a Low-Cost Transitional Turbulence Model for Low-Reynolds-Number External Aerodynamics. *American Institute of Aeronautics and Astronautics*.
- Crivellini, A., D'Alessandro, V., di Benedetto, D., Montelpare, S., & Ricci, R. (2014). Study of laminar separation bubble on low Reynolds number operating airfoils: RANS modelling by means of an high-accuracy solver and experimental verification. In *Journal of Physics: Conference Series* (Vol. 501). Institute of Physics Publishing.
- D. L. Smith, R. P. Paxson, 1/Lt, R. D. Talmadge, & E. R. Notz. (1970). Measurements of the radiated noise from sailplanes.
- Derksen, R. W., Agelinchaab, M., & Tachie, M. (2008). Characteristics of the flow over a NACA 0012 airfoil at low Reynolds numbers. In *WIT Transactions on Engineering Sciences* (Vol. 59, pp. 143–152).
- Desquesnes, G., Terracol, M., & Sagaut, P. (2007). Numerical investigation of the tone noise mechanism over laminar airfoils. *Journal of Fluid Mechanics*, 591, 155–182.
- E. Malkiel, & R. E. Mayle. (1996). Transition in a Separation Bubble. *Turbomachinery*.
- Eastman N. Jacobs and Albert Sherman. (1939). Airfoil Section Characteristics as Affected by Variations of the Reynolds Number.

- ElJack, E. (2017). High-fidelity numerical simulation of the flow field around a NACA-0012 aerofoil from the laminar separation bubble to a full stall. *International Journal of Computational Fluid Dynamics*, 31(4–5), 230–245.
- Faridul Alam, M., Keith Walters, D., & Thompson, D. S. (2011). Simulations of Separated Flow around an Airfoil with Ice Shape using Hybrid RANS/LES Models Nomenclature.
- Ffowcs Williams, J. E., & Hawkings, D. L. (1969). Sound Generation by Turbulence and Surfaces in Arbitrary Motion. *Source: Philosophical Transactions of the Royal Society of London. Series A, Mathematical and Physical Sciences* (Vol. 264).
- Fink, M. R. (1975). Prediction of airfoil tone frequencies. *Journal of Aircraft*, 12(2), 118–120.
- Frink, N. T., Bonhaus, D. L., Vatsa, V. N., Bauer, S. X. S., & Tinetti, A. F. (2003). Boundary condition for simulation of flow over porous surfaces. *Journal of Aircraft*, 40(4), 692–698.
- Fujii, K. (2005). Progress and future prospects of CFD in aerospace - Wind tunnel and beyond. *Progress in Aerospace Sciences*. Elsevier Ltd.
- Galbraith, M. C., & Visbal, M. R. (2010). Computational Sciences Branch, Aeronautical Sciences Division.
- Gaster, M. (1963). On the stability of parallel flows and the behaviour of separation bubbles. University of London, Queen Mary.
- Gaster, M. (1969). Vortex shedding from slender cones at low Reynolds numbers. *J. Fluid Mech* (Vol. 38).
- Germano, M., Piomelli, U., Moin, P., & Cabot, W. H. (1991). A dynamic subgrid-scale eddy viscosity model. *Physics of Fluids A*, 3(7), 1760–1765.
- Geyer, T. F., & Sarradj, E. (2018). Noise reduction and aerodynamics of airfoils with porous trailing edges. In *Impact and Noise Control Engineering*.
- Geyer, T., Sarradj, E., & Fritzsche, C. (2010). Measurement of the noise generation at the trailing edge of porous airfoils. *Experiments in Fluids*, 48(2), 291–308.
- Geyer, Thomas, & Sarradj, E. (2014). Trailing edge noise of partially porous airfoils. In *20th AIAA/CEAS Aeroacoustics Conference*. American Institute of Aeronautics and Astronautics Inc.
- Geyer, Thomas, Sarradj, E., & Fritzsche, C. (2010a). Porous airfoils: noise reduction and boundary layer effects (Vol. 9).



- Geyer, Thomas, Sarradj, E., & Fritzsche, C. (2010b). Porous airfoils: noise reduction and boundary layer effects (Vol. 9).
- Goldstein, M. E. (1976). *Aeroacoustics*. New York: McGraw-Hill International Book Co.
- Grille Guerra, A. (2021). Unsteady Evolution of a Laminar Separation Bubble Subjected to Wing Structural Motion. *APS Division of Fluid Dynamics* .
- Gruber, M. (2012). *Airfoil noise reduction by edge treatments*.
- Gruber, M., Joseph, P. F., & Chong, T. P. (2011a). On the mechanisms of serrated airfoil trailing edge noise reduction. In *17th AIAA/CEAS Aeroacoustics Conference 2011 (32nd AIAA Aeroacoustics Conference)*. American Institute of Aeronautics and Astronautics Inc.
- Gruber, M., Joseph, P. F., & Chong, T. P. (2011b). On the mechanisms of serrated airfoil trailing edge noise reduction. In *17th AIAA/CEAS Aeroacoustics Conference 2011 (32nd AIAA Aeroacoustics Conference)*. American Institute of Aeronautics and Astronautics Inc.
- Gruber, M., Joseph, P. F., & Pei Chong, T. (2010). Experimental investigation of airfoil self noise and turbulent wake reduction by the use of trailing edge serrations. *American Institute of Aeronautics and Astronautics*.
- Guo, Y., & Thomas, R. H. (2019). On aircraft trailing edge noise. In *25th AIAA/CEAS Aeroacoustics Conference, 2019*. American Institute of Aeronautics and Astronautics Inc, AIAA.
- Herr, M. (2007a). Design Criteria for Low-Noise Trailing-Edges.
- Herr, M. (2007b). Design Criteria for Low-Noise Trailing-Edges.
- Herr, M., & Reichenberger, J. (2011). In search of airworthy trailing-edge noise reduction means. In *17th AIAA/CEAS Aeroacoustics Conference 2011 (32nd AIAA Aeroacoustics Conference)*. American Institute of Aeronautics and Astronautics Inc.
- Horton, H. P. (1967). A semi-empirical theory for the growth and bursting of laminar separation bubbles.
- Howe, M. S. (1978). A review of the theory of trailing edge noise. *Journal of Sound and Vibration*.
- Howe, M. S. (1979). On the added mass of a perforated shell, with application to the generation of aerodynamic sound by a perforated trailing edge. *Proc R Soc London Ser A*, 365(1721), 209–233.

- Howe, M. S. (1999). Trailing edge noise at low mach numbers. *Journal of Sound and vibration* (Vol. 225).
- Howe, M. S. (n.d.). *Noise produced by a sawtooth trailing edge*.
- Hwang, D. (2004, November). Review of research into the concept of the microblowing technique for turbulent skin friction reduction. *Progress in Aerospace Sciences*.
- Ibren, M., Andan, A. D., Asrar, W., & Sulaeman, E. (2021). Laminar Separation Bubble and Flow Topology of NACA 0015 at Low Reynolds Number. *CFD Letters*, 13(10), 36–51.
- J. smagorinsky. (1963). general circulation experiments with the primitive equations i. the basic experiment. retrieved from washington, D.C.
- Jakobsen, J. ; A. B. (1993). *Aerodynamical noise from wind turbine generators*.
- Jaworski, J. W., & Peake, N. (2019). Aeroacoustics of Silent Owl Flight. *Annu. Rev. Fluid Mech.* 2020, 52, 395–420.
- Jaworski, J. W., & Peake, N. (2020). Annual Review of Fluid Mechanics Aeroacoustics of Silent Owl Flight. *Annual. Rev. Fluid Mech.*
- Jones, L. E., & Sandberg, R. D. (2012). Acoustic and hydrodynamic analysis of the flow around an aerofoil with trailing-edge serrations. *Journal of Fluid Mechanics*, 706, 295–322.
- Jones, Lloyd E, & Sandberg, R. D. (2010). Numerical investigation of airfoil self-noise reduction by addition of trailing-edge serrations. In *16th AIAA/CEAS Aeroacoustics Conference*.
- Joslin, R. D. (1998). *Aircraft laminar flow control 1*. *Annu. Rev. Fluid Mech* (Vol. 30).
- Khorrami, M. R., & Choudhari, M. M. (2003). *Application of Passive Porous Treatment to Slat Trailing Edge Noise*.
- Kim, D. H., & Chang, J. W. (2014). Low-Reynolds-number effect on the aerodynamic characteristics of a pitching NACA0012 airfoil. *Aerospace Science and Technology*, 32(1), 162–168.
- Kim, S.-E. (2004). Large Eddy Simulation Using an Unstructured Mesh Based Finite-Volume Solver. *American Institute of Aeronautics and Astronautics*.
- Kurelek, J. W., Tuna, B. A., Yarusevych, S., & Kotsonis, M. (2021). Three-dimensional development of coherent structures in a two-dimensional laminar separation bubble. *AIAA Journal*, 59(2), 493–505.
- L T. Glark. (1971). The Radiation of Sound From an Airfoil Immersed in a Laminar Flow. *Journal of Engineering for Power*.

- Langtry, R. B., & Menter, F. R. (2009). Correlation-based transition modeling for unstructured parallelized computational fluid dynamics codes. *AIAA Journal*, 47(12), 2894–2906.
- Lau, A. S. H., Haeri, S., & Kim, J. W. (2013). The effect of wavy leading edges on aerofoil-gust interaction noise. *Journal of Sound and Vibration*, 332(24), 6234–6253.
- Lee, B., & Baeder, J. D. (2021). Prediction and validation of laminar-turbulent transition using sa- $\gamma$  transition model. In *AIAA Scitech 2021 Forum* (pp. 1–21). American Institute of Aeronautics and Astronautics Inc, AIAA.
- Lee, S. (2019). The Effect of Airfoil Shape on Trailing Edge Noise. *Journal of Theoretical and Computational Acoustics*, 27(2).
- Lee, S. H., & Kim, D. (2017). Aerodynamics of a translating comb-like plate inspired by a fairyfly wing. *Physics of Fluids*, 29(8).
- Lei, J., Guo, F., & Huang, C. (2013). Numerical study of separation on the trailing edge of a symmetrical airfoil at a low Reynolds number. *Chinese Journal of Aeronautics*, 26(4), 918–925.
- Lilley, G. M. (1998). A study of the silent flight of the owl. In *4th AIAA/CEAS Aeroacoustics Conference*. American Institute of Aeronautics and Astronautics Inc, AIAA.
- Lissaman, P. B. S. (1983). *Low-Reynolds-Number Airfoils*. *Ann. Rev. Fluid Mech* (Vol. 15).
- Liu, Y., Dowling, A. P., & Shin, H.-C. (2006). *Effects of Surface Roughness on Airframe Noise*.
- Lodefier, K., Merci, B., de Langhe, C., & Dick, E. (2003). *Transition Modelling With the SST Turbulence Model and an Intermittency Transport Equation*.
- Lowson, M. v, Mcalpine, A., & Nash, E. C. (1997). *The generation of boundary instability noise on aerofoils*.
- Lyu, B., & Azarpeyvand, M. (2017). On the noise prediction for serrated leading edges. *Journal of Fluid Mechanics*, 826, 205–234.
- Lyu, B., Azarpeyvand, M., & Sinayoko, S. (2016). Prediction of noise from serrated trailing edges. *Journal of Fluid Mechanics*, 793, 556–588.
- M. A lam, & N. D. Sandham. (2000). Direct numerical simulation of ‘short’ laminar separation bubbles with turbulent reattachment. *J. Fluid Mech*, 410, 1–28.

- M. J. Lighthill. (1952). On sound generated aerodynamically I. General theory. *Proceedings of the Royal Society of London. Series A. Mathematical and Physical Sciences*, 211(1107), 564–587.
- M. J. Lighthill. (1954). On sound generated aerodynamically II. Turbulence as a source of sound. *Proceedings of the Royal Society of London. Series A. Mathematical and Physical Sciences*, 222(1148), 1–32.
- Ma, D., Zhao, Y., Qiao, Y., & Li, G. (2015, August 1). Effects of relative thickness on aerodynamic characteristics of airfoil at a low Reynolds number. *Chinese Journal of Aeronautics*. Chinese Journal of Aeronautics.
- Manela, A. (2013). On the acoustic radiation of a pitching airfoil. *Physics of Fluids*, 25(7).
- Manni, L., Nishino, T., & Delafin, P. L. (2016). Numerical study of airfoil stall cells using a very wide computational domain. *Computers and Fluids*, 140, 260–269.
- Mcgranahan, B. D., & Selig, M. S. (2003). Surface oil flow measurements on several airfoils at low Reynolds numbers. *AIAA*, 500, 23–26.
- Miozzi, M., Capone, A., Costantini, M., Fratto, L., Klein, C., & di Felice, F. (2019). Skin friction and coherent structures within a laminar separation bubble. *Experiments in Fluids*, 60(1).
- Moreau, D. J., Brooks, L. A., & Doolan, C. J. (2011). Flat plate self-noise reduction at low-to-moderate Reynolds number with trailing edge serrations. In *Proceedings of ACOUSTICS 2011* (Vol. 46).
- Moreau, D. J., & Doolan, C. J. (2013a). Noise-reduction mechanism of a flat-plate serrated trailing edge. In *AIAA Journal* (Vol. 51, pp. 2513–2522).
- Moreau, D. J., & Doolan, C. J. (2013b). Noise-reduction mechanism of a flat-plate serrated trailing edge. In *AIAA Journal* (Vol. 51, pp. 2513–2522).
- Moreau, D. J., Doolan, C. J., Nathan Alexander, W., Meyers, T. W., & Devenport, W. J. (2016). Wall-mounted finite airfoil-noise production and prediction. In *AIAA Journal* (Vol. 54, pp. 1637–1651). American Institute of Aeronautics and Astronautics Inc.
- Nakano, T., Fujisawa, N., & Lee, S. (2006). Measurement of tonal-noise characteristics and periodic flow structure around NACA0018 airfoil. *Experiments in Fluids*, 40(3), 482–490.
- Oerlemans, S., Fisher, M., Maeder, T., & Kögler, K. (2009a). Reduction of wind turbine noise using optimized airfoils and trailing-edge serrations. In *AIAA Journal* (Vol. 47, pp. 1470–1481).

- Oerlemans, S., Fisher, M., Maeder, T., & Kögler, K. (2009b). Reduction of wind turbine noise using optimized airfoils and trailing-edge serrations. In *AIAA Journal* (Vol. 47, pp. 1470–1481).
- Oerlemans, Schepers, JG, Guidati, & Wagner. (2001). Experimental demonstration of wind turbine noise reduction through optimized airfoil noise reduction through optimized airfoil shape and trailing-edge serrations.
- Ol, M. v, Mcauliffe, B. R., Hanff, E. S., Scholz, U., & Kähler, C. (2005). Comparison of Laminar Separation Bubble Measurements on a Low Reynolds Number Airfoil in Three Facilities. *American Institute of Aeronautics and Astronautics*.
- P. R. Owen, B. Sc., & L. Klanfer, B. Sc. (1953). *On the laminar boundary layer separation from the leading edge of a thin aerofoil*.
- Parchen, R. (1996a). *Results of a wind tunnel study on the reduction of airfoil self-noise by the application of serrated blade trailing edges*.
- Parchen, R. (1996b). *Results of a wind tunnel study on the reduction of airfoil self-noise by the application of serrated blade trailing edges*.
- Park, D., & Park, S. O. (2013). Study of tonal noise behavior of an airfoil by using parabolized stability equations. *Theoretical and Computational Fluid Dynamics*, 27(1–2), 71–88.
- Park, D., Shim, H., & Lee, Y. (2020). PIV Measurement of Separation Bubble on an Airfoil at Low Reynolds Numbers. *Journal of Aerospace Engineering*, 33(1).
- Paterson, R. W., Vogt, P. G., Fink, M. R., & Munch, C. L. (1973). Vortex noise of isolated airfoils. *Journal of Aircraft*, 10(5), 296–302.
- Plogmann, B., Herrig, A., & Würz, W. (2013, May). Experimental investigations of a trailing edge noise feedback mechanism on a NACA 0012 airfoil. *Experiments in Fluids*.
- Ramírez, W. A., & Wolf, W. R. (2016). The effects of suction and blowing on tonal noise generation by blunt trailing edges. In *21st AIAA/CEAS Aeroacoustics Conference*. American Institute of Aeronautics and Astronautics Inc, AIAA.
- Revell, J. D., Kuntz, H. L., Balena, F. J., Home, C., Storms, B. L., & Dougherty, R. P. (1997). Trailing-edge flap noise reduction by porous acoustic treatment. In *3rd AIAA/CEAS Aeroacoustics Conference* (pp. 493–505). American Institute of Aeronautics and Astronautics Inc, AIAA.
- Rezaeiha, A., Montazeri, H., & Blocken, B. (2019). On the accuracy of turbulence models for CFD simulations of vertical axis wind turbines. *Energy*, 180, 838–857.

- Rumsey, C. L., & Greenblatt, D. (2009). Flow control predictions using unsteady reynolds-averaged navier-stokes modeling: A parametric study. *AIAA Journal*, 47(9), 2259–2262.
- S. J. (Stanley Jay) Miley. (1982). *A catalog of low Reynolds number airfoil data for wind turbine applications*.
- Sandberg, R. D., & Jones, L. E. (2011). Direct numerical simulations of low Reynolds number flow over airfoils with trailing-edge serrations. In *Journal of Sound and Vibration* (Vol. 330, pp. 3818–3831).
- Sandberg, R. D., Jones, L. E., Sandham, N. D., & Joseph, P. F. (2009). Direct numerical simulations of tonal noise generated by laminar flow past airfoils. *Journal of Sound and Vibration*, 320(4–5), 838–858.
- Sarradj, E., & Geyer, T. (2013). Airfoil noise analysis using symbolic regression. In *19th AIAA/CEAS Aeroacoustics Conference* (p. 11). American Institute of Aeronautics and Astronautics Inc.
- Schlinker, R. (1976). *Prediction of rotating-blade vortex noise from noise of nonrotating blades Assessment of unsteady flows in turbines View project*.
- Schumacher, K. L., Doolan, C. J., & Kelso, R. M. (2014). The effect of acoustic forcing on an airfoil tonal noise mechanism. *The Journal of the Acoustical Society of America*, 136(2), EL78–EL83.
- Selig, M. S., Guglielmo, J. J., Broeren, A. P., & Giguère, P. (1996). Experiments on airfoils at low reynolds numbers. In *34th Aerospace Sciences Meeting and Exhibit*. American Institute of Aeronautics and Astronautics Inc, AIAA.
- Singh, N. K. (2019). Instability and transition in a laminar separation bubble. *Journal of Applied Fluid Mechanics*, 12(5), 1511–1525.
- Stalnov, O., Chaitanya, P., & Joseph, P. F. (2016). Towards a non-empirical trailing edge noise prediction model. *Journal of Sound and Vibration*, 372, 50–68.
- Suluksna, K., & Juntasaro, E. (2008). Assessment of intermittency transport equations for modeling transition in boundary layers subjected to freestream turbulence. *International Journal of Heat and Fluid Flow*, 29(1), 48–61.
- Szőke, M., Fiscaletti, D., & Azarpeyvand, M. (2019). Uniform suction for the reduction of the trailing edge noise. In *25th AIAA/CEAS Aeroacoustics Conference, 2019*. American Institute of Aeronautics and Astronautics Inc, AIAA.
- Szoke, M., Fiscaletti, D., & Azarpeyvand, M. (2020). Uniform flow injection into a turbulent boundary layer for trailing edge noise reduction. *Physics of Fluids*, 32(8).
- Tam, C. K. W. (1974). *Discrete tones of isolated airfoils*.

- Tam, C. K. W., & Ju, H. (2011). Airfoil tones at moderate Reynolds number: A computational study. In *17th AIAA/CEAS Aeroacoustics Conference 2011 (32nd AIAA Aeroacoustics Conference)*.
- Thomas F. Geyer. (2011). *Trailing Edge Noise Generation of Porous Airfoils*.
- Thomas Fritz Geyer, & Sarradj, E. (2019). Self Noise Reduction and Aerodynamics of Airfoils With Porous Trailing Edges. *Acoustics*, 1(2), 393–409.
- Tillman, T. G., & Hwang, D. P. (1999). *Drag Reduction on a Large-Scale Nacelle Using a Micro-Blowing Technique*.
- UPNM. (2014). *LW-9300R Wind Tunnel Introduction*.
- UPNM. (2022). *UPNM: Wind Tunnel Lab*.
- Uthra, M. P., & Daniel Antony, A. (2020). Comparative investigation of laminar separation bubble on a wing at low reynolds number. *International Journal of Vehicle Structures and Systems*, 12(3), 337–342.
- van der Velden, W. C. P., Avallone, F., & Ragni, D. (2017). Numerical analysis of noise reduction mechanisms of serrated trailing edges under zero lift condition. In *23rd AIAA/CEAS Aeroacoustics Conference, 2017*. American Institute of Aeronautics and Astronautics Inc, AIAA.
- Vathylakis, A., Chong, T. P., & Joseph, P. F. (2015). Poro-serrated trailing-edge devices for airfoil self-noise reduction. *AIAA Journal*, 52(11), 3379–3394.
- Wagner, C. A., Hüttl, T., & Sagaut, P. (2007). *Large-eddy simulation for acoustics*. Cambridge University Press.
- Wang, M., & Moin, P. (2000). Computation of trailing-edge flow and noise using large-eddy simulation. *AIAA Journal*, 38(12), 2201–2209.
- Wang, S., Ingham, D. B., Ma, L., Pourkashanian, M., & Tao, Z. (2010). Numerical investigations on dynamic stall of low Reynolds number flow around oscillating airfoils. *Computers and Fluids*, 39(9), 1529–1541.
- Wauters, J., Degroote, J., & Vierendeels, J. (2019). Comparative study of transition models for high-angle-of-attack behavior. *AIAA Journal*, 57(6), 2356–2371.
- Wen Zhong Shen, Weijun Zhu, & Jens Nørkær Sørensen. (2009). Aeroacoustic computations for turbulent airfoil flows. *AIAA Journal*, 47(6), 1518–1527.
- Wilkinson, S. P., Nasa, S. P., & Hampton, L. R. (1983). Influence of Wall Permeability on Turbulent Boundary-Layer Properties.

- Williams, J. E. F., & Hall, L. H. (1970). Aerodynamic sound generation by turbulent flow in the vicinity of a scattering half plane. *Journal of Fluid Mechanics*, 40(4), 657–670.
- Yarusevych, S., Kawall, J. G., & Sullivan, P. E. (2008). Unsteady separated flow characterization on airfoils using time-resolved surface pressure measurements. In *AIAA Journal* (Vol. 46, pp. 508–516).
- Zhang, M., & Chong, T. P. (2020). Experimental investigation of the impact of porous parameters on trailing-edge noise. *Journal of Sound and Vibration*, 489.
- Zhao, D. N. H. E. G. J. C. and A. R. (2019). *Wind turbines and aerodynamics energy harvesters*.
- Zheng, X., Liu, C., Liu, F., & Yang, C. (1998). Turbulent transition simulation using the k-w. *international journal for numerical methods in engineering Int. J. Numer. Meth. Engng* (Vol. 42).
- Zhou, T., Sun, Y., Fattah, R., Zhang, X., & Huang, X. (2019). An experimental study of trailing edge noise from a pitching airfoil. *The Journal of the Acoustical Society of America*, 145(4), 2009–2021.
- Zhu, W. J., Shen, W. Z., Barlas, E., Bertagnolio, F., & Sørensen, J. N. (2018, May 1). Wind turbine noise generation and propagation modeling at DTU Wind Energy: A review. *Renewable and Sustainable Energy Reviews*. Elsevier Ltd.



## **PUBLICATIONS**

- Ibren, M., Andan, A. D., Asrar, W., & Sulaeman, E. (2022). A Review on Generation and Mitigation of Airfoil Self-Induced Noise. *Journal of Advanced Research in Fluid Mechanics and Thermal Sciences*, 90(1), 163-178.
- Ibren, M., Andan, A. D., Asrar, W., & Sulaeman, E. (2021). Laminar Separation Bubble and Flow Topology of NACA 0015 at Low Reynolds Number. *CFD Letters*, 13(10), 36-51.
- Mohamed, E. S., & Abidin, A. D. A. Z. (2022, June). Influence of Surface Discontinuity on Sound Absorption Coefficient of Vehicle Interior Material. In *IOP Conference Series: Materials Science and Engineering* (Vol. 1244, No. 1, p. 012003). IOP Publishing.
- Numerical prediction of trailing edge noise at Low Reynolds number with modified trailing edges of a NACA 0015 airfoil.” submitted to Acoustical Physics (WOS “SCIE”, IF= 1.2), Under Review.
- Experimental Investigation of Low Reynolds number flow around a Serrated NACA 0015 airfoil.” submitted to Acta Mechanica (WOS “SCIE”, IF = 2.645), Under Review.
- Large Eddy Simulation of Low Reynolds number flow around a NACA0015 airfoil with modified trailing edges.” submitted to International Journal of Computational Fluid Dynamics (WOS “SCIE”, IF= 1.5), Under Review

## APPENDIX A: ISO-POINTS JOURNAL

|   |                 |                       |                       |              |
|---|-----------------|-----------------------|-----------------------|--------------|
| <b> "/file/set-tui-version ""20.2""</b> |                 |                       |                       |              |
| <b>/surface/point-surface</b>           | <b>point-1</b>  | <b>0.000093088362</b> | <b>0.000126251760</b> | <b>0.149</b> |
| <b>/surface/point-surface</b>           | <b>point-2</b>  | <b>0.000159372110</b> | <b>0.000705965620</b> | <b>0.149</b> |
| <b>/surface/point-surface</b>           | <b>point-3</b>  | <b>0.000527716240</b> | <b>0.001787966000</b> | <b>0.149</b> |
| <b>/surface/point-surface</b>           | <b>point-4</b>  | <b>0.000829776570</b> | <b>0.002290252400</b> | <b>0.149</b> |
| <b>/surface/point-surface</b>           | <b>point-5</b>  | <b>0.001558468700</b> | <b>0.003196656500</b> | <b>0.149</b> |
| <b>/surface/point-surface</b>           | <b>point-6</b>  | <b>0.001985100100</b> | <b>0.003600773900</b> | <b>0.149</b> |
| <b>/surface/point-surface</b>           | <b>point-7</b>  | <b>0.003393820700</b> | <b>0.004653649400</b> | <b>0.149</b> |
| <b>/surface/point-surface</b>           | <b>point-8</b>  | <b>0.004405793300</b> | <b>0.005252224900</b> | <b>0.149</b> |
| <b>/surface/point-surface</b>           | <b>point-9</b>  | <b>0.004926722000</b> | <b>0.005526420500</b> | <b>0.149</b> |
| <b>/surface/point-surface</b>           | <b>point-10</b> | <b>0.005988613200</b> | <b>0.006033007100</b> | <b>0.149</b> |
| <b>/surface/point-surface</b>           | <b>point-11</b> | <b>0.006529577100</b> | <b>0.006265397600</b> | <b>0.149</b> |
| <b>/surface/point-surface</b>           | <b>point-12</b> | <b>0.007623458700</b> | <b>0.006700236600</b> | <b>0.149</b> |
| <b>/surface/point-surface</b>           | <b>point-13</b> | <b>0.008176377000</b> | <b>0.006902686000</b> | <b>0.149</b> |
| <b>/surface/point-surface</b>           | <b>point-14</b> | <b>0.009219235700</b> | <b>0.007260964700</b> | <b>0.149</b> |
| <b>/surface/point-surface</b>           | <b>point-15</b> | <b>0.009300114600</b> | <b>0.007285039900</b> | <b>0.149</b> |
| <b>/surface/point-surface</b>           | <b>point-16</b> | <b>0.009407765200</b> | <b>0.007316475300</b> | <b>0.149</b> |
| <b>/surface/point-surface</b>           | <b>point-17</b> | <b>0.009501711500</b> | <b>0.007343324400</b> | <b>0.149</b> |
| <b>/surface/point-surface</b>           | <b>point-18</b> | <b>0.009599966900</b> | <b>0.007371990000</b> | <b>0.149</b> |
| <b>/surface/point-surface</b>           | <b>point-19</b> | <b>0.009701331100</b> | <b>0.007499900000</b> | <b>0.149</b> |
| <b>/surface/point-surface</b>           | <b>point-20</b> | <b>0.009780981600</b> | <b>0.007438254100</b> | <b>0.149</b> |
| <b>/surface/point-surface</b>           | <b>point-21</b> | <b>0.009798259500</b> | <b>0.007443399600</b> | <b>0.149</b> |
| <b>/surface/point-surface</b>           | <b>point-22</b> | <b>0.009852027500</b> | <b>0.007459346200</b> | <b>0.149</b> |
| <b>/surface/point-surface</b>           | <b>point-23</b> | <b>0.009907686200</b> | <b>0.007475773300</b> | <b>0.149</b> |
| <b>/surface/point-surface</b>           | <b>point-24</b> | <b>0.010000632000</b> | <b>0.007502988000</b> | <b>0.149</b> |
| <b>/surface/point-surface</b>           | <b>point-25</b> | <b>0.010218848000</b> | <b>0.007565820100</b> | <b>0.149</b> |
| <b>/surface/point-surface</b>           | <b>point-26</b> | <b>0.010310506000</b> | <b>0.007591764000</b> | <b>0.149</b> |
| <b>/surface/point-surface</b>           | <b>point-27</b> | <b>0.010400442000</b> | <b>0.007618000000</b> | <b>0.149</b> |
| <b>/surface/point-surface</b>           | <b>point-28</b> | <b>0.010505964000</b> | <b>0.007650000000</b> | <b>0.149</b> |
| <b>/surface/point-surface</b>           | <b>point-29</b> | <b>0.010606433000</b> | <b>0.007699000000</b> | <b>0.149</b> |
| <b>/surface/point-surface</b>           | <b>point-30</b> | <b>0.010710612000</b> | <b>0.007719183800</b> | <b>0.149</b> |
| <b>/surface/point-surface</b>           | <b>point-31</b> | <b>0.010854571000</b> | <b>0.007758393900</b> | <b>0.149</b> |
| <b>/surface/point-surface</b>           | <b>point-32</b> | <b>0.010908357000</b> | <b>0.007772900000</b> | <b>0.149</b> |
| <b>/surface/point-surface</b>           | <b>point-33</b> | <b>0.011007749000</b> | <b>0.007804000000</b> | <b>0.149</b> |
| <b>/surface/point-surface</b>           | <b>point-34</b> | <b>0.011201166000</b> | <b>0.007870000000</b> | <b>0.149</b> |
| <b>/surface/point-surface</b>           | <b>point-35</b> | <b>0.011299971000</b> | <b>0.007889000000</b> | <b>0.149</b> |
| <b>/surface/point-surface</b>           | <b>point-36</b> | <b>0.011445091000</b> | <b>0.007930000000</b> | <b>0.149</b> |
| <b>/surface/point-surface</b>           | <b>point-37</b> | <b>0.011508989000</b> | <b>0.007941068200</b> | <b>0.149</b> |

|                        |          |                |                |       |
|------------------------|----------|----------------|----------------|-------|
| /surface/point-surface | point-38 | 0.011609051000 | 0.007967679800 | 0.149 |
| /surface/point-surface | point-39 | 0.011705577000 | 0.007990000000 | 0.149 |
| /surface/point-surface | point-40 | 0.011837217000 | 0.008030000000 | 0.149 |
| /surface/point-surface | point-41 | 0.011903890000 | 0.008044200900 | 0.149 |
| /surface/point-surface | point-42 | 0.012003866000 | 0.008069969700 | 0.149 |
| /surface/point-surface | point-43 | 0.013007973000 | 0.008321215400 | 0.149 |
| /surface/point-surface | point-44 | 0.014002088000 | 0.008559900000 | 0.149 |
| /surface/point-surface | point-45 | 0.015002797000 | 0.008770000000 | 0.149 |
| /surface/point-surface | point-46 | 0.016001038000 | 0.008963410700 | 0.149 |
| /surface/point-surface | point-47 | 0.017015420000 | 0.009164711500 | 0.149 |
| /surface/point-surface | point-48 | 0.018010816000 | 0.009349900000 | 0.149 |
| /surface/point-surface | point-49 | 0.019011050000 | 0.009599000000 | 0.149 |
| /surface/point-surface | point-50 | 0.020043837000 | 0.009666282700 | 0.149 |
| /surface/point-surface | point-51 | 0.021010337000 | 0.009899000000 | 0.149 |
| /surface/point-surface | point-52 | 0.022004774000 | 0.009945000000 | 0.149 |
| /surface/point-surface | point-53 | 0.023013132000 | 0.010089900000 | 0.149 |
| /surface/point-surface | point-54 | 0.024007058000 | 0.010200000000 | 0.149 |
| /surface/point-surface | point-55 | 0.025004691000 | 0.010295000000 | 0.149 |
| /surface/point-surface | point-56 | 0.026016848000 | 0.010399000000 | 0.149 |
| /surface/point-surface | point-57 | 0.027044287000 | 0.010599000000 | 0.149 |
| /surface/point-surface | point-58 | 0.028000942000 | 0.010600000000 | 0.149 |
| /surface/point-surface | point-59 | 0.029002422000 | 0.010668695000 | 0.149 |
| /surface/point-surface | point-60 | 0.030000279000 | 0.010745394000 | 0.149 |
| /surface/point-surface | point-61 | 0.031029150000 | 0.010820000000 | 0.149 |
| /surface/point-surface | point-62 | 0.032126110000 | 0.010890000000 | 0.149 |
| /surface/point-surface | point-63 | 0.033083912000 | 0.010960000000 | 0.149 |
| /surface/point-surface | point-64 | 0.034005713000 | 0.010990000000 | 0.149 |
| /surface/point-surface | point-65 | 0.035000566000 | 0.011030090000 | 0.149 |
| /surface/point-surface | point-66 | 0.036059510000 | 0.011075392000 | 0.149 |
| /surface/point-surface | point-67 | 0.037017975000 | 0.011112731000 | 0.149 |
| /surface/point-surface | point-68 | 0.038106322000 | 0.011159990000 | 0.149 |
| /surface/point-surface | point-69 | 0.039008886000 | 0.011179900000 | 0.149 |
| /surface/point-surface | point-70 | 0.040011495000 | 0.011191815000 | 0.149 |
| /surface/point-surface | point-71 | 0.041002307000 | 0.011208900000 | 0.149 |
| /surface/point-surface | point-72 | 0.042003129000 | 0.011227000000 | 0.149 |
| /surface/point-surface | point-73 | 0.043047339000 | 0.011250000000 | 0.149 |
| /surface/point-surface | point-74 | 0.044047590000 | 0.011248000000 | 0.149 |
| /surface/point-surface | point-75 | 0.045025017000 | 0.011250281000 | 0.149 |



|                        |           |                 |                |       |
|------------------------|-----------|-----------------|----------------|-------|
| /surface/point-surface | point-76  | 0.046001215000  | 0.011240858000 | 0.149 |
| /surface/point-surface | point-77  | 0.047038455000  | 0.011241257000 | 0.149 |
| /surface/point-surface | point-78  | 0.048015937000  | 0.011230000000 | 0.149 |
| /surface/point-surface | point-79  | 0.049014628000  | 0.011220000000 | 0.149 |
| /surface/point-surface | point-80  | 0.050082356000  | 0.011200237000 | 0.149 |
| /surface/point-surface | point-81  | 0.051054012000  | 0.011178282000 | 0.149 |
| /surface/point-surface | point-82  | 0.052100550000  | 0.011156683000 | 0.149 |
| /surface/point-surface | point-83  | 0.053010155000  | 0.011139900000 | 0.149 |
| /surface/point-surface | point-84  | 0.054007340000  | 0.011119990000 | 0.149 |
| /surface/point-surface | point-85  | 0.055067062000  | 0.011075000000 | 0.149 |
| /surface/point-surface | point-86  | 0.056003463000  | 0.011040813000 | 0.149 |
| /surface/point-surface | point-87  | 0.057007115000  | 0.011004578000 | 0.149 |
| /surface/point-surface | point-88  | 0.058033735000  | 0.010968000000 | 0.149 |
| /surface/point-surface | point-89  | 0.059001986000  | 0.010928000000 | 0.149 |
| /surface/point-surface | point-90  | 0.060018778000  | 0.010879000000 | 0.149 |
| /surface/point-surface | point-91  | 0.061035272000  | 0.010830578000 | 0.149 |
| /surface/point-surface | point-92  | 0.062052429000  | 0.010783000000 | 0.149 |
| /surface/point-surface | point-93  | 0.063034989000  | 0.010740000000 | 0.149 |
| /surface/point-surface | point-94  | 0.064073920000  | 0.010680000000 | 0.149 |
| /surface/point-surface | point-95  | 0.065121002000  | 0.010612580000 | 0.149 |
| /surface/point-surface | point-96  | 0.066029102000  | 0.010557893000 | 0.149 |
| /surface/point-surface | point-97  | 0.067020662000  | 0.010500000000 | 0.149 |
| /surface/point-surface | point-98  | 0.068069942000  | 0.010434000000 | 0.149 |
| /surface/point-surface | point-99  | 0.069070466000  | 0.010363813000 | 0.149 |
| /surface/point-surface | point-100 | 0.070028536000  | 0.010297567000 | 0.149 |
| /surface/point-surface | point-101 | 0.071020298000  | 0.010227608000 | 0.149 |
| /surface/point-surface | point-102 | 0.072034538000  | 0.010157000000 | 0.149 |
| /surface/point-surface | point-103 | 0.073132642000  | 0.010077000000 | 0.149 |
| /surface/point-surface | point-104 | 0.074015833000  | 0.010005990000 | 0.149 |
| /surface/point-surface | point-105 | 0.075042658000  | 0.009923268100 | 0.149 |
| /surface/point-surface | point-106 | 0.076076262000  | 0.009839790900 | 0.149 |
| /surface/point-surface | point-107 | 0.077053390000  | 0.009761182600 | 0.149 |
| /surface/point-surface | point-108 | 0.0780666923000 | 0.009679000000 | 0.149 |
| /surface/point-surface | point-109 | 0.079033189000  | 0.009593912400 | 0.149 |
| /surface/point-surface | point-110 | 0.080001570000  | 0.009507953200 | 0.149 |
| /surface/point-surface | point-111 | 0.081121959000  | 0.009405734900 | 0.149 |
| /surface/point-surface | point-112 | 0.082010053000  | 0.009326456100 | 0.149 |
| /surface/point-surface | point-113 | 0.083004795000  | 0.009234342700 | 0.149 |
| /surface/point-surface | point-114 | 0.084001727000  | 0.009150000000 | 0.149 |
| /surface/point-surface | point-115 | 0.085047834000  | 0.009050000000 | 0.149 |
| /surface/point-surface | point-116 | 0.086001419000  | 0.008948360600 | 0.149 |
| /surface/point-surface | point-117 | 0.087004252000  | 0.008848721200 | 0.149 |
| /surface/point-surface | point-118 | 0.088066518000  | 0.008745000000 | 0.149 |
| /surface/point-surface | point-119 | 0.090043880000  | 0.008645764700 | 0.149 |
| /surface/point-surface | point-120 | 0.095003150000  | 0.008029990000 | 0.149 |
| /surface/point-surface | point-121 | 0.100029290000  | 0.007458000000 | 0.149 |
| /surface/point-surface | point-122 | 0.105081560000  | 0.006858000000 | 0.149 |
| /surface/point-surface | point-123 | 0.110036040000  | 0.006250000000 | 0.149 |
| /surface/point-surface | point-124 | 0.115009540000  | 0.005594000000 | 0.149 |
| /surface/point-surface | point-125 | 0.120007130000  | 0.004915021400 | 0.149 |
| /surface/point-surface | point-126 | 0.125004530000  | 0.004208290500 | 0.149 |
| /surface/point-surface | point-127 | 0.130038710000  | 0.003470000000 | 0.149 |
| /surface/point-surface | point-128 | 0.135014130000  | 0.002720000000 | 0.149 |
| /surface/point-surface | point-129 | 0.140081810000  | 0.001905900000 | 0.149 |
| /surface/point-surface | point-130 | 0.144502160000  | 0.001178115000 | 0.149 |
| /surface/point-surface | point-131 | 0.147007870000  | 0.000754613370 | 0.149 |

## APPENDIX B: ISO-SURFACE JOURNAL

| "/file/set-tui-version ""20.2"" |              |       |   |                |   |
|---------------------------------|--------------|-------|---|----------------|---|
| /surface/iso-surface            | x-coordinate | x=10  | 0 | 0.000093088362 | 0 |
| /surface/iso-surface            | x-coordinate | x=20  | 0 | 0.000159372110 | 0 |
| /surface/iso-surface            | x-coordinate | x=30  | 0 | 0.000527716240 | 0 |
| /surface/iso-surface            | x-coordinate | x=40  | 0 | 0.000829776570 | 0 |
| /surface/iso-surface            | x-coordinate | x=50  | 0 | 0.001558468700 | 0 |
| /surface/iso-surface            | x-coordinate | x=60  | 0 | 0.001985100100 | 0 |
| /surface/iso-surface            | x-coordinate | x=70  | 0 | 0.003393820700 | 0 |
| /surface/iso-surface            | x-coordinate | x=80  | 0 | 0.004405793300 | 0 |
| /surface/iso-surface            | x-coordinate | x=90  | 0 | 0.004926722000 | 0 |
| /surface/iso-surface            | x-coordinate | x=100 | 0 | 0.005988613200 | 0 |
| /surface/iso-surface            | x-coordinate | x=110 | 0 | 0.006529577100 | 0 |
| /surface/iso-surface            | x-coordinate | x=120 | 0 | 0.007623458700 | 0 |
| /surface/iso-surface            | x-coordinate | x=130 | 0 | 0.008176377000 | 0 |
| /surface/iso-surface            | x-coordinate | x=140 | 0 | 0.009219235700 | 0 |
| /surface/iso-surface            | x-coordinate | x=150 | 0 | 0.009300114600 | 0 |
| /surface/iso-surface            | x-coordinate | x=160 | 0 | 0.009407765200 | 0 |
| /surface/iso-surface            | x-coordinate | x=170 | 0 | 0.009501711500 | 0 |
| /surface/iso-surface            | x-coordinate | x=180 | 0 | 0.009599966900 | 0 |
| /surface/iso-surface            | x-coordinate | x=190 | 0 | 0.009701331100 | 0 |
| /surface/iso-surface            | x-coordinate | x=200 | 0 | 0.009780981600 | 0 |
| /surface/iso-surface            | x-coordinate | x=210 | 0 | 0.009798259500 | 0 |
| /surface/iso-surface            | x-coordinate | x=220 | 0 | 0.009852027500 | 0 |
| /surface/iso-surface            | x-coordinate | x=230 | 0 | 0.009907686200 | 0 |
| /surface/iso-surface            | x-coordinate | x=240 | 0 | 0.010000632000 | 0 |
| /surface/iso-surface            | x-coordinate | x=250 | 0 | 0.010218848000 | 0 |
| /surface/iso-surface            | x-coordinate | x=260 | 0 | 0.010310506000 | 0 |
| /surface/iso-surface            | x-coordinate | x=270 | 0 | 0.010400442000 | 0 |
| /surface/iso-surface            | x-coordinate | x=280 | 0 | 0.010505964000 | 0 |
| /surface/iso-surface            | x-coordinate | x=290 | 0 | 0.010606433000 | 0 |
| /surface/iso-surface            | x-coordinate | x=300 | 0 | 0.010710612000 | 0 |
| /surface/iso-surface            | x-coordinate | x=310 | 0 | 0.010854571000 | 0 |
| /surface/iso-surface            | x-coordinate | x=320 | 0 | 0.010908357000 | 0 |
| /surface/iso-surface            | x-coordinate | x=330 | 0 | 0.011007749000 | 0 |
| /surface/iso-surface            | x-coordinate | x=340 | 0 | 0.011201166000 | 0 |
| /surface/iso-surface            | x-coordinate | x=350 | 0 | 0.011299971000 | 0 |
| /surface/iso-surface            | x-coordinate | x=360 | 0 | 0.011445091000 | 0 |
| /surface/iso-surface            | x-coordinate | x=370 | 0 | 0.011508989000 | 0 |

|                      |              |       |   |                |   |
|----------------------|--------------|-------|---|----------------|---|
| /surface/iso-surface | x-coordinate | x=290 | 0 | 0.010606433000 | 0 |
| /surface/iso-surface | x-coordinate | x=300 | 0 | 0.010710612000 | 0 |
| /surface/iso-surface | x-coordinate | x=310 | 0 | 0.010854571000 | 0 |
| /surface/iso-surface | x-coordinate | x=320 | 0 | 0.010908357000 | 0 |
| /surface/iso-surface | x-coordinate | x=330 | 0 | 0.011007749000 | 0 |
| /surface/iso-surface | x-coordinate | x=340 | 0 | 0.011201166000 | 0 |
| /surface/iso-surface | x-coordinate | x=350 | 0 | 0.011299971000 | 0 |
| /surface/iso-surface | x-coordinate | x=360 | 0 | 0.011445091000 | 0 |
| /surface/iso-surface | x-coordinate | x=370 | 0 | 0.011508989000 | 0 |
| /surface/iso-surface | x-coordinate | x=380 | 0 | 0.011609051000 | 0 |
| /surface/iso-surface | x-coordinate | x=390 | 0 | 0.011705577000 | 0 |
| /surface/iso-surface | x-coordinate | x=400 | 0 | 0.011837217000 | 0 |
| /surface/iso-surface | x-coordinate | x=410 | 0 | 0.011903890000 | 0 |
| /surface/iso-surface | x-coordinate | x=420 | 0 | 0.012003866000 | 0 |
| /surface/iso-surface | x-coordinate | x=430 | 0 | 0.013007973000 | 0 |
| /surface/iso-surface | x-coordinate | x=440 | 0 | 0.014002088000 | 0 |
| /surface/iso-surface | x-coordinate | x=450 | 0 | 0.015002797000 | 0 |
| /surface/iso-surface | x-coordinate | x=460 | 0 | 0.016001038000 | 0 |
| /surface/iso-surface | x-coordinate | x=470 | 0 | 0.017015420000 | 0 |
| /surface/iso-surface | x-coordinate | x=480 | 0 | 0.018010816000 | 0 |
| /surface/iso-surface | x-coordinate | x=490 | 0 | 0.019011050000 | 0 |
| /surface/iso-surface | x-coordinate | x=500 | 0 | 0.020043837000 | 0 |
| /surface/iso-surface | x-coordinate | x=510 | 0 | 0.021010337000 | 0 |
| /surface/iso-surface | x-coordinate | x=520 | 0 | 0.022004774000 | 0 |
| /surface/iso-surface | x-coordinate | x=530 | 0 | 0.023013132000 | 0 |
| /surface/iso-surface | x-coordinate | x=540 | 0 | 0.024007058000 | 0 |
| /surface/iso-surface | x-coordinate | x=550 | 0 | 0.025004691000 | 0 |
| /surface/iso-surface | x-coordinate | x=560 | 0 | 0.026016848000 | 0 |
| /surface/iso-surface | x-coordinate | x=570 | 0 | 0.027044287000 | 0 |
| /surface/iso-surface | x-coordinate | x=580 | 0 | 0.028000942000 | 0 |
| /surface/iso-surface | x-coordinate | x=590 | 0 | 0.029002422000 | 0 |
| /surface/iso-surface | x-coordinate | x=600 | 0 | 0.030000279000 | 0 |
| /surface/iso-surface | x-coordinate | x=610 | 0 | 0.031029150000 | 0 |
| /surface/iso-surface | x-coordinate | x=620 | 0 | 0.032126110000 | 0 |
| /surface/iso-surface | x-coordinate | x=630 | 0 | 0.033083912000 | 0 |
| /surface/iso-surface | x-coordinate | x=640 | 0 | 0.034005713000 | 0 |
| /surface/iso-surface | x-coordinate | x=650 | 0 | 0.035000566000 | 0 |
| /surface/iso-surface | x-coordinate | x=660 | 0 | 0.036059510000 | 0 |



|  |               |          |                       |          |
|--|---------------|----------|-----------------------|----------|
| <i>/surface/iso-surface x-coordinate</i> | <i>x=670</i>  | <i>0</i> | <i>0.037017975000</i> | <i>0</i> |
| <i>/surface/iso-surface x-coordinate</i> | <i>x=680</i>  | <i>0</i> | <i>0.038106322000</i> | <i>0</i> |
| <i>/surface/iso-surface x-coordinate</i> | <i>x=690</i>  | <i>0</i> | <i>0.039008886000</i> | <i>0</i> |
| <i>/surface/iso-surface x-coordinate</i> | <i>x=700</i>  | <i>0</i> | <i>0.040011495000</i> | <i>0</i> |
| <i>/surface/iso-surface x-coordinate</i> | <i>x=710</i>  | <i>0</i> | <i>0.041002307000</i> | <i>0</i> |
| <i>/surface/iso-surface x-coordinate</i> | <i>x=720</i>  | <i>0</i> | <i>0.042003129000</i> | <i>0</i> |
| <i>/surface/iso-surface x-coordinate</i> | <i>x=730</i>  | <i>0</i> | <i>0.043047339000</i> | <i>0</i> |
| <i>/surface/iso-surface x-coordinate</i> | <i>x=740</i>  | <i>0</i> | <i>0.044047590000</i> | <i>0</i> |
| <i>/surface/iso-surface x-coordinate</i> | <i>x=750</i>  | <i>0</i> | <i>0.045025017000</i> | <i>0</i> |
| <i>/surface/iso-surface x-coordinate</i> | <i>x=760</i>  | <i>0</i> | <i>0.046001215000</i> | <i>0</i> |
| <i>/surface/iso-surface x-coordinate</i> | <i>x=770</i>  | <i>0</i> | <i>0.047038455000</i> | <i>0</i> |
| <i>/surface/iso-surface x-coordinate</i> | <i>x=780</i>  | <i>0</i> | <i>0.048015937000</i> | <i>0</i> |
| <i>/surface/iso-surface x-coordinate</i> | <i>x=790</i>  | <i>0</i> | <i>0.049014628000</i> | <i>0</i> |
| <i>/surface/iso-surface x-coordinate</i> | <i>x=800</i>  | <i>0</i> | <i>0.050082356000</i> | <i>0</i> |
| <i>/surface/iso-surface x-coordinate</i> | <i>x=810</i>  | <i>0</i> | <i>0.051054012000</i> | <i>0</i> |
| <i>/surface/iso-surface x-coordinate</i> | <i>x=820</i>  | <i>0</i> | <i>0.052100550000</i> | <i>0</i> |
| <i>/surface/iso-surface x-coordinate</i> | <i>x=830</i>  | <i>0</i> | <i>0.053010155000</i> | <i>0</i> |
| <i>/surface/iso-surface x-coordinate</i> | <i>x=840</i>  | <i>0</i> | <i>0.054007340000</i> | <i>0</i> |
| <i>/surface/iso-surface x-coordinate</i> | <i>x=850</i>  | <i>0</i> | <i>0.055067062000</i> | <i>0</i> |
| <i>/surface/iso-surface x-coordinate</i> | <i>x=860</i>  | <i>0</i> | <i>0.056003463000</i> | <i>0</i> |
| <i>/surface/iso-surface x-coordinate</i> | <i>x=870</i>  | <i>0</i> | <i>0.057007115000</i> | <i>0</i> |
| <i>/surface/iso-surface x-coordinate</i> | <i>x=880</i>  | <i>0</i> | <i>0.058033735000</i> | <i>0</i> |
| <i>/surface/iso-surface x-coordinate</i> | <i>x=890</i>  | <i>0</i> | <i>0.059001986000</i> | <i>0</i> |
| <i>/surface/iso-surface x-coordinate</i> | <i>x=900</i>  | <i>0</i> | <i>0.060018778000</i> | <i>0</i> |
| <i>/surface/iso-surface x-coordinate</i> | <i>x=910</i>  | <i>0</i> | <i>0.061035272000</i> | <i>0</i> |
| <i>/surface/iso-surface x-coordinate</i> | <i>x=920</i>  | <i>0</i> | <i>0.062052429000</i> | <i>0</i> |
| <i>/surface/iso-surface x-coordinate</i> | <i>x=930</i>  | <i>0</i> | <i>0.063034989000</i> | <i>0</i> |
| <i>/surface/iso-surface x-coordinate</i> | <i>x=940</i>  | <i>0</i> | <i>0.064073920000</i> | <i>0</i> |
| <i>/surface/iso-surface x-coordinate</i> | <i>x=950</i>  | <i>0</i> | <i>0.065121002000</i> | <i>0</i> |
| <i>/surface/iso-surface x-coordinate</i> | <i>x=960</i>  | <i>0</i> | <i>0.066029102000</i> | <i>0</i> |
| <i>/surface/iso-surface x-coordinate</i> | <i>x=970</i>  | <i>0</i> | <i>0.067020662000</i> | <i>0</i> |
| <i>/surface/iso-surface x-coordinate</i> | <i>x=980</i>  | <i>0</i> | <i>0.068069942000</i> | <i>0</i> |
| <i>/surface/iso-surface x-coordinate</i> | <i>x=990</i>  | <i>0</i> | <i>0.069070466000</i> | <i>0</i> |
| <i>/surface/iso-surface x-coordinate</i> | <i>x=1000</i> | <i>0</i> | <i>0.070028536000</i> | <i>0</i> |
| <i>/surface/iso-surface x-coordinate</i> | <i>x=1010</i> | <i>0</i> | <i>0.071020298000</i> | <i>0</i> |
| <i>/surface/iso-surface x-coordinate</i> | <i>x=1020</i> | <i>0</i> | <i>0.072034538000</i> | <i>0</i> |
| <i>/surface/iso-surface x-coordinate</i> | <i>x=1030</i> | <i>0</i> | <i>0.073132642000</i> | <i>0</i> |
| <i>/surface/iso-surface x-coordinate</i> | <i>x=1040</i> | <i>0</i> | <i>0.074015833000</i> | <i>0</i> |

|  |              |          |                       |          |
|--|--------------|----------|-----------------------|----------|
| <i>/surface/iso-surface x-coordinate</i> | <i>x=105</i> | <i>0</i> | <i>0.075042658000</i> | <i>0</i> |
| <i>/surface/iso-surface x-coordinate</i> | <i>x=106</i> | <i>0</i> | <i>0.076076262000</i> | <i>0</i> |
| <i>/surface/iso-surface x-coordinate</i> | <i>x=107</i> | <i>0</i> | <i>0.077053390000</i> | <i>0</i> |
| <i>/surface/iso-surface x-coordinate</i> | <i>x=108</i> | <i>0</i> | <i>0.078066923000</i> | <i>0</i> |
| <i>/surface/iso-surface x-coordinate</i> | <i>x=109</i> | <i>0</i> | <i>0.079033189000</i> | <i>0</i> |
| <i>/surface/iso-surface x-coordinate</i> | <i>x=110</i> | <i>0</i> | <i>0.080001570000</i> | <i>0</i> |
| <i>/surface/iso-surface x-coordinate</i> | <i>x=111</i> | <i>0</i> | <i>0.081121959000</i> | <i>0</i> |
| <i>/surface/iso-surface x-coordinate</i> | <i>x=112</i> | <i>0</i> | <i>0.082010053000</i> | <i>0</i> |
| <i>/surface/iso-surface x-coordinate</i> | <i>x=113</i> | <i>0</i> | <i>0.083004795000</i> | <i>0</i> |
| <i>/surface/iso-surface x-coordinate</i> | <i>x=114</i> | <i>0</i> | <i>0.084001727000</i> | <i>0</i> |
| <i>/surface/iso-surface x-coordinate</i> | <i>x=115</i> | <i>0</i> | <i>0.085047834000</i> | <i>0</i> |
| <i>/surface/iso-surface x-coordinate</i> | <i>x=116</i> | <i>0</i> | <i>0.086001419000</i> | <i>0</i> |
| <i>/surface/iso-surface x-coordinate</i> | <i>x=117</i> | <i>0</i> | <i>0.087004252000</i> | <i>0</i> |
| <i>/surface/iso-surface x-coordinate</i> | <i>x=118</i> | <i>0</i> | <i>0.088066518000</i> | <i>0</i> |
| <i>/surface/iso-surface x-coordinate</i> | <i>x=119</i> | <i>0</i> | <i>0.090043880000</i> | <i>0</i> |
| <i>/surface/iso-surface x-coordinate</i> | <i>x=120</i> | <i>0</i> | <i>0.095003150000</i> | <i>0</i> |
| <i>/surface/iso-surface x-coordinate</i> | <i>x=121</i> | <i>0</i> | <i>0.100029290000</i> | <i>0</i> |
| <i>/surface/iso-surface x-coordinate</i> | <i>x=122</i> | <i>0</i> | <i>0.105081560000</i> | <i>0</i> |
| <i>/surface/iso-surface x-coordinate</i> | <i>x=123</i> | <i>0</i> | <i>0.110036040000</i> | <i>0</i> |
| <i>/surface/iso-surface x-coordinate</i> | <i>x=124</i> | <i>0</i> | <i>0.115009540000</i> | <i>0</i> |
| <i>/surface/iso-surface x-coordinate</i> | <i>x=125</i> | <i>0</i> | <i>0.120007130000</i> | <i>0</i> |
| <i>/surface/iso-surface x-coordinate</i> | <i>x=126</i> | <i>0</i> | <i>0.125004530000</i> | <i>0</i> |
| <i>/surface/iso-surface x-coordinate</i> | <i>x=127</i> | <i>0</i> | <i>0.130038710000</i> | <i>0</i> |
| <i>/surface/iso-surface x-coordinate</i> | <i>x=128</i> | <i>0</i> | <i>0.135014130000</i> | <i>0</i> |
| <i>/surface/iso-surface x-coordinate</i> | <i>x=129</i> | <i>0</i> | <i>0.140081810000</i> | <i>0</i> |
| <i>/surface/iso-surface x-coordinate</i> | <i>x=130</i> | <i>0</i> | <i>0.144502160000</i> | <i>0</i> |
| <i>/surface/iso-surface x-coordinate</i> | <i>x=131</i> | <i>0</i> | <i>0.147007870000</i> | <i>0</i> |



## APPENDIX C: AUTOMATIC JOURNAL

```
/file/set-tui-version "20.2"  
(cx-gui-do cx-activate-item "MenuBar*ReadSubMenu*Case...")  
(cx-gui-do cx-set-file-dialog-entries "Select File" ("F:/#IBREN/#PhD Work/ANSYS/Sunil work/  
Mesh - All Models/Other model Meshes/Serration1.cas") "All Case Files (*.cas* *.msh* *.MSH*") )  
  
(cx-gui-do cx-set-list-tree-selections "NavigationPane*List_Tree1" (list "Setup|General"))  
(cx-gui-do cx-activate-item "NavigationPane*List_Tree1")  
(cx-gui-do cx-set-list-tree-selections "NavigationPane*List_Tree1" (list "Setup|General"))  
(cx-gui-do cx-set-toggle-button2 "General*Table1*Table2(Solver)*ToggleBox5(Time)*Steady" #t)  
(cx-gui-do cx-activate-item "General*Table1*Table2(Solver)*ToggleBox5(Time)*Steady")  
  
(cx-gui-do cx-set-list-tree-selections "NavigationPane*List_Tree1" (list "Setup|Models"))  
(cx-gui-do cx-activate-item "NavigationPane*List_Tree1")  
(cx-gui-do cx-set-list-tree-selections "NavigationPane*List_Tree1" (list "Setup|Models"))  
(cx-gui-do cx-set-list-selections "Models*Table1*List1(Models)" ( 2))  
(cx-gui-do cx-activate-item "Models*Table1*List1(Models)")  
(cx-gui-do cx-activate-item "Models*Table1*PushButton2(Edit)")  
(cx-gui-do cx-set-toggle-button2 "Viscous Model*Table1*ToggleBox1(Model)*k-omega (2 eqn)" #t)  
(cx-gui-do cx-activate-item "Viscous Model*Table1*ToggleBox1(Model)*k-omega (2 eqn)")  
(cx-gui-do cx-set-toggle-button2 "Viscous Model*Table1*ToggleBox7(k-omega Model)*SST" #t)  
(cx-gui-do cx-activate-item "Viscous Model*Table1*ToggleBox7(k-omega Model)*SST")  
(cx-gui-do cx-activate-item "Viscous Model*PanelButtons*PushButton1(OK)")  
  
(cx-gui-do cx-set-list-tree-selections "NavigationPane*List_Tree1" (list "Setup|Materials|Fluid|air"))  
(cx-gui-do cx-activate-item "NavigationPane*List_Tree1")  
(cx-gui-do cx-set-list-tree-selections "NavigationPane*List_Tree1" (list "Setup|Materials|Fluid|air"))  
(cx-gui-do cx-set-real-entry-list "Create/Edit Materials*RealEntry10" ( 1.225))  
(cx-gui-do cx-set-real-entry-list "Create/Edit Materials*RealEntry16" ( 1.7894e-05))  
(cx-gui-do cx-activate-item "Create/Edit Materials*PanelButtons*PushButton3(Change/Create)")  
(cx-gui-do cx-activate-item "Create/Edit Materials*PanelButtons*PushButton1(Close)")  
  
(cx-gui-do cx-set-list-tree-selections "NavigationPane*List_Tree1" (list "Setup|Boundary Conditions"))  
(cx-gui-do cx-activate-item "NavigationPane*List_Tree1")  
(cx-gui-do cx-set-list-tree-selections "NavigationPane*List_Tree1" (list "Setup|Boundary Conditions"))  
(cx-gui-do cx-set-list-selections "Boundary Conditions*Table1*List2(Zone)" ( 4))  
(cx-gui-do cx-activate-item "Boundary Conditions*Table1*List2(Zone)")  
(cx-gui-do cx-activate-item "Boundary Conditions*Table1*Table3*Table4*ButtonBox1*PushButton1(Edit)")  
(cx-gui-do cx-activate-tab-index "Velocity Inlet*Frame2*Frame2" 0)  
(cx-gui-do cx-activate-tab-index "Velocity Inlet*Frame2*Frame2" 1)  
(cx-gui-do cx-activate-tab-index "Velocity Inlet*Frame2*Frame2" 0)  
(cx-gui-do cx-activate-tab-index "Velocity Inlet*Frame2*Frame2" 2)  
(cx-gui-do cx-activate-tab-index "Velocity Inlet*Frame2*Frame2" 0)  
(cx-gui-do cx-activate-tab-index "Velocity Inlet*Frame2*Frame2" 3)  
(cx-gui-do cx-activate-tab-index "Velocity Inlet*Frame2*Frame2" 0)  
(cx-gui-do cx-activate-tab-index "Velocity Inlet*Frame2*Frame2" 4)  
(cx-gui-do cx-activate-tab-index "Velocity Inlet*Frame2*Frame2" 0)  
(cx-gui-do cx-activate-tab-index "Velocity Inlet*Frame2*Frame2" 5)  
(cx-gui-do cx-activate-tab-index "Velocity Inlet*Frame2*Frame2" 0)  
(cx-gui-do cx-activate-tab-index "Velocity Inlet*Frame2*Frame2" 6)  
(cx-gui-do cx-activate-tab-index "Velocity Inlet*Frame2*Frame2" 0)  
(cx-gui-do cx-activate-tab-index "Velocity Inlet*Frame2*Frame2" 7)  
(cx-gui-do cx-activate-tab-index "Velocity Inlet*Frame2*Frame2" 0)  
(cx-gui-do cx-set-list-selections "Velocity Inlet*Frame2*Frame2*Frame1(Momentum)  
*Table1*DropDownList6(Velocity Specification Method)" ( 0))  
(cx-gui-do cx-enable-apply-button "Velocity Inlet")  
(cx-gui-do cx-activate-item "Velocity Inlet*Frame2*Frame2*Frame1(Momentum)  
*Table1*DropDownList6(Velocity Specification Method)")  
(cx-gui-do cx-set-expression-entry "Velocity Inlet*Frame2*Frame2*Frame1(Momentum)  
*Table1*Table8*ExpressionEntry1(Velocity Magnitude)" ("15" . 0))  
(cx-gui-do cx-set-expression-entry "Velocity Inlet*Frame2*Frame2*Frame1(Momentum)  
*Table1*Table19*ExpressionEntry1(X-Component of Flow Direction)" ("0.995" . 0))  
(cx-gui-do cx-set-expression-entry "Velocity Inlet*Frame2*Frame2*Frame1(Momentum)  
*Table1*Table20*ExpressionEntry1(Y-Component of Flow Direction)" ("0.0125" . 0))  
(cx-gui-do cx-activate-item "Velocity Inlet*PanelButtons*PushButton1(OK)")  
(cx-gui-do cx-activate-item "Velocity Inlet*PanelButtons*PushButton2(Cancel)")  
  
(cx-gui-do cx-set-list-tree-selections "NavigationPane*List_Tree1" (list "Setup|Reference Values"))  
(cx-gui-do cx-activate-item "NavigationPane*List_Tree1")  
(cx-gui-do cx-set-list-tree-selections "NavigationPane*List_Tree1" (list "Setup|Reference Values"))  
(cx-gui-do cx-set-list-selections "Reference Values*DropDownList1(Compute from)" ( 10))  
(cx-gui-do cx-activate-item "Reference Values*DropDownList1(Compute from)")  
(cx-gui-do cx-set-real-entry-list "Reference Values*Table2(Reference Values)*RealEntry1(Area)" ( 0.0444))  
(cx-gui-do cx-activate-item "Reference Values*Table2(Reference Values)*RealEntry1(Area)")  
(cx-gui-do cx-set-real-entry-list "Reference Values*Table2(Reference Values)*RealEntry5(Length)" ( 0.15))  
(cx-gui-do cx-activate-item "Reference Values*Table2(Reference Values)*RealEntry5(Length)")
```

```

(cx-gui-do cx-set-list-tree-selections "NavigationPane*List_Tree1" (list "Solution|Methods"))
(cx-gui-do cx-activate-item "NavigationPane*List_Tree1")
(cx-gui-do cx-set-list-tree-selections "NavigationPane*List_Tree1" (list "Solution|Methods"))
(cx-gui-do cx-set-list-selections "Solution Methods*Table1*Table2(Pressure-Velocity Coupling)
*DropDownList2(Scheme)" ( 3))
(cx-gui-do cx-activate-item "Solution Methods*Table1*Table2(Pressure-Velocity Coupling)
*DropDownList2(Scheme)")
(cx-gui-do cx-set-list-selections "Solution Methods*Table1*Table3(Spatial Discretization)
*DropDownList1(Gradient)" ( 1))
(cx-gui-do cx-activate-item "Solution Methods*Table1*Table3(Spatial Discretization)
*DropDownList1(Gradient)")
(cx-gui-do cx-set-list-selections "Solution Methods*Table1*Table3(Spatial Discretization)
*DropDownList2(Pressure)" ( 0))
(cx-gui-do cx-activate-item "Solution Methods*Table1*Table3(Spatial Discretization)
*DropDownList2(Pressure)")
(cx-gui-do cx-set-list-selections "Solution Methods*Table1*Table3(Spatial Discretization)
*DropDownList3(Momentum)" ( 0))
(cx-gui-do cx-activate-item "Solution Methods*Table1*Table3(Spatial Discretization)
*DropDownList3(Momentum)")
(cx-gui-do cx-set-list-selections "Solution Methods*Table1*Table3(Spatial Discretization)
*DropDownList4(Turbulent Kinetic Energy)" ( 0))
(cx-gui-do cx-activate-item "Solution Methods*Table1*Table3(Spatial Discretization)
*DropDownList4(Turbulent Kinetic Energy)")
(cx-gui-do cx-set-list-selections "Solution Methods*Table1*Table3(Spatial Discretization)
*DropDownList5(Specific Dissipation Rate)" ( 0))
(cx-gui-do cx-activate-item "Solution Methods*Table1*Table3(Spatial Discretization)
*DropDownList5(Specific Dissipation Rate)")
(cx-gui-do cx-set-toggle-button2 "Solution Methods*Table1*Table7*CheckBox1(High Order Term Relaxation)" #t)
(cx-gui-do cx-activate-item "Solution Methods*Table1*Table7*CheckBox1(High Order Term Relaxation)")
(cx-gui-do cx-activate-item "Solution Methods*Table1*Table7*PushButton2(Options)")
(cx-gui-do cx-set-real-entry-list "Relaxation Options*Table2(Relaxation Factor)*RealEntry1" ( 0.75))
(cx-gui-do cx-activate-item "Relaxation Options*PanelButtons*PushButton1(OK)")

(cx-gui-do cx-set-list-tree-selections "NavigationPane*List_Tree1" (list "Solution|Controls"))
(cx-gui-do cx-activate-item "NavigationPane*List_Tree1")
(cx-gui-do cx-set-list-tree-selections "NavigationPane*List_Tree1" (list "Solution|Controls"))
(cx-gui-do cx-set-real-entry-list "Solution Controls*Table1*Table*RealEntry2(Flow Courant Number)" ( 0.5))
(cx-gui-do cx-activate-item "Solution Controls*Table1*Table*RealEntry2(Flow Courant Number)")
(cx-gui-do cx-activate-item "Solution Controls*Table1*Table2*PushButton5(Limits)")
(cx-gui-do cx-set-real-entry-list "Solution Limits*Table1*RealEntry1(Minimum Absolute Pressure)" ( 1e+20))
(cx-gui-do cx-set-real-entry-list "Solution Limits*Table1*RealEntry2(Maximum Absolute Pressure)" ( 1e+20))
(cx-gui-do cx-set-real-entry-list "Solution Limits*Table1*RealEntry16(Maximum Turb Viscosity Ratio)" ( 1e+20))
(cx-gui-do cx-activate-item "Solution Limits*PanelButtons*PushButton1(OK)")

(cx-gui-do cx-set-list-tree-selections "NavigationPane*List_Tree1" (list "Solution|Monitors"))
(cx-gui-do cx-activate-item "NavigationPane*List_Tree1")
(cx-gui-do cx-set-list-tree-selections "NavigationPane*List_Tree1" (list "Solution|Monitors"))
(cx-gui-do cx-set-list-tree-selections "NavigationPane*List_Tree1" (list "Solution|Monitors|Residual"))
(cx-gui-do cx-set-list-tree-selections "NavigationPane*List_Tree1" (list "Solution|Monitors|Residual"))
(cx-gui-do cx-activate-item "NavigationPane*List_Tree1")
(cx-gui-do cx-set-list-tree-selections "NavigationPane*List_Tree1" (list "Solution|Monitors|Residual"))
(cx-gui-do cx-set-toggle-button2 "Residual Monitors*Table1*Table2*CheckBox3(Show Advanced Options)" #t)
(cx-gui-do cx-activate-item "Residual Monitors*Table1*Table2*CheckBox3(Show Advanced Options)")
(cx-gui-do cx-set-list-selections "Residual Monitors*Table1*Table2*Table4*Table1*Table3
*DropDownList1(Convergence Criterion)" ( 1))
(cx-gui-do cx-activate-item "Residual Monitors*Table1*Table2*Table4*Table1*Table3
*DropDownList1(Convergence Criterion)")
(cx-gui-do cx-activate-item "Residual Monitors*PanelButtons*PushButton1(OK)")

(cx-gui-do cx-set-list-tree-selections "NavigationPane*List_Tree1" (list "Solution|Initialization"))
(cx-gui-do cx-activate-item "NavigationPane*List_Tree1")
(cx-gui-do cx-set-list-tree-selections "NavigationPane*List_Tree1" (list "Solution|Initialization"))
(cx-gui-do cx-set-toggle-button2 "Solution Initialization*Table1*ToggleBox3(Initialization Methods)
*Standard Initialization" #t)
(cx-gui-do cx-activate-item "Solution Initialization*Table1*ToggleBox3(Initialization Methods)
*Standard Initialization")
(cx-gui-do cx-set-list-selections "Solution Initialization*Table1*DropDownList1(Compute from)" ( 5))
(cx-gui-do cx-activate-item "Solution Initialization*Table1*DropDownList1(Compute from)")
(cx-gui-do cx-activate-item "Solution Initialization*Table1*Frame8*PushButton1(Initialize)")

(cx-gui-do cx-set-list-tree-selections "NavigationPane*List_Tree1" (list "Solution|Calculation Activities"))
(cx-gui-do cx-set-list-tree-selections "NavigationPane*List_Tree1" (list "Solution|Calculation Activities"))
(cx-gui-do cx-activate-item "NavigationPane*List_Tree1")
(cx-gui-do cx-set-list-tree-selections "NavigationPane*List_Tree1" (list "Solution|Calculation Activities"))
(cx-gui-do cx-set-integer-entry "Calculation Activities*Table1*IntegerEntry1(Autosave Every (Iterations))" 500)
(cx-gui-do cx-activate-item "Calculation Activities*Table1*IntegerEntry1(Autosave Every (Iterations))")

```

```
(cx-gui-do cx-set-list-tree-selections "NavigationPane*List_Tree1" (list "Solution/Run Calculation"))
(cx-gui-do cx-activate-item "NavigationPane*List_Tree1")
(cx-gui-do cx-set-list-tree-selections "NavigationPane*List_Tree1" (list "Solution/Run Calculation"))
(cx-gui-do cx-set-integer-entry "Run Calculation*Table1*Table3(Parameters)*Table1*Table1*IntegerEntry1(Number of Iterations)" 1000)
(cx-gui-do cx-activate-item "Run Calculation*Table1*Table3(Parameters)*Table1*Table1*IntegerEntry1(Number of Iterations)")
(cx-gui-do cx-set-integer-entry "Run Calculation*Table1*Table3(Parameters)*Table3*Table1*IntegerEntry1(Reporting Interval)" 50)
(cx-gui-do cx-activate-item "Run Calculation*Table1*Table3(Parameters)*Table3*Table1*IntegerEntry1(Reporting Interval)")
(cx-gui-do cx-set-integer-entry "Run Calculation*Table1*Table3(Parameters)*Table1*Table1*IntegerEntry3(Profile Update Interval)" 50)
(cx-gui-do cx-activate-item "Run Calculation*Table1*Table3(Parameters)*Table1*Table1*IntegerEntry3(Profile Update Interval)")
(cx-gui-do cx-activate-item "Run Calculation*Table1*Table6(Solution Advancement)*Table1*PushButton1(Calculate)')
```

